Doctoral Dissertation

Application of Ag-based complex for low-temperature die-bonding

WANG CHUNCHENG

January 2025

Graduate School of Engineering,
Osaka University

Supervisor

Professor Hiroshi Nishikawa, Ph.D.

Joining and Welding Research Institute

Osaka University

Doctoral Committee

Professor Hiroshi Nishikawa, Ph.D.

Joining and Welding Research Institute

Osaka University

Professor Shinji Fukumoto, Ph.D.

Division of Materials and Manufacturing Science, Graduate School of Engineering

Osaka University

Professor Keisuke Uenishi, Ph.D.

Department of Management of Industry and Technology, Graduate School of Engineering

Osaka University

Contents

List of Tables

List of Figures

Chapter 1: Research background

1.1 Challenge of power devices in harsh working conditions

1.1.1 Application of power devices in advanced technologies

Green-energy-related fields, such as photovoltaic generation systems, wind turbines, electric vehicles (EVs), and quick charging stations, have recently developed rapidly to reduce carbon dioxide (CO_2) emissions [1–3]. Power devices commonly used in power supplies, converters, inverters, and various high-power electronics are important in using green energy efficiently [4]. The main function of the power device is to control and adjust the electricity transferred in the orthogonal circuit to stabilize current, voltage, and power control [5,6]. Therefore, power devices are essential for the entire process of green energy use such as power generation, transmission, and consumption. Over the last few decades, silicon (Si) has dominated semiconductor materials for power devices because of its low cost and mature manufacturing process [7]. However, these newly developed technologies have presented significant challenges for Si-based power devices as the small band gap of 1.12 eV of Si cannot meet their high voltage requirements [8]. Under this condition, researchers have to find alternative candidates to replace Si in power devices.

1.1.2 Application of wide bandgap (WBG) power devices in harsh working conditions

Nowadays, WBG semiconductors, such as silicon carbide (SiC) and gallium nitride (GaN), are considered the most promising candidates for application in power devices due to their

superior intrinsic physical properties, including high breakdown voltage, thermal conductivity, chemical resistance, and electron mobility [9]. **Table 1.1** compares the physical properties of Si, SiC, and GaN. Their excellent physical properties allow WBG power devices to operate at higher current density, voltage, frequency, and temperature than Si-based power devices [10–12]. For example, the breakdown voltage of 1700 V SiC-based Schottky barrier diodes (SBDs) is over 8 times that of 200 V Si-based SBDs [13]. The breakdown voltage of SiC metal-oxide-semiconductor field-effect transistors (MOSFETs) is approximately 10 kV, which is approximately 10 times that of 1 kV Si MOSFETs [13]. SiC devices excel in switching performance compared with Si devices, demonstrating a significantly reduced reverse recovery rate at the same voltage level [14]. **Fig. 1.1** demonstrates that these superior properties render WBG power devices suitable for a wide range of applications such as domestic appliances, EVs, and transportation.

1.1.3 Insulated gate bipolar transistor (IGBT) power modules and main reliability issues

Onboard converters and inverters must have high power density and low weight to meet the EV requirements [15]. An IGBT is a promising candidate to meet the above requirements. An IGBT is a voltage-driven power module that combines the advantages of bipolar junction transistor (BJT) and MOSFET [16,17]. Therefore, an IGBT is capable of both the high-current single-gate control characteristics of MOSFETs and the low-saturation-voltage capability of BJT. IGBTs are divided into two categories according to the package modules: press-packed and soldered [18,19]. The soldered IGBT module is most commonly used in

Table 1.1 Physical property differences between Si, SiC and GaN [9].

Physical property	Si	SiC	GaN	unit
Band Gap	1.1	3.26	3.44	eV
Thermal Conductivity	1.5	3.7	1.3	W/cm. K
Electron Mobility	1300	900	900-1200	$Cm^2/V.\ s$
Electron Saturation Velocity	10	22	25	(10^6)cm/\sec
Critical Field	0.3	3	3.5	(10^6)V/cm

industry and normally consists of bonding wire, dies, bondline, ceramic, copper layer, heat sink, and encapsulation materials as shown in **Fig. 1.2** [18,20]. One of the key manufacturing processes is reflow soldering. As shown in **Fig. 1.3**, the reflow soldering of IGBT can be divided into two categories: die and substrate bonding. For die bonding, the back side of the die is bonded on the top Cu layer of the direct bond copper (DBC) substrate. Subsequently, the DBC substrate is bonded on a base plate [21]. This means that the bondline provides mechanical support and electrical conductivity and is also essential for the heat dissipation of IGBT power modules [22].

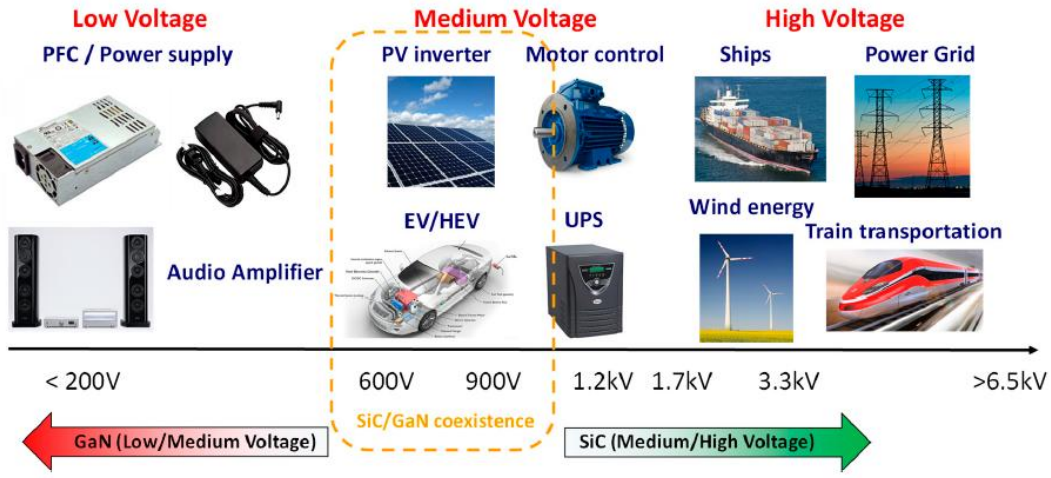

Fig. 1.1 Various applications of GaN and SiC power devices [12].

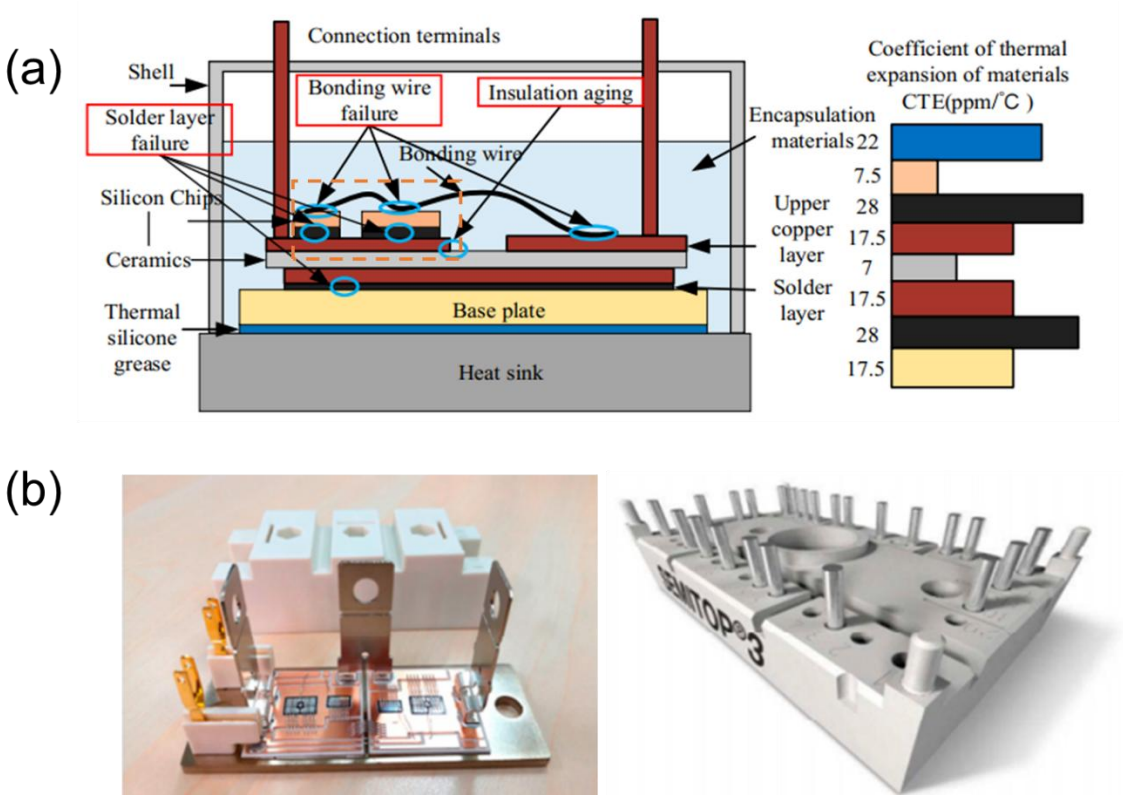

Fig. 1.2 Structure of IGBT module. (a) Schematic diagram of the package structure of a solder-type IGBT module and (b) the corresponding optical image [20].

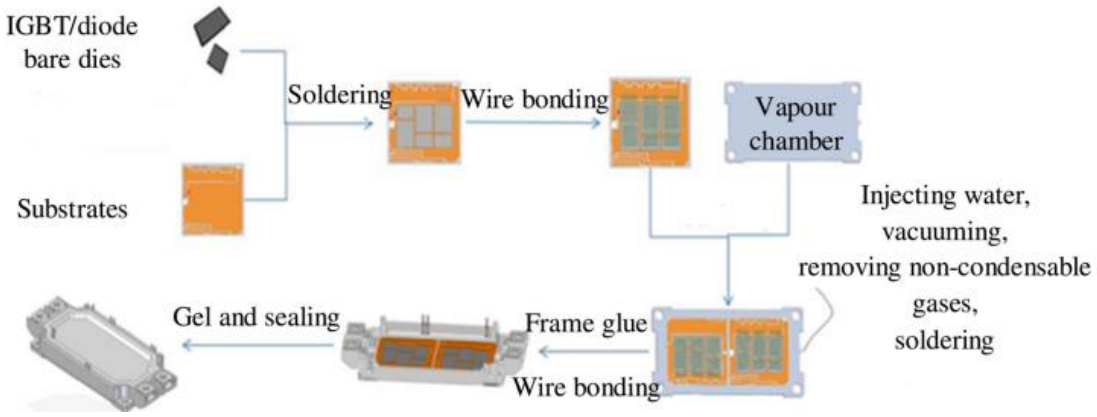

Fig. 1.3 Fabrication process of IGBT semiconductor [21].

The IGBT module is one of the most frequent failure devices in EVs because of their various work conditions such as start, stop, acceleration, and deceleration [23]. For researchers and engineers, determining the causes of failure is an effective means of prolonging the lifetime of WBG power devices. There are several causes for WBG power device failures such as temperature, vibration, humidity, overvoltage, and overcurrent [20]. Temperature comprises the largest proportion of these factors of failures [24]. A high junction temperature can easily lead to the breakdown of the PN junction of power devices, which affects the voltage transmission characteristics and interference resistance [20,25]. Furthermore, persistent temperature changes can lead to fatigue failure of bond wires, aging of the bondline, and cracking of the substrate in **Fig. 1.4** [20]. High junction temperatures can be avoided by dissipating the heat generated by the dies into the air by a heat sink. In this process, the heat passes through the die, upper bondline, DBC substrates, lower bondline, base plate, and heat sink in turn [26]. Therefore, the two bondlines are important in ensuring

the heat dispersion and lifespan of WBG power modules, and this is the starting point of the present study to investigate the bondline.

1.2 Advanced die-bonding techniques in the packaging of WBG power devices

1.2.1 High-temperature alloy solders for die-bonding

In industrial production, Sn-based solders, listed in **Table 1.2**, are commonly used in electronics because of their low cost and good processability [27–29]. These solders are heated by reflow, which is a multi-step process, including preheating, reflow, and cooling [30]. Additionally, a reasonable heating profile and vacuum atmosphere are necessary to avoid voids trapped in solder joints [31]. During reflow soldering, melting solders react with the substrate to generate intermetallic compounds (IMC), such as Cu_6Sn_5 and $CuSn_3$, which provide high strength for the interface [32,33]. However, the high operation temperature of

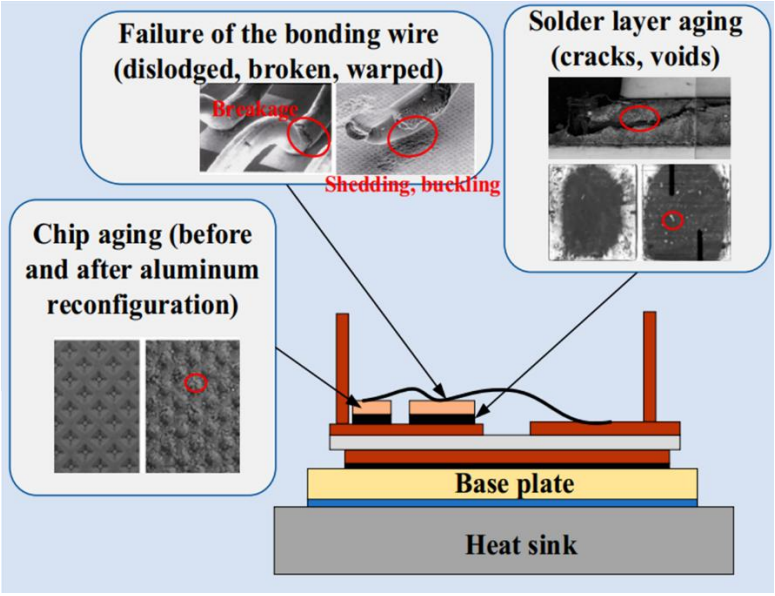

Fig. 1.4 Common failures caused by temperature [20].

WBG power devices tends to cause serious reliability issues because of the low melting point of Sn-based solder [34,35]. A commonly used solder alloy in power device die-bonding is Sn-3.0Ag-0.5Cu (SAC305) due to its good processability and mechanical properties. SAC305 has a melting point about 217 ºC, and its reflow temperature usually is up to 250 ºC [36,37]. Therefore, "high-temperature solder alloy" in the study refers to the solder alloy with a process temperature higher than 250 ºC.

In the past few years, some high-temperature devices used solder alloys containing Pb or Au due to their high melting points, such as 296 ºC of Pb–5Sn–2.5Ag [38] and 278 ºC of Au–20Sn [39]. Pb-containing solders exhibited good bonding performance and low cost but were banned by the Restriction of Hazardous Substances (RoHS) as they are highly toxic to

Table 1.2 Commonly used Sn-based solder alloys in electronics [29].

Alloy system	Composition	Melting range (ºC)
Melting temperature range 180–200 ºC		
Sn-Zn-Bi	Sn-8Zn3Bi	189–199
Sn-Zn	Sn-9Zn (eutectic)	198.5
Melting temperature range 200–230 ºC		
Sn-Ag	Sn-3.5Ag (eutectic)	221
	Sn-2Ag	221–226
Sn-Ag-Cu	Sn3.9Ag0.6Cu	~217
	Sn-3Ag-0.5Cu (SAC305)	~217
Sn-Cu	Sn-0.7Cu (eutectic)	227

the environment and humans [40]. In addition, the high cost of Au-containing solders limits their wide application. Therefore, there is an urgent need to develop low-cost Pb-free bonding materials with a high melting point to fulfill the requirements of WBG power devices.

1.2.2 Transient liquid phase (TLP) bonding

Pb-free die-bonding processes, such as TLP bonding [41] and metal-particle bonding [42,43], were recently proposed to meet the requirements of high-temperature reliability. The two Pb-free die-bonding processes can be processed at low temperatures below 250 ^{o}C but operate at much higher temperatures above 300 ^{o}C. **Table 1.3** compares the current die-bonding processes [44].

Soldering involves melting, wetting, and formation of solid bonds by solidification of liquid alloy [45]. Unlikely, the formation of solid bonds during the TLP bonding process could be attributed to several possible ways. (1) Melted low-temperature phase (LTP) at the bonding temperature (T_B) diffuses into the high-temperature phase (HTP) to form a solid solution. (2) Continuous consumption of at least one ingredient of LTPs through the formation of IMCs changes the composition of liquid until no liquid remains. (3) A phase precipitates when the phase equilibrium reaction at the liquid-solid interface changes from a two-phase (liquid + IMC) to a three-phase equilibrium (liquid + IMC + precipitates) [46]. To enhance understanding, **Fig. 1.5** depicts a schematic diagram that illustrates a typical process of TLP bonding [47].

As shown in **Fig. 1.6**, TLP bonding techniques can be classified into layer type and paste type [48], which each has its advantages and disadvantages. For example, the die-bondline-substrate sandwich structure is easy to prepare by placing prefabricated metal film [49].

Table 1.3 Typical die-bonding processes and their advantages and disadvantages [44].

		High-temperature alloy soldering		TLP bonding	Sintered Ag bonding
		Pb5Sn2.5Ag soldering	AuSn soldering		
Physical and mechanical properties	Melting temperature (°C)	296	280	>300	961
	Shear strength (MPa)	28	130	20–40	20–80
	Electrical resistivity (μΩ·cm)	19	16.4	—	5
	Thermal conductivity (W/mK)	23	59	—	>100
Form	Paste	Yes	Yes	Yes	Yes
	Wire	Yes	Yes	No	No
	Preform	Yes	Yes	Yes	Yes
Cost	Relative to Pb2Sn2.5Ag	1	>2000	Varied	>40

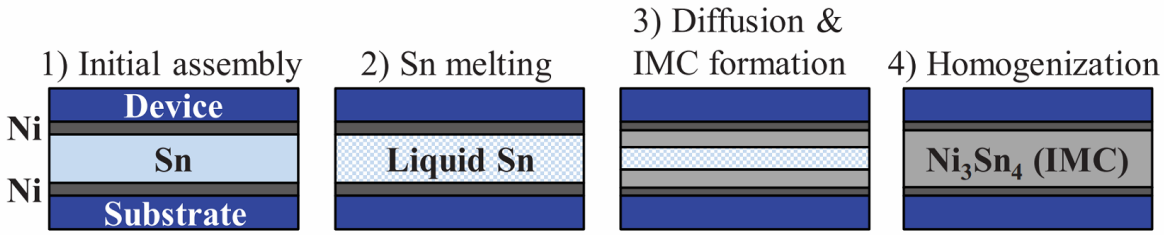

Fig. 1.5 Schematic diagram illustrating a typical TLP process [47].

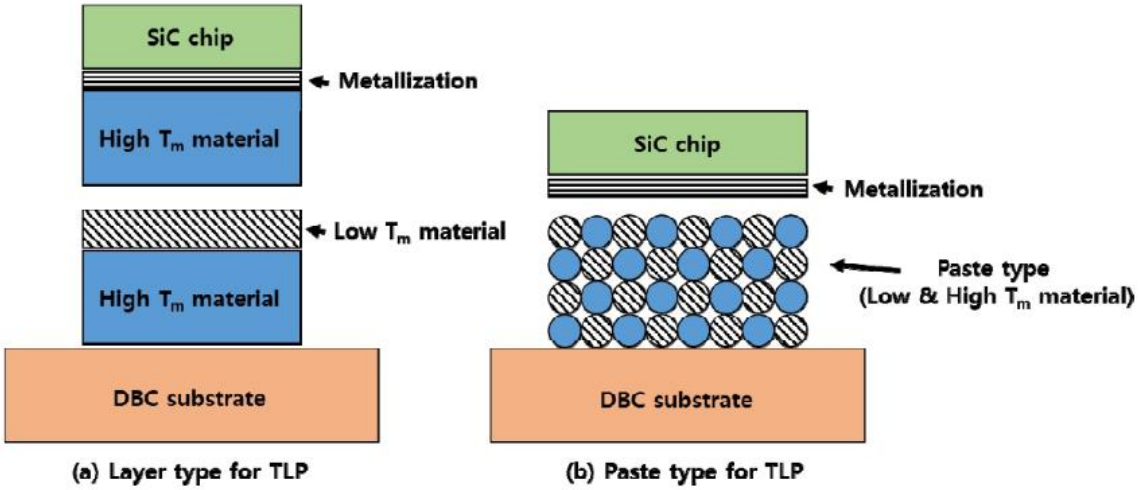

Fig. 1.6 Schematic diagram of TLP bonding technologies. (a) layer type and (b) paste type [48].

However, it needs a long reaction and isothermal solidification time because of the limited contact area between the melted metals and high-melting-point metals [50]. Metal particles in paste type have larger specific surface areas than metal films, resulting in a short process time [51]. However, the formula of paste is complex, and the particle agglomeration is one of the biggest issues [52]. In addition to the type of TLP, the selection of metals is also a

challenge when applying TLP. Sn- and In-based metals are most commonly used in TLP, such as Ni-Sn [53], Cu-Sn [54], Ag-In [55], and Au-In [56]. In terms of the Ag-In group, generating of ζ (Ag_3In) resulted in a remarkably high shear strength of 82.9 MPa at 250 ºC with 10 MPa for 40 min [55]. Although TLP bonding achieves a robust bondline, some issues persist. For example, the volume shrinkage of IMC formation results in voids at the interface, deteriorating bondline reliability [57]. On the other hand, sufficient consumption of LTPs leads to a fully reacted bondline. Some brittle IMCs, such as Cu_3Sn and Ni_3Sn_4, are created, resulting in die-attachments with poor external shock resistance [58,59].

1.2.3 Metal-particle bonding

For die-bonding, metal-particle bonding generally refers to the sintering of Cu or Ag particles [60–62]. Due to the size effect, metal-particle bonding can be conducted at a temperature much lower than the melting temperature of bulk metals [63,64]. After bonding, the obtained joints exhibit similar properties to bulk Cu or Ag, such as high thermal conductivity, high electrical conductivity, and high melting point [65–67]. This means that metal-particle bonding can be processed at temperatures below 250 ºC and serve at high temperatures close to the melting temperature of bulk metals. Therefore, many researchers and engineers focus on the application of metal-particle bonding for die-bonding.

(a) Cu particle bonding

Cu particle bonding exhibits both cost advantages and superior physical properties such as good thermal conductivity and high strength. For example, robust Cu sintered joints with a

high shear strength of 67.41 MPa were achieved at 260 ^{o}C with 5 MPa for 5 min by copper formate coated Cu nanoparticles (Cu-FA) [68]. However, one of the most serious issues of Cu particle bonding is poor oxidation resistance. Given its intrinsic property, the surface of Cu particles tends to be oxidized by the oxygen in the air. The generated Cu oxidation layer blocks the diffusion of Cu atoms during the bonding process. Therefore, high bonding temperatures, high assisted pressures, or specific atmospheres are required to achieve efficient Cu bonding [69]. Several strategies have been proposed to eliminate the negative effects of the Cu oxidation layer, such as using reducing agents [70], Cu@Ag particles [71], and inert or reductive atmospheres [42]. Gao et al. conducted the Cu bonding process in a reductive formic acid atmosphere. During this process, Cu oxides reacted with formic acid, resulting in Cu formate. Subsequently, the Cu formate decomposed into pure Cu and thereby achieved Cu sintered joints with a shear strength of 23 MPa at 300 ^{o}C for 30 min [42]. These hash bonding conditions or complex processes make the practical application of Cu particle bonding difficult.

(b) Ag particle bonding

Compared with Cu particle bonding, Ag particle bonding has been widely used in the die-bonding of WBG power devices. Unlike the negative effects of oxygen on Cu sintering, oxygen facilitates Ag sintering due to Ag nano-volcanic eruption [72]. As shown in **Fig. 1.7**, the prerequisite for this phenomenon is that oxygen atoms easily penetrate the interior of Ag along grain boundaries. This results in Ag-O mixtures with a low melting point at the grain boundary regions. With elevated temperature, thermal stress induces grain boundary

liquation and the spurt of Ag-O fluid. The spurted Ag and Ag_2O redeposit on the parent Ag. Subsequently, an amorphous Ag layer forms after the thermal decomposition of Ag_2O. Homogeneous nucleation and gain growth within the amorphous Ag layer result in massive highly active Ag hillocks, which promote Ag sintering. In addition, the generation of Cu oxides during thermal aging seriously deteriorates joint properties, such as shear strength, thermal conductivity, and electrical conductivity [73]. Therefore, good oxygen resistance renders better production processibility to Ag particle bonding and higher reliability to sintered Ag joints.

1.3 Bonding mechanism and factors determining the formation of robust joints

1.3.1 Underlying mechanism responsible for the particle sintering

Sintering is the process of transforming powder into bulk material by applying pressure or heat without melting it [74,75]. **Fig. 1.8** demonstrates that sintering is generally divided into three stages [76]. At the initial stage, surface diffusion dominates creating necks between adjacent particles, and increasing shear strength [77]. In the second stage, interpenetrating pores shrink along the radial direction, continuously improving density to 90–92% [78]. In the third stage, the collapse of tubular pores leads to small-diameter spherical pores. Ideally, all pores can be eliminated if the bonding conditions are well-optimized [78].

Unlike traditional soldering, sintering occurs through the reduction of Gibbs free energy, which is achieved by substituting high-energy surfaces with low-energy grain boundaries [76]. The high-energy surfaces are attributed to the unsaturated coordination of the atoms at

the surface, whose energy is higher than the atoms inside the particles [76,79]. Subsequently, the grain boundaries are eliminated through grain growth. The change in Gibbs free energy during sintering can be expressed as Equation 1.1:

$$\Delta G = \gamma \Delta A + A \Delta \gamma \qquad 1.1$$

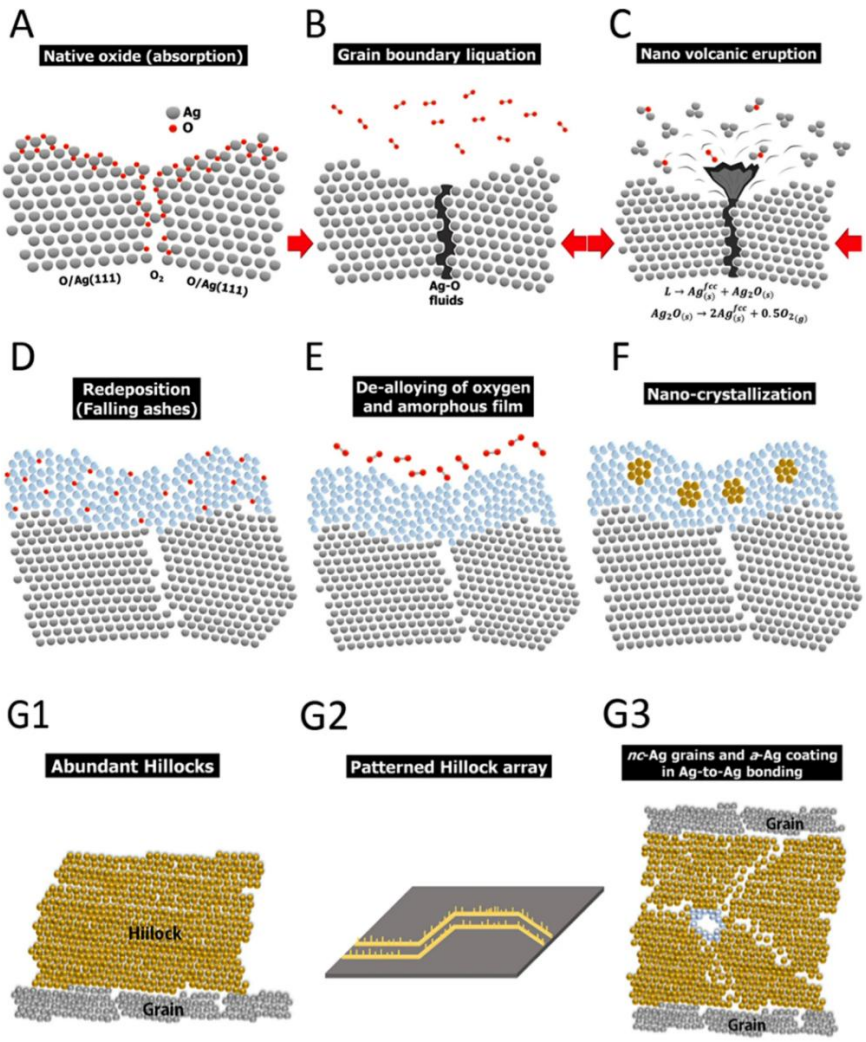

Fig. 1.7 Schematic diagram of Ag nano-volcanic eruption for Ag sintering [72]

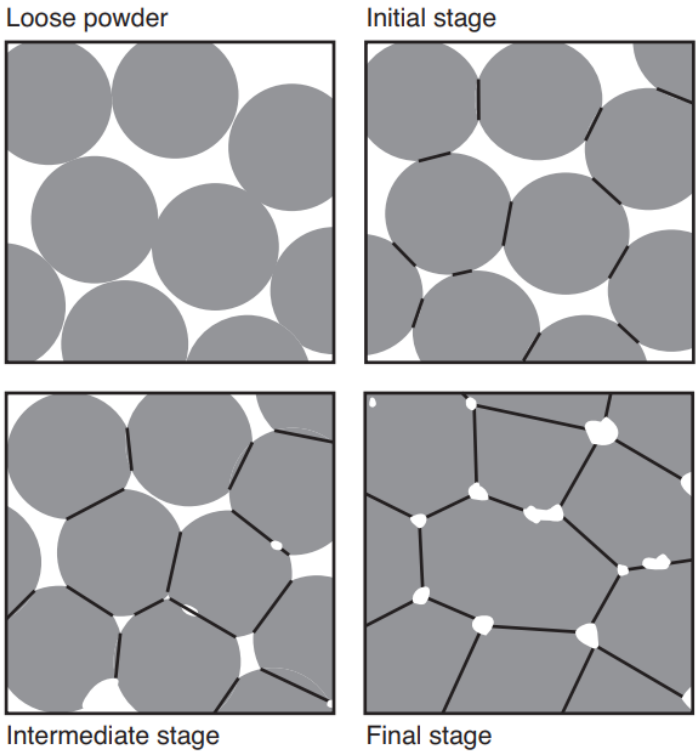

Fig. 1.8 Schematic illustration of the particle sintering process [76].

Where ΔG is the change of Gibbs free energy, γ_s is the surface energy, and ΔA is the change of surface area. During sintering process, the neck formation decreases the total area of particles. Therefore, the first term in Equation 1.1 is negative. In addition, the curvature r at the neck region in **Fig. 1.9** decreases with continuous sintering, decreasing the surface energy. Thus, the second term of Equation 1.1 is also negative. This means that ΔG is always negative in this process, indicating that sintering can occur spontaneously by the reduction of Gibbs free energy [80]. Generally, a decrease in particle size contributes to an increase in the curvature and surface energy. This is why Ag nanoparticle (NP) sintering can occur at lower temperatures than the melting temperature of bulk Ag [81].

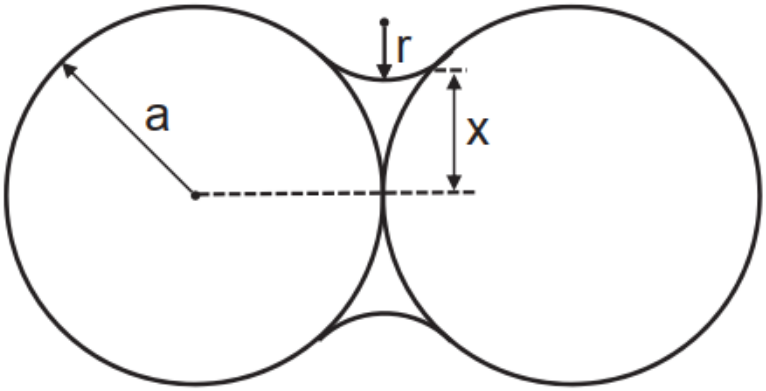

Fig. 1.9 Classical schematic diagram of neck growth during sintering. (a: particle radius, X: neck thickness, and r: neck region curvature) [80].

During the sintering process, the transition from powders to joints can be regarded as a result of mass diffusion. Conventional sintering theory suggests that the concentration difference in vacancies serves as the driving force for mass diffusion [82]. This difference in vacancy concentration can be characterized by Equation 1.2.

$$\Delta C_v = C_{v0} exp(-\frac{\gamma k \Omega}{KT}) - C_{v0} = C_{v0}[exp(-\frac{\gamma k \Omega}{KT}) - 1] \quad 1.2$$

Where C_v is the vacancy concentration for a surface with curvature k, C_{v0} is the vacancy concentration of a flat surface, γ is the surface energy, Ω is the atom volume, K is Boltzmann's constant, and T is the absolute temperature.

As depicted in **Fig. 1.10**, Jia et al. investigated the sintering mechanism by molecular dynamics (MD) simulations with a two-particle model. In Equation 1.2, ΔC_v is positive as the curvature (k) of the neck regions is negative. This means that vacancies with a high

concentration were trapped at the connection area as the formation of necks. As a result, the neck exhibits rapid growth because of the driven diffusion of atoms. Crystal structure changes also accompany the sintering process. As a connection is established between two particles, an amorphous crystal structure first occurs at the necking region, resulting in local disorder with a rapid decline in the face center cubic (*fcc*) structure. With continuous sintering, a shell with amorphous crystal structures appears on the particle surfaces, which indicates that surface diffusion is crucial in the sintering [83].

1.3.2 Effects of bonding conditions

For the die-bonding of WBG power devices, particle bonding aims to achieve robust sintered joints with good joint properties such as high density, high shear strength, and high thermal and electrical conductivity [84]. As shown in **Fig. 1.11**, a reasonable bonding profile

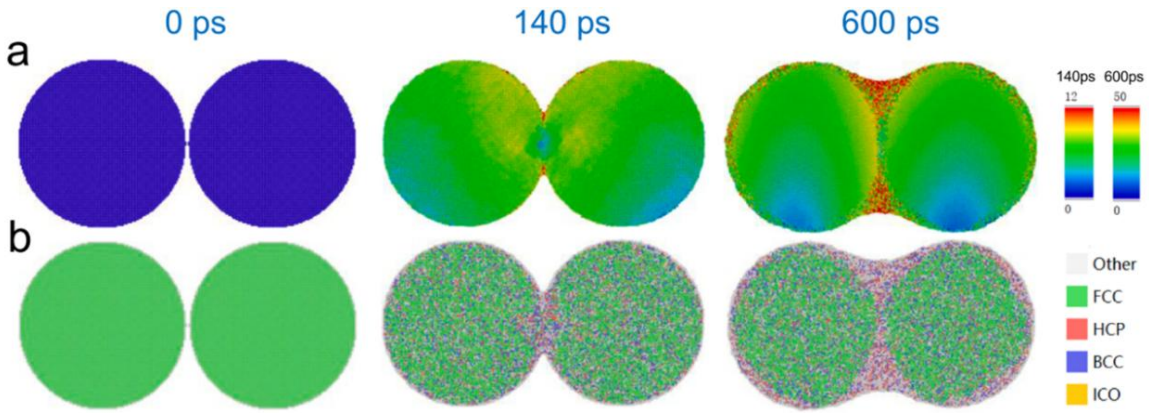

Fig. 1.10 MD simulation of sintering behavior of Ag20Pd nanoalloy at 1175 K. (a) Atom displacement; (b) crystal structure evolution [83].

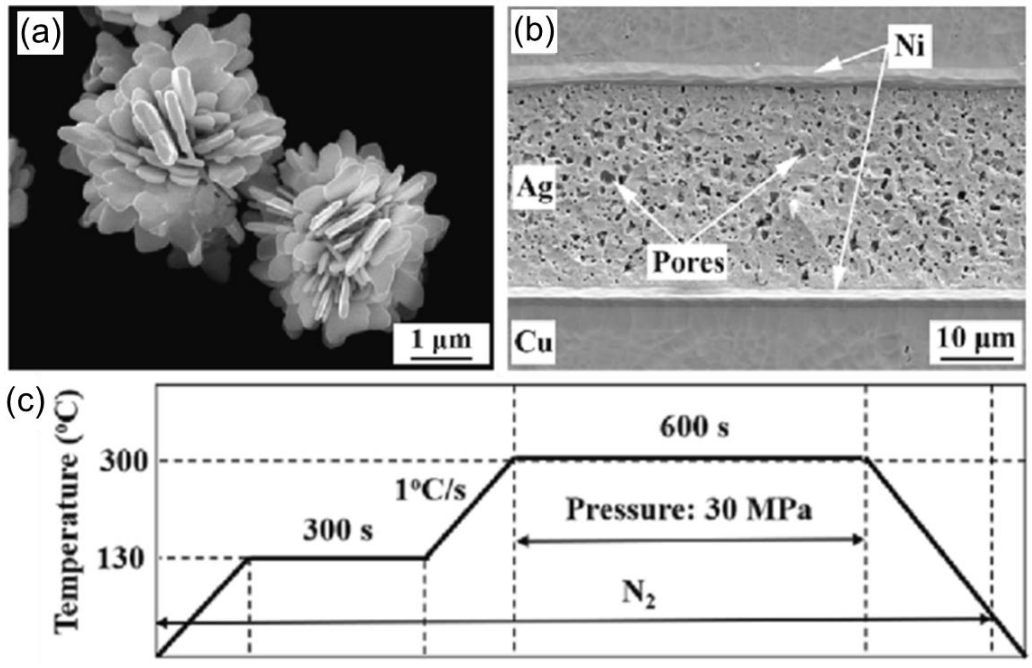

Fig. 1.11 SEM of (a) Ag particles and (b) sintered Ag joints. (c) Corresponding profile for bonding [85].

is necessary to realize robust Ag sintered joints [85]. Generally, a typical bonding profile contains three main factors: temperature, time, and assisted pressure.

(a) Effects of temperature

Organic additives are added to Ag pastes to modify their dispersibility, viscosity, and wettability, enhancing their processability and bonding properties [86]. However, these organics anchoring to the Ag particle surface tend to form an organic shell in **Fig. 1.12** [65,87]. This organic shell hinders sintering by preventing atomic diffusion and intimate contact between Ag particles. High temperatures are required to provide the necessary desorption energy (E_d) and evaporation energy (E_v) to remove absorbed organics [88]. On the other hand, higher sintering temperatures increase the atomic movement and diffusion

rate. As shown in **Fig. 1.13**, the temperature is important in triggering and facilitating neck formation between Ag particles and results in dense Ag joints [74,75].

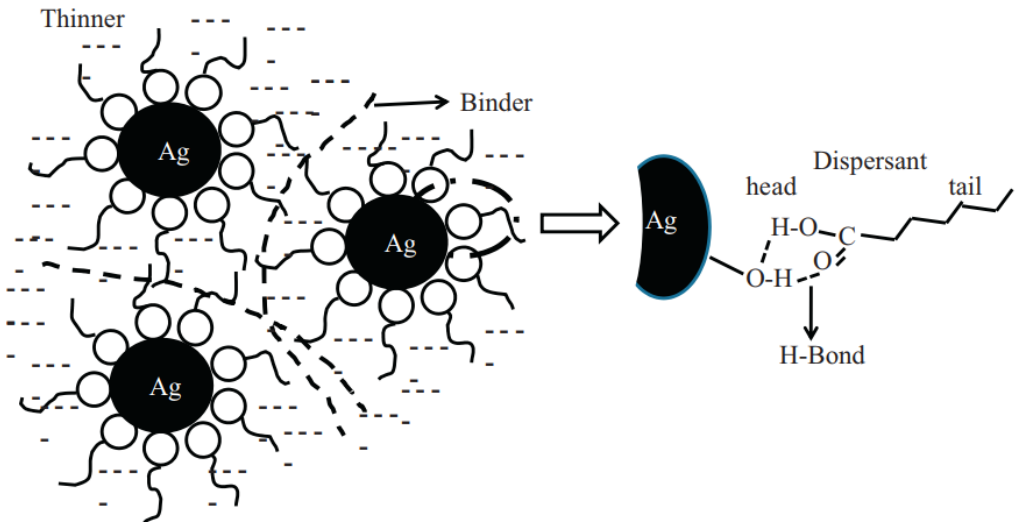

Fig. 1.12 Schematic diagram of the function of organics in Ag paste [65].

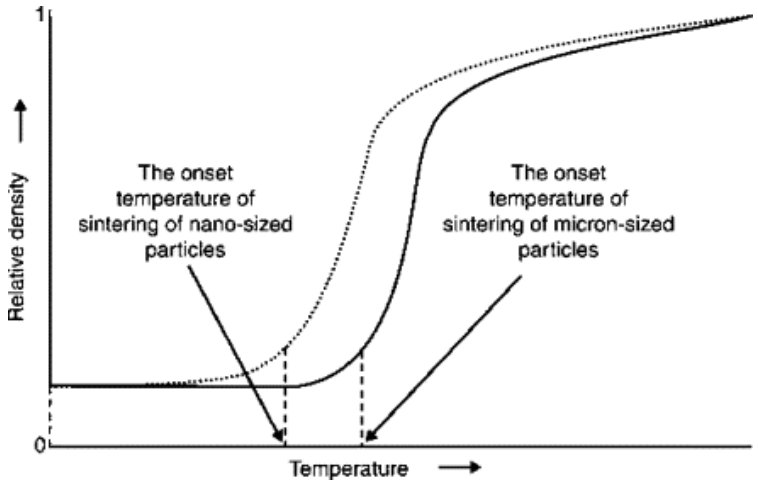

Fig. 1.13 Different onset temperatures of sintering nano and micron-sized particles [75].

Table 1. 4 Theoretical equation of mass transport types responsible for neck growth [89].

Mass transport type	Theoretical equation for neck growth	$(x/r)^n = Bt$	Exponent n	Ref.
Viscous flow	$\frac{x^2}{r} = \frac{3\gamma}{2\eta(T)}t$	$\left(\frac{x}{r}\right)^2 = \frac{3\gamma}{2\eta(T)r}t$	2	[90]
Volume diffusion	$\frac{x^4}{r} = \left(\frac{16\sigma\delta^3}{kT}\right)D_v t$	$\left(\frac{x}{r}\right)^4 = \left(\frac{16\sigma\delta^3}{kTr^3}\right)D_v t$	4	[91]
Grain boundary diffusion	$\frac{x^5}{r^2} = \left(\frac{40\sigma\delta^3}{kT}\right)D_v t$	$\left(\frac{x}{r}\right)^5 = \left(\frac{40\sigma\delta^3}{kTr^3}\right)D_v t$	5	[92]
	$\frac{x^6}{r^2} = \left(\frac{48\sigma\delta^4}{\pi kT}\right)D_b t$	$\left(\frac{x}{r}\right)^6 = \left(\frac{48\sigma\delta^4}{\pi kTr^4}\right)D_b t$	6	[91]
Surface diffusion	$\frac{x^7}{r^3} = \left(\frac{56\sigma\delta^4}{kT}\right)D_s t$	$\left(\frac{x}{r}\right)^7 = \left(\frac{56\sigma\delta^4}{kTr^4}\right)D_s t$	7	[92]

Note: r is the original particle radius; x is the radius of neck growth; T is the absolute temperature; γ is the surface energy, which is temperature dependent; $\eta(T)$ is the temperature-related shear viscosity; t is the time; δ is the interatomic distance; σ is the surface tension; k is the Boltzmann constant; D_v, D_b, and D_s are the coefficients of volume self-diffusion, grain boundary self-diffusion, and surface diffusion coefficient, respectively; and n is a mechanism-characteristic exponent.

In addition, the temperature is one of the factors to affect the sintering mechanism. According to **Table 1.4**, the relationship between neck growth and time can be simplified to Equation 1.3:

$$(x/r)^n = Bt \tag{1.3}$$

Equation 1.3 is converted into Equation 1.4 via logarithmic transformation.

$$log(x/r) = (1/n)log(t) + (1/n)log(B) \quad 1.4$$

As *B* is a constant value, the reciprocal of exponent *n* is the slope of the fitting line between log(*t*) and log(*x/r*). The experimental logarithm plots in **Fig. 1.14** demonstrate that there is an approximately linear relationship between log(*t*) and log(*x/r*). In addition, the slope of fitting lines is altered with the temperature. The exponent *n* is 6.7, 8.8, and 8.4 as the sintering temperature is 160 °C, 200 °C, and 250 °C respectively. This means that surface diffusion at low temperatures dominates the sintering mechanism. When the sintering temperatures increase to 300 °C and 350 °C, the corresponding exponent *n* is 3.7 and 3.8, respectively. This indicates that volume diffusion is dominant in the sintering process at higher temperatures [89].

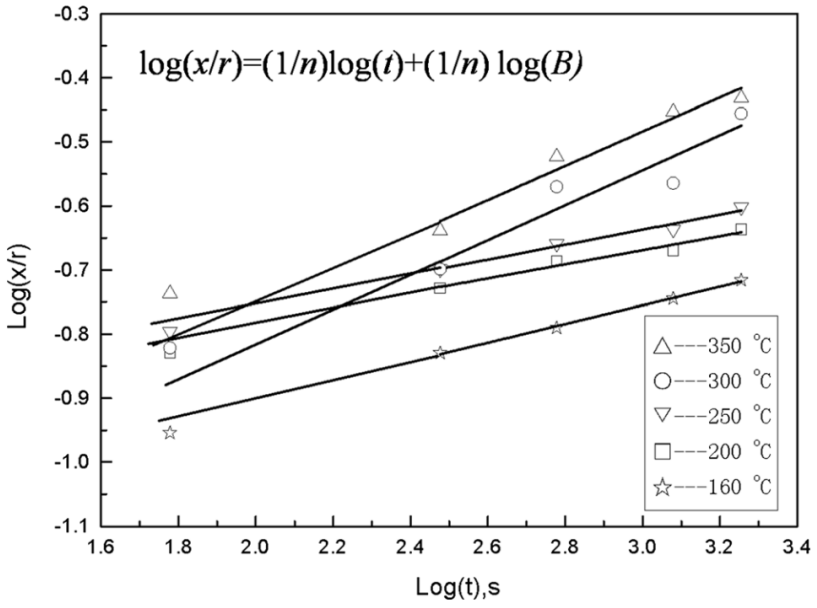

Fig. 1.14 Logarithm plots of interparticle neck size ratio (x/r) with sintering time (t) at different temperatures [89].

(b) Effects of bonding time

Sintering time is a key factor that significantly affects joint properties, as the extended time allows more active particles to participate in sintering [93]. In addition, sintering is a process related to diffusion, and atom migration requires time. Therefore, an extended sintering time could increase the shear strength and density of sintered joints under various conditions [94]. The effects of sintering time on joint properties also depend on the sintering temperature. At higher temperatures, the extended sintering time promotes the densification of joints, increasing density and shear strength. However, continuous heating at lower temperatures only results in grain growth rather than densification, contributing to a limited increase in shear strength [95].

(c) Effects of assisted pressure

During bonding, the assisted pressure induces hydrostatic pressure and shear stress in the paste. The hydrostatic pressure increases the sintering rate by promoting the establishment of connections between more particles. In addition, the induced shear strain facilitates the elimination of pores within the sintered joints. In this way, the assisted pressure increases the diffusion path and the driving force for sintering simultaneously [78]. However, high assisted pressures tend to damage dies because semiconductor materials, such as Si, SiC, and GaN, are brittle and fragile. Although pressureless bonding can achieve die-bonding, the obtained sintered joints exhibit higher porosity and lower shear strength than pressure-assisted bonding [96]. For example, a low assisted pressure of 5 MPa at 300 ^{o}C led to a shear strength

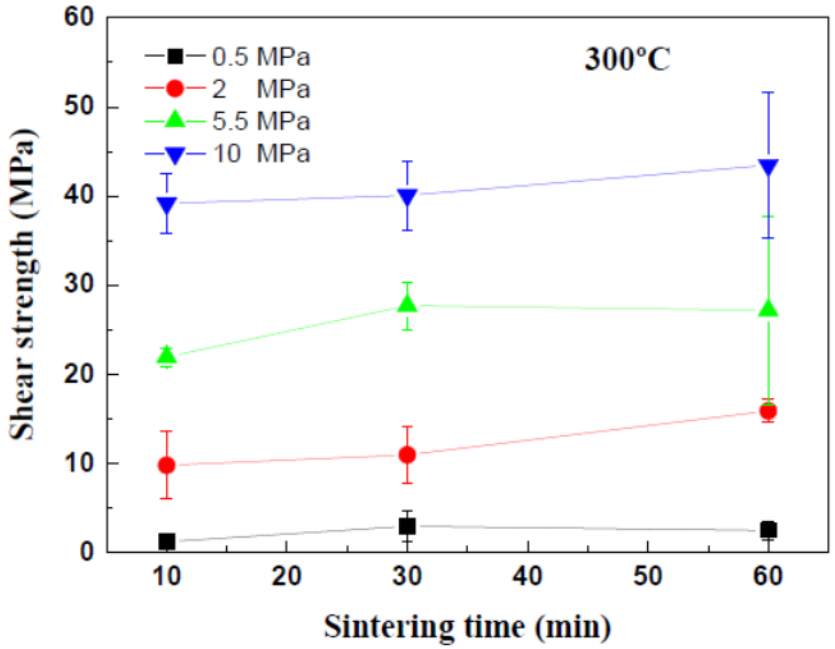

Fig. 1.15 Evolution of shear strength with sintering time and pressure [97].

more than 10 times higher than that of assisted pressure of 0.5 MPa in **Fig. 1.15** [97]. Therefore, particle bonding with moderate pressure is a promising alternative to preparing reliable sintered joints.

1.4 Ag bonding by organic-free Ag nanoporous sheet

1.4.1 Possible issues related to organics in the Ag paste

As multiple layers of different materials are stacked on top of dies, mechanical stress induced by the coefficient of thermal expansion (CTE) mismatch tends to cause structural damage or failure of dies during bonding [98]. To prevent unexpected die damage, the processing temperature should be low to minimize mechanical stress. For die-bonding, the bonding performance of Ag pastes is a key factor in determining the process temperature.

Accordingly, the bonding performance can be improved through several means, such as reducing the particle size [63], using hybrid Ag particles [99], using Ag particles with specific shapes [100], and adding sintering aids [101]. For example, robust sintered Ag joints were achieved at 270 ^{o}C with 28.8 MPa pressure by using hybrid Ag particles that contained both Ag NPs and micro-particles (MPs) [102]. Ag NPs tended to fill the gaps of MPs, which increased the particle stacking density and facilitated the formation of dense and robust sintered Ag joints [103,104].

However, the Ag NPs with high surface energy are susceptible to van der Waals forces between close proximity NPs, which leads to the agglomeration of Ag NPs [105]. This agglomeration has serious negative effects on Ag NP sintering by reducing the surface energy and destroying the uniformity of Ag pastes [52,65]. Organic additives are necessary for Ag pastes to prevent Ag NP agglomeration and modify dispersibility, viscosity, and wettability, thus enhancing the processability and bonding properties [86]. Specific function groups of these additives can anchor on the Ag particle surface to reduce the surface energy and induce steric and electrostatic stabilizations [87]. During the bonding process, these organic additives are converted into gases through evaporation or decomposition and released into the air. As depicted in **Fig. 1.16**, the rapid and random release of gas can cause defects such as voids and cracks in the sintered Ag joints, resulting in joint property deterioration [106,107].

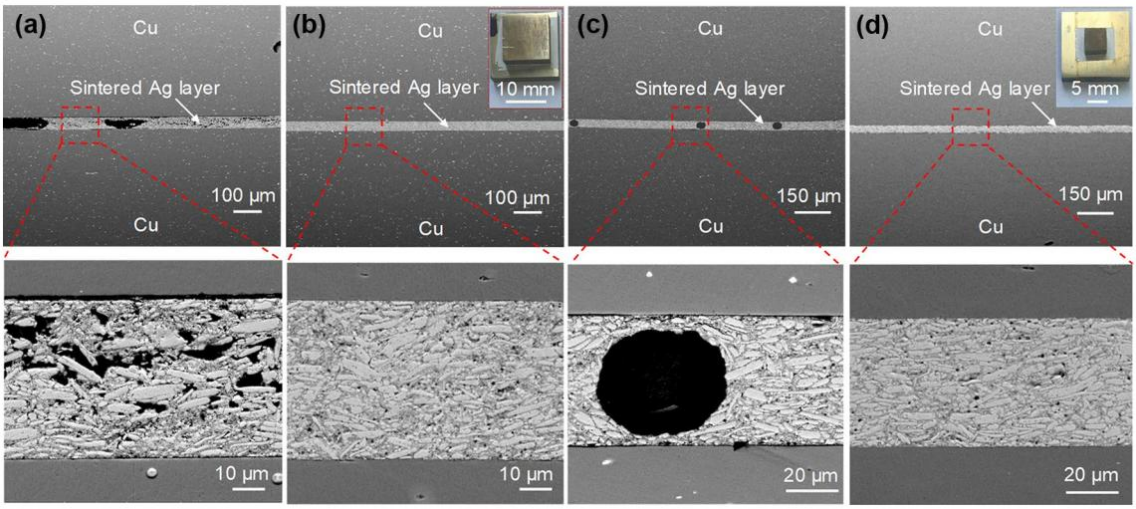

Fig. 1.16 Cross-sectional SEM images with a bonding area of (a, b) 10 × 10 mm2 and (c, d) 5 × 5 mm2 fabricated without (a, c) and with (b, d) pre-treatment for solvent removal after sintering at 200 °C for 10 min in air [106].

1.4.2 Organic-free Ag nanoporous sheet for robust Ag joints

A novel bonding technology using an organic-free Ag nanoporous sheet was recently proposed for the facile preparation of reliable high-temperature die attachments by forming a die-Ag joint-substrate sandwich structure [108,109]. There are several methods for fabricating porous Ag, such as Ag paste sintering [110], pulsed laser deposition (PLD) [111], and dealloying [112]. In Ag paste sintering, as depicted in **Fig. 1.17**, Ag paste was printed on the substrate and die by a metal mask. Upon volatilization of the organic additives with heating, sintering occurred between the intimate contact Ag NPs, resulting in Ag porous films. The Ag porous films were polished with abrasive paper (#4000) to flatten the surface and ensure intimate contact between the two films during bonding. This process yielded Ag joints

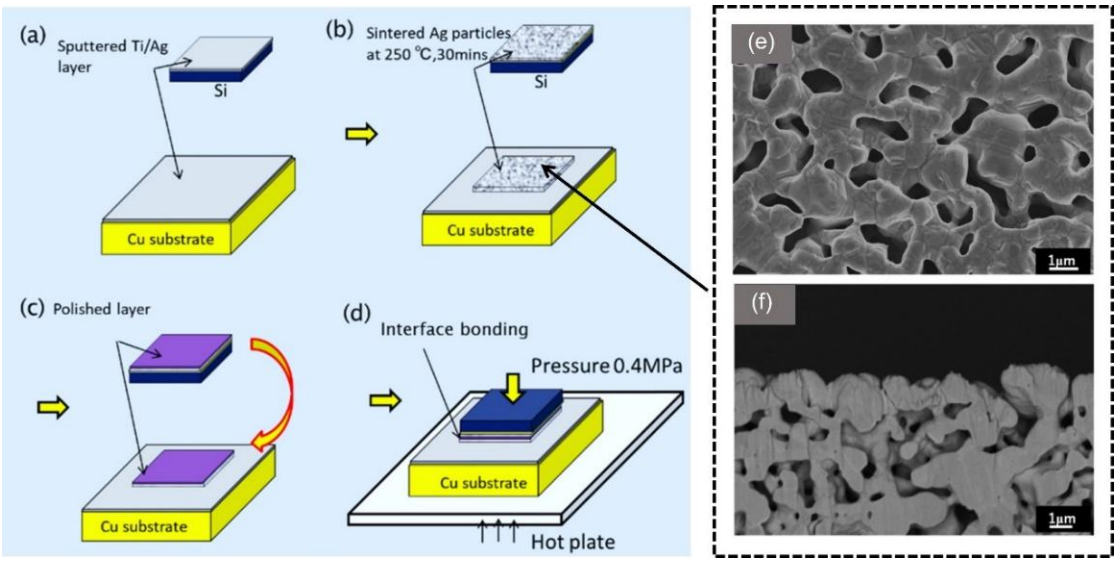

Fig. 1.17 Die-bonding using Ag porous films derived from Ag paste sintering. (a)-(d) Schematic diagram illustrating the fabrication and bonding of Ag porous films. (e) (f) Microstructures of the prepared Ag porous film [110].

with a shear strength of about 25 MPa at 250 ^{o}C for 60 min with 0.4 MPa. However, polishing with abrasive paper could cause unexpected damage to the easily broken Ag porous film [110].

In terms of physical method, high-energy lasers evaporate Ag targets, and the evaporated Ag redeposit on the substrate to form an Ag nanostructure layer in **Fig. 1.18**. The uniformity of the prepared Ag nanostructure layer is ensured by continuously rotating the Ag target and substrate during the PLD process [63]. The Ag nanostructure layers derived from PLD were sintered into Ag sintered joints with a high shear strength over 60 MPa at 250 ^{o}C for 30 min with 30 MPa [111]. However, the high price of the PLD equipment limits the wide application of this physical method.

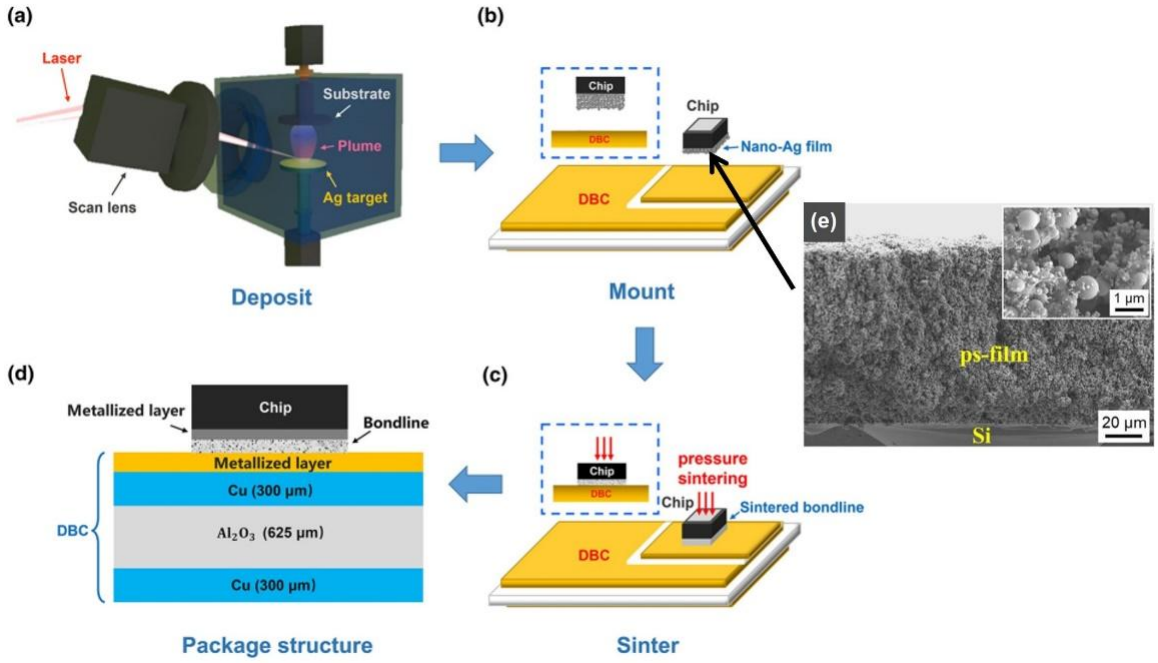

Fig. 1.18 Die-bonding using Ag porous layer derived from PLD. (a)-(d) Schematic diagram illustrating the PLD process and bonding process of the Ag nanostructure layer. (e) Microstructures of the prepared Ag nanostructure layer [63].

For a typical dealloying process in **Fig. 1.19**, a binary alloy containing Ag and a less-noble element is immersed in an acid solution, the less-noble element is removed by acid, and the Ag remains as a nanoporous sheet [109,112]. After dealloying, the obtained Ag sheet exhibits a nanoscale surface, which contributes to Ag sintered joints with a high shear strength of 37 MPa at 300 ^{o}C for 10 min with 20 MPa [109]. As shown in **Fig. 1.20**, conventional Ag paste is converted into Ag joints via a multistep process. It is unlikely that preformed Ag nanoporous sheets can be directly placed on a substrate and bonded at the target temperature due to the absence of organics in the Ag porous sheets. However, the generated waste solution contains acid and heavy metal cations, which have negative effects on the environment and human health [113]. Moreover, the fragility of the preformed Ag porous sheets and the

necessary high bonding pressure render its practical use difficult. Therefore, developing a harmless and straightforward method to prepare nanoporous Ag sheets is essential for nanoporous Ag bonding.

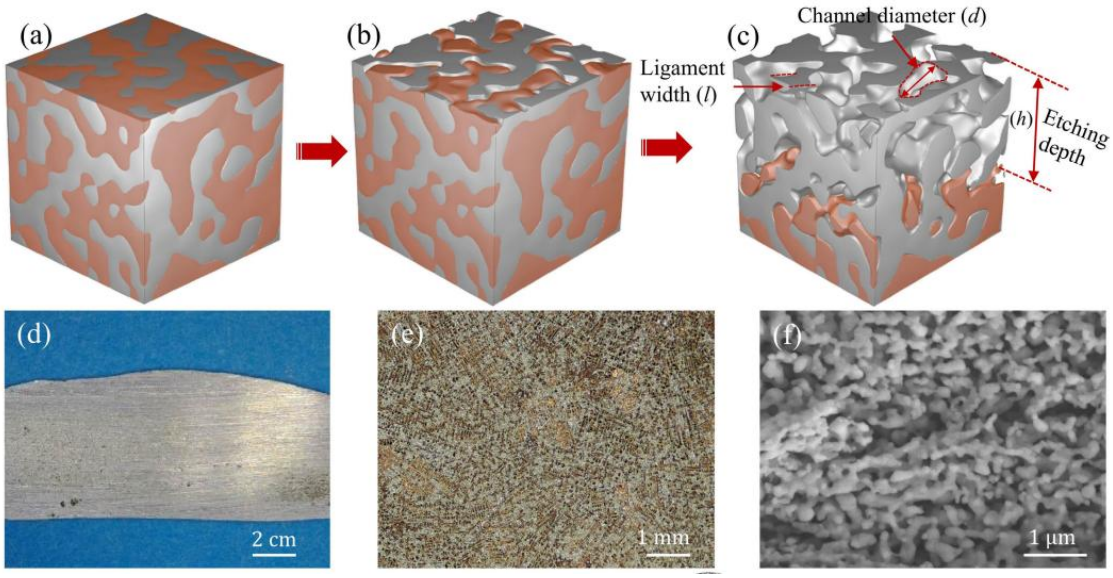

Fig. 1.19 Preparation of Ag nanoporous sheet via dealloying. (a)-(c) Schematic of Ag nanoporous sheet preparation. (d)-(f) Structure change during dealloying [109].

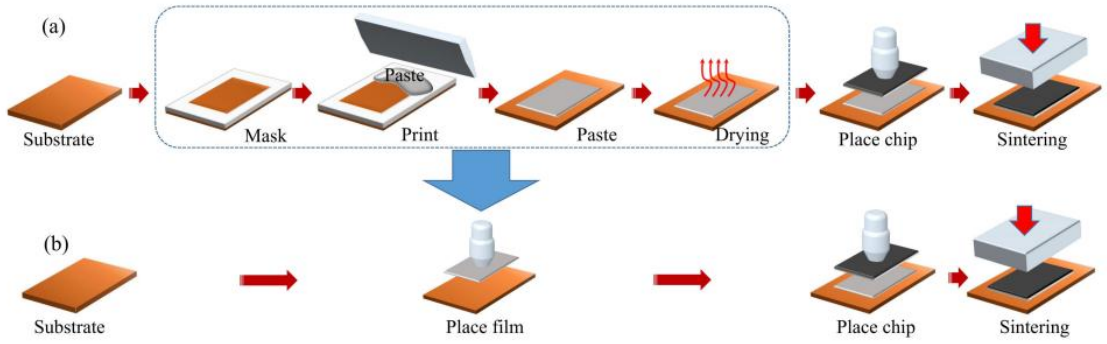

Fig. 1.20 Schematic diagram illustrating the application process of (a) Ag paste and (b) an Ag nanoporous sheet [109].

1.4.3 Ag nanostructures derived from the decomposition of Ag-based complexes

Metal-based complexes can be widely utilized to prepare conductive nanostructure films for organic light emitting diodes (OLED), radio-frequency identification (RFID), and flexible displays [114]. As shown in **Fig. 1.21a**, a metal-based complex is typically a compound that consists of a central metallic cation ion and several ligands [115]. Metal-based complexes can be synthesized by a facile coordination reaction between metal salts and amine agents without byproduct generation [116]. There are various abundant candidates for the metal slats and amine agents, and part of them is listed in **Table 1.5**.

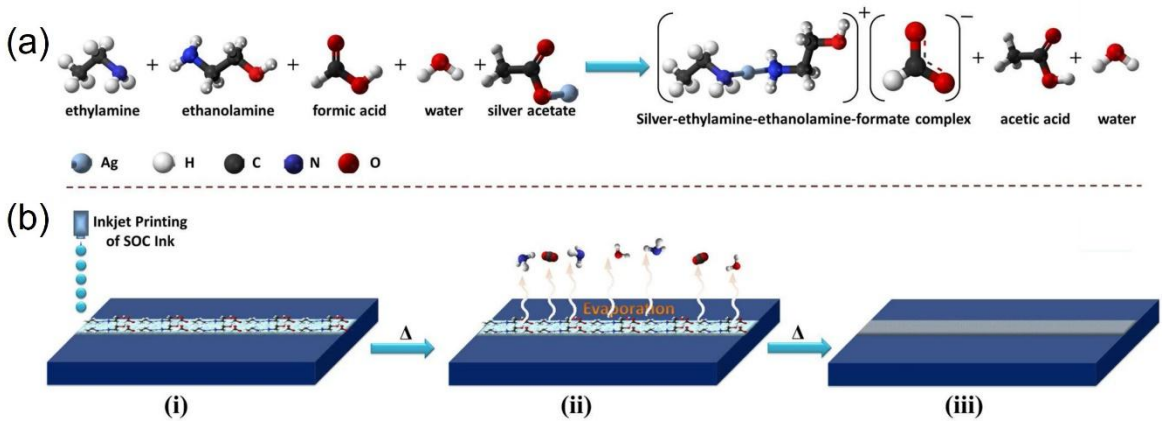

Fig. 1.21 Schematic diagram illustrating the (a) chemical reaction for the formulation of complex-based ink and (b) thermal decomposition process of printed ink [115].

Table 1.5 Metal-based complex derived from various precursors and complexing agents.

Precursor	Complexing agents	Solvent	Heating condition	Resistivity (μΩ cm)	Metal content (wt%)	Ref.
Silver oxalate	Ethylamine	Ethylene glycol, Ethanol	150 °C, 30 min	8.6	27.6	[117]
Silver acetate	Ethanolamine formic acid	H_2O	Microwave, 150 °C, 30 min	7.1	22.44	[118]
Silver citrate	ethylenediamine	Propanol, Ethylene glycol	150 °C, 60 min	79.4	10	[119]
Hydrous copper formate	2-amino-2-methyl-1-propanol	none	N2, 190 ^{o}C, 2 min	10.9	26	[120]
Copper acetate	Isopropanolamine	Isopropyl alcohol, ethanol	150 °C, 30 min, N2	590	none	[121]
Copper format	Hexylamine and 2-amino-2-methyl-1-propanol	Isopropyl alcohol	Laser sintering	17	none	[122]
Nickel formate dihydrate	Ethanolamine	Ethylene glycol, Ethanol	500 ^{o}C, 40 min	20.6	< 10%	[123]

Although there is a great variety of metal-based complexes, the thermal decomposition of metal-based complexes follows a general process in **Fig. 1.22**, involving ligand dissociation, Ag ion reduction, Ag cluster or nuclei nucleation, organic gasification, and Ag particle growth [119,124–128]. This process can be conducted at low temperatures (90–200 ºC) as the metal-based complex automatically provides a reductive atmosphere for metallic cations via the amine group, which dramatically reduces the thermal decomposition temperature [125]. For instance, Yang et al. proved that the 155 °C thermal decomposition temperature of the Ag-based complex was approximately 43 °C lower than that of the Ag precursor, and the obtained Ag film had a low resistivity of 7.94×10^{-5} Ω·cm after sintering at 155 °C for 60 min [119]. **Fig. 1.23** demonstrates that the high conductivity of the Ag film may be due to the high surface energy of the nanostructures derived from the decomposition of metal-based complexes, which facilitates sintering [118].

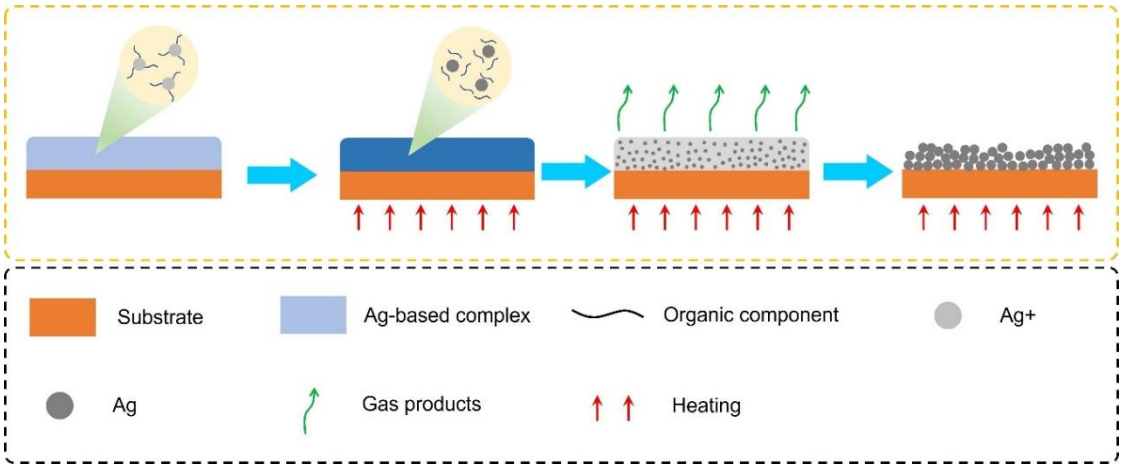

Fig. 1.22 Schematic diagram of the representative decomposition process of a metal-based complex

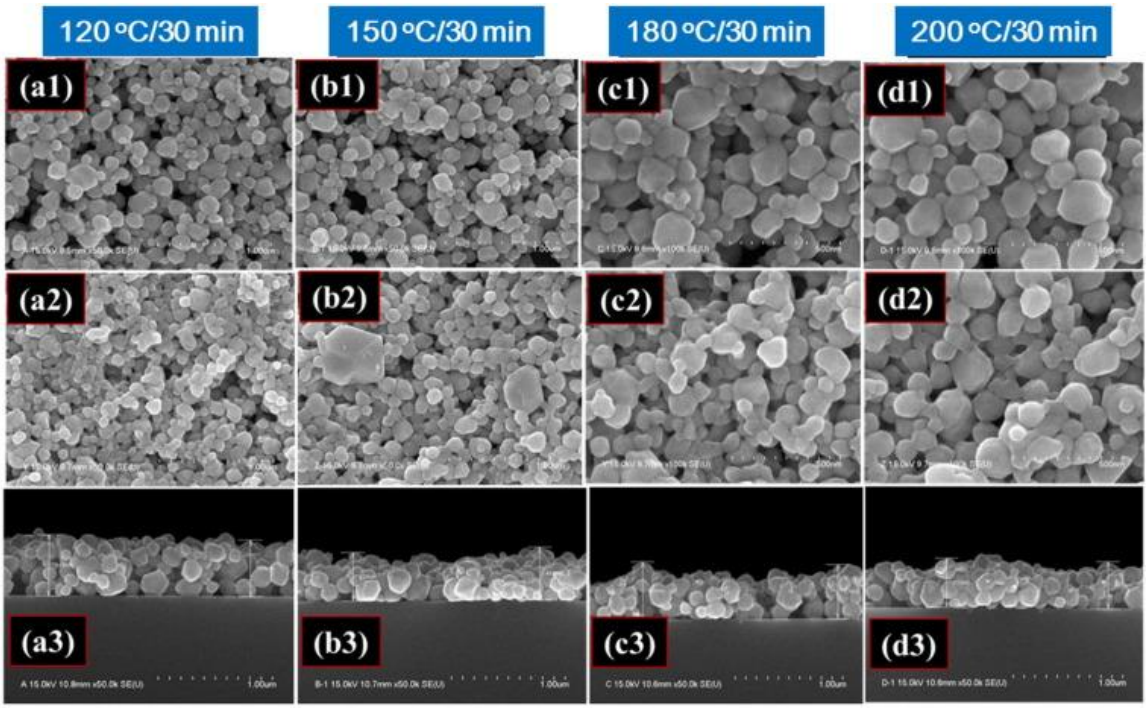

Fig. 1.23 FESEM images of the films deposited on glass using Ag-based complex ink as a function of temperature for 30 min: (a) 120 °C, (b) 150 °C, (c) 180 °C and (d) 200 °C [118].

Low process temperatures of 90–200 °C render metal-based complexes suitable for various flexible substrates and allow the cheap and rapid manufacture of electronics. Additionally, agglomeration is not considered when using the Ag-based complex as the metal component is in an ionic form [119]. However, the weight ratio of metal components in the metal-based content is less than 30 %, which limits their application in die-bonding. If the metal-based complex is directly used in die-bonding, the organic component gasification could induce abundant defects within the joints.

1.5 Reliability of Ag sintered joints

Bondline derived from Ag particle bonding exhibited similar properties to Ag bulk such as high thermal conductivity, high electrical conductivity, and high melting point [65,66].

Even so, reliability concerns remain when applying the Ag particle bonding. Several common reliability tests, such as thermal aging [129], thermal shock [130], and power cycling [131], are utilized to evaluate the reliability of Ag sintered joints.

1.5.1 Thermal aging

Thermal aging test is conducted in a fixed high-temperature atmosphere for a long time to test the impacts of high operation temperature on the joint characteristics such as shear strength, pore size, and grain size [85,132]. The evolution of joint characteristics could be affected by various factors such as temperature, time, atmosphere, and substrate metallization layer [132,133]. Among these factors, aging temperature has significant effects on the shear strength. As shown in **Fig. 1.24**, the impact of an aging temperature of 125 ^{o}C on the shear strength was very slight. By contrast, the remaining shear strength was 9.5 MPa after aging at 350 ^{o}C for 500 h, indicating a significant decrease. This was because coarsening occurred at high aging temperatures, increasing grain and pore sizes and decreasing the internal connection. Additionally, high aging temperature resulted in Cu oxidation layer at the interface, which made the Ag sintered joints suffer from interfacial separation [134]. To improve the thermal aging resistance, Wang et al. used AlN-particle dropped Ag paste to prepare Ag sintered joints. During the thermal aging, the microstructural stability of Ag sintered joints was improved by the block effect of AlN particles on the Ag atom diffusion [85].

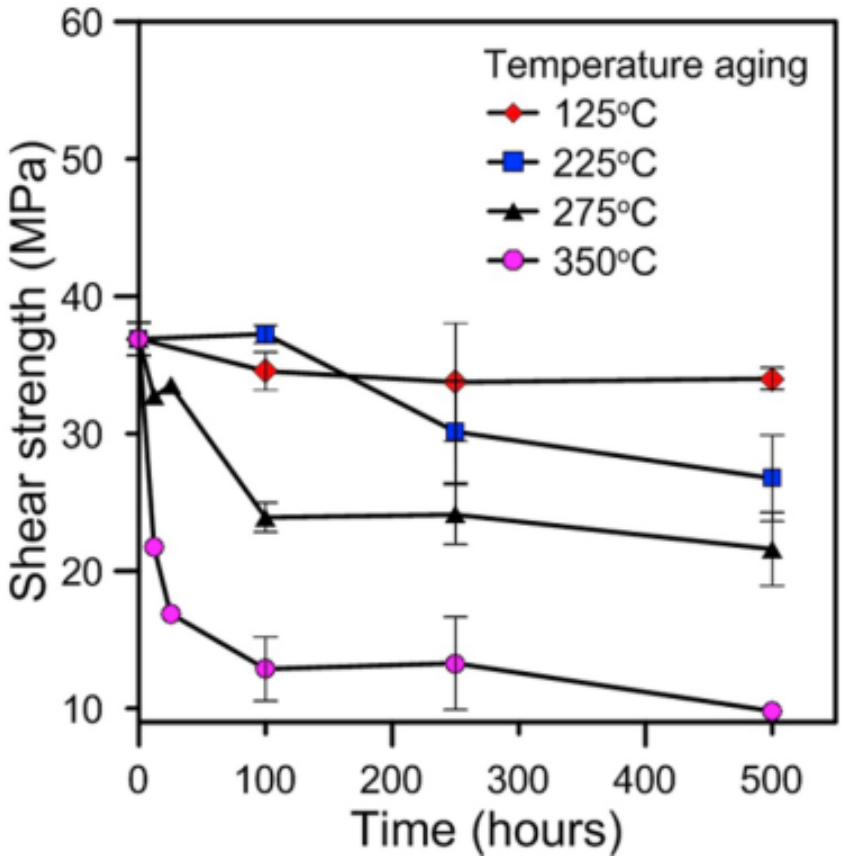

Fig. 1.24 Shear strength evolution with aging time at different aging temperatures [134].

1.5.2 Thermal shock

A typical power module consists of multilayered materials [20]. With elevated temperatures, thermal stress derived from CTE mismatch of multilayered materials could induce serious reliability issues [135]. Thermal shock test conducted under repeated temperature variations and rapid temperature change was used to verify the effects CTE mismatch on the reliability of Ag joints [136]. I previous study, optimizing the metallization layer of substrate or ingredient of Ag paste could improve the thermal shock resistance of Ag

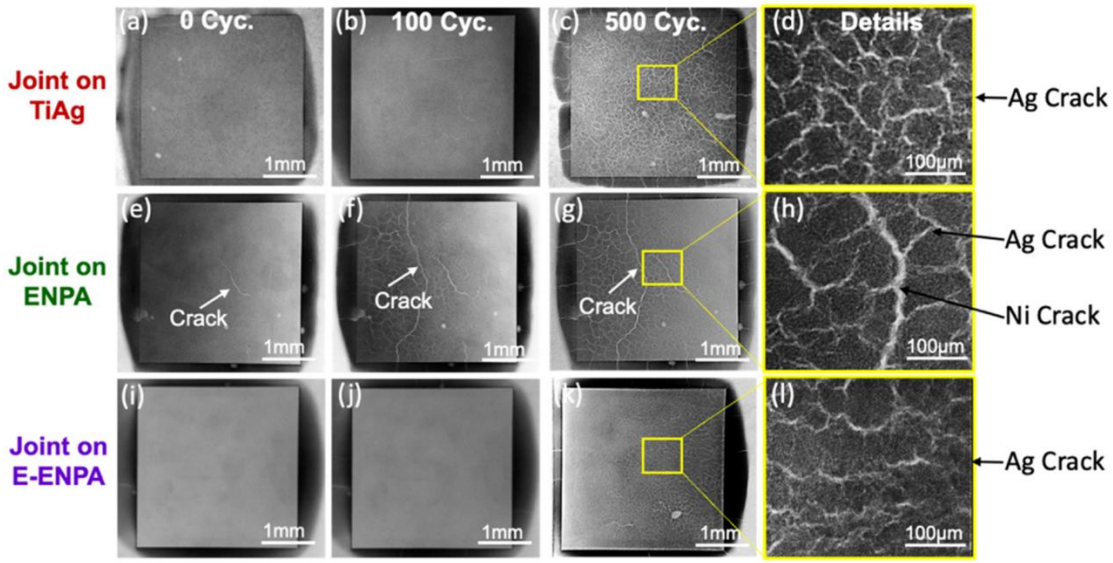

Fig. 1.25 X-ray images of Ag sintered joints on three substrates before and after thermal shock [137].

sintered joints [137,138]. For example, Liu et al. compared the thermal shock properties of Ag joints on DBC substrate with three different metallization layers: sputtering Ti-/Ag (TiAg), electroless Ni-/Pt-/Ag (ENPA), and electroplating Ni-/electroless Ni-/Pt-/Ag (E-ENPA). As shown in **Fig.1.25**, the Ag joints on the E-ENPA substrate exhibited less obvious cracks than those on TiAg and ENPA substrates. This is because the electroplated Ni layer is ductile, which could act as a stress-relaxation layer and enable the Ag sintered joints high microstructure stability [137].

1.5.3 Power cycling

Unlike thermal aging and thermal cycling, the power modules in the power cycling were heated by periodic input power [139]. This periodic input power is intended to simulate the effects of rapid temperature rise and fall on the performance and reliability of the power

module during practical operation. Several parameters could be used to reflect the effects of power cycling on the power devices such as thermal resistance, electrical resistivity, and microstructure evolution [135,139]. Although sintered Ag performed better than other lead-free die-attach materials in power cycling, the performance and microstructure of power devices still degraded at very high cycle numbers [140]. **Fig. 1.26** shows the X-ray images of the Ag sintered joints after 10000 and 16500 power cycles [141]. A high density of cracks was observed, and their number and area increased with the number of cycles. This is because the cracks reduced the thermal conductivity of the sintered Ag and increased the temperature of the power module. The increased module temperature accelerated the expansion of the cracks. For the formation of cracks, it was attributed to the thermal stress induced by the CTE mismatch of multilayer materials. Therefore, to enhance the stability of power modules during power cycling, minimizing CTE mismatch by optimizing the module structure is an effective way [142].

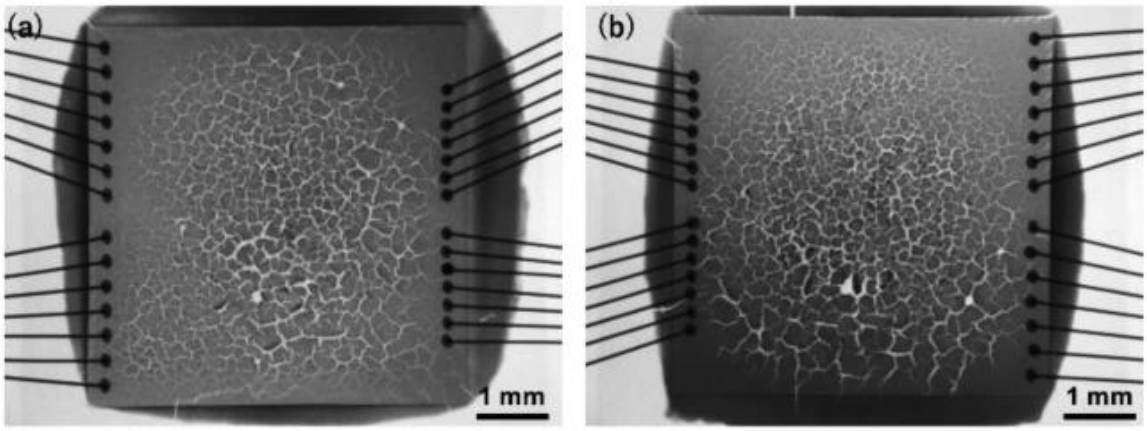

Fig. 1.26 X-ray images of the Ag sintered joints after (a) 10000 and (b) 16500 power cycles [141].

1. 6 Research motivation

According to the literature reviews, high-temperature reliable lead-free bonding processes, such as TLP bonding, Cu particle bonding, and Ag particle bonding, are essential to fulfill the requirements of WBG power devices. Among these processes, Ag particle bonding is particularly appealing because bulk Ag has a high melting temperature of 961.9 °C, which provides excellent high-temperature reliability. During bonding, Ag NPs with high surface energies can be easily sintered into bulk Ag at temperatures far lower than its melting temperature. Additionally, the Ag bonding does not create fragile IMCs as TLP bonding would. Compared with Cu particle bonding, Ag particle bonding is more practical because it does not require an inert atmosphere during processing. However, the organic gasification in the Ag paste could cause abundant defects within the Ag sintered joints, significantly deteriorating joint properties, such as porosity, shear strength, and thermal conductivity. Therefore, researchers have proposed an organic-free bonding strategy using Ag nanoporous sheets. dealloying is a commonly used method to fabricate Ag nanoporous sheets. The fabricated Ag nanoporous sheets exhibit high sintering activity owing to the unique nano-scale structure on their surface. However, incompletely flat surfaces could lead to large pores at the interface between the Ag nanoporous sheet and substrate. High pressures over 20 MPa are needed to eliminate the negative effects of large pores on bonding [109]. However, such high pressures tend to cause damage to the fragile dies.

Previous studies proposed a facile approach for preparing Ag nanostructures by the thermal decomposition of Ag-based complexes [143]. The Ag-based complex can be readily

synthesized through a simple complexation reaction between the metal salt and amine agents, with no generation of byproducts. In addition, sintering can easily occur between the newly generated Ag nanostructures because of their naked surface. Given these excellent properties, Ag-based complexes are commonly used in flexible electronics [125], but applying this promising material for die-bonding remains rare. Hence, finding a solution to effectively integrate the low thermal decomposable Ag-based complex and Ag nanostructures for die-bonding is crucial. In addition, the bonding performance of Ag nanostructures is a key factor in determining joint properties. As Ag nanostructures are derived from the thermal decomposition of Ag-based complexes, the effects of the decomposition conditions, such as temperature and time, on the sintering properties should be clear. Diverse metallization layers are pre-fabricated on the back side of dies and the top surface of substrates. The interface conditions between Ag nanostructures and the metallization layer significantly determine the joint properties. Therefore, the main motivations of this work are:

1) Find a solution to confirm a feasibility of applying an Ag-based complex in the preparation of die-attachment.

2) Investigate the effects of thermal decomposition conditions on the bonding performance of Ag nanostructures.

3) Figure out the influences of interactions between the Ag-based complex and substrates on the formation of Ag nanostructures and joint properties.

In addition, the innovation points of this study should be introduced. First, we investigated the thermal decomposition behaviors of an Ag-based complex and identified the effects of

thermal conditions on the morphology and ingredients of Ag nanostructures. Then, the feasibility of applying an Ag-based complex in die-bonding was confirmed. Based on this, the factors that determine the low-temperature bonding performance were discussed. Finally, a substrate-dependent bonding performance was discovered, and the bonding mechanism corresponding to each substrate was discussed.

1.7 Objective and outline of this dissertation

The first purpose was to confirm the feasibility of using an Ag-based complex as a die-attachment material because it was commonly used for preparing conductive film in previous studies [115,144]. Bonding performance is an important indicator for evaluating die-attach materials. The second main purpose was to investigate the factors that affect the bonding performance of Ag nanostructures, such as thermal decomposition time, temperature, and substrate. The outline of this study is as follows:

In Chapter 1, a comprehensive literature review of WBG power device packaging and die-bonding materials was introduced. Based on this, utilizing an Ag-based complex as die-bonding material was solidified as the primary objective of this dissertation.

In Chapter 2, the feasibility of utilizing an Ag-based complex as die-attach material was confirmed. Subsequently, the effects of thermal conditions of the Ag-based complex on the bonding performance were investigated, and the underlying mechanism responsible for the evolution of bonding performance was discussed.

In Chapter 3, an Ag-based complex was decomposed on three commonly used substrates, Ag, Al, and Cu, to investigate the effects of the substrate on the gradients and morphology of Ag nanostructures. The reaction between the Ag-based complex and Cu substrate was discussed and confirmed.

In Chapter 4, a bonding performance of Ag nanostructures on the four above-mentioned substrates was evaluated by shear strength and microstructures of sintered Ag joints. The determining factors that affect the bonding performance were discussed.

In Chapter 5, the interaction between Ag-based complex and Cu substrate was utilized to fabricate Ag-Cu composite joints. The electromigration property of pure Ag joints and Ag-Cu composite joints was investigated.

In Chapter 6, the research results and future research plan were presented.

Reference

[1] H. Wang, X. Song, Z. Li, D. Li, X. Xu, Y. Chen, P. Liu, X. Zhou, T. Zhai, Recent advances in two-dimensional photovoltaic devices, Journal of Semiconductors 45 (2024) 051701. https://doi.org/10.1088/1674-4926/45/5/051701.

[2] S. Yan, J. Wang, J. Zhang, Z. Gao, Y. Bai, Experimental investigation of wind turbine stress and power characteristics under dynamic changes in wind direction, Energy Sources, Part A: Recovery, Utilization, and Environmental Effects 46 (2024) 1925–1943. https://doi.org/10.1080/15567036.2024.2302956.

[3] A. Zahoor, F. Mehr, G. Mao, Y. Yu, A. Sápi, The carbon neutrality feasibility of worldwide and in China's transportation sector by E-car and renewable energy sources before 2060, J Energy Storage 61 (2023) 106696. https://doi.org/https://doi.org/10.1016/j.est.2023.106696.

[4] W. Saito, A Future Outlook of Power Devices From the Viewpoint of Power Electronics Trends, IEEE Trans Electron Devices 71 (2024) 1356–1364. https://doi.org/10.1109/TED.2023.3332611.

[5] G. Liu, Y. Wu, K. Li, Y. Wang, C. Li, Development of high power SiC devices for rail traction power systems, J Cryst Growth 507 (2019) 442–452. https://doi.org/https://doi.org/10.1016/j.jcrysgro.2018.10.037.

[6] G. Zulauf, Z. Tong, J.D. Plummer, J.M. Rivas-Davila, Active Power Device Selection in High- and Very-High-Frequency Power Converters, IEEE Trans Power Electron 34 (2019) 6818–6833. https://doi.org/10.1109/TPEL.2018.2874420.

[7] K. Jayaswal, D.K. Palwalia, Role of reliability assessment in Si-based non-Isolated DC-DC power electronic converters, Mater Today Proc 60 (2022) 1113–1119. https://doi.org/https://doi.org/10.1016/j.matpr.2022.02.241.

[8] J. Li, Y. Liang, Y. Mei, X. Tang, G.-Q. Lu, Packaging Design of 15 kV SiC Power Devices With High-Voltage Encapsulation, IEEE Transactions on Dielectrics and Electrical Insulation 29 (2022) 47–53. https://doi.org/10.1109/TDEI.2022.3146569.

[9] S.K. Pullabhatla, P.B. Bobba, S. Yadlapalli, Comparison of GAN, SIC, SI Technology for High Frequency and High Efficiency Inverters, E3S Web Conf. 184 (2020). https://doi.org/10.1051/e3sconf/202018401012.

[10] T. KIMOTO, High-voltage SiC power devices for improved energy efficiency, Proceedings of the Japan Academy, Series B 98 (2022) 161–189. https://doi.org/10.2183/pjab.98.011.

[11] Z. Chen, A.Q. Huang, High Performance SiC Power Module Based on Repackaging of Discrete SiC Devices, IEEE Trans Power Electron 38 (2023) 9306–9310. https://doi.org/10.1109/TPEL.2023.3263466.

[12] F. Roccaforte, G. Greco, P. Fiorenza, F. Iucolano, An overview of normally-off GaN-based high electron mobility transistors, Materials 12 (2019). https://doi.org/10.3390/ma12101599.

[13] R. Wu, J. Wen, K. Yu, D. Zhao, A Discussion of SiC Prospects in Next Electrical Grid, in: 2012 Asia-Pacific Power and Energy Engineering Conference, 2012: pp. 1–4. https://doi.org/10.1109/APPEEC.2012.6307214.

[14] A. Deshpande, R. Paul, A. Imran Emon, Z. Yuan, H. Peng, F. Luo, Si-IGBT and SiC-MOSFET hybrid switch-based 1.7 kV half-bridge power module, Power Electronic Devices and Components 3 (2022) 100020. https://doi.org/https://doi.org/10.1016/j.pedc.2022.100020.

[15] D. Chen, W. Hong, S. Zhang, X. Shen, Y. Lin, H. Lin, A High Power Density Low Voltage Static Var Generator Based on Wide Band Gap Semiconductor Devices, IEEE Access 11 (2023) 141753–141763. https://doi.org/10.1109/ACCESS.2023.3338366.

[16] B.J. Baliga, Chapter 2 - IGBT Structure and Operation, in: B.J. Baliga (Ed.), The IGBT Device (Second Edition), Elsevier, 2023: pp. 21–35. https://doi.org/https://doi.org/10.1016/B978-0-323-99912-0.00004-0.

[17] B.J. Baliga, Chapter 3 - IGBT Structural Design, in: B.J. Baliga (Ed.), The IGBT Device (Second Edition), Elsevier, 2023: pp. 37–121. https://doi.org/https://doi.org/10.1016/B978-0-323-99912-0.00022-2.

[18] S. Gao, R. Wang, H. Wang, R. Kang, Warping model of high-power IGBT modules subjected to reflow soldering process, Int J Mech Sci 251 (2023) 108350. https://doi.org/https://doi.org/10.1016/j.ijmecsci.2023.108350.

[19] W. Lai, H. Li, M. Chen, S. Kang, H. Ren, R. Yao, L. Pan, R. Jin, Investigation on the Effects of Unbalanced Clamping Force on Multichip Press Pack IGBT Modules, IEEE J Emerg Sel Top Power Electron 7 (2019) 2314–2322. https://doi.org/10.1109/JESTPE.2018.2876768.

[20] Y. Kang, L. Dang, L. Yang, Z. Wang, Y. Meng, S. Li, Y. Sun, Y. Wang, H. Dong, Research Progress in Failure Mechanism and Health State Evaluation Index System of Welded IGBT Power Modules, Electronics (Switzerland) 12 (2023). https://doi.org/10.3390/electronics12153248.

[21] Y. Chen, B. Li, X. Wang, X. Wang, Y. Yan, X. Li, Y. Wang, F. Qi, H. Li, Direct Phase-Change Cooling of Vapor Chamber Integrated with IGBT Power Electronic Module for Automotive Application, IEEE Trans Power Electron 36 (2021) 5736–5747. https://doi.org/10.1109/TPEL.2020.3031372.

[22] Y. Jia, Y. Huang, F. Xiao, H. Deng, Y. Duan, F. Iannuzzo, Impact of Solder Degradation on VCE of IGBT Module: Experiments and Modeling, IEEE J Emerg Sel Top Power Electron 10 (2022) 4536–4545. https://doi.org/10.1109/JESTPE.2019.2928478.

[23] H. Han, G. Song, Consideration on IGBT Module Lifetime for Electrical Vehicle (EV) Applications, in: PCIM Europe 2014; International Exhibition and Conference for Power Electronics, Intelligent Motion, Renewable Energy and Energy Management, 2014: pp. 1–7.

[24] X. Ma, Y. Huang, Y. Luo, IGBT Failure mechanism and boundary analysis under large current and high temperature turn-off, J Phys Conf Ser 1754 (2021) 012036. https://doi.org/10.1088/1742-6596/1754/1/012036.

[25] Z. Wang, B. Tian, W. Qiao, L. Qu, Real-Time Aging Monitoring for IGBT Modules Using Case Temperature, IEEE Transactions on Industrial Electronics 63 (2016) 1168–1178. https://doi.org/10.1109/TIE.2015.2497665.

[26] L. Tan, P. Liu, C. She, P. Xu, L. Yan, H. Quan, Heat Dissipation Characteristics of IGBT Module Based on Flow-Solid Coupling, Micromachines (Basel) 13 (2022). https://doi.org/10.3390/mi13040554.

[27] S. He, R. Gao, Y.-A. Shen, J. Li, H. Nishikawa, Wettability, interfacial reactions, and impact strength of Sn–3.0Ag–0.5Cu solder/ENIG substrate used for fluxless soldering under formic acid atmosphere, J Mater Sci 55 (2020) 3107–3117. https://doi.org/10.1007/s10853-019-04153-9.

[28] X. Luo, J. Peng, W. Zhang, S. Wang, S. Cai, X. Wang, CALPHAD-guided alloy design of Sn–In based solder joints with multiphase structure and their mechanical properties, Materials Science and Engineering: A 860 (2022) 144284. https://doi.org/10.1016/J.MSEA.2022.144284.

[29] H.R. Kotadia, P.D. Howes, S.H. Mannan, A review: On the development of low melting temperature Pb-free solders, Microelectronics Reliability 54 (2014) 1253–1273. https://doi.org/https://doi.org/10.1016/j.microrel.2014.02.025.

[30] T.-N. Tsai, Development of an integrated reflow soldering control system using incremental hybrid process knowledge, Expert Syst Appl 28 (2005) 681–692. https://doi.org/https://doi.org/10.1016/j.eswa.2004.12.025.

[31] T.-N. Tsai, Thermal parameters optimization of a reflow soldering profile in printed circuit board assembly: A comparative study, Appl Soft Comput 12 (2012) 2601–2613. https://doi.org/https://doi.org/10.1016/j.asoc.2012.03.066.

[32] S. He, Y.-A. Shen, B. Xiong, F. Huo, J. Li, J. Ge, Z. Pan, W. Li, C. Hu, H. Nishikawa, Behavior of Sn-3.0Ag-0.5Cu solder/Cu fluxless soldering via Sn steaming under formic acid atmosphere, Journal of Materials Research and Technology 21 (2022) 2352–2361. https://doi.org/https://doi.org/10.1016/j.jmrt.2022.10.056.

[33] H. Tatsumi, S. Kaneshita, Y. Kida, Y. Sato, M. Tsukamoto, H. Nishikawa, Highly efficient soldering of Sn-Ag-Cu solder joints using blue laser, J Manuf Process 82 (2022) 700–707. https://doi.org/https://doi.org/10.1016/j.jmapro.2022.08.025.

[34] C.-H. Yang, Y.-C. Liu, Y. Hirata, H. Nishikawa, S.-K. Lin, Mechanical properties of Sn-Bi-Ag low-temperature Pb-free solders, in: 2022 International Conference on Electronics Packaging (ICEP), 2022: pp. 37–38. https://doi.org/10.23919/ICEP55381.2022.9795572.

[35] G.-S. Gan, L.-Q. Gan, J.-Z. Guo, D.-Q. Xia, C. Zhang, D. Yang, Y. Wu, C. Liu, Ultrasonic-Assisted Soldering of Low-Ag SAC Lead-Free Solder Paste at Low-Temperature, Mater Trans 59 (2018) 359–366. https://doi.org/10.2320/matertrans.M2017255.

[36] P. Zhang, S. Xue, L. Liu, J. Wang, H. Tatsumi, H. Nishikawa, Study on Thermal Cycling Reliability of Epoxy-Enhanced SAC305 Solder Joint, Polymers (Basel) 16 (2024). https://doi.org/10.3390/polym16182597.

[37] X. Hu, T. Xu, L.M. Keer, Y. Li, X. Jiang, Microstructure evolution and shear fracture behavior of aged Sn3Ag0.5Cu/Cu solder joints, Materials Science and Engineering: A 673 (2016) 167–177. https://doi.org/https://doi.org/10.1016/j.msea.2016.07.071.

[38] H. Schoeller, S. Bansal, A. Knobloch, D. Shaddock, J. Cho, Effect of alloying elements on the creep behavior of high Pb-based solders, Materials Science and Engineering: A 528 (2011) 1063–1070. https://doi.org/https://doi.org/10.1016/j.msea.2010.10.083.

[39] J.-W. Yoon, H.-S. Chun, S.-B. Jung, Reliability evaluation of Au–20Sn flip chip solder bump fabricated by sequential electroplating method with Sn and Au, Materials Science and Engineering: A 473 (2008) 119–125. https://doi.org/https://doi.org/10.1016/j.msea.2007.03.050.

[40] S. Zhong, L. Zhang, M. Li, W. Long, F. Wang, Development of lead-free interconnection materials in electronic industry during the past decades: Structure and properties, Mater Des 215 (2022) 110439. https://doi.org/https://doi.org/10.1016/j.matdes.2022.110439.

[41] R. Mohd Said, M.A.A. Mohd Salleh, N. Saud, M.I.I. Ramli, H. Yasuda, K. Nogita, Microstructure and growth kinetic study in Sn–Cu transient liquid phase sintering solder paste, Journal of Materials Science: Materials in Electronics 31 (2020) 11077–11094. https://doi.org/10.1007/s10854-020-03657-4.

[42] R. Gao, S. He, J. Li, Y.-A. Shen, H. Nishikawa, Interfacial transformation of preoxidized Cu microparticles in a formic-acid atmosphere for pressureless Cu–Cu bonding, Journal of Materials Science: Materials in Electronics 31 (2020) 14635–14644. https://doi.org/10.1007/s10854-020-04026-x.

[43] M.-H. Roh, H. Nishikawa, S. Tsutsumi, N. Nishiwaki, K. Ito, K. Ishikawa, A. Katsuya, N. Kamada, M. Saito, Pressureless Bonding by Micro-Sized Silver Particle Paste for High-Temperature Electronic Packaging, Mater Trans 57 (2016) 1209–1214. https://doi.org/10.2320/matertrans.MD201513.

[44] S. Chen, H. Zhang, Silver Sintering and Soldering: Bonding Process and Comparison, in: K.S. Siow (Ed.), Die-Attach Materials for High Temperature Applications in

Microelectronics Packaging: Materials, Processes, Equipment, and Reliability, Springer International Publishing, Cham, 2019: pp. 1–33. https://doi.org/10.1007/978-3-319-99256-3_1.

[45] N. Ismail, A. Atiqah, A. Jalar, M.A. Bakar, R.A.A. Rahim, A.G. Ismail, A.A. Hamzah, L.K. Keng, A systematic literature review: The effects of surface roughness on the wettability and formation of intermetallic compound layers in lead-free solder joints, J Manuf Process 83 (2022) 68–85. https://doi.org/10.1016/j.jmapro.2022.08.045.

[46] J.R. Holaday, C.A. Handwerker, Transient Liquid Phase Bonding, in: K.S. Siow (Ed.), Die-Attach Materials for High Temperature Applications in Microelectronics Packaging: Materials, Processes, Equipment, and Reliability, Springer International Publishing, Cham, 2019: pp. 197–249. https://doi.org/10.1007/978-3-319-99256-3_9.

[47] M. Noguchi, S.N. Joshi, E.M. Dede, Design of Mechanical Properties of Transient Liquid Phase Bonds with Tertiary Metal Particles, in: Proceedings - Electronic Components and Technology Conference, Institute of Electrical and Electronics Engineers Inc., 2016: pp. 1235–1240. https://doi.org/10.1109/ECTC.2016.26.

[48] D.H. Jung, A. Sharma, M. Mayer, J.P. Jung, A review on recent advances in transient liquid phase (TLP) bonding for thermoelectric power module, Reviews on Advanced Materials Science 53 (2018) 147–160. https://doi.org/10.1515/rams-2018-0011.

[49] X. Liu, H. Tatsumi, J. Wang, Z. Jin, Z. Chen, H. Nishikawa, Analysis of microstructures and fractures in Ag–In transient liquid phase bonded joints, Materials Science and Engineering: A 892 (2024) 146045. https://doi.org/https://doi.org/10.1016/j.msea.2023.146045.

[50] K. Chu, Y. Sohn, C. Moon, A comparative study of Cn/Sn/Cu and Ni/Sn/Ni solder joints for low temperature stable transient liquid phase bonding, Scr Mater 109 (2015) 113–117. https://doi.org/10.1016/j.scriptamat.2015.07.032.

[51] X. Liu, S. He, H. Nishikawa, Low temperature solid-state bonding using Sn-coated Cu particles for high temperature die attach, J Alloys Compd 695 (2017) 2165–2172. https://doi.org/https://doi.org/10.1016/j.jallcom.2016.11.064.

[52] H. Kim, M. Seo, J. Song, Effect of particle size and mass on nano to micron particle agglomeration, in: SICE 2004 Annual Conference, 2004: pp. 1923–1926 vol. 3.

[53] G. Yan, V. Gill, C.L. Gan, Z. Chen, Microstructure and mechanical properties of electroplated Ni-Sn TLP bonded joints with different bonding and aging times, Mater Charact 194 (2022) 112452. https://doi.org/https://doi.org/10.1016/j.matchar.2022.112452.

[54] B.-S. Lee, J.-W. Yoon, Cu-Sn Intermetallic Compound Joints for High-Temperature Power Electronics Applications, J Electron Mater 47 (2018) 430–435. https://doi.org/10.1007/s11664-017-5792-2.

[55] X. Liu, H. Tatsumi, J. Wang, Z. Jin, Z. Chen, H. Nishikawa, Analysis of microstructures and fractures in Ag–In transient liquid phase bonded joints, Materials Science and Engineering: A 892 (2024). https://doi.org/10.1016/j.msea.2023.146045.

[56] M. Wang, H. Liu, R. Wang, J. Peng, Thermally stable Ni/Au–Sn/Ni joint fabricated via transient liquid-phase bonding, Materials Science and Engineering: A 773 (2020) 138738. https://doi.org/https://doi.org/10.1016/j.msea.2019.138738.

[57] H. Shao, A. Wu, Y. Bao, Y. Zhao, Elimination of pores in Ag–Sn TLP bonds by the introduction of dissimilar intermetallic phases, J Mater Sci 52 (2017) 3508–3519. https://doi.org/10.1007/s10853-016-0645-6.

[58] P. Matkowski, Influence of the intermetallic compounds on the reliability of solder joints, in: Proc.SPIE, 2006: p. 61591V. https://doi.org/10.1117/12.675094.

[59] K. Chu, Y. Sohn, C. Moon, A comparative study of Cn/Sn/Cu and Ni/Sn/Ni solder joints for low temperature stable transient liquid phase bonding, Scr Mater 109 (2015) 113–117. https://doi.org/10.1016/j.scriptamat.2015.07.032.

[60] G. Elger, S. Krishna Bhogaraju, M. Schneider-Ramelow, Hybrid Cu sinter paste for low temperature bonding of bare semiconductors, Mater Lett 372 (2024) 136973. https://doi.org/https://doi.org/10.1016/j.matlet.2024.136973.

[61] W. Zhang, J. Chen, Z. Deng, Z. Liu, Q. Huang, W. Guo, J. Huang, The pressureless sintering of micron silver paste for electrical connections, J Alloys Compd 795 (2019) 163–167. https://doi.org/https://doi.org/10.1016/j.jallcom.2019.04.270.

[62] K. Zhao, X. Guan, J. Zhao, W. Cao, B. Dai, J. Zhu, Rapid preparation of sintered Ag nanoparticles pastes for high-power electronic packaging, Mater Lett 355 (2024) 135562. https://doi.org/https://doi.org/10.1016/j.matlet.2023.135562.

[63] Z. Deng, G. Zou, R. Du, Q. Jia, H. Zhang, L. Liu, Particle Size Effects of Nano-Ag Films on the Interface Sintered Bonding for Die Attachment, J Electron Mater 53 (2024) 473–488. https://doi.org/10.1007/s11664-023-10786-z.

[64] J.H. Jeong, T.S. Cho, Sintering behaviors of ag nanopowders with different particle sizes: A real-time synchrotron X-ray scattering study, J Nanosci Nanotechnol 17 (2017) 7799–7803. https://doi.org/10.1166/jnn.2017.14846.

[65] K.S. Siow, Mechanical properties of nano-silver joints as die attach materials, J Alloys Compd 514 (2012) 6–19. https://doi.org/https://doi.org/10.1016/j.jallcom.2011.10.092.

[66] S. Chen, H. Zhang, Silver Sintering and Soldering: Bonding Process and Comparison, in: K.S. Siow (Ed.), Die-Attach Materials for High Temperature Applications in Microelectronics Packaging: Materials, Processes, Equipment, and Reliability, Springer International Publishing, Cham, 2019: pp. 1–33. https://doi.org/10.1007/978-3-319-99256-3_1.

[67] X. Lu, W. Ke, C. Zhou, Y. Wu, Q. Zhang, S. Huang, W. Xia, L. Ye, A. Zehri, J. Liu, The influence of sintering process on thermal properties of nano-silver paste, in: 2018 19th International Conference on Electronic Packaging Technology (ICEPT), 2018: pp. 1157–1160. https://doi.org/10.1109/ICEPT.2018.8480545.

[68] D. Dai, J. Qian, J. Li, Y. Huang, Z. Wang, J. Yu, X. Wang, X. Chen, A rapid-sintering Cu-Cu joints with ultrahigh shear strength and super reliability for power electronics package, Mater Sci Semicond Process 178 (2024) 108405. https://doi.org/https://doi.org/10.1016/j.mssp.2024.108405.

[69] T.F. Chen, K.S. Siow, Comparing the mechanical and thermal-electrical properties of sintered copper (Cu) and sintered silver (Ag) joints, J Alloys Compd 866 (2021) 158783. https://doi.org/https://doi.org/10.1016/j.jallcom.2021.158783.

[70] Y. Gao, W. Li, C. Chen, H. Zhang, J. Jiu, C.-F. Li, S. Nagao, K. Suganuma, Novel copper particle paste with self-reduction and self-protection characteristics for die attachment of power semiconductor under a nitrogen atmosphere, Mater Des 160 (2018) 1265–1272. https://doi.org/https://doi.org/10.1016/j.matdes.2018.11.003.

[71] K. Wang, J. Wen, J. Feng, Y. Wang, P. Wu, S. Wang, Y. Tian, A novel Cu@Ag nano paste with low porosity for rapidly sintering in air condition, Mater Charact 209 (2024) 113762. https://doi.org/https://doi.org/10.1016/j.matchar.2024.113762.

[72] S. Lin, S. Nagao, E. Yokoi, C. Oh, H. Zhang, Y. Liu, S. Lin, K. Suganuma, Nano-volcanic Eruption of Silver, Sci Rep 6 (2016) 34769. https://doi.org/10.1038/srep34769.

[73] D. Dai, J. Li, J. Qian, Z. Wang, K. Zheng, J. Yu, X. Chen, The formation of Cu-Cu joints by low temperature sintering Cu NPs with copper formate layer and its oxidation enhancement, Mater Lett 339 (2023) 134087. https://doi.org/https://doi.org/10.1016/j.matlet.2023.134087.

[74] A. Molinari, Fundamentals of Sintering: Solid State Sintering, in: F.G. Caballero (Ed.), Encyclopedia of Materials: Metals and Alloys, Elsevier, Oxford, 2022: pp. 471–480. https://doi.org/https://doi.org/10.1016/B978-0-12-819726-4.00096-X.

[75] Z.Z. Fang, H. Wang, 13 - Sintering of ultrafine and nanosized ceramic and metallic particles, in: R. Banerjee, I. Manna (Eds.), Ceramic Nanocomposites, Woodhead Publishing, 2013: pp. 431–473. https://doi.org/https://doi.org/10.1533/9780857093493.3.431.

[76] R.M. German, 1 - Thermodynamics of sintering, in: Z.Z. Fang (Ed.), Sintering of Advanced Materials, Woodhead Publishing, 2010: pp. 3–32. https://doi.org/https://doi.org/10.1533/9781845699949.1.3.

[77] E.Z. da Silva, G.M. Faccin, T.R. Machado, N.G. Macedo, M. de Assis, S. Maya-Johnson, J.C. Sczancoski, J. Andrés, E. Longo, M.A. San-Miguel, Connecting Theory with Experiment to Understand the Sintering Processes of Ag Nanoparticles, The Journal of Physical Chemistry C 123 (2019) 11310–11318. https://doi.org/10.1021/acs.jpcc.9b02107.

[78] K. Lu, Sintering of nanoceramics, International Materials Reviews 53 (2008) 21–38. https://doi.org/10.1179/174328008X254358.

[79] S.J. Dillon, Y. Ma, J. Oyang, D.K. Coffman, O. Hussein, K. Hattar, F. Abdeljawad, Interface nucleation rate limited densification during sintering, Acta Mater 242 (2023) 118448. https://doi.org/https://doi.org/10.1016/j.actamat.2022.118448.

[80] A.P. Lange, A. Samanta, H. Majidi, S. Mahajan, J. Ging, T.Y. Olson, K. van Benthem, S. Elhadj, Dislocation mediated alignment during metal nanoparticle coalescence, Acta Mater 120 (2016) 364–378. https://doi.org/https://doi.org/10.1016/j.actamat.2016.08.061.

[81] Y. Tang, W. He, S. Wang, Z. Tao, L. Cheng, New insight into the size-controlled synthesis of silver nanoparticles and its superiority in room temperature sintering, CrystEngComm 16 (2014) 4431–4440. https://doi.org/10.1039/C3CE42439A.

[82] Z.Z. Fang, H. Wang, Densification and grain growth during sintering of nanosized particles, International Materials Reviews 53 (2008) 326–352. https://doi.org/10.1179/174328008X353538.

[83] Q. Jia, G. Zou, H. Zhang, W. Wang, H. Ren, Z. A, Z. Deng, S. Yan, D. Shen, L. Liu, Sintering mechanism of Ag-Pd nanoalloy film for power electronic packaging, Appl Surf Sci 554 (2021) 149579. https://doi.org/https://doi.org/10.1016/j.apsusc.2021.149579.

[84] J. Li, C.M. Johnson, C. Buttay, W. Sabbah, S. Azzopardi, Bonding strength of multiple SiC die attachment prepared by sintering of Ag nanoparticles, J Mater Process Technol 215 (2015) 299–308. https://doi.org/https://doi.org/10.1016/j.jmatprotec.2014.08.002.

[85] J. Wang, S. Yodo, H. Tatsumi, H. Nishikawa, Reliability-enhanced microscale Ag sintered joint doped with AlN nanoparticles, Mater Lett 349 (2023) 134845. https://doi.org/https://doi.org/10.1016/j.matlet.2023.134845.

[86] J. Jiu, H. Zhang, S. Nagao, T. Sugahara, N. Kagami, Y. Suzuki, Y. Akai, K. Suganuma, Die-attaching silver paste based on a novel solvent for high-power semiconductor devices, J Mater Sci 51 (2016) 3422–3430. https://doi.org/10.1007/s10853-015-9659-8.

[87] G. Bai, G.-Q. Lu, Low -temperature sintering of nanoscale silver paste for semiconductor device interconnection, 2005. https://www.proquest.com/dissertations-theses/low-temperature-sintering-nanoscale-silver-paste/docview/305381996/se-2?accountid=16714.

[88] M. Tobita, Y. Yasuda, E. Ide, J. Ushio, T. Morita, Optimal design of coating material for nanoparticles and its application for low-temperature interconnection, Journal of Nanoparticle Research 12 (2010) 2135–2144. https://doi.org/10.1007/s11051-009-9775-y.

[89] J. Yan, G. Zou, L. Liu, D. Zhang, H. Bai, A. ping Wu, Y.N. Zhou, Sintering mechanisms and mechanical properties of joints bonded using silver nanoparticles for electronic packaging applications, Welding in the World 59 (2015) 427–432. https://doi.org/10.1007/s40194-014-0216-x.

[90] R.L. Coble, Sintering Crystalline Solids. I. Intermediate and Final State Diffusion Models, J Appl Phys 32 (1961) 787–792. https://doi.org/10.1063/1.1736107.

[91] A.J. Shaler, J. Wulff, Mechanism of Sintering, Ind Eng Chem 40 (1948) 838–842. https://doi.org/10.1021/ie50461a014.

[92] J.A. Frenkel, Viscous flow of crystalline bodies under the action of surface tension, J. Phys.(USS R) 9 (1945) 385.

[93] A. Hu, J.Y. Guo, H. Alarifi, G. Patane, Y. Zhou, G. Compagnini, C.X. Xu, Low temperature sintering of Ag nanoparticles for flexible electronics packaging, Appl Phys Lett 97 (2010) 153117. https://doi.org/10.1063/1.3502604.

[94] T. Wang, X. Chen, G.-Q. Lu, G.-Y. Lei, Low-Temperature Sintering with Nano-Silver Paste in Die-Attached Interconnection, J Electron Mater 36 (2007) 1333–1340. https://doi.org/10.1007/s11664-007-0230-5.

[95] J.G. Bai, T.G. Lei, J.N. Calata, G.-Q. Lu, Control of nanosilver sintering attained through organic binder burnout, J Mater Res 22 (2007) 3494–3500. https://doi.org/DOI: 10.1557/JMR.2007.0440.

[96] F. Yu, R.W. Johnson, M.C. Hamilton, Pressureless Sintering of Microscale Silver Paste for 300 °C Applications, IEEE Trans Compon Packaging Manuf Technol 5 (2015) 1258–1264. https://doi.org/10.1109/TCPMT.2015.2455811.

[97] J.W. Yoon, J.H. Back, Effect of sintering conditions on the mechanical strength of Cu-sintered joints for high-power applications, Materials 11 (2018). https://doi.org/10.3390/MA11112105.

[98] H. Kino, H. Hashiguchi, S. Tanikawa, Y. Sugawara, S. Ikegaya, T. Fukushima, M. Koyanagi, T. Tanaka, Effect of local stress induced by thermal expansion of underfill in three-dimensional stacked IC, Jpn J Appl Phys 55 (2016) 04EC03. https://doi.org/10.7567/JJAP.55.04EC03.

[99] K. Suganuma, S. Sakamoto, N. Kagami, D. Wakuda, K.-S. Kim, M. Nogi, Low-temperature low-pressure die attach with hybrid silver particle paste, Microelectronics Reliability 52 (2012) 375–380. https://doi.org/https://doi.org/10.1016/j.microrel.2011.07.088.

[100] J. Wang, S. Yodo, H. Tatsumi, H. Nishikawa, Thermal conductivity and reliability reinforcement for sintered microscale Ag particle with AlN nanoparticles additive, Mater Charact 203 (2023) 113150. https://doi.org/https://doi.org/10.1016/j.matchar.2023.113150.

[101] T. Matsuda, R. Seo, A. Hirose, Highly strong interface in Ag/Si sintered joints obtained through Ag2O–Ag composite paste, Materials Science and Engineering: A 865 (2023) 144647. https://doi.org/10.1016/J.MSEA.2023.144647.

[102] S.-Y. Zhao, X. Li, Y.-H. Mei, G.-Q. Lu, Novel interface material used in high power electronic die-attaching on bare Cu substrates, Journal of Materials Science: Materials in Electronics 27 (2016) 10941–10950. https://doi.org/10.1007/s10854-016-5208-8.

[103] M. Li, Y. Xiao, Z. Zhang, J. Yu, Bimodal Sintered Silver Nanoparticle Paste with Ultrahigh Thermal Conductivity and Shear Strength for High Temperature Thermal Interface Material Applications, ACS Appl Mater Interfaces 7 (2015) 9157–9168. https://doi.org/10.1021/acsami.5b01341.

[104] D. Yang, Y. Huang, Y. Tian, Microstructure of Ag Nano Paste Joint and Its Influence on Reliability, Crystals (Basel) 11 (2021) 1537. https://doi.org/10.3390/cryst11121537.

[105] S. Joo, D.F. Baldwin, Adhesion mechanisms of nanoparticle silver to substrate materials: identification, Nanotechnology 21 (2010) 055204. https://doi.org/10.1088/0957-4484/21/5/055204.

[106] H. Fang, C. Wang, S. Zhou, Q. Kang, T. Wang, D. Yang, Y. Tian, T. Suga, Rapid pressureless and low-temperature bonding of large-area power chips by sintering two-step activated Ag paste, Journal of Materials Science: Materials in Electronics 31 (2020) 6497–6505. https://doi.org/10.1007/s10854-020-03207-y.

[107] C. Wang, X. Zhang, Y. Zhang, T. Zhao, P. Zhu, R. Sun, H. Nishikawa, L. Xu, Pressureless and low temperature sintering by Ag paste for the high temperature die-attachment in power device packaging, in: 2022 IEEE 72nd Electronic Components and Technology Conference (ECTC), 2022: pp. 2256–2262. https://doi.org/10.1109/ECTC51906.2022.00356.

[108] M.-S. Kim, K. Matsunaga, Y.-H. Ko, C.-W. Lee, H. Nishikawa, Reliability of Ag Nanoporous Bonding Joint for High Temperature Die Attach under Temperature Cycling, Mater Trans 57 (2016) 1192–1196. https://doi.org/10.2320/matertrans.MD201518.

[109] H. Zhang, H. Zhang, Q. Jia, C. Yin, Z. Deng, W. Guo, Z. Wan, Novel SiC-Based Power Device Bonding Materials of Nano Foam Sheet and Its Characteristic and Properties, IEEE Trans Compon Packaging Manuf Technol 13 (2023) 897–905. https://doi.org/10.1109/TCPMT.2023.3288389.

[110] C. Chen, D. Kim, Z. Wang, Z. Zhang, Y. Gao, C. Choe, K. Suganuma, Low temperature low pressure solid-state porous Ag bonding for large area and its high-reliability design in die-attached power modules, Ceram Int 45 (2019) 9573–9579. https://doi.org/10.1016/J.CERAMINT.2018.10.046.

[111] W. Wang, G. Zou, Q. Jia, H. Zhang, B. Feng, Z. Deng, L. Liu, Mechanical properties and microstructure of low temperature sintered joints using organic-free silver nanostructured film for die attachment of SiC power electronics, Materials Science and Engineering: A 793 (2020) 139894. https://doi.org/https://doi.org/10.1016/j.msea.2020.139894.

[112] M.-S. Kim, H. Nishikawa, Effects of bonding temperature on microstructure, fracture behavior and joint strength of Ag nanoporous bonding for high temperature die attach, Materials Science and Engineering: A 645 (2015) 264–272. https://doi.org/https://doi.org/10.1016/j.msea.2015.08.015.

[113] N.A.A. Qasem, R.H. Mohammed, D.U. Lawal, Removal of heavy metal ions from wastewater: a comprehensive and critical review, NPJ Clean Water 4 (2021) 36. https://doi.org/10.1038/s41545-021-00127-0.

[114] Y. Choi, K. Seong, Y. Piao, Metal−Organic Decomposition Ink for Printed Electronics, Adv Mater Interfaces 6 (2019) 1901002. https://doi.org/https://doi.org/10.1002/admi.201901002.

[115] M. Vaseem, G. McKerricher, A. Shamim, Robust Design of a Particle-Free Silver-Organo-Complex Ink with High Conductivity and Inkjet Stability for Flexible Electronics, ACS Appl Mater Interfaces 8 (2016) 177–186. https://doi.org/10.1021/acsami.5b08125.

[116] X. Zeng, P. He, M. Hu, W. Zhao, H. Chen, L. Liu, J. Sun, J. Yang, Copper inks for printed electronics: a review, Nanoscale 14 (2022) 16003–16032. https://doi.org/10.1039/D2NR03990G.

[117] Y. Dong, X. Li, S. Liu, Q. Zhu, J.-G. Li, X. Sun, Facile synthesis of high silver content MOD ink by using silver oxalate precursor for inkjet printing applications, Thin Solid Films 589 (2015) 381–387. https://doi.org/https://doi.org/10.1016/j.tsf.2015.06.001.

[118] M. Vaseem, S.-K. Lee, J.-G. Kim, Y.-B. Hahn, Silver-ethanolamine-formate complex based transparent and stable ink: Electrical assessment with microwave plasma vs thermal sintering, Chemical Engineering Journal 306 (2016) 796–805. https://doi.org/https://doi.org/10.1016/j.cej.2016.08.003.

[119] W. Yang, C. Wang, V. Arrighi, An organic silver complex conductive ink using both decomposition and self-reduction mechanisms in film formation, Journal of Materials Science: Materials in Electronics 29 (2018) 2771–2783. https://doi.org/10.1007/s10854-017-8205-7.

[120] Y. Farraj, M. Grouchko, S. Magdassi, Self-reduction of a copper complex MOD ink for inkjet printing conductive patterns on plastics, Chemical Communications 51 (2015) 1587–1590. https://doi.org/10.1039/C4CC08749F.

[121] Y. Yong, M.T. Nguyen, H. Tsukamoto, M. Matsubara, Y.-C. Liao, T. Yonezawa, Effect of decomposition and organic residues on resistivity of copper films fabricated via low-temperature sintering of complex particle mixed dispersions, Sci Rep 7 (2017) 45150. https://doi.org/10.1038/srep45150.

[122] J. Lee, B. Lee, S. Jeong, Y. Kim, M. Lee, Microstructure and electrical property of laser-sintered Cu complex ink, Appl Surf Sci 307 (2014) 42–45. https://doi.org/https://doi.org/10.1016/j.apsusc.2014.03.127.

[123] W. Xie, X. Li, M. Zhang, Q. Zhu, J.G. Li, X. Sun, A nickel metal-organic-decomposition ink of nickel-ethanolamine complex leading to highly conductive nickel patterns for printed electronic applications, Thin Solid Films 744 (2022). https://doi.org/10.1016/j.tsf.2022.139081.

[124] M. Nakano, T. Fujiwara, N. Koga, Thermal Decomposition of Silver Acetate: Physico-Geometrical Kinetic Features and Formation of Silver Nanoparticles, Journal of Physical Chemistry C 120 (2016) 8841–8854. https://doi.org/10.1021/acs.jpcc.6b02377.

[125] K.R. Zope, D. Cormier, S.A. Williams, Reactive Silver Oxalate Ink Composition with Enhanced Curing Conditions for Flexible Substrates, ACS Appl Mater Interfaces 10 (2018) 3830–3837. https://doi.org/10.1021/acsami.7b19161.

[126] W. Yang, C. Liu, Z. Zhang, Y. Liu, S. Nie, One step synthesis of uniform organic silver ink drawing directly on paper substrates, J Mater Chem 22 (2012) 23012–23016. https://doi.org/10.1039/C2JM34264B.

[127] Y. Tao, Y. Tao, B. Wang, L. Wang, Y. Tai, A facile approach to a silver conductive ink with high performance for macroelectronics, Nanoscale Res Lett 8 (2013) 296. https://doi.org/10.1186/1556-276X-8-296.

[128] W. Yang, Z. Dong, Z. Guo, C. Wang, Tailored Silver Malonate Conductive Ink with Tunable Performance Formulated from Mixed Silver Dicarboxylates, ACS Appl Electron Mater 5 (2023) 2598–2607. https://doi.org/10.1021/acsaelm.3c00085.

[129] H. Zhang, W. Wang, H. Bai, G. Zou, L. Liu, P. Peng, W. Guo, Microstructural and mechanical evolution of silver sintering die attach for SiC power devices during high temperature applications, J Alloys Compd 774 (2019) 487–494. https://doi.org/https://doi.org/10.1016/j.jallcom.2018.10.067.

[130] Y. Xu, X. Qiu, W. Li, S. Wang, N. Ma, M. Ueshima, C. Chen, K. Suganuma, Development of high thermal conductivity of Ag/diamond composite sintering paste and its thermal shock reliability evaluation in SiC power modules, Journal of Materials Research and Technology 26 (2023) 1079–1093. https://doi.org/https://doi.org/10.1016/j.jmrt.2023.07.254.

[131] W.S. Hong, M.S. Kim, Power Cycling Reliability with Temperature Deviation of Pressureless Silver Sintered Joint for Silicon Carbide Power Module, JOM 76 (2024) 2763–2771. https://doi.org/10.1007/s11837-024-06398-5.

[132] C. Chen, C. Choe, D. Kim, Z. Zhang, X. Long, Z. Zhou, F. Wu, K. Suganuma, Effect of oxygen on microstructural coarsening behaviors and mechanical properties of Ag sinter paste during high-temperature storage from macro to micro, J Alloys Compd 834 (2020) 155173. https://doi.org/https://doi.org/10.1016/j.jallcom.2020.155173.

[133] S.T. Chua, K.S. Siow, Microstructural studies and bonding strength of pressureless sintered nano-silver joints on silver, direct bond copper (DBC) and copper substrates aged at 300 °C,

J Alloys Compd 687 (2016) 486–498. https://doi.org/https://doi.org/10.1016/j.jallcom.2016.06.132.

[134] Y. Tan, X. Li, G. Chen, Q. Gao, G.-Q. Lu, X. Chen, Effects of thermal aging on long-term reliability and failure modes of nano-silver sintered lap-shear joint, Int J Adhes Adhes 97 (2020) 102488. https://doi.org/https://doi.org/10.1016/j.ijadhadh.2019.102488.

[135] Z. Cui, Q. Jia, H. Zhang, Y. Wang, L. Ma, G. Zou, F. Guo, Review on Shear Strength and Reliability of Nanoparticle Sintered Joints for Power Electronics Packaging, J Electron Mater 53 (2024) 2703–2726. https://doi.org/10.1007/s11664-024-10970-9.

[136] Y.-R. Jang, S.-J. Park, J.-H. Baek, T.-H. Kim, H.-S. Kim, Thermal Shock Life Prediction of the SiC Wide Bandgap Power Module Semiconductor Package Considering Creep Behavior of the Ag Sintered Interconnect and Viscoelastic Properties of the Epoxy Molding Compound, ACS Appl Electron Mater 5 (2023) 5513–5526. https://doi.org/10.1021/acsaelm.3c00763.

[137] Y. Liu, C. Chen, Z. Zhang, M. Ueshima, T. Sakamoto, T. Naoe, H. Nishikawa, Y. Oda, K. Suganuma, Development of crack-less and deformation-resistant electroplated Ni/electroless Ni/Pt/Ag metallization layers for Ag-sintered joint during a harsh thermal shock, Mater Des 224 (2022) 111389. https://doi.org/https://doi.org/10.1016/j.matdes.2022.111389.

[138] L. Wang, Y. Ji, S. Li, P. Mei, Effect of Particle Shapes on Thermal Shock Reliability of Sintered Ag Joints under Low-Temperature Pressureless Sintering, J Mater Eng Perform 32 (2023) 4427–4436. https://doi.org/10.1007/s11665-022-07411-1.

[139] Y.H. Mei, Z. Wang, K.S. Siow, Reliability and Failure Mechanisms of Sintered Silver as Die Attach Joint, in: K.S. Siow (Ed.), Die-Attach Materials for High Temperature Applications in Microelectronics Packaging: Materials, Processes, Equipment, and Reliability, Springer International Publishing, Cham, 2019: pp. 125–150. https://doi.org/10.1007/978-3-319-99256-3_5.

[140] A.A. Bajwa, E. Möller, J. Wilde, Die-attachment technologies for high-temperature applications of Si and SiC-based power devices, in: 2015 IEEE 65th Electronic Components and Technology Conference (ECTC), 2015: pp. 2168–2174. https://doi.org/10.1109/ECTC.2015.7159903.

[141] C. Chen, D. Kim, Z. Zhang, N. Wakasugi, Y. Liu, M.-C. Hsieh, S. Zhao, A. Suetake, K. Suganuma, Interface-Mechanical and Thermal Characteristics of Ag Sinter Joining on Bare DBA Substrate During Aging, Thermal Shock and 1200 W/cm2 Power Cycling Tests, IEEE Trans Power Electron 37 (2022) 6647–6659. https://doi.org/10.1109/TPEL.2022.3142286.

[142] R. Amro, J. Lutz, J. Rudzki, M. Thoben, A. Lindemann, Double-sided low-temperature joining technique for power cycling capability at high temperature, in: 2005 European Conference on Power Electronics and Applications, 2005: pp. 10 pp.-P.10. https://doi.org/10.1109/EPE.2005.219523.

[143] S.B. Walker, J.A. Lewis, Reactive Silver Inks for Patterning High-Conductivity Features at Mild Temperatures, J Am Chem Soc 134 (2012) 1419–1421. https://doi.org/10.1021/ja209267c.

[144] W. Yang, E.J.W. List-Kratochvil, C. Wang, Metal particle-free inks for printed flexible electronics, J Mater Chem C Mater 7 (2019) 15098–15117. https://doi.org/10.1039/C9TC05463D.

Chapter 2: Ag sintered joints derived from Ag nanostructures via the thermal decomposition of an Ag-based complex

2.1 Introduction

The purpose of this chapter is to verify the feasibility of using an Ag-based complex as a die-attach material. For die-bonding, the priority is to achieve robust joints [1]. Therefore, this study considered the shear strength value of Ag sintered joints as an index to confirm the feasibility. This goal was achieved by dividing the experiments into two steps: Ag nanostructure preparation and die-bonding. As organic components are a major part of the Ag-based complex, organic gasification could cause serious issues if the Ag-based complex is directly used as a die-attach material [2,3]. Herein, Ag nanostructures derived from the thermal decomposition of Ag-based complex were utilized as an intermediate medium for die-bonding.

Thermal decomposition temperature and time are two key factors that determine the fabrication of Ag nanostructures. Therefore, the feasibility experiments were conducted via the Ag nanostructures obtained at different thermal decomposition temperatures and times. Ag nanostructures derived from different thermal decomposition conditions were bonded under the same bonding conditions. The bonding performance of the prepared Ag nanostructures was evaluated using shear tests. Cross-sections and fracture surfaces were observed to uncover the mechanism of shear strength evolution.

2.2 Materials and Experimental Procedure

2.2.1 Materials

Silver acetate (99%, FUJIFILM), 2-amino-2-methyl-1-propanol (AMP, FUJIFILM), distilled water, and ethanol were purchased and used without further purification. Electroless nickel/immersion gold (ENIG) Cu substrates were used as dummy dies (D = 3 mm) and dummy substrates (D = 10 mm). Before using the ENIG Cu substrates, possible surface impurities were removed by ultrasound in ethanol for 9 min.

2.2.2 Synthesis of Ag-based complex

A typical process of Ag-based complex synthesizing is shown in **Fig. 2.1**. As shown in **Fig. 2.1a**, the Ag-based complex was prepared by mixing silver acetate, AMP, and distilled water via magnetic stirring at a weight ratio of 1:1.1:20 for 30 min without exposure to light. This reaction is expressed by Equation (1) [4]:

$$Ag(CH_3COO)\ (s) + (CH_3)_2C(NH_2)CH_2OH\ (l) \xrightarrow{H_2O} Ag[(CH_3)_2C(NH_2)CH_2OH]_2(CH_3COO)\ (l) \quad (1)$$

Consequently, the solid silver acetate vanished, and a transparent solution was obtained in **Fig. 2.1b**, indicating the successful synthesis of an Ag-based complex. The obtained transparent Ag-based complex solution was purified by freeze-drying with pressure < 20 Pa at temperatures < -45 ^{o}C for 72 h to remove the distilled water. **Fig. 2.1c** depicts the Ag-based complex after freeze-drying.

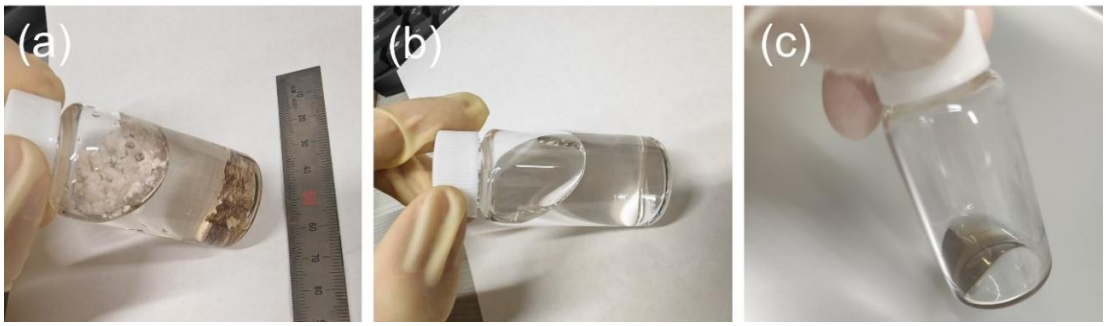

Fig. 2.1 Optical mages showing the synthesis process of Ag-based complex. Optical image of (a) the mixture of silver acetate and AMP in distilled water, (b) prepared Ag-based complex solution, and (c) Ag-based complex after freeze-drying.

2.2.3 Preparation of Ag nanostructures

Fig. 2.2 shows the detailed information of Ag nanostructure preparation. As shown in Fig. **2.2a-c**, predetermined amounts of 60 and 10 mg Ag-based complex were printed on substrates and dies, then heated with the heating profile in **Fig. 2.2d** to prepare Ag nanostructures. The Ag nanostructures derived from the decomposition of the Ag-based complex at 180 ºC for 2, 5, 10, 20, 30, and 60 min were named Ag-NS-2, Ag-NS-5, Ag-NS-10, Ag-NS-20, Ag-NS-30, and Ag-NS-60, respectively. The Ag nanostructures obtained at 160 ºC, 180 ºC, and 200 ºC for 30 min were named Ag-NS-160, Ag-NS-180, and Ag-NS-200, respectively. The difference between the setting temperature and actual temperature was determined by measuring the temperatures of the top surface of the ENIG substrate by a thermal couple. The actual temperatures of setting temperatures 160, 180, and 200 ºC were 159.7, 179.4, and 199.2 ºC, respectively, indicating a negligible difference between them. Therefore, the setting temperatures were used to represent the actual temperatures in the following section.

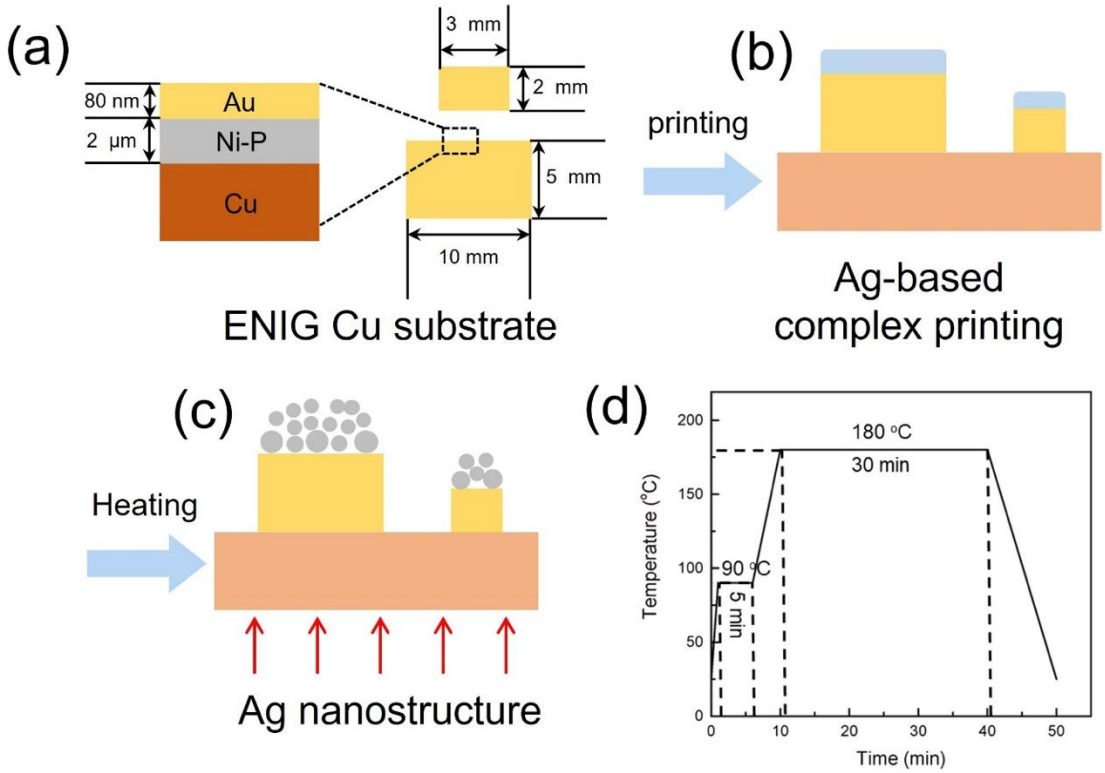

Fig. 2.2 Preparation of Ag nanostructures. (a)-(c) Schematic diagrams of the preparation process of Ag nanostructures. (d) Heating profile of the preparation of the Ag nanostructures.

2.2.4 Preparation of Ag sintered joints

The feasibility tests of using an Ag-based complex as die-bonding material were conducted based on various thermal decomposition conditions. **Fig. 2.3** depicts the flow of the die-bonding process and corresponding heating conditions. The Ag nanostructure of the die was placed directly on the substrate to prepare die-attachment samples. As shown in **Fig. 2.3a**, three samples were placed at the corners of an equilateral triangle in a fixture to ensure that each sample was subjected to the same pressure. As shown in **Fig. 2.3b**, three samples were bonded simultaneously in the bonding machine. As no solvent or surface ligands were added, the bonding process was conducted by a simple temperature profile with a rapid ramping rate

of 60 ºC/min in **Fig. 2.3c**, and the bonding temperature, holding time, and assistant pressure were set to 200 ºC, 40 min, and 5 MPa, respectively. Finally, Ag joints were obtained.

2.2.5 Characterization

The purity of the Ag-based complex used in Ag nanostructure preparation was determined by characterizing the complex before and after freeze-drying using high-performance liquid chromatography with methanol solution (HPLC, Agilent 1260 Infinity II). The actual thermal decomposition temperatures of the Ag-based complex were measured by a thermal couple (midi LOGGER GL240). The thermal decomposition behaviors of the Ag-based complex were analyzed by thermogravimetric analysis (TGA, HITACHI STA7200) and differential scanning calorimetry (DSC, HITACHI DSC7020) with a heating rate of 10 ºC/ min in N_2. The morphological changes during the thermal decomposition were recorded by a reflow oven with a heating rate of 10 ºC/min at a temperature range 40 to 300 ºC in N_2 atmosphere with O_2 less than 1000 ppm (SMT Scope SK-5000). The compositions of the thermally decomposed Ag-based complexes were investigated using X-ray diffraction (XRD, Ultima IV, Rigaku). The bonding was performed using a hot-press machine (RB-100D, Ayumi Industry Co., Ltd.). The cross-section of the sintered Ag joint was fabricated by sandpaper polishing and ion polishing (IB-19530CP, JEOL). A scanning electron microscope (SEM) equipped with energy dispersive spectroscopy (EDS) (SEM, FEI Nova Nana SEM 450) was used to analyze the microstructure and elemental distribution.

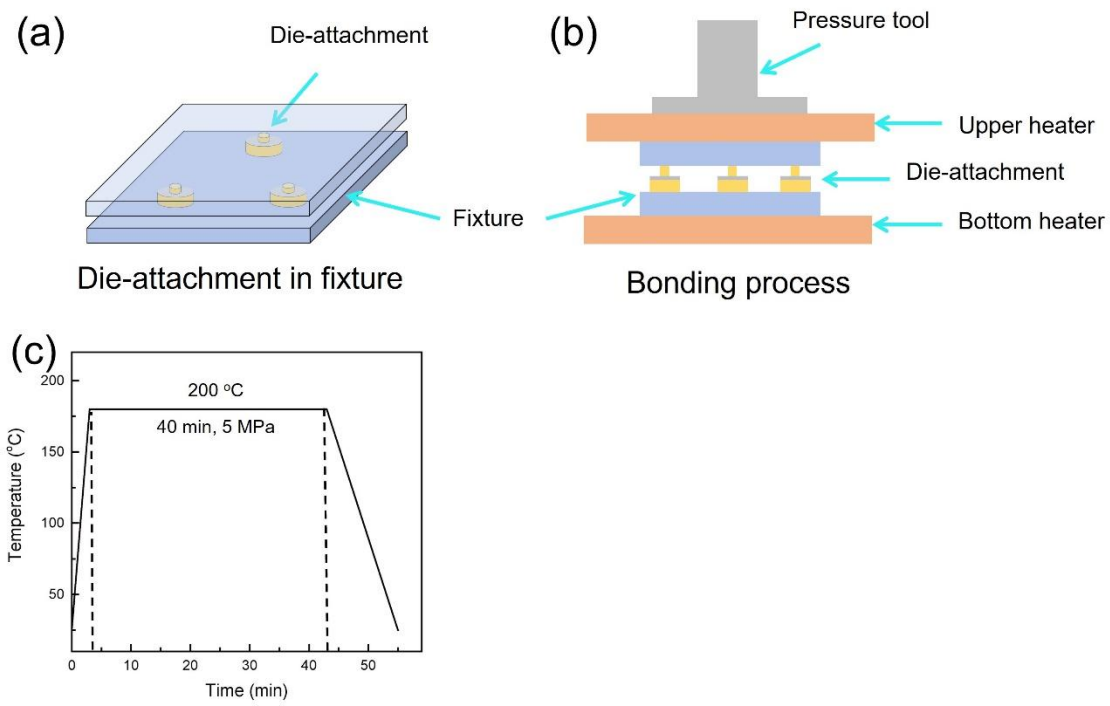

Fig. 2.3 Preparation of Ag sintered joints. (a)-(b) Schematic diagrams of the preparation process of Ag sintered joints. (c) Heating profile of the bonding process.

2.2.6 Measurement of shear strength

Fig. 2.4 shows the measurement of shear strength and particle size of the Ag nanostructures. The shear strength of sintered Ag joints was tested by conducting the die-shear test (STR-1000, Rhesca) with a shear height of 200 μm and a shear speed of 1 mm/min in **Fig. 2.4a**

2.2.7 Calculation of particle size

As depicted in **Fig. 2.4b**, the diameter of a single Ag particle was measured using the ImageJ software. Three hundred Ag particles per sample were measured to ensure the statistical accuracy of the particle size distribution.

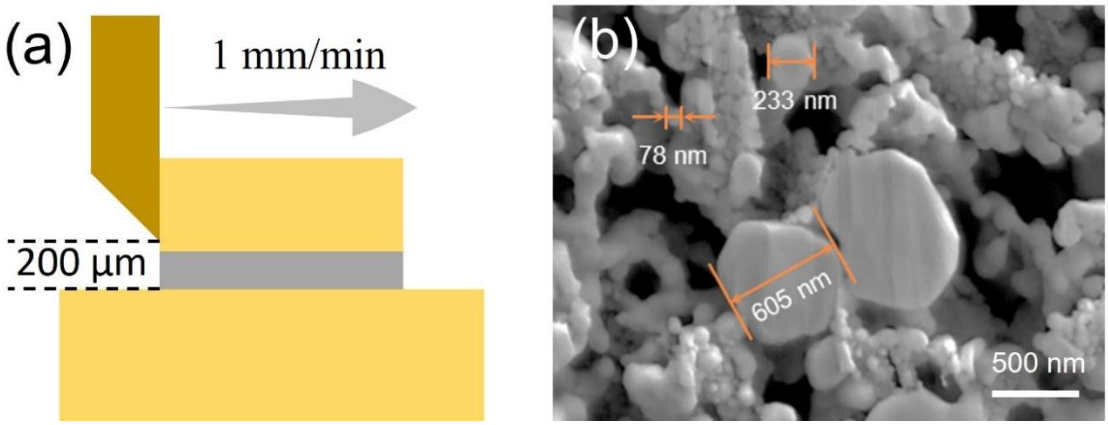

Fig. 2.4 Characterization of samples. Measurement of (a) shear strength and (b) particle size.

2.3 Results and Discussion

2.3.1 Characterization of the Ag-based complex

In this study, silver acetate was selected as silver precursor because of its high Ag content 64.6%. To reduce the organic residuals, a basic rule for selecting the complexing agent is that severe carbamate polymerization should be prevented. The amino group of AMP is attached to a tertiary carbon atom, resulting in a sterically hindered primary amine [5]. This makes it difficult for the carbamate polymerization to occur. The Ag-based complex was synthesized in distilled water. Excess distilled water in the prepared transparent solution significantly resulted in a low content of Ag-based complex. To improve the purity of the Ag-based complex, the distilled water in the transparent solution was removed by freeze-drying. HPLC is a commonly used method to qualitatively and quantitatively analyze sample components. Therefore, the prepared Ag-based complexes before and after freeze-drying were characterized by HPLC. **Fig. 2.5** depicts the HPLC spectra of the Ag-based complex before

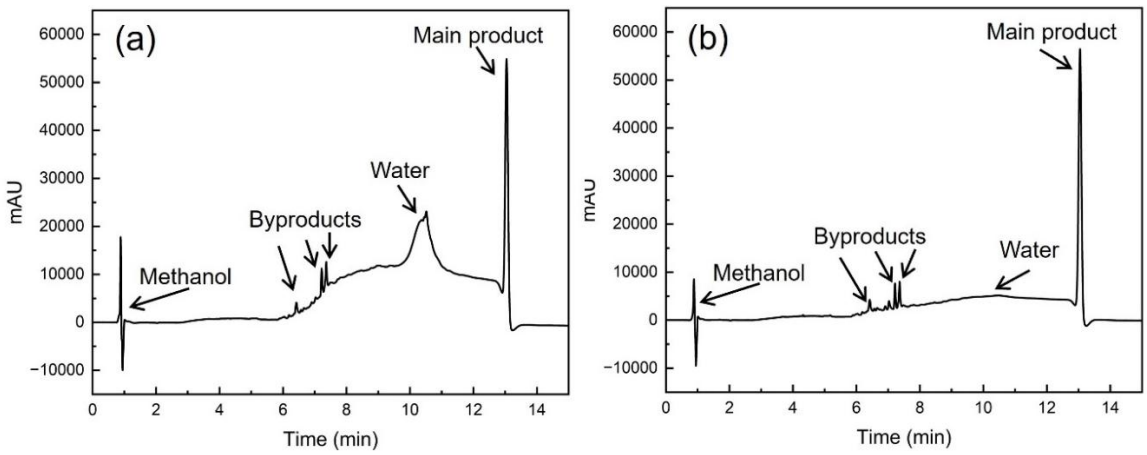

Fig. 2.5 HPLC characterization (solvent: methanol) of the as-synthesized Ag-based complex (a) before and (b) after freeze-drying.

and after freeze-drying. As shown in **Fig. 2.5a** and **2.5b**, the peak intensity at 10.5 min decreased dramatically after freeze-drying, which may be attributed to the removal of the distilled water. The highest peak in **Fig. 2.5a** and **2.5b** could be attributed to the main products of the complexing reaction between silver acetate and AMP. The HPLC spectra can quantitatively analyze the sample components according to the area of peaks. The area of each peak was measured by Image-J, and the results demonstrated that the concentration of the main products was as high as 90.4% after freeze-drying.

2.3.2 Thermal decomposition behaviors of Ag-based complex

The thermal decomposition of the Ag-based complex involves multiple steps [6–9]. Understanding the thermal decomposition of the synthesized Ag-based complex is crucial in Ag nanostructure preparation. Thermal decomposition of the Ag-based complex is related to weight loss and thermal changes. TG and DSC are common and straightforward methods to reveal the decomposition behaviors of Ag-based complexes [4]. Additionally, the

morphological changes with heating are helpful in understanding the decomposition behaviors of Ag-based complexes. Therefore, the thermal decomposition behaviors of the Ag-based complex and silver acetate were investigated using TG analysis, DSC, and a reflow oven equipped with a camera. **Fig. 2.6** depicts the TG and DSC results, and **Fig. 2.7** illustrates the optical images of the decomposition process of the Ag-based complex. As the TG curve

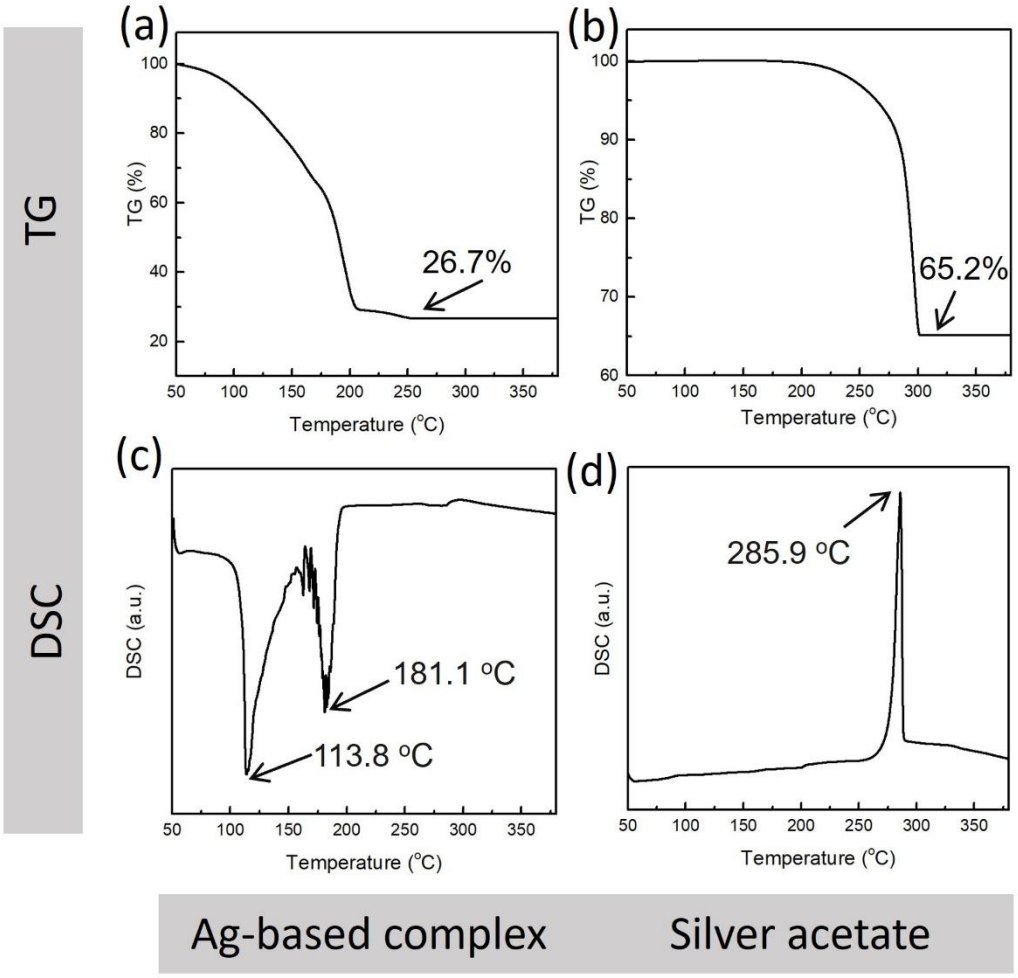

Fig. 2.6 Thermal behaviors of Ag-based complex and silver acetate. TGA curve of (a) Ag-based complex and (b)silver acetate; DSC curves of (c) the Ag-based complex and (d) silver acetate.

of Ag-based complex shown in **Fig. 2.6a**, the weight loss started at 50 ^{o}C and a significant weight loss was recorded at 160-200 ^{o}C, and the remaining weight after equilibrium was 26.7%, which was higher than the Ag-based complex in previous studies [9,10]. The Ag-based complex demonstrated two endothermic peaks in **Fig. 2.6c**, which may be attributed to its multistep decomposition [6–9]. The first peak at 113.8 °C dropping near 100 ^{o}C may be attributed to water evaporation and the acetic ligand dissociation and evaporation, with boiling points of 100 ^{o}C and 117.9 ^{o}C, respectively [7]. The recorded optical images of **Fig. 2.7** at 100–150 ^{o}C corresponded very well to the DSC curve in **Fig. 2.6c**. The Ag-based complex became black at 100–150 ^{o}C indicating the beginning of the decomposition of Ag-based complex. This color change could be attributed to the generation of intermediate products. The second peak at 181.1 °C in **Fig. 2.6c** may be attributed to the transformation from the intermediate products to Ag (0) [8,11]. Correspondingly, the black intermediate products were converted into a solid-state grayish Ag film at 160-210 ^{o}C in **Fig. 2.7** [9]. **Fig. 2.6b** shows that the thermal decomposition of silver acetate resulted in a sharp weight loss close to 286 °C, and the remaining weight was 65.2%, which was close to the theoretical silver content of 64.6% of silver acetate. The exothermic peak at 285.9 °C in **Fig. 2.6d** indicated that the thermal decomposition temperature of silver acetate was approximately 105 ^{o}C higher than that of the prepared Ag-based complex. This result meant that the formation of the Ag-based complex dramatically decreased the thermal decomposition temperature and allowed Ag nanostructures to be prepared at low temperatures.

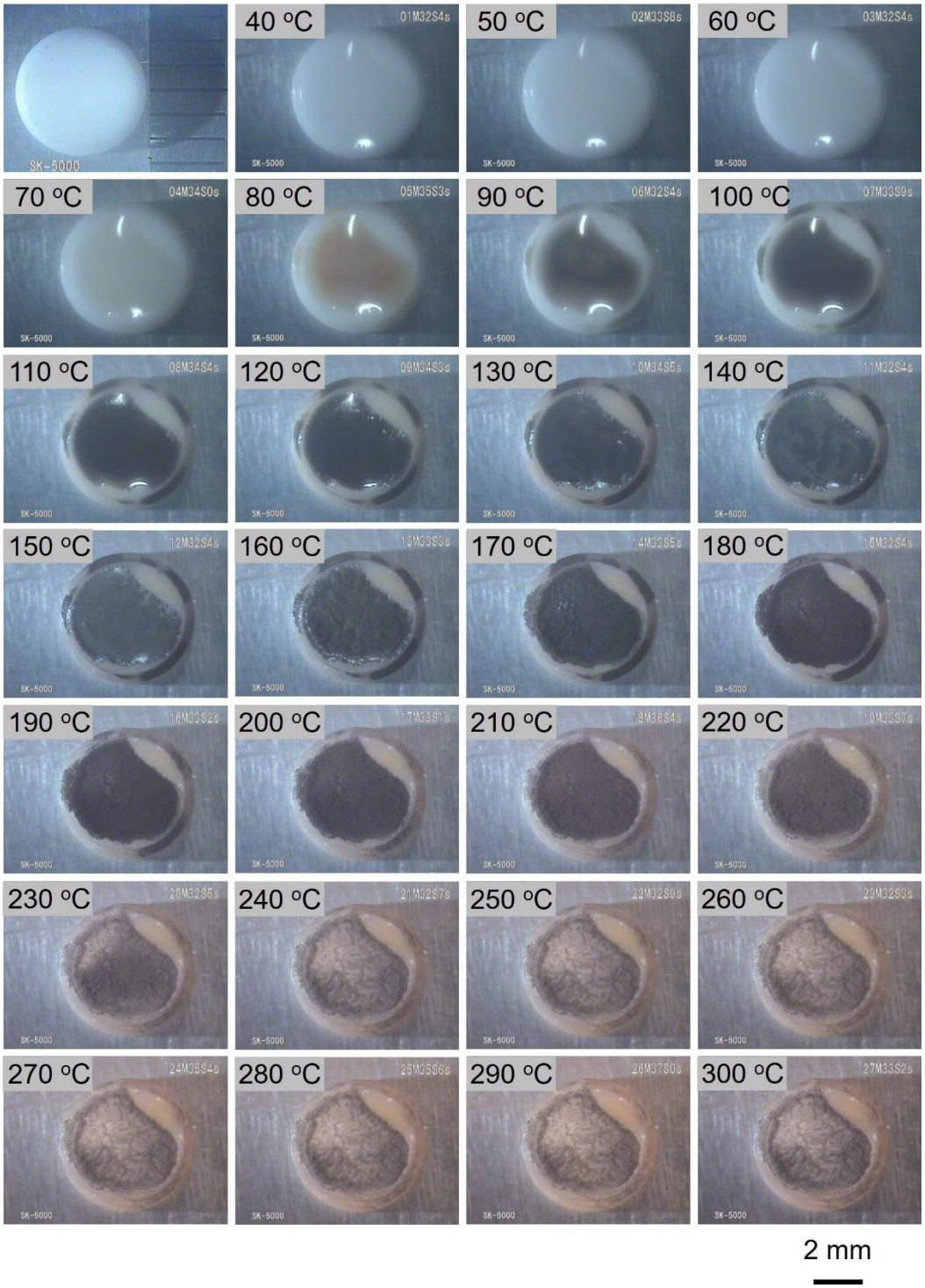

Fig. 2.7 In-situ observation of the thermal decomposition process of the Ag-based complex from 40-300 ^{o}C with a heating rate of 10 ^{o}C/min.

2.2.3 Effects of heating time on the formation of Ag nanostructures

According to the TGA and DSC results in **Fig. 2.6**, the thermal decomposition temperature of Ag-based complex was approximately 180 ^{o}C. Therefore, the decomposition temperature was set to a constant value of 180 ^{o}C, when we investigated the effects of time on the formation of Ag nanostructures. The Ag nanostructures were prepared at 180 ^{o}C for 2, 5, 10, 20, 30, and 60 min. The Ag (I) was expected to be reduced to Ag during the thermal decomposition of the Ag-based complex [12]. The composition changes with decomposition time were confirmed using XRD. **Fig. 2.8** shows the XRD patterns of the Ag nanostructure derived from different time. For a short heating time of 2 min, five characteristic peaks: (111), (200), (220), (311), and (222), of face-centered cubic (*fcc*) crystal structure of Ag (JCPDS No. 04-0783) were detected, which indicated that the thermal decomposition of the Ag-based complex converted Ag (I) to Ag (0) [13]. Along with the Ag characteristic peaks, the characterization peak of silver acetate was detected in the XRD patterns of 2 and 5 min [14]. This is because the ligand dissociation resulted in free silver acetate, which agreed with the DSC result in **Fig. 2.6c**. The intensity of the Ag characteristic peaks increased with the increased heating time. Contrastingly, the characteristic peaks of silver acetate almost disappeared as the heating time increased to 20 min. This result indicated that prolonged heating time promoted the thermal decomposition of the Ag-based complexes.

The TGA, DSC, and XRD results indicated that the Ag-based complex can decompose to Ag at a low temperature of 180 ^{o}C. Several factors determine the bonding performance of Ag material, such as shape, size, and dispersibility [15–17]. Therefore, the Ag-based complex

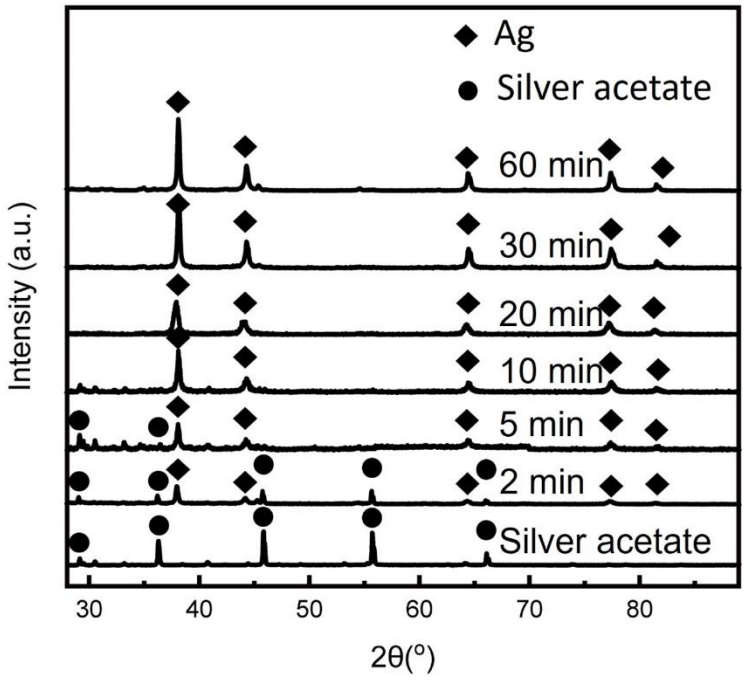

Fig. 2.8. XRD patterns of silver acetate and thermally decomposed Ag-based complex at 180 °C for 2, 5, 10, 20, 30, and 60 min.

after thermal decomposition was characterized by SEM and TEM. **Fig. 2.9** illustrates the representative microstructures of the Ag nanostructures after heating at 180 °C for 30 min. **Fig. 2.9a** demonstrates that the Ag nanostructure consisted of three distinct layers: I) NP layer, II) loose layer, and III) dense layer. The SEM images in **Fig. 2.9b** and **2.9c** demonstrate that both the top surface layer and tiny NP layer consisted of a large number of NPs, whose size distribution was 20–150 nm and 20–220 nm, respectively, according to **Fig. 2.9b1** and **2.9c1**. In terms of loose and dense layers, submicron and micron Ag particles were detected in **Fig. 2.9d** and **2.9e**. **Fig. 2.9d1** and **2.9e1** demonstrate that the size of the largest particle was approximately 30 and 20 times the size of the smallest particle, respectively. These wide-size distributions facilitated the filling of interspaces of larger Ag particles by the small Ag

particles. The interspace filling reduced the air gap volume and improved the stacking density, possibly facilitating the formation of dense sintered Ag joints [18]. In addition, **Fig. 2.9c$_1$-e$_1$** depicts an increase in the Ag particle size from top to bottom.

The relationship between the loose and dense layers was determined by characterizing the white rectangles in **Fig. 2.9a**. **Fig.2.10** shows the amplified SEM images of the interface between the loose and dense layers, which is located at the white rectangle in **Fig. 2.9a**. Besides the larger particle size of the dense layer, the SEM images in **Fig. 2.10a** and **2.10b** demonstrate that the Ag nanoparticles of the loose layer were gradually absorbed by the submicron or micron Ag particles of the dense layer, which could be attributed to Ostwald ripening [19,20]. This observed phenomenon could result in more submicron and micron particles in the dense layer and increase its thickness.

Fig. 2.11 shows the TEM characterization of the Ag particles of the nanostructures. Some Ag NPs smaller than 20 nm that were hardly detected by SEM were detected by TEM in **Fig. 2.11a** and **2.11b**. More importantly, no surface ligands were detected on the surface of the Ag NPs in **Fig. 2.11b**. These results suggested that the advantages of the high surface energy of Ag nanostructures will be exploited without limitations, which is beneficial for enhancing the bonding performance of Ag porous nanostructures [21]. In summary, it is expected that Ag NPs with naked surfaces and wide-size distribution will result in an excellent bonding performance of Ag nanostuctures [21,22].

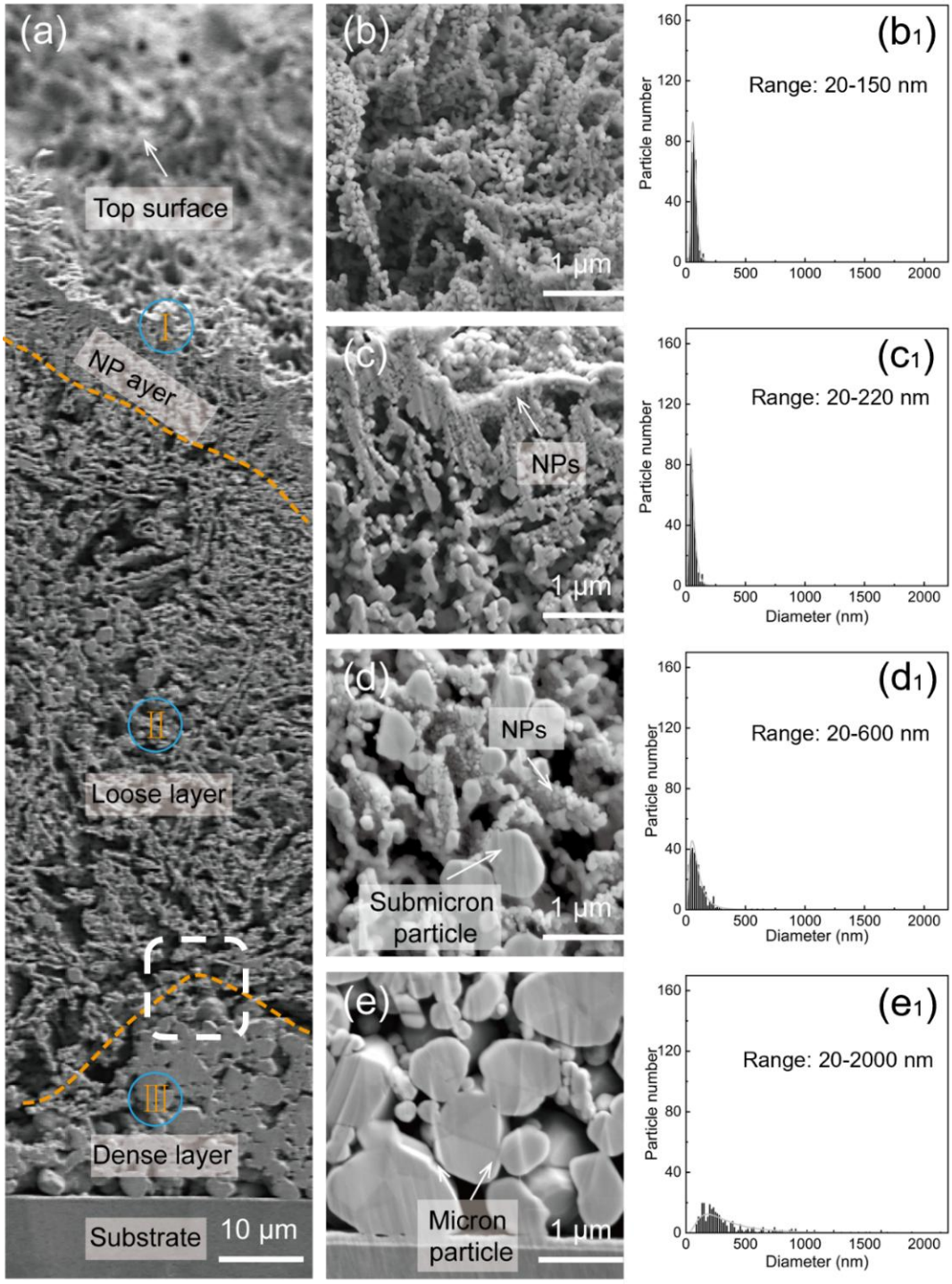

Fig. 2.9 Characterizations of the Ag-NS-30. (a) Overall view of the Ag nanostructure. (b-e) High-magnification views of regions (b) top surface, (c), I (d) II, and (e) III. (b_1-e_1) Corresponding size distribution of (b-e) respectively.

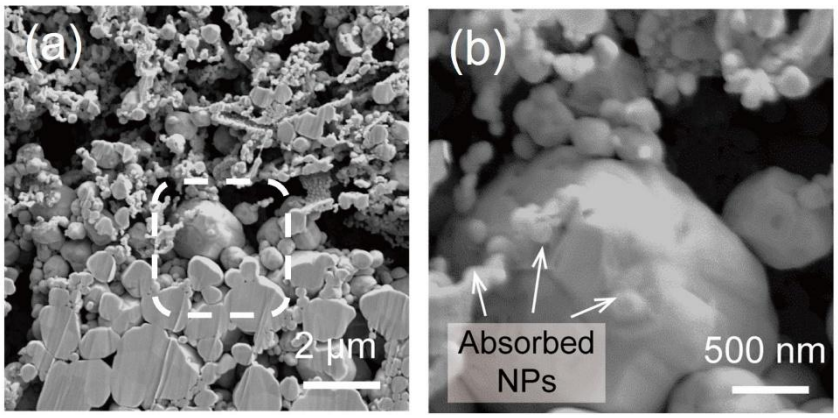

Fig. 2.10 (a) SEM images of the interface between regions II and III in Fig. 2.9a. (b) High-magnification SEM of the white rectangles in (a).

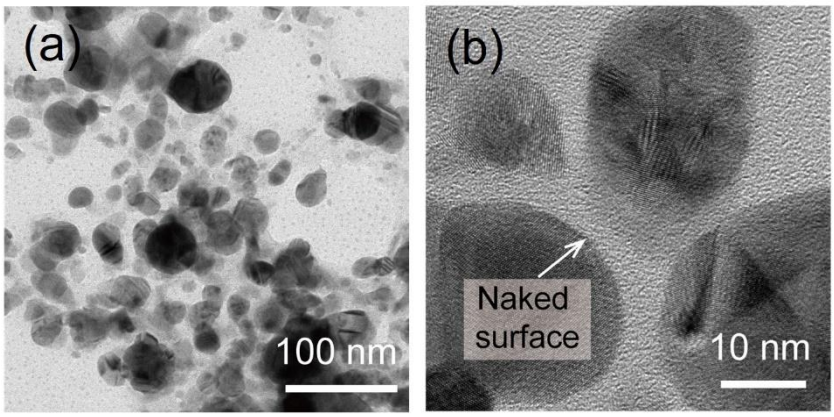

Fig. 2.11 (a) TEM and (b) HRTEM observations of Ag particles of the Ag-NS-30.

The results in **Fig. 2.9** demonstrate that the decomposition of Ag-based complex results in Ag nanostructures with a multilayer structure. Consequently, the top surface and cross-section (I NP layer, II loose layer, and III dense layer) of the Ag nanostructures were observed by SEM to reveal the effects of time on the Ag nanostructure formation. Four Ag nanostructures of **Fig. A1.1** were selected as representatives to depict the microstructures and corresponding particle size distribution of the Ag nanostructures in **Fig. 2.12**. **Fig. 2.12a-d** demonstrates that the Ag nanostructures exhibited a rugged top surface with huge grooves.

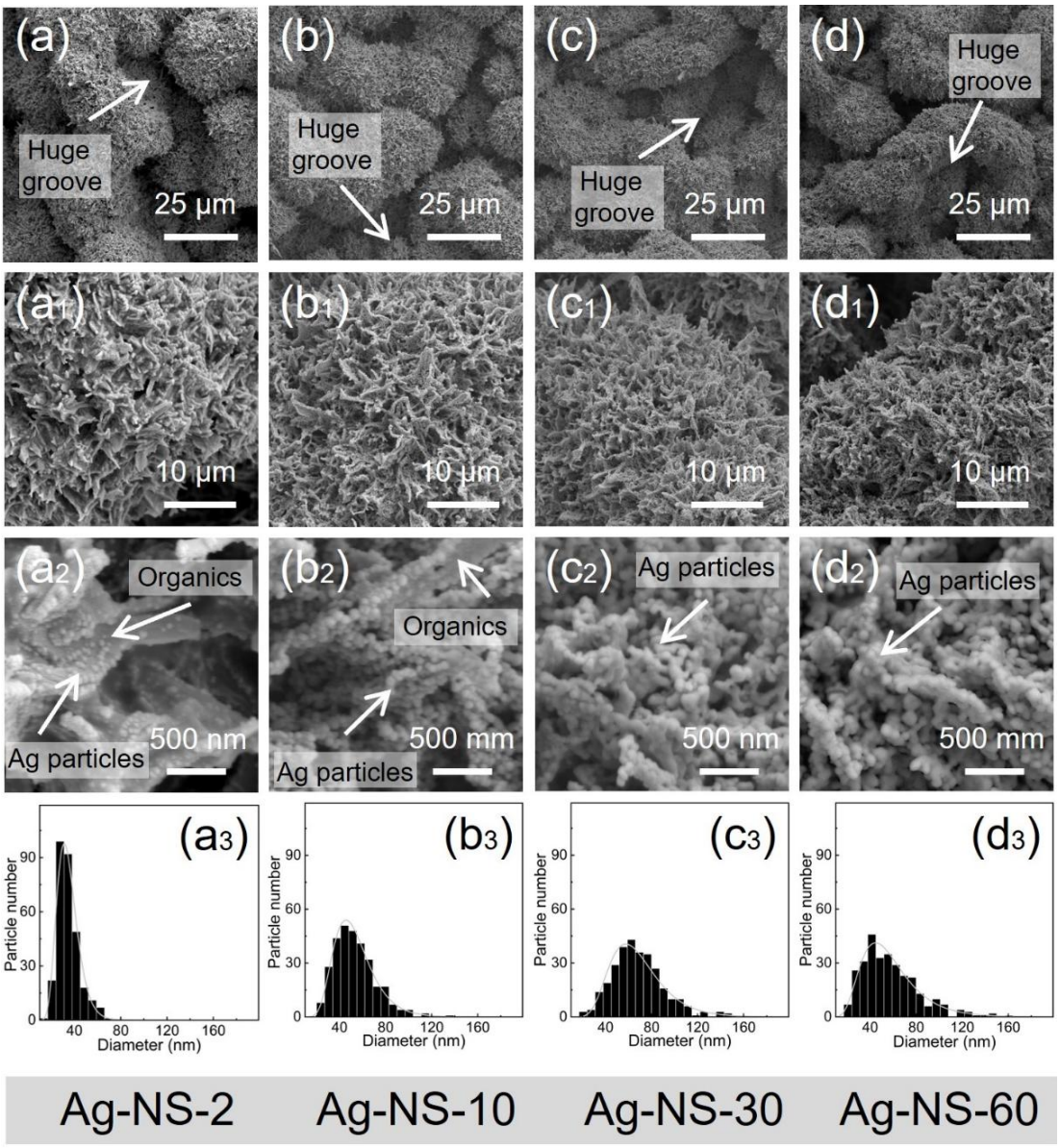

Fig. 2.12 Top surface of Ag nanostructure. SEM image of (a) Ag-NS-2, (b) Ag-NS-10, (c) Ag-NS-30, and (d) Ag-NS-60. (a_1)-(d_1), (a_2)-(d_2) magnified SEM images of (a)-(d) respectively. (a_3)-(d_3) article size distribution of (a_2)-(d_2) respectively.

Fig. 2.12a_1-d_1 demonstrates that the rugged top surface was composed of clustered branches. According to the high-magnification SEM images in **Fig. 2.12a_2-b_2**, the branches of Ag-NS-2 and Ag-NS-10 consisted of Ag NPs and organic intermediate products, whereas those of

Ag-NS-30 and Ag-NS-60 in **Fig. 2.12c$_2$-d$_2$** comprised Ag NPs. **Fig. 2.12 c$_3$-d$_3$** demonstrates that the extended time increased particle size. The corresponding average particle size distribution increased from 34.7 nm of Ag-NS-2 to 58.0 nm of Ag-NS-60. Nevertheless, the average particle size of Ag-NS-60 in **Fig. 2.8d$_3$** remained in the nanoscale. This result means that extending the heating time at 180 ^{o}C promoted the Ag-based complex thermal decomposition but did not sharply increase particle size.

Organic substances typically contain C. Therefore, the vanishing of organics with extended time was confirmed by EDS. **Fig. 2.13** shows the evolution of C and Ag content of the Ag nanostructures with heating time. The C content of the Ag nanostructures in **Fig. 2.13** decreased dramatically at the very beginning of heating, and the remaining C in the Ag

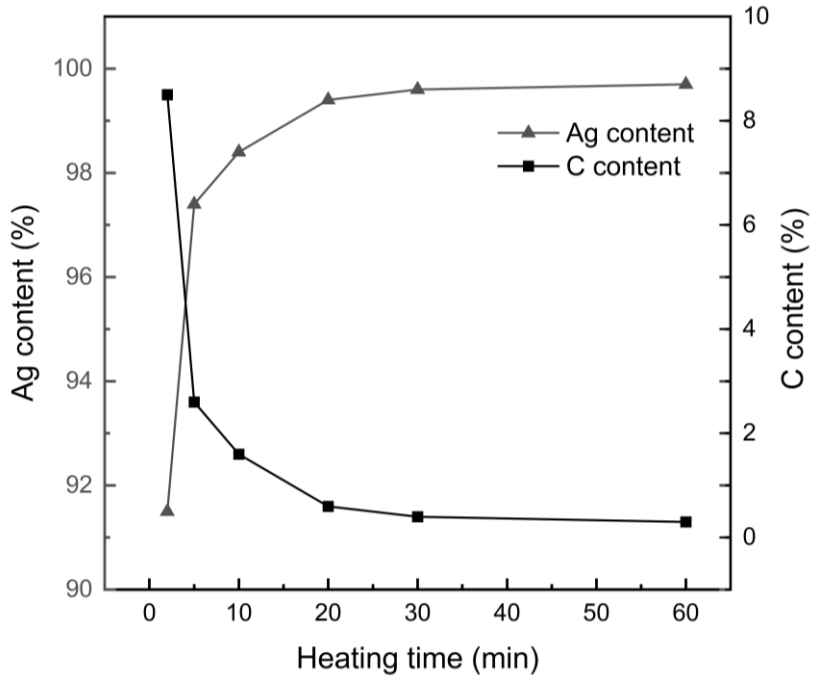

Fig. 2.13 Evolution of Ag and C contents of Ag nanostructures with thermal decomposition time.

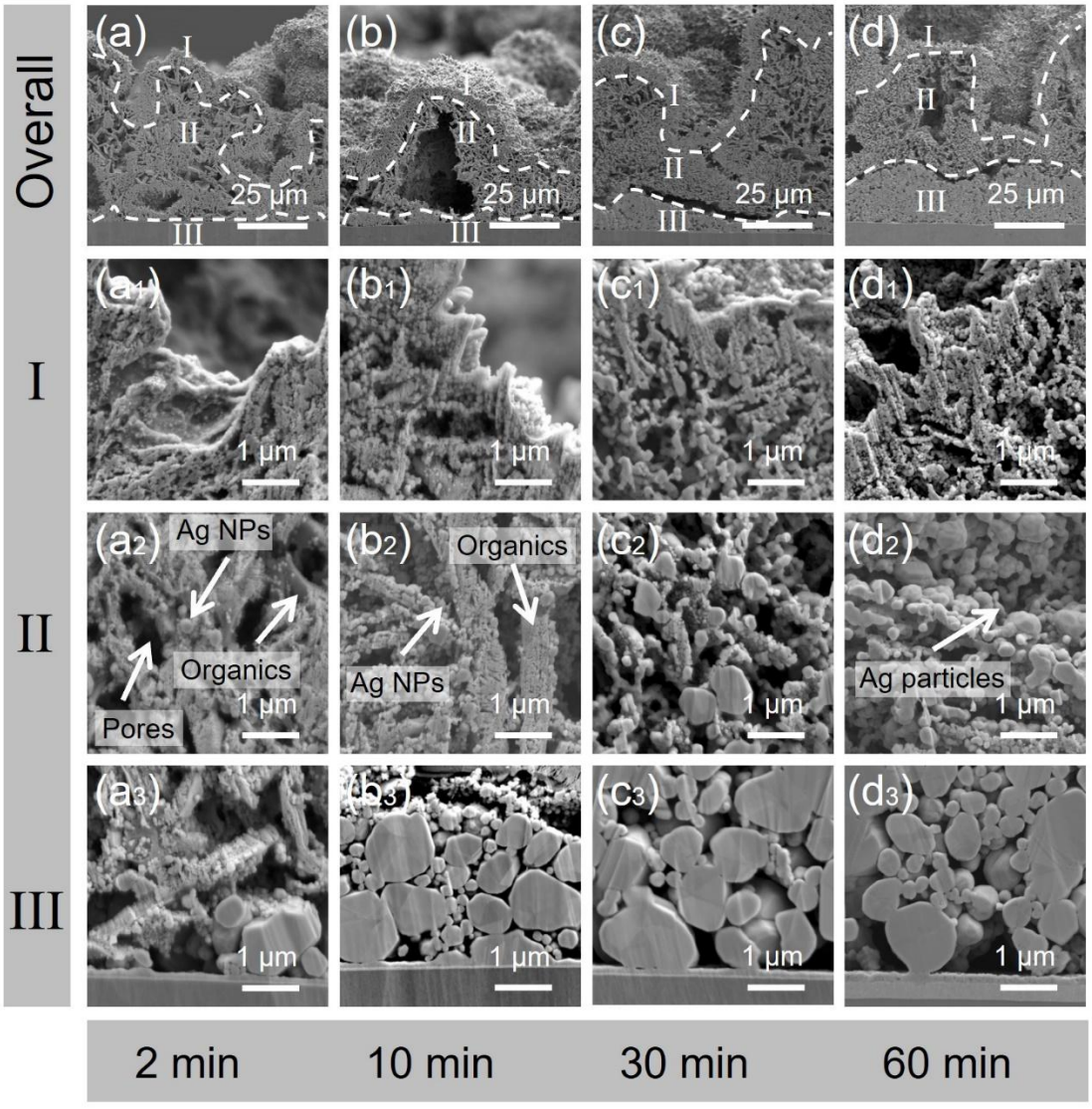

Fig. 2.14 Cross-section of Ag nanostructure. Cross-section of (a) Ag-NS-2, (b) Ag-NS-10, (c) Ag-NS-30, and (d) Ag-NS-60. Amplified SEM images in (a_1)-(d_1) I, (a_2)-(d_2) II, and (a_3)-(d_3) III of (a)-(d) of Ag-NS-2, Ag-NS-10, Ag-NS-30, and Ag-NS-60, respectively.

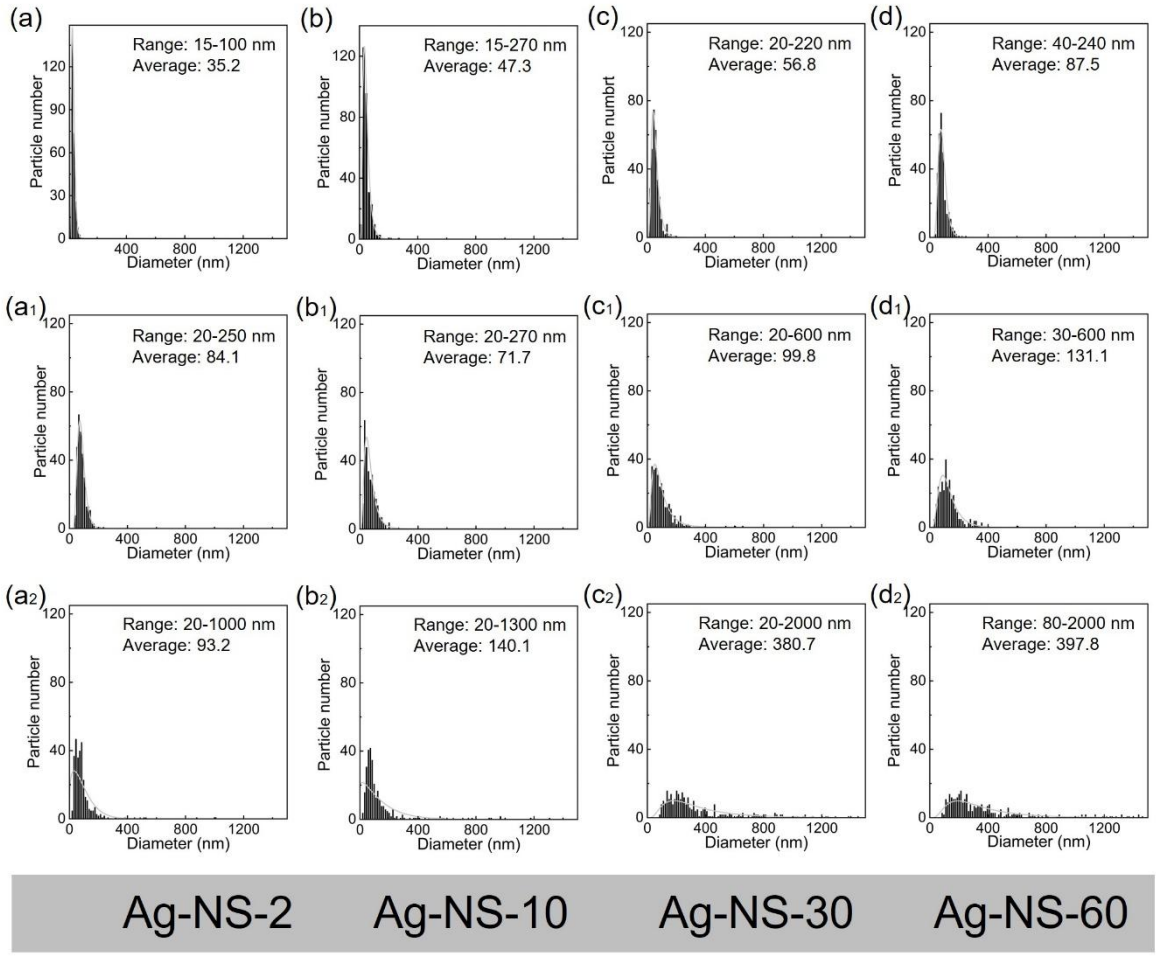

Fig. 2.15 Particle size distribution of Ag nanostructures. Particle size distribution of (a)-(d) I, (a_1)-(d_1) II, and (a_2)-(d_2) III of Ag-NS-2, Ag-NS-10, Ag-NS-30, and Ag-NS-60, respectively.

nanostructures was only 0.3 wt% when the heating time was 60 min. This extremely low C content indicated complete decomposition of the Ag-based complex.

In addition to the surface characterizations of the Ag nanostructures in **Fig. 2.12**, the interior of Ag nanostructures was examined by cross-section, and the corresponding particle size distributions were measured. **Fig. 2.14** depicts the cross-sections of Ag nanostructures derived from different heating times. **Fig. 2.15** illustrates the corresponding size distribution

of the cross-sections in **Fig. 2.14**. **Fig. A1.2** and **A1.3** illustrate the cross-section and particle size distribution of all Ag nanostructures. Based on **Fig. 2.14a-d**, the Ag nanostructures exhibited a multilayer porous structure. The interior information was revealed using high magnification of three typical regions, such as the top, mid, and interface, of the Ag nanostructure, and the corresponding size distributions are presented in **Fig. 2.15**. The SEM images in **Figs. 2.14a$_1$-a$_3$**, **2.14b$_1$-b$_3$**, **2.14c$_1$-c$_3$**, and **2.14d$_1$-d$_3$** and the size distributions in **Figs. 2.15a-a$_2$**, **2.15b-b$_2$**, **2.15c-c$_2$**, and **2.15d-d$_2$** reveal an increase in the Ag particle size from the top to the bottom in the Ag nanostructure. This phenomenon could be attributed to the hot plate heating of the Ag-based complex, resulting in heat flow from the bottom to the top. Inadequate heat transfer through pores and remaining organics inside the Ag nanostructures in **Fig. 2.14a$_2$** led to a vertical temperature gradient. In addition, the connection between the generated Ag particles in **Fig. 2.14b$_3$** was poor and most of them appeared as a single dispersed individual particle, indicating insufficient thermal conducting paths. Consequently, Ag particles at the bottom region, with higher temperatures, exhibited faster growth than those at the top region [13]. As shown in **Fig. 2.14a$_2$-d$_2$**, the influence of heating time on the process was also confirmed in the cross-sections. A combination of spherical Ag nanoparticles and organic intermediate products was observed for a short heating time of 2min in **Fig. 2.14a$_2$**. As the heating time increased to 60 min, the presence of Ag submicron particles and the vanishing of organic intermediate products in **Fig. 2.14d$_2$** indicated the complete decomposition of the Ag-based complex.

The microstructures in **Fig. 2.12** and **Fig. 2.14** and EDS analysis in **Fig. 2.13** indicated that the extended heating time promoted the thermal decomposition of the Ag-based complex.

Hence, we created a schematic diagram to illustrate this process. **Fig. 2.16** shows a schematic diagram of the decomposition process of the Ag-based complex. When the Ag-based complex is subjected to elevated temperature, organic gasification results in volume shrinkage [8] and clusters consisting of Ag nanoparticles and organics. With an extended heating time, the removal of organics leads to Ag nanostructures with extremely low C content. This result meant that extending the heating time promoted the thermal

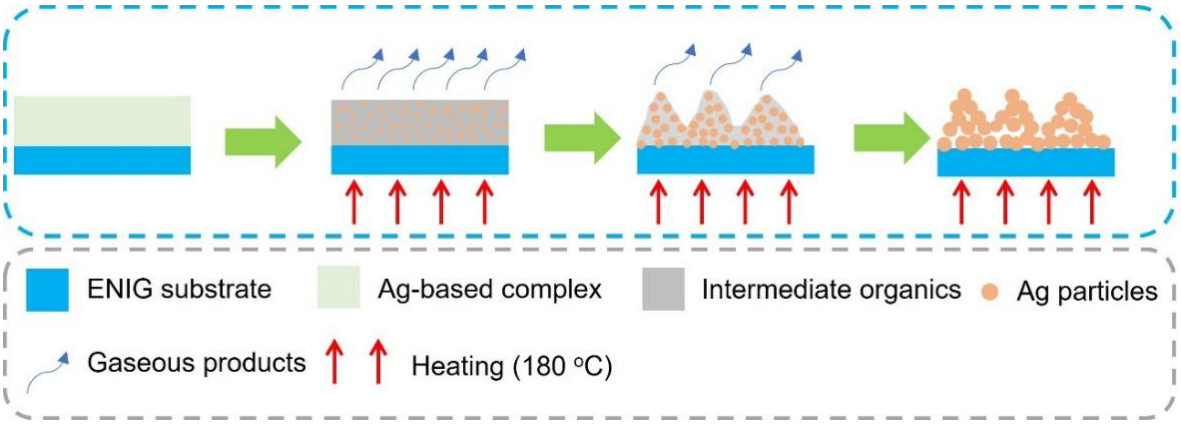

Fig. 2.16 Schematic diagram illustrating the decomposition process of the Ag-based complex with continuous heating.

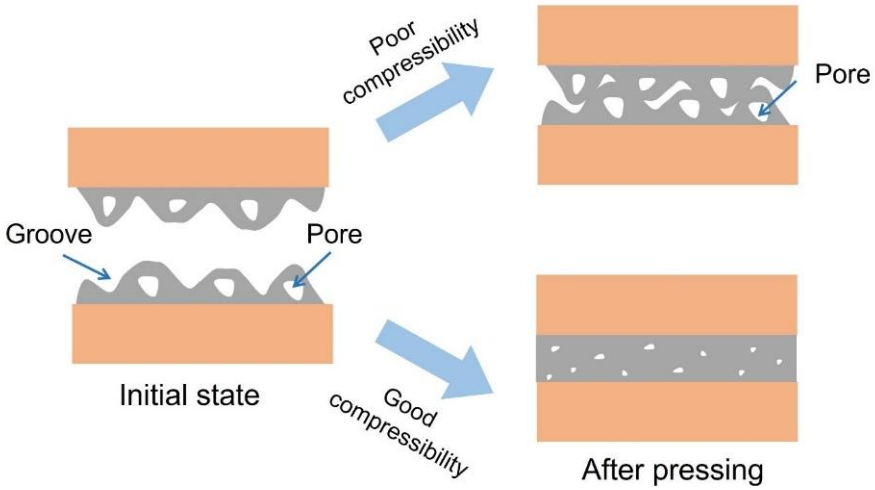

Fig. 2.17 Schematic diagram demonstrating the effects of compressibility on die-bonding.

decomposition of the Ag-based complex. In addition, the Ag particle size also increased with the extended time but remained at the nanoscale (top surface) for 60 min.

The microstructure characterizations detected grooves and pores in the Ag nanostructures, which can be regarded as air gaps within the Ag nanostructures. Air gaps complicate diffusion, which has serious negative effects on the bonding process [23]. Good compressibility is required so that the air gaps are reduced or eliminated. To aid understanding, a schematic diagram illustrating the effects of compressibility on die-bonding

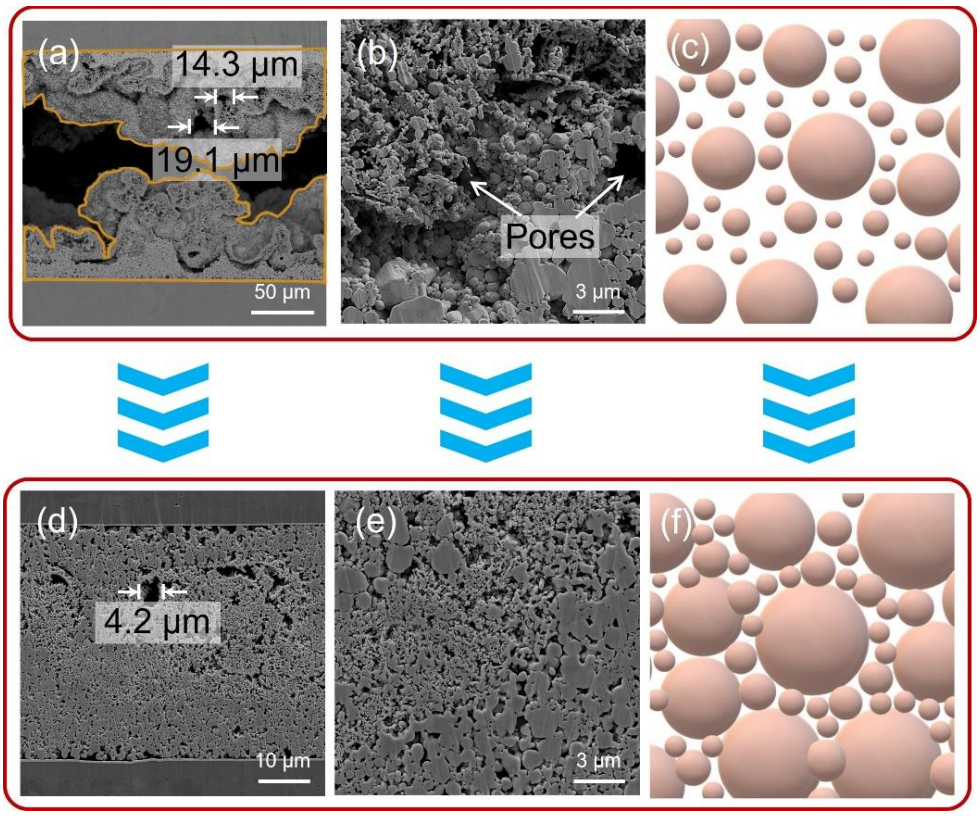

Fig. 2.18 Compressibility of Ag nanostructures. (a) (b) Microstructures and (c) schematic diagram of Ag nanostructures before being pressed with 5 MPa. (d) (e) Microstructures and (c) (f) schematic diagram of Ag nanostructures before and after being pressed with 5 MPa.

was created in **Fig. 2.17**. If the Ag nanostructure exhibits poor compressibility, large-volume pores will remain during the bonding process, resulting in poor joint properties. With good compressibility, the Ag nanostructure deformation reduces the pore volume and increases the stacking density of Ag particles for bonding. Therefore, the Ag nanostructures in this study should have good compressibility to prepare robust Ag joints. Herein, the Ag nanostructure compressibility was investigated by applying 5 MPa pressure on the substrate-Ag layer-die sandwich structure. **Fig. 2.18** shows the Ag nanostructures before and after pressing with 5 MPa. As shown in **Fig. 2.18a** and **d**, the average thickness of the Ag nanostructures dramatically decreased from 155.9 μm to 44.8 μm, a reduction of 71.3%. This result indicated that the Ag nanostructures derived from the Ag-based complex had substantial compressibility. This compressibility reduced the pore size in **Fig. 2.18 b** and **2.18e**, shortened the gaps between the Ag particles in **Fig. 2.18c** and **f**, and increased the stacking density and bonding performance.

2.3.4 Effects of heating time on the bonding performance of Ag nanostructures

The above results indicated that the heating time significantly affected the thermal decomposition of the Ag-based complex and the ingredients of the Ag nanostructures. However, additional research is necessary to confirm the feasibility of using Ag-based complexes as die-attach materials and identify the ideal thermal decomposition conditions. To address this, the Ag nanostructure of the die was directly overlaid on that of the substrate to form a die-Ag layer-substrate sandwich structure as shown in **Fig. 2.3**, which was bonded at a low temperature of 200°C with 5 MPa for 40 min. **Fig. 2.19** shows the relationship

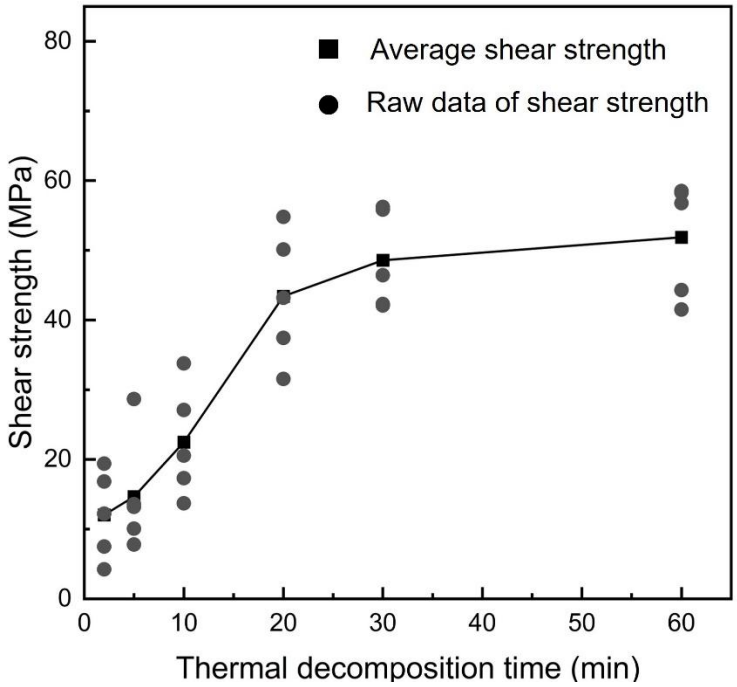

Fig. 2.19 Evolution of shear strength with thermal decomposition time (bonding condition:200 ^{o}C, 40 min, 5 MPa).

between the shear strength of Ag joints and the thermal decomposition time of the Ag-based complex. As depicted in **Fig. 2.19**, prolonged thermal decomposition time rendered better bonding performance to the Ag nanostructures, increasing the shear strength. Ag-NS-60 demonstrated the highest bonding performance, resulting in a shear strength of 50.3 MPa. This robust shear strength firmly demonstrates the feasibility of using an Ag-based complex as a die-bonding material.

The shear strength in **Fig. 2.19** demonstrated that the thermal decomposition time significantly affected the bonding performance of the Ag nanostructures. This effect was validated by characterizing the sintered Ag joints via cross-section analysis and the porosity was measured by Image-J. **Fig. 2.20** depicts the representative SEM images of the cross-

sections, and the corresponding porosity is illustrated in **Fig. 2.21**. Images including all cross-sections are presented in **Fig. A1.4**. The overview revealed that the cross-section of bonded Ag-NS-2 in **Fig. 2.20a** was greatly different from those in **Fig. 2.20b-d**. The large pores in **Fig. 2.20a** could have been caused by the organic gasification [3,24]. Besides huge pores, residual organics were observed in **Fig. 2.20a**. Given the blocking effects of organics on the Ag atom diffusion, the formation of necks within the sintered Ag was insufficient in **Fig. 2.20a$_1$** [21]. While necks formed at the interface region in **Fig. 2.20a$_2$**, the huge pore in **Fig. 2.20a** dramatically deteriorated the connection between the sintered Ag joints and substrates. Poor sintering degree and huge pores within the sintered Ag resulted in lower shear strength in **Fig. 2.19**. As the thermal decomposition time increased from 10 min to 60 min, the Ag particles with thin necks in **Fig. 2.20b$_1$** were sintered to continuous Ag joints with thick necks in **Fig. 2.20c$_1$** and **2.20d$_1$**, resulting in the continuous decrease in porosity in **Fig. 2.21**. In addition, the necks between the sintered Ag and substrate in **Fig. 2.20b$_2$-d$_2$** thickened as the thermal decomposition time increased from 10 min to 60 min. These phenomena contributed to the increase in shear strength in **Fig. 2.19**, meaning that the increased thermal decomposition time enhanced the bonding performance of the Ag nanostructures. In summary, the thermal decomposition time improves the bonding performance of Ag nanostructures by reducing the organic content, which confirms the advantages of the organic-free strategy for die-bonding.

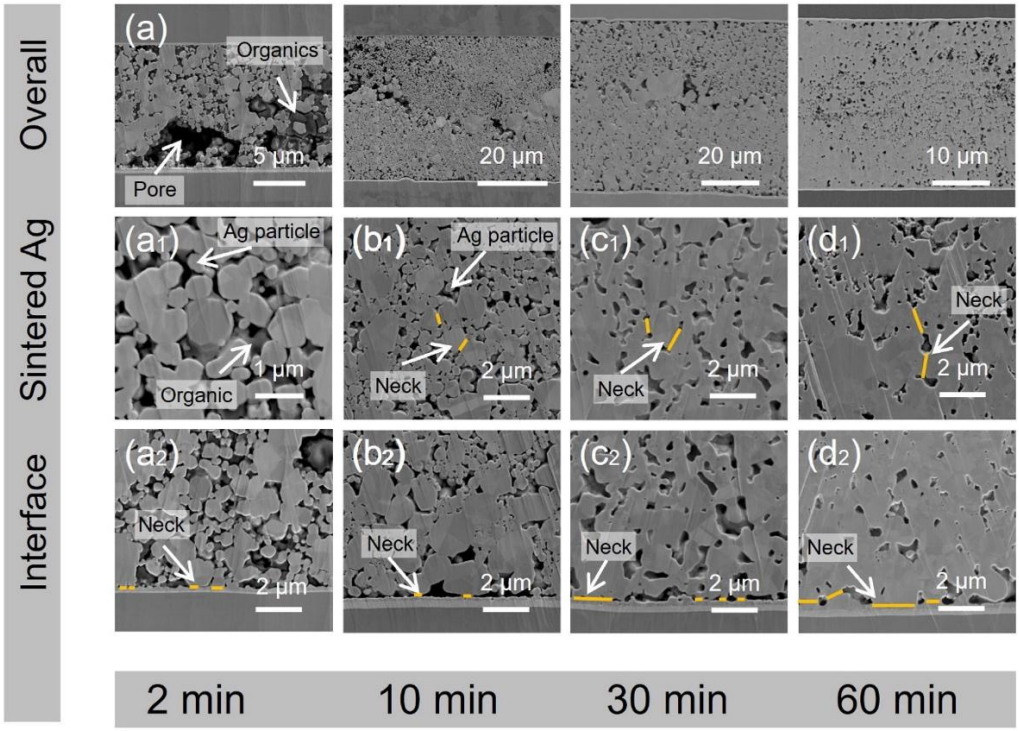

Fig. 2.20 SEM images of the cross-sections of the sintered Ag joint derived from (a)-(a_2) Ag-NS-2, (b)-(b_2) Ag-NS-10, (c)-(c_2) Ag-NS-30, and (d)-(d_2) Ag-NS-60.

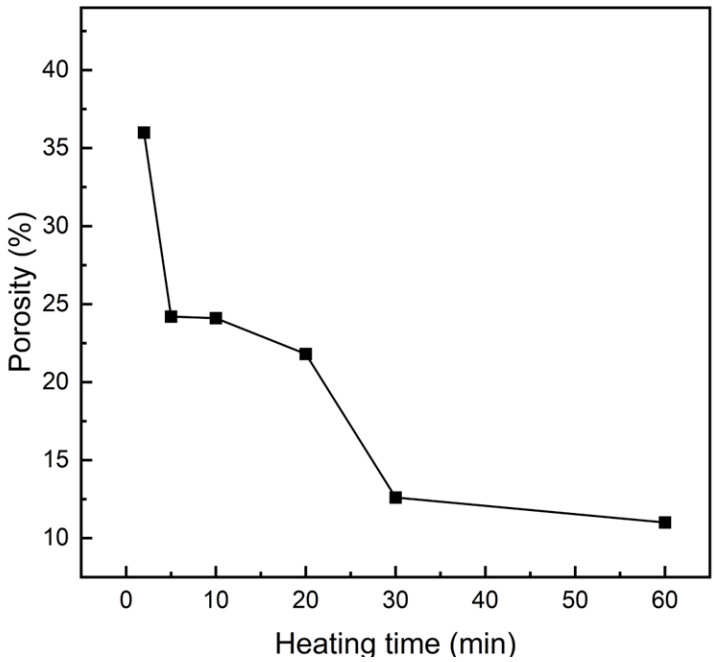

Fig. 2.21 Evolution of porosity with heating time (bonding condition:200 °C, 40 min, 5 MPa).

The fracture surfaces of the Ag sintered joints were observed to reveal the evolution of the shear strength with the thermal decomposition time. **Fig. A1.5** and **A1.6** demonstrate that the fracture model of the bonded Ag nanostructures can be divided into two categories. The fracture surfaces of bonded Ag-NS-2 and Ag-NS-30 were selected as representatives to reveal the relationship between the shear strength of thermal decomposition time. **Fig. 2.22** shows the fracture surface of the bonded Ag-NS-2 and Ag-NS-30 and the corresponding fracture model. As depicted in **Fig. 2.22a** and **b**, most of the sintered Ag was left on the die side, indicating that the sintered Ag joints derived from Ag-NS-2 fractured close to the interface between the sintered Ag and substrate (**Fig. 2.22f**). A huge tunnel across the sintered Ag was observed in **Fig. 2.22c**, which could be attributed to the organic gasification during the bonding process of Ag-NS-2. Gasification, such as evaporation or decomposition, of organics results in gaseous phases and creates a high vapor force inside Ag joints [3,24]. This vapor force enlarges the distance between neighboring Ag particles, resulting in tunnels within the sintered Ag. The created tunnels act as paths for gas release. In addition, the tunnels can be considered defects within the sintered Ag, reducing the valid bonding area between the sintered Ag and substrates [25].

Ductile deformed Ag was observed in **Fig. 2.22d**, which means that some strong connections had formed within the sintered Ag joints [26]. However, dark gray substances along with the ductile deformations were also detected in **Fig. 2.22d**. **Fig. 2.23** shows the EDS results of the fracture surface of bonded Ag-NS-2. High-intensity C was detected in **Fig. 2.23c**, indicating that the dark substances in **Fig. 2.22d** could be attributed to trapped organics in the sintered Ag. The amplified SEM image in **Fig. 2.22e** demonstrated that these organics

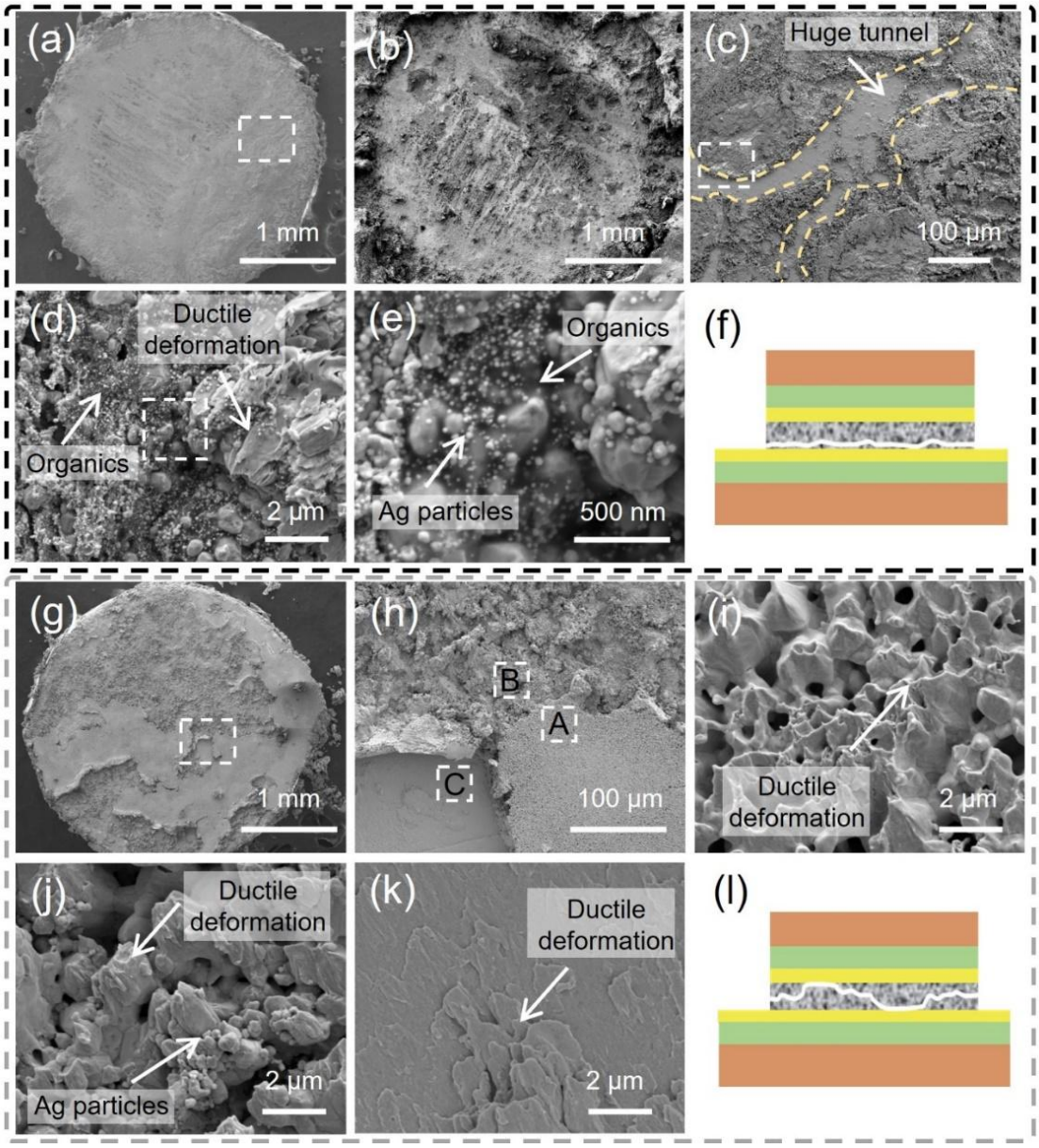

Fig. 2.22 Microstructure of the fracture surfaces. Fracture surfaces of Ag joints derived from Ag-NS-2 (a) die side and (b) substrate side. (c) Amplified SEM image of the white rectangle in (a). (d) Amplified SEM image of the white rectangle in (c). (e) Amplified SEM image of the white rectangle in (d). (f) Corresponding schematic diagram of fracture model. (g) Fracture surfaces of Ag joints derived from Ag-NS-30. (h) Amplified SEM image of the white rectangle in (g). (i), (j), and (k) Amplified SEM image of the white rectangle A, B, and C in (g), respectively. (l) Corresponding schematic diagram of fracture model.

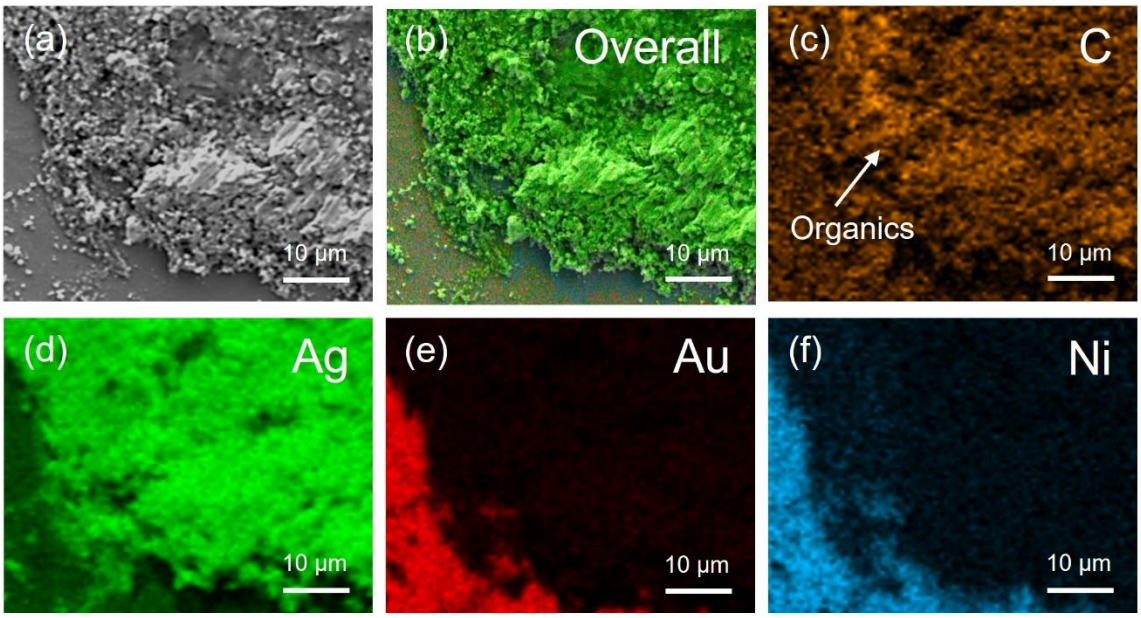

Fig. 2.23 (a) SEM of the fracture surfaces of Ag joints derived from Ag-NS-2 and the corresponding EDS of (b) overall, (c) C, (d) Ag, (e) Au, and (f) Ni.

covered the surface of massive Ag particles. The organics on the Ag particle surface could block the Ag atom diffusion during bonding [21]. This resulted in monodispersed Ag particles and a poor sintering degree within the Ag joints. In summary, the organics of Ag-NS-2 deteriorated the joint properties by blocking effect and gasification.

The overview of the fracture surfaces in **Fig. 2.22g** demonstrates that the Ag joints derived from Ag-NS-30 fractured at both the interface region and inside the Ag joints, agreeing with the fracture model in **Fig. 2.22l**. **Fig. 2.22h** shows that this hybrid fracture model resulted in three typical fracture morphologies. The amplified SEM images of regions A, B, and C in **Fig. 2.22h** are depicted in **Fig. 2.22i, 2.22j,** and **2.22k**, respectively. Abundant ductile deformations were observed in all three amplified SEM images, which indicated strong connections both within the sintered Ag and at the interface between the sintered Ag and substrate. **Fig. 2.22** demonstrates that reducing the organic content by extending thermal

decomposition time at 180 ^{o}C enhanced the bonding performance of the Ag nanostructures effectively.

Characterization of the cross-sections and fracture surfaces revealed that organic intermediate products are important in determining the bonding performance of Ag nanostructures. **Fig. 2.24** shows the bonding behaviors of Ag nanostructures with and without organics. As shown in **Fig. 2.24a**, incompletely decomposed Ag-based complexes resulted in residual organic intermediate products in the Ag nanostructures. During bonding, elevated temperatures caused organic gasification, which created large pores (tunnels) inside the sintered Ag. Larger pores inside the Ag joints markedly reduce the internal connection, resulting in low shear strength. Complete decomposition of the Ag-based complex led to organic-free Ag nanostructures. As shown in **Fig. 2.24**, these Ag nanostructures were easily converted into dense Ag joints because their Ag particles exhibited small sizes and naked surfaces.

2.3.5 Effect of decomposition temperature on the formation of Ag nanostructures

Besides the thermal decomposition time, thermal decomposition temperature might be one of the most crucial factors in determining the formation of Ag nanostructures. The shear strength results in **Fig. 2.19** revealed that the shear strength increased slightly from 48.6 MPa to 50.3 MPa when the thermal decomposition time increased from 30 min to 60 min. Therefore, the Ag-based complex was heated at 160, 180, and 200 ^{o}C for 30 min to investigate

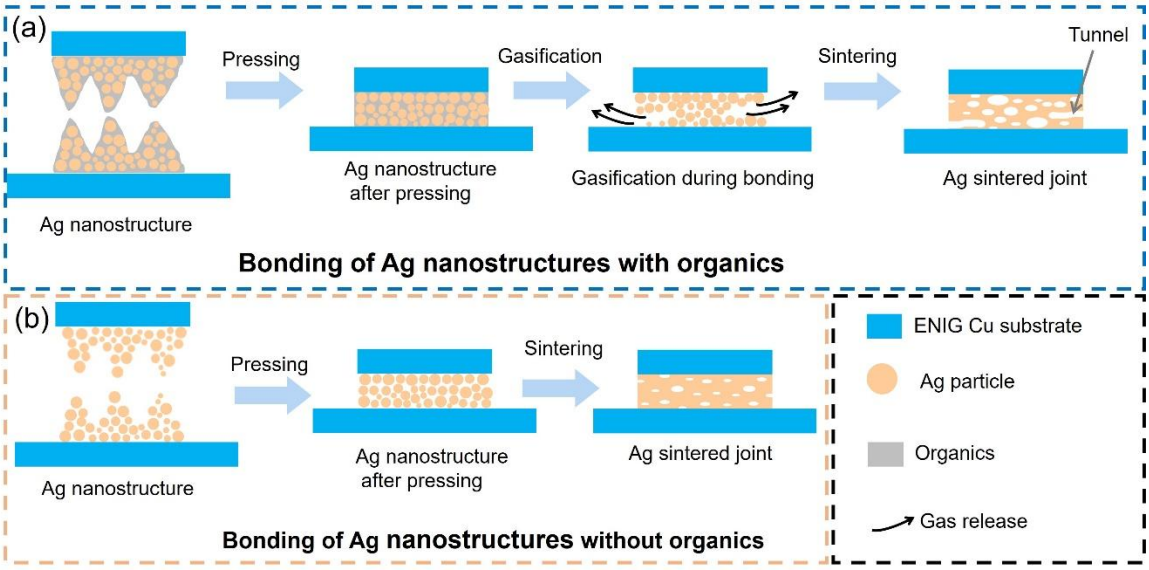

Fig. 2.24 Schematic diagram illustrating the sintering process of Ag nanostructures (a) with and (b) without organics.

the effects of the thermal decomposition temperature on the bonding performance of the Ag nanostructures. **Fig. 2.25** shows the top view of Ag-NS-160, Ag-NS-180, and Ag-NS-200. As depicted in **Fig. 2.25a-c**, the three Ag nanostructures were composed of clustered branches. The branches in **Fig. 2.25a$_1$** consisted of monodispersed Ag NPs and organic intermediate products. This result was because 160 °C is lower than the thermal decomposition temperature of 180 °C of the Ag-based complex, resulting in incomplete decomposition [27]. The Ag nanostructures in **Fig. 2.25b$_1$** were derived from the same thermal decomposition condition as that in **Fig. 2.9**. The TEM and EDS results proved that the thermal conditions at 180 °C for 30 min led to the complete decomposition of the Ag-based complex. Therefore, Ag-NS-180 in **Fig. 2.25b$_1$** can be considered the product of the complete decomposition of the Ag-based complex. As the thermal decomposition

temperature increased from 180 ºC to 200 ºC, the monodispersed Ag particles in **Fig. 2.25b$_1$** were converted into linked Ag NPs in **Fig. 2.25c$_1$**. The thermal decomposition of Ag-based complexes involves the reduction of Ag(I), nucleation, and particle growth [6–8,28]. This means that sintering occurred after the decomposition had ended. The corresponding particle sizes in **Fig. 2.25a$_2$-c$_2$** increased with the increasing thermal decomposition temperature. The results indicated that an increase in temperature promoted the thermal decomposition of the Ag-based complex, and the sintering of Ag NPs could occur after the decomposition process had been completed at 200 ºC.

The cross-sections revealed the internal information of the Ag nanostructures. **Fig. 2.26** shows the cross-section of the Ag nanostructures derived from various temperatures. As shown in **Fig. 2.26a**, an Ag porous nanostructure consisted of three distinct layers. Based on the amplified SEM images in **Fig. 2.26b-b$_2$, 2.26c-c$_2$,** and **2.26d-d$_2$**, the corresponding size distribution of the three distinct regions was measured by Image-J. **Fig. 2.27** shows the particle size distribution of the three Ag nanostructures. The particle size in **Fig. 2.27a-c**, **2.27a$_1$-c$_1$**, and **2.27a$_2$-c$_2$** demonstrated that increasing the temperature enhanced the particle size. The cross-sections also demonstrated the effect of the thermal decomposition temperature on microstructure change. For example, both spherical Ag NPs and organic intermediate products were observed in **Fig. 2.26b$_1$**. As the thermal decomposition temperature increased to 180 ºC, Ag NPs mixed with monodispersed Ag submicron particles were detected in **Fig. 2.26c$_1$**. When the thermal decomposition temperature was 200 ºC, necks between the Ag submicron particles in **Fig. 2.26d$_1$** indicated that the increased temperatures resulted in the sintering of Ag particles.

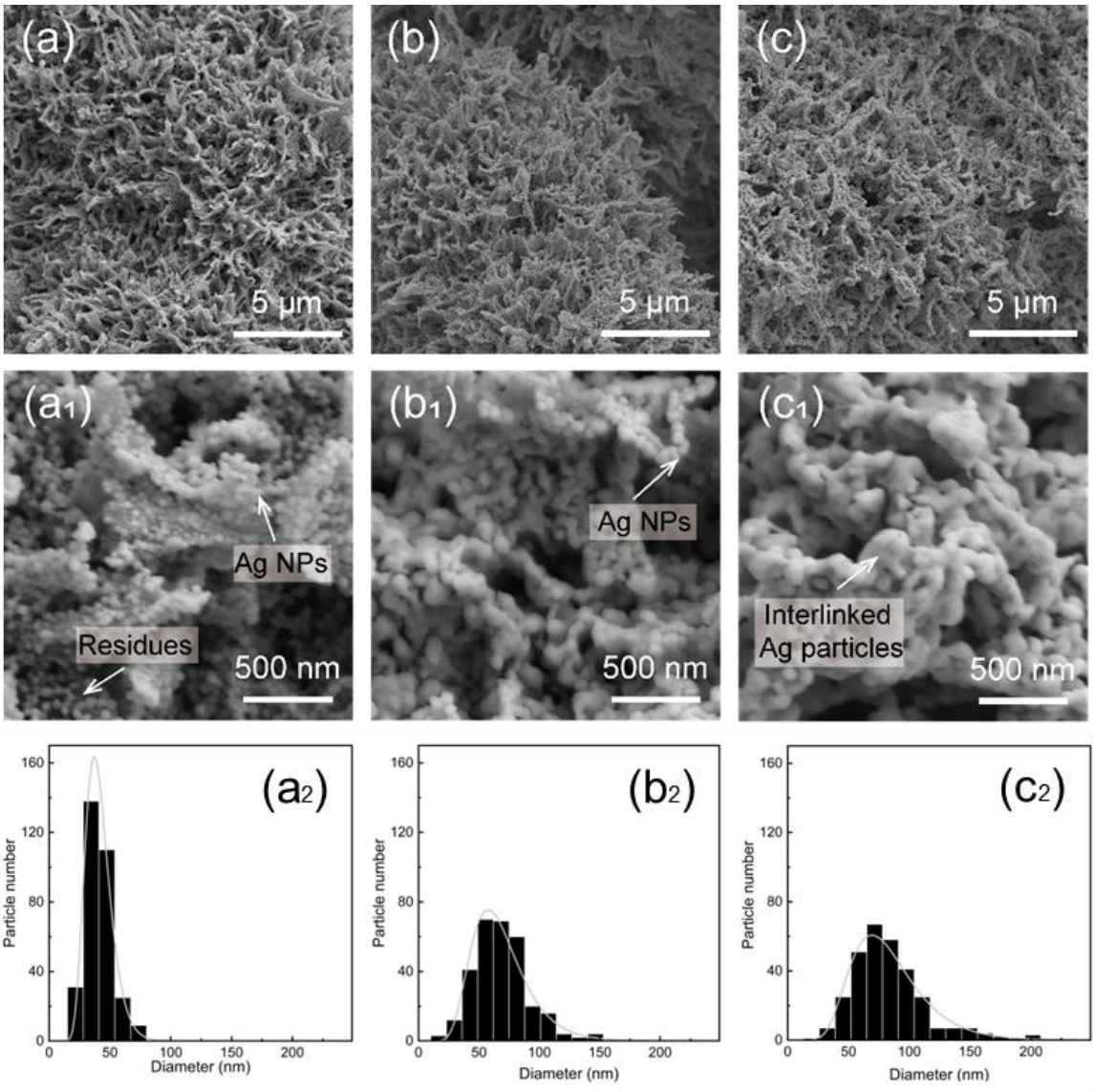

Fig. 2.25 Characterization of Ag nanostructures from the top view. (a) (a_1), (b) (b_1), and (c) (c_1) SEM image of Ag-NS-160, Ag-NS-180, and Ag-NS-200, respectively. (a_2)-(c_2) Corresponding particle size distribution of (a_1)-(c_1).

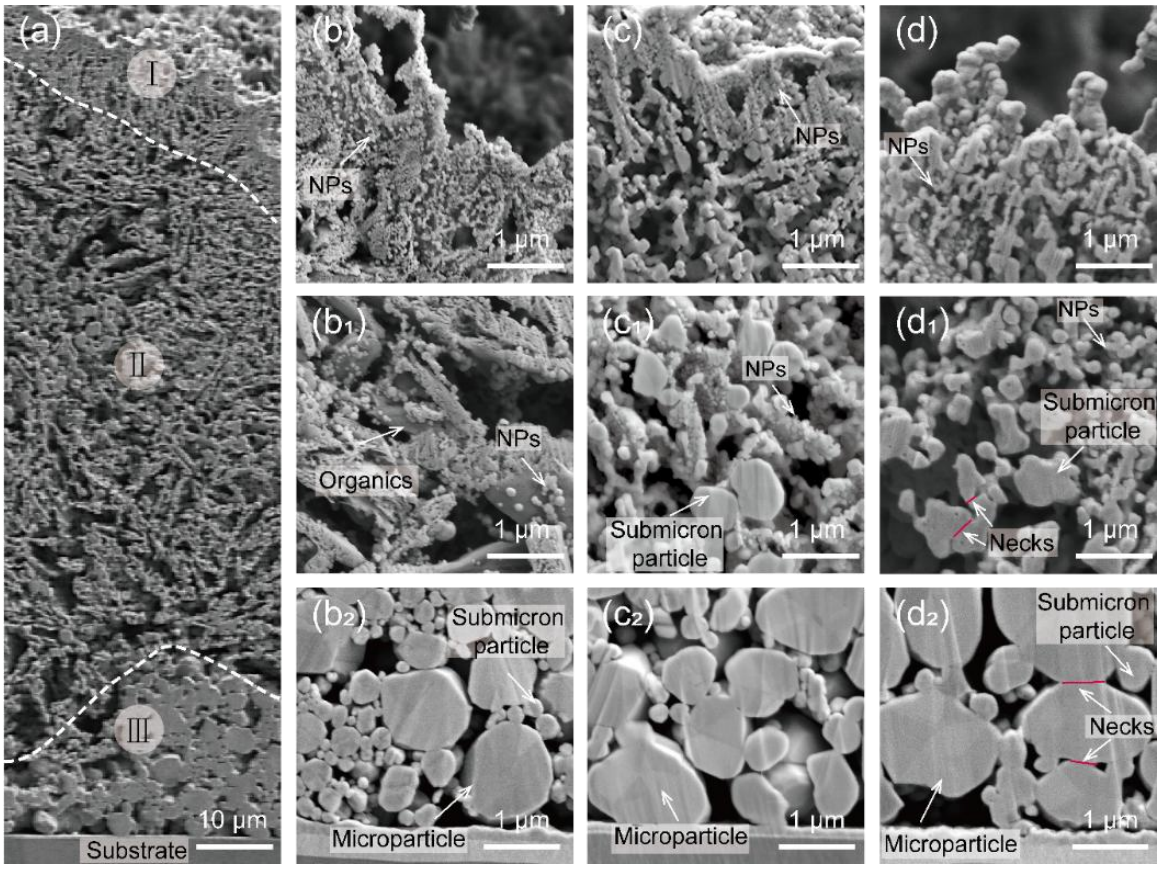

Fig. 2.26 Characterizations of Ag nanostructures from the cross-sectional view. (a) Overall view of Ag-NS-180. High-magnification views of region (b) I, (b_1) II, and (b_2) III of Ag-NS-160. High-magnification views of region (c) I, (c_1) II, and (c_2) III of Ag-NS-180. High-magnification views of region (d) I, (d_1) II, and (d_2) III of Ag-NS-200.

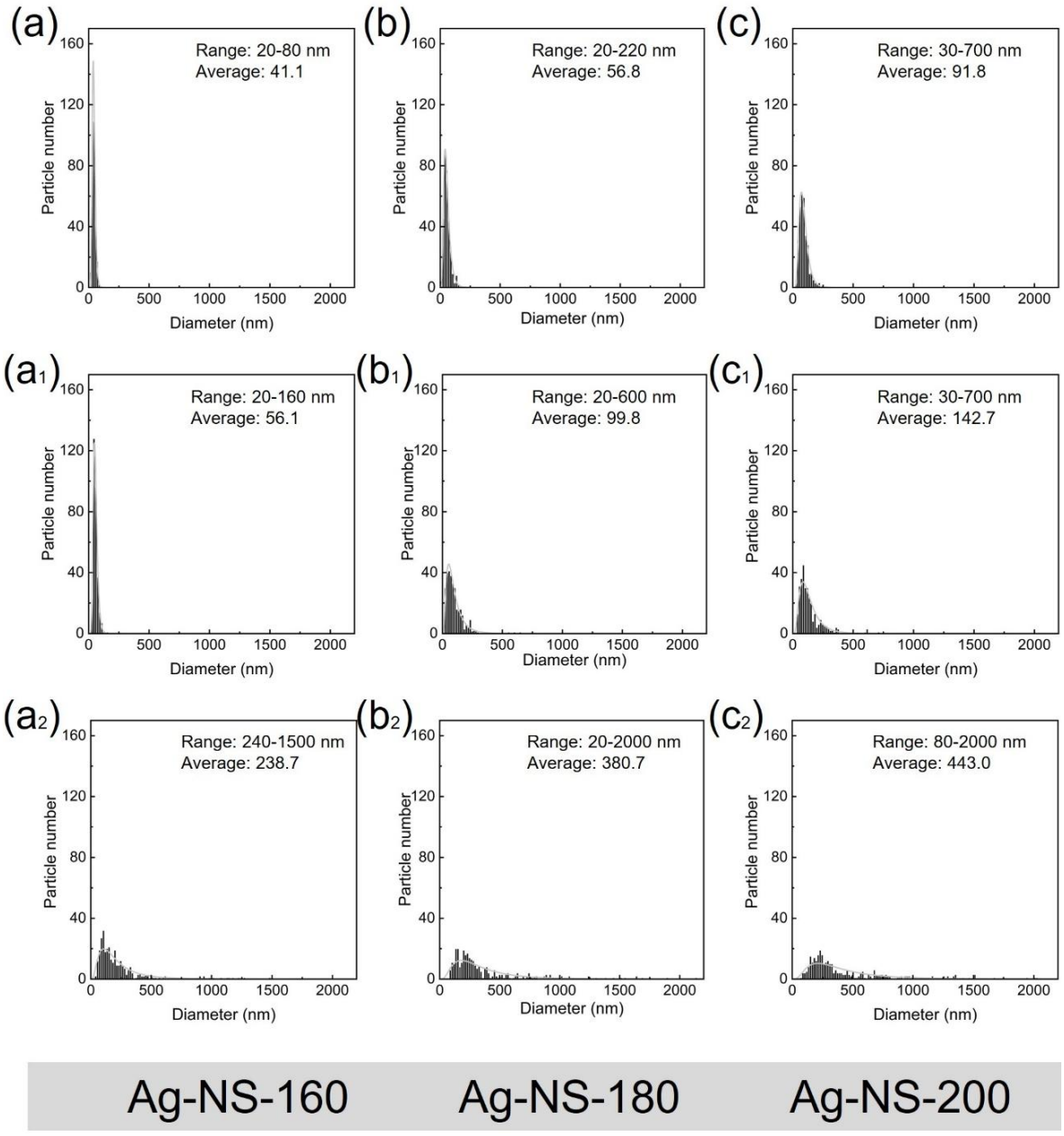

Fig. 2.27 Particle size distribution of region (a) I, (a_1) II, and (a_2) III of Ag-NS-160. Particle size distribution of region (b) I, (b_1) II, and (b_2) III of Ag-NS-180. Particle size distribution of region (c) I, (c_1) II, and (c_2) III of Ag-NS-200.

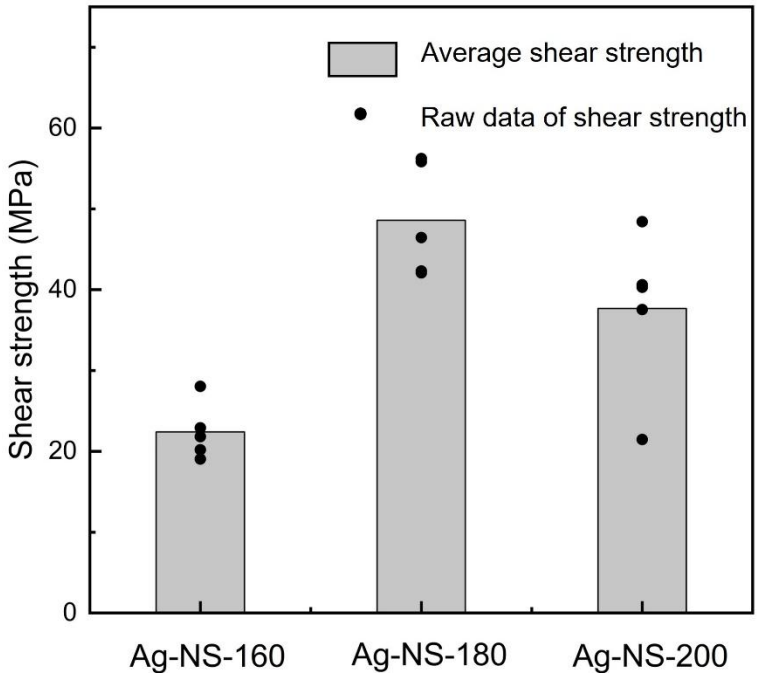

Fig. 2.28 Evolution of shear strength with thermal decomposition temperature (bonding condition:200 ^{o}C, 40 min, 5 MPa).

2.3.6 Effect of decomposition temperature on the bonding performance of Ag nanostructures

The effects of thermal decomposition temperature on the bonding performance were evaluated by bonding three kinds of Ag nanostructures at 200 ^{o}C with 5 MPa for 40 min. **Fig. 2.28** depicts the evolution of shear strength with the thermal decomposition temperature of an Ag-based complex. As depicted in **Fig. 2.28**, the thermal decomposition temperature significantly affected the shear strength of Ag sintered joints. Ag-NS-180 exhibited the best bonding performance among the three Ag nanostructures, resulting in the highest shear strength of 48.6 MPa.

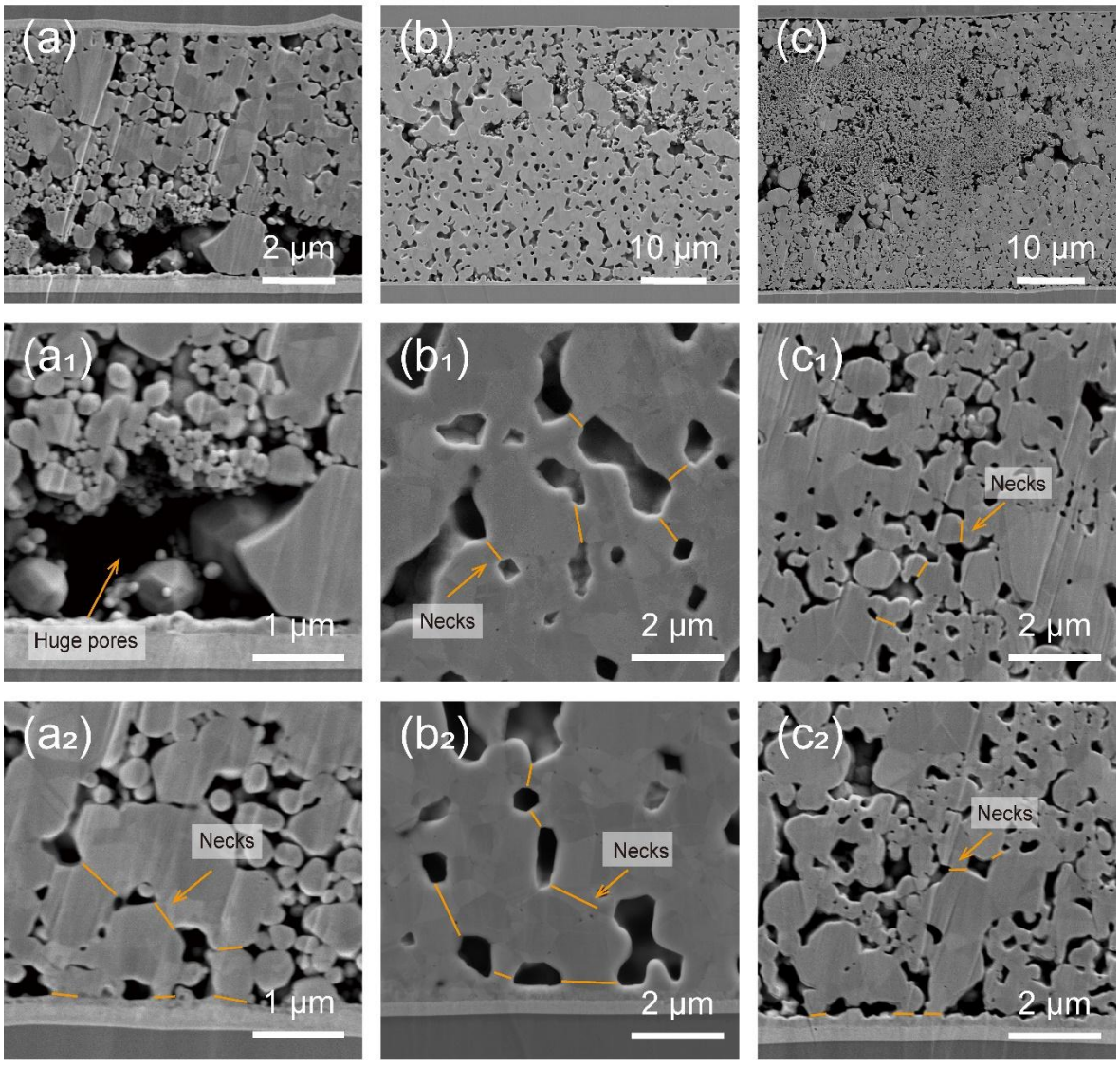

Fig. 2.29 Microstructure of the cross-sections of Ag joints bonded at 200 ºC. SEM images of the cross-sections of the sintered Ag joint derived from (a)-(a_2) Ag-NS-160, (b)-(b_2) Ag-NS-180, and (c)-(c_2) Ag-NS-200.

The evolution of shear strength in **Fig. 2.28** demonstrated that the thermal decomposition temperature significantly affected the bonding performance of the Ag nanostructures. This effect was validated by observing the sintered Ag joints through cross-sectional analysis. **Fig.**

2.29 shows the overview and amplified SEM images of the cross-sections. Compared with **Fig. 2.29b** and **2.29c**, huge pores were observed in **Fig. 2.29a**. Although necks formed both inside the sintered Ag and at the interface region in **Fig. 2.29a**$_2$, the large pores in **Fig. 2.29a** and **2.29a**$_1$ dramatically deteriorated the connection between the sintered Ag joints and the substrates, resulting in a lower shear strength in **Fig. 2.28**. Like the huge pores in **Fig. 2.20a**, the prominent pores in **Fig. 2.29a** and **2.29a**$_2$ could be induced by the gasification of the organic compounds of Ag-NS-160 [3,24]. This observation further proved the significantly negative effects of trapped organics in Ag nanostructures. The necks in **Fig. 2.29b**$_1$ and **b**$_2$ were thicker than those in **Fig. 2.29c**$_1$ and **2.29c**$_2$, indicating that Ag-NS-180 had a better bonding performance than Ag-NS-200. The observed phenomenon can be attributed to the fact that the pre-sintering of Ag-NS-200 in **Fig. 2.26d**$_1$ reduced surface energy [16]. With a high surface energy, Ag-NS-180 was bonded into robust Ag joints with the highest shear strength in **Fig. 2.28**.

The fracture surfaces were investigated to reveal the evolution of shear strength with the thermal decomposition temperature. **Fig. 2.30** shows the evolution of fracture with thermal decomposition of the Ag-based complex. According to the overall views in **Fig. 2.30a-c**, the sintered Ag joints derived from Ag-NS-160 followed the fracture model in **Fig. 2.22f**. The fracture of the sintered Ag joints derived from Ag-NS-180 and Ag-NS-200 agreed with the fracture model in **Fig. 2.22l**, which fractured at both the interface region and inside the Ag joints.

A flat fracture surface with narrow grooves was observed in **Fig. 2.30a$_1$**, indicating that the joint strength of the bonded Ag-NS-160 was governed by the interface condition between the sintered Ag and substrate [29]. Monodisperse ductile deformation in **Fig. 2.30a$_2$** indicated that connections were formed between the sintered Ag and substrates. However, the bottom regions of grooves in **Fig. 2.30a$_3$** were invalid connections, dramatically decreasing the connection area at the interface and resulting in poor shear strength in **Fig. 2.28**. Following the schematic diagram in **Fig. 2.24a**, the formation of gullies may be attributed to the gasification of the organic intermediate products of Ag-NS-160 in **Fig. 2.26b$_1$** [3,24]. Thus, the negative effects of organics in Ag-NS-160 strongly and directly demonstrated the advantage of organic-free Ag sintering in this study.

Continuous ductile deformations with long sliding traces were observed at the fracture surfaces derived from Ag-NS-180 in **Fig. 2.30b$_1$-b$_3$**. This result indicated that significant connections were formed both inside the Ag joint and at the interface. As the strength of a joint is mainly determined by the internal and interfacial connections [30], these increased connections greatly improved the shear strength to 48.6 MPa in **Fig. 2.28**. When the thermal decomposition temperature was 200 ^{o}C, monodispersed ductile deformations in **Fig. 2.30c$_1$-c$_3$** indicated insufficient sintering of Ag-NS-200. According to sintering theory, sintering occurs by reducing Gibbs free energy, which involves substituting high-energy surfaces with low-energy grain boundaries [16,31]. As shown in **Fig. 2.26d$_1$**, the pre-sintering of Ag particles occurred in Ag-NS-200, which reduced the surface energy and decreased shear strength.

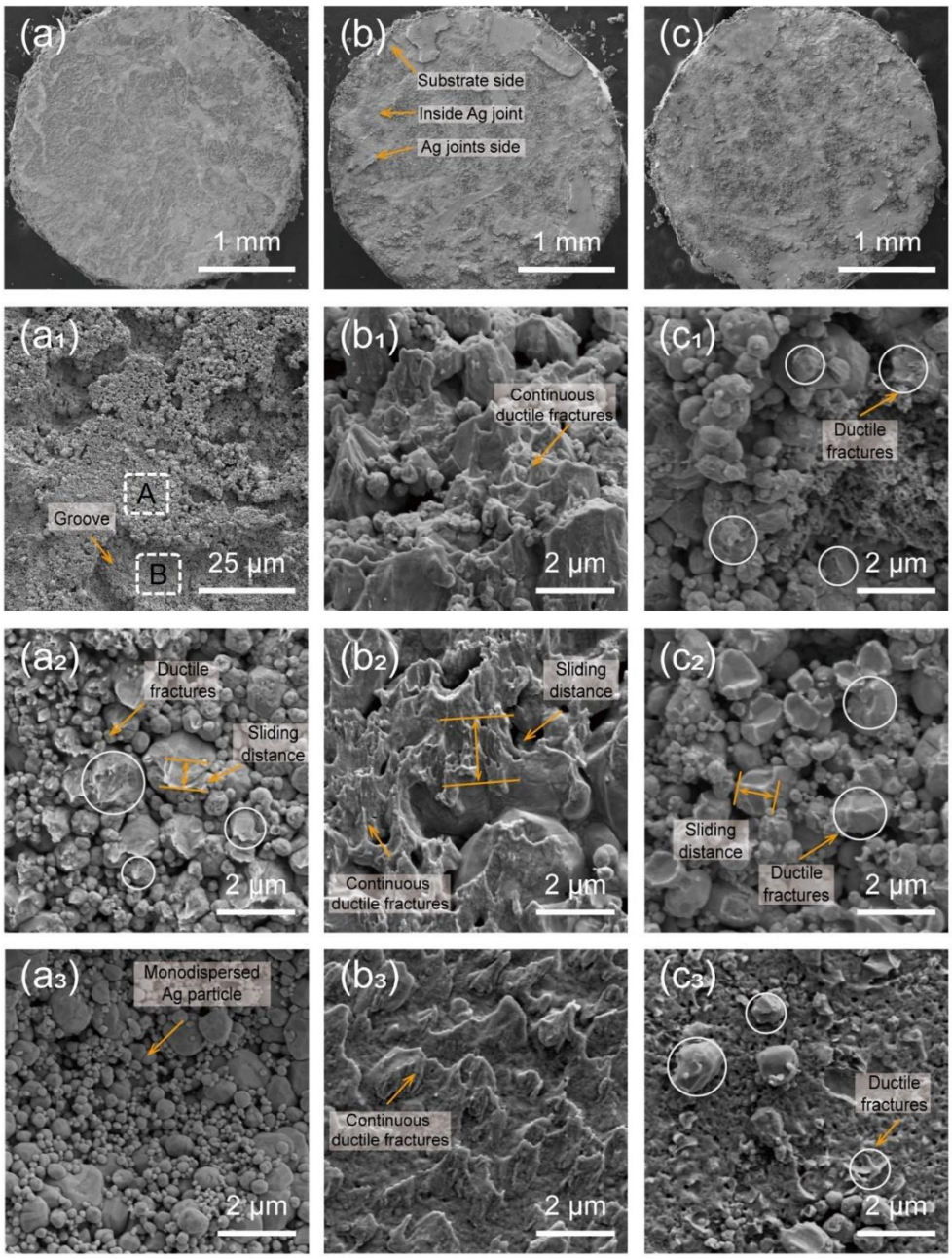

Fig. 2.30 Microstructure of the fracture surfaces of Ag joints sintered at 200 °C. SEM images of the fracture surface of the sintered Ag joint derived from (a)-(a_1) Ag-NS-160. (a_2) and (a_3) Amplified SEM image of the white rectangle A and B in (a_1), respectively. SEM images of the fracture surface of the sintered Ag joint derived from (b)-(b_3) Ag-NS-180, and (c)-(c_3) Ag-NS-200.

2.4 Conclusion

This study confirmed the feasibility of using an Ag-based complex. In addition, the effects of thermal decomposition conditions of the Ag-based complex on the bonding performance of Ag nanostructures were investigated. The results demonstrated that the thermal decomposition conditions could determine two factors of the Ag nanostructures: I) the content of organic intermediate products and II) the sintering of Ag particles. The existence of organic intermediate products for a short time or at low thermal decomposition temperatures resulted in gaseous products. Removing the gaseous products created large pores inside the sintered Ag joints, which deteriorated the joint properties. As excessive decomposition occurred, sintering between the Ag particles of the Ag nanostructures decreased the surface energy and driving force for sintering. Comparatively, Ag NPs with naked surfaces rendered remarkable bonding performance to Ag-NS-180, resulting in a shear strength of 48.6 MPa at 200 ^{o}C. In summary, the Ag-based complex thermal decomposition temperature-dependent bonding performance of the Ag nanostructures, explored herein, provided a new understanding for optimizing Ag nanostructure sintering.

Reference

[1] H. Yang, W. Zhu, Study on the main influencing factors of shear strength of nano-silver joints, Journal of Materials Research and Technology 9 (2020) 4133–4138. https://doi.org/https://doi.org/10.1016/j.jmrt.2020.02.040.

[2] Y. Dong, X. Li, S. Liu, Q. Zhu, J.-G. Li, X. Sun, Facile synthesis of high silver content MOD ink by using silver oxalate precursor for inkjet printing applications, Thin Solid Films 589 (2015) 381–387. https://doi.org/https://doi.org/10.1016/j.tsf.2015.06.001.

[3] H. Fang, C. Wang, S. Zhou, Q. Kang, T. Wang, D. Yang, Y. Tian, T. Suga, Rapid pressureless and low-temperature bonding of large-area power chips by sintering two-step activated Ag paste, Journal of Materials Science: Materials in Electronics 31 (2020) 6497–6505. https://doi.org/10.1007/s10854-020-03207-y.

[4] Y. Choi, K. Seong, Y. Piao, Metal−Organic Decomposition Ink for Printed Electronics, Adv Mater Interfaces 6 (2019) 1901002. https://doi.org/https://doi.org/10.1002/admi.201901002.

[5] D.-H. Shin, S. Woo, H. Yem, M. Cha, S. Cho, M. Kang, S. Jeong, Y. Kim, K. Kang, Y. Piao, A Self-Reducible and Alcohol-Soluble Copper-Based Metal–Organic Decomposition Ink for Printed Electronics, ACS Appl Mater Interfaces 6 (2014) 3312–3319. https://doi.org/10.1021/am4036306.

[6] K.R. Zope, D. Cormier, S.A. Williams, Reactive Silver Oxalate Ink Composition with Enhanced Curing Conditions for Flexible Substrates, ACS Appl Mater Interfaces 10 (2018) 3830–3837. https://doi.org/10.1021/acsami.7b19161.

[7] W. Yang, C. Liu, Z. Zhang, Y. Liu, S. Nie, One step synthesis of uniform organic silver ink drawing directly on paper substrates, J Mater Chem 22 (2012) 23012–23016. https://doi.org/10.1039/C2JM34264B.

[8] Y. Tao, Y. Tao, B. Wang, L. Wang, Y. Tai, A facile approach to a silver conductive ink with high performance for macroelectronics, Nanoscale Res Lett 8 (2013) 296. https://doi.org/10.1186/1556-276X-8-296.

[9] W. Yang, C. Wang, V. Arrighi, An organic silver complex conductive ink using both decomposition and self-reduction mechanisms in film formation, Journal of Materials Science: Materials in Electronics 29 (2018) 2771–2783. https://doi.org/10.1007/s10854-017-8205-7.

[10] M. Vaseem, S.-K. Lee, J.-G. Kim, Y.-B. Hahn, Silver-ethanolamine-formate complex based transparent and stable ink: Electrical assessment with microwave plasma vs thermal sintering, Chemical Engineering Journal 306 (2016) 796–805. https://doi.org/https://doi.org/10.1016/j.cej.2016.08.003.

[11] G. Kang, Y. Zhong, X. Du, Z. Shao, J. Jiang, X. Wang, W. Li, S. Guo, L. Gao, Z. Fang, G. Zheng, Low-temperature sintering of silver-ammonia complex organic composite ink shows high conductivity for humidity sensors, Mater Des 234 (2023) 112374. https://doi.org/https://doi.org/10.1016/j.matdes.2023.112374.

[12] J. Li, X. Zhang, X. Liu, Q. Liang, G. Liao, Z. Tang, T. Shi, Conductivity and foldability enhancement of Ag patterns formed by PVAc modified Ag complex inks with low-temperature and rapid sintering, Mater Des 185 (2020) 108255. https://doi.org/https://doi.org/10.1016/j.matdes.2019.108255.

[13] W. Yang, Z. Dong, Z. Guo, C. Wang, Tailored Silver Malonate Conductive Ink with Tunable Performance Formulated from Mixed Silver Dicarboxylates, ACS Appl Electron Mater 5 (2023) 2598–2607. https://doi.org/10.1021/acsaelm.3c00085.

[14] B.M. Abu-Zied, A.M. Asiri, An investigation of the thermal decomposition of silver acetate as a precursor for nano-sized Ag-catalyst, Thermochim Acta 581 (2014) 110–117. https://doi.org/https://doi.org/10.1016/j.tca.2014.02.020.

[15] C. Chen, K. Suganuma, Microstructure and mechanical properties of sintered Ag particles with flake and spherical shape from nano to micro size, Mater Des 162 (2019) 311–321. https://doi.org/https://doi.org/10.1016/j.matdes.2018.11.062.

[16] Z. Deng, G. Zou, R. Du, Q. Jia, H. Zhang, L. Liu, Particle Size Effects of Nano-Ag Films on the Interface Sintered Bonding for Die Attachment, J Electron Mater 53 (2024) 473–488. https://doi.org/10.1007/s11664-023-10786-z.

[17] G. Qu, Z. Deng, W. Guo, Z. Peng, Q. Jia, E. Deng, H. Zhang, The Heat-Dissipation Sintered Interface of Power Chip and Heat Sink and Its High-Temperature Thermal Analysis, IEEE Trans Compon Packaging Manuf Technol 13 (2023) 816–822. https://doi.org/10.1109/TCPMT.2023.3290303.

[18] Z. Deng, G. Zou, Q. Jia, B. Feng, H. Zhang, H. Ren, L. Liu, Effect of Ag Sintered Bondline Thickness on High-Temperature Reliability of SiC Power Devices, IEEE Trans Compon Packaging Manuf Technol 11 (2021) 1889–1895. https://doi.org/10.1109/TCPMT.2021.3110997.

[19] Y. Lee, S.-G. Oh, Ostwald ripening and control of Ag ion reduction degree by ammonium hydroxide in alcohol reduction process, Journal of Industrial and Engineering Chemistry 21 (2015) 768–771. https://doi.org/https://doi.org/10.1016/j.jiec.2014.04.010.

[20] Z. Zhang, Z. Wang, S. He, C. Wang, M. Jin, Y. Yin, Redox reaction induced Ostwald ripening for size- and shape-focusing of palladium nanocrystals, Chem Sci 6 (2015) 5197–5203. https://doi.org/10.1039/C5SC01787D.

[21] M.A. Asoro, D. Kovar, P.J. Ferreira, Effect of surface carbon coating on sintering of silver nanoparticles: in situ TEM observations, Chemical Communications 50 (2014) 4835–4838. https://doi.org/10.1039/C4CC01547A.

[22] K. Suganuma, S. Sakamoto, N. Kagami, D. Wakuda, K.-S. Kim, M. Nogi, Low-temperature low-pressure die attach with hybrid silver particle paste, Microelectronics Reliability 52 (2012) 375–380. https://doi.org/https://doi.org/10.1016/j.microrel.2011.07.088.

[23] W. Wei, L. Gao, Y. Tan, X. Li, M. Wang, Y. Mei, G. Lu, Feasibility Investigation and Characterization of Liquid Dispersant–Assisted Sintering of Silver to Bond Large-Area Plates, Adv Eng Mater 25 (2023) 2201574. https://doi.org/https://doi.org/10.1002/adem.202201574.

[24] C. Wang, X. Zhang, Y. Zhang, T. Zhao, P. Zhu, R. Sun, H. Nishikawa, L. Xu, Pressureless and low temperature sintering by Ag paste for the high temperature die-attachment in power device packaging, in: 2022 IEEE 72nd Electronic Components and Technology Conference (ECTC), 2022: pp. 2256–2262. https://doi.org/10.1109/ECTC51906.2022.00356.

[25] Y. Xu, X. Qiu, W. Li, S. Wang, N. Ma, M. Ueshima, C. Chen, K. Suganuma, Development of high thermal conductivity of Ag/diamond composite sintering paste and its thermal shock reliability evaluation in SiC power modules, Journal of Materials Research and Technology 26 (2023) 1079–1093. https://doi.org/https://doi.org/10.1016/j.jmrt.2023.07.254.

[26] T. Yamakawa, T. Takemoto, M. Shimoda, H. Nishikawa, K. Shiokawa, N. Terada, Influence of Joining Conditions on Bonding Strength of Joints: Efficacy of Low-Temperature Bonding Using Cu Nanoparticle Paste, J Electron Mater 42 (2013) 1260–1267. https://doi.org/10.1007/s11664-013-2583-2.

[27] W. Yang, F. Hermerschmidt, F. Mathies, E.J.W. List-Kratochvil, Comparing low-temperature thermal and plasma sintering processes of a tailored silver particle-free ink, Journal of Materials Science: Materials in Electronics 32 (2021) 6312–6322. https://doi.org/10.1007/s10854-021-05347-1.

[28] W. Yang, C. Wang, V. Arrighi, An organic silver complex conductive ink using both decomposition and self-reduction mechanisms in film formation, Journal of Materials Science: Materials in Electronics 29 (2018) 2771–2783. https://doi.org/10.1007/s10854-017-8205-7.

[29] Y. Liu, C. Chen, Z. Zhang, M. Ueshima, T. Sakamoto, T. Naoe, H. Nishikawa, Y. Oda, K. Suganuma, Development of crack-less and deformation-resistant electroplated Ni/electroless Ni/Pt/Ag metallization layers for Ag-sintered joint during a harsh thermal shock, Mater Des 224 (2022) 111389. https://doi.org/https://doi.org/10.1016/j.matdes.2022.111389.

[30] S.A. Paknejad, G. Dumas, G. West, G. Lewis, S.H. Mannan, Microstructure evolution during 300°C storage of sintered Ag nanoparticles on Ag and Au substrates, J Alloys Compd 617 (2014) 994–1001. https://doi.org/https://doi.org/10.1016/j.jallcom.2014.08.062.

[31] A.P. Lange, A. Samanta, H. Majidi, S. Mahajan, J. Ging, T.Y. Olson, K. van Benthem, S. Elhadj, Dislocation mediated alignment during metal nanoparticle coalescence, Acta Mater 120 (2016) 364–378. https://doi.org/https://doi.org/10.1016/j.actamat.2016.08.061.

Chapter 3: Thermal decomposition behaviors of Ag-based complex on Ag, Al, and Cu substrates

3.1 Introduction

In Chapter 2, the thermal decomposition behaviors of Ag-based complexes were investigated on the electroless nickel immersion gold (ENIG) substrate. The decomposition of the Ag-based complex on the Au substrate was not disturbed due to the high stability of Au. However, there are various candidates for substrates such as Ag [1], Al [2], and Cu [3]. Whether other substrates interrupt the reduction of Ag^+ during Ag-based complex decomposition remains unknown.

This study investigated the effects of substrates on the thermal decomposition process of Ag-based complexes using three common substrates (Ag, Al, and Cu). The microstructural characteristics, particle size distributions, and elemental compositions of nanostructures obtained from Ag-based complex thermal decomposition were analyzed. By comparing, the Ag-based complex decomposition behaviors were divided into two categories. The indicator determining the decomposition behaviors was whether or not the substrate reacted with the Ag-based complex.

3.2 Materials and methods

3.2.1 Materials

Silver acetate (99%, FUJIFILM), 2-amino-2-methyl-1-propanol (FUJIFILM), distilled

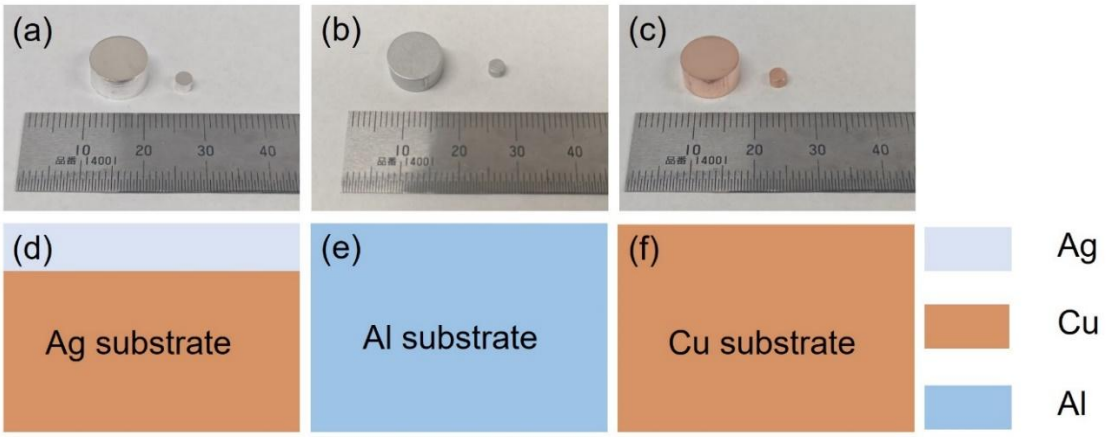

Fig. 3.1 Detail information of substrate. Optical images of (a) Ag, (b) Al, and (c) Cu substrate. Schematic diagram illustrating the structure of (d) Ag, (e) Al, and (f) Cu substrate.

water and ethanol were directly used without purification. Ag, Cu (C1020, 99.96%), and Al (A1050, 99.50%) substrates with a diameter of 10 mm and 3 mm underwent ultrasound cleaning in ethanol before being utilized. **Fig. 3.1** shows the detailed information of three kinds of substrates. As shown in **Fig. 3.1a-c**, Ag, Cu (C1020, 99.96%), and Al (A1050, 99.50%) substrates with a diameter of 10 mm and 3 mm were used as dummy substrates and dies, respectively. For the Ag substrate in **Fig. 3.1d**, an Ag layer of approximately 4 μm was electroplated on the Cu substrate because of the high cost of Ag. **Fig. 3.1e** and **3.1f** demonstrate that the Al and Cu substrates were pure Al and Cu, respectively.

3.2.2 Preparation of Ag nanostructures

The Ag-based complex was synthesized using the same complexation reaction as in Chapter 2. **Fig. 3.2** shows the preparation process of the Ag nanostructure on the three substrates. As shown in **Fig. 3.2a**, 60 mg Ag-based complex was printed on the Ag, Al, and Cu substrates. The Ag nanostructures were created using a two-step heating profile

containing a preheating stage at 90 ºC for 5 min and a heating stage at 180 ºC for 30 min. **Fig. 3.2b** and **3.2c** show that the top surface of the Ag and Al substrates retained their original

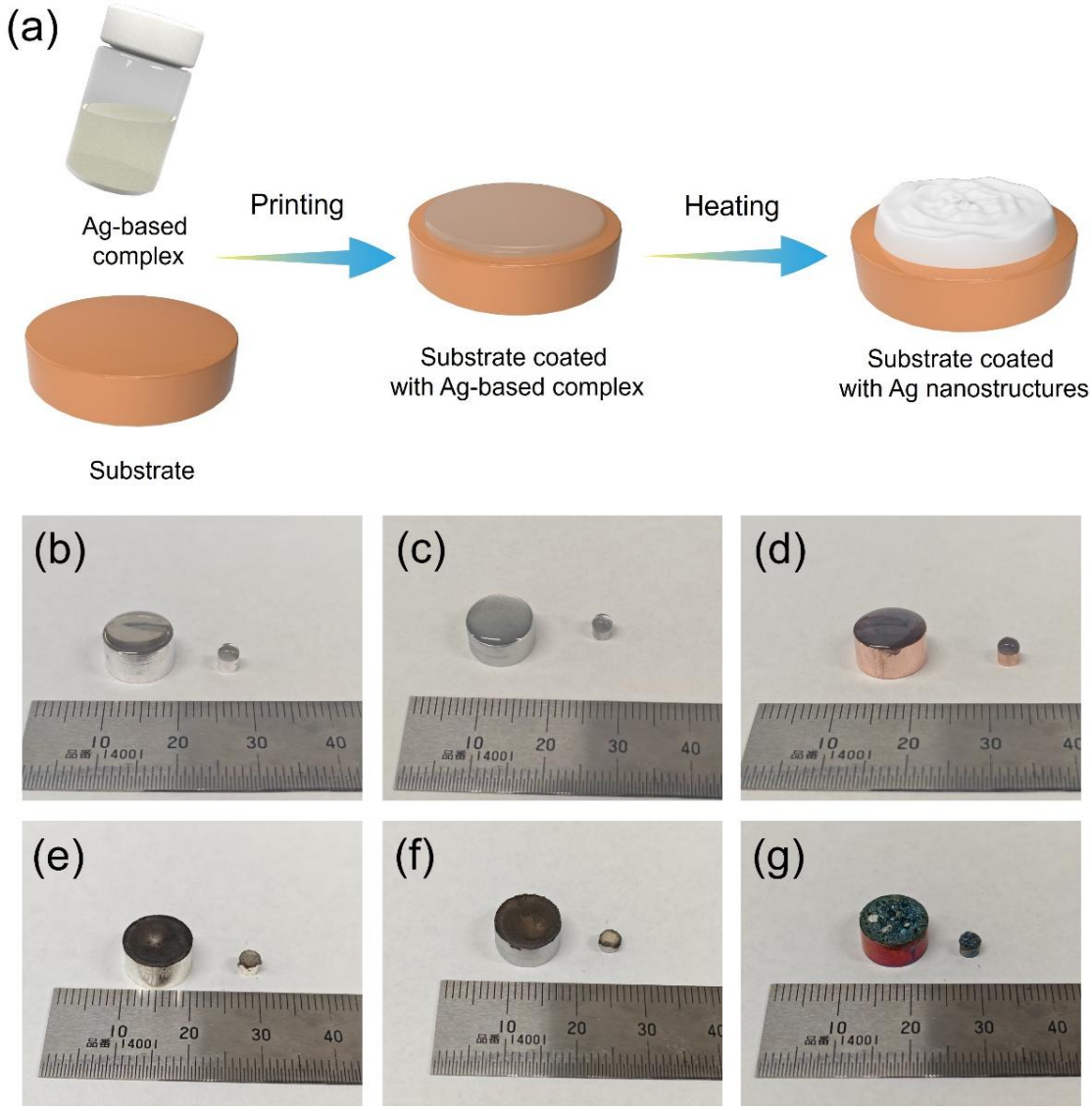

Fig. 3.2 Ag nanostructure preparation. (a) Schematic diagrams of the fabrication of Ag nanostructures derived from an Ag-based complex. Optical image of (b) Ag, (c) Al, and (d) Cu substrates coated with Ag-based complex. Optical image of Ag nanostructures on the (e) Ag, (f) Al, and (g) Cu substrates.

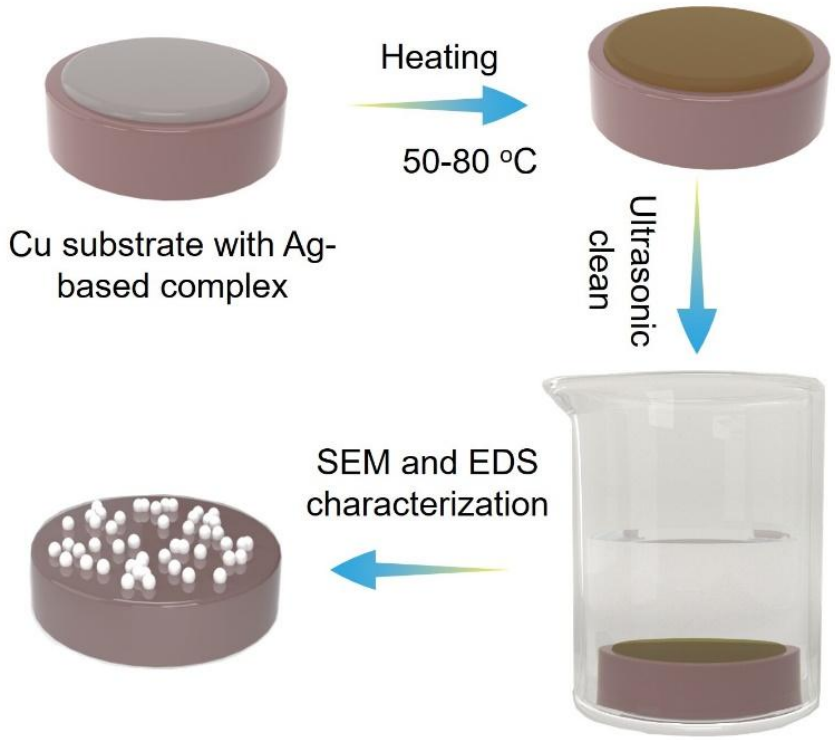

Fig. 3.3 Schematic diagram of the corroborative experiment of the reaction between the Ag-based complex and Cu substrate.

state after being coated with the Ag-based complex. However, the top surface of the Cu substrate became black after being coated with the Ag-based complex. **Fig. 3.2e-g** depicts the optical images of the Ag nanostructures on the Ag, Al, and Cu substrates, which are denoted as NS-Ag, NS-Al, and NS-Cu, respectively. **Fig. 3.3** depicts a corroborative experiment on the Cu substrate. The Cu substrates coated with the Ag-based complex were heated at low temperatures of 50-80 °C for 30 min to avoid interfering with thermal decomposition. After heating, the liquid Ag-based complex was removed by ultrasonic cleaning in distilled water.

3.2.3 Characterization

The Ag nanostructure composition on the three substrates was confirmed using X-ray diffraction (XRD, Ultima IV, Rigaku). The Ag nanostructures on the Ag, Al, and Cu substrates and the elemental composition of the Ag nanostructures were characterized using a field-emission scanning electron microscope (FE-SEM, FEI Nova Nana SEM 450) and energy-dispersive spectrometer (EDS), respectively. The cross-section was polished using a cross-section ion polishing machine (IB-19530CP, JEOL). The diameter of a single Ag particle was measured by ImageJ. Three hundred Ag particles per Ag nanostructure were measured to ensure the statistical accuracy of particle size distribution. For the corroborative experiment, the Cu substrates were characterized by SEM and EDS.

3.3 Results and discussion

3.3.1 Ag nanostructures on Ag, Al, and Cu substrates

The Ag-based complex was heated at 180°C for 30 min on the Ag, Al, and Cu substrates. In Chapter 2, we confirmed that the thermal decomposition temperature of the Ag-based complex is approximately 181.1 ºC. When the Ag-based complex was heated at 180 ºC, the Ag-based complex decomposition was expected to translate Ag (I) into Ag (0), resulting in Ag nanostructures [4]. This translation was confirmed by characterizing the nanostructures on the three substrates by XRD. **Fig. 3.4** shows the XRD patterns of the three nanostructures. XRD results in **Fig. 3.4a-c** revealed high-intensity characteristic peaks of Ag, indicating that Ag (I) of the Ag-based complex was reduced to Ag after thermal decomposition [5].

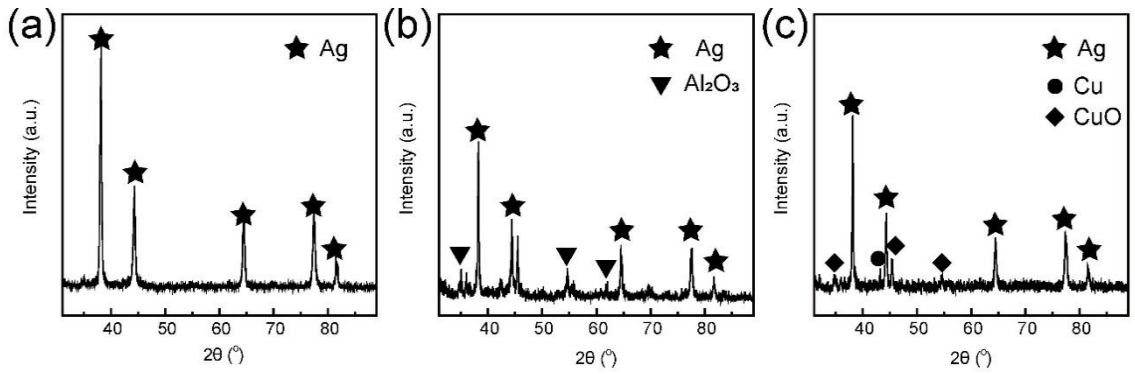

Fig. 3.4 XRD pattern of (a) NS-Ag, (b) NS-Al, and (c) NS-Cu.

Besides the Ag peaks, the characteristic peaks of Al_2O_3 and CuO were detected in NS-Al and NS-Cu, respectively.

The XRD detection results in **Fig. 3.4** demonstrated the generation of Ag. However, the effects of the substrate on the morphology of Ag nanostructures remained unclear. The effect of substrate was investigated by observing the microstructure of the Ag nanostructure by SEM. **Fig. 3.5** depicts the microstructures and particle size distribution of the top surface of the three Ag nanostructures. **Fig. 3.5a-c** show that the three kinds of Ag nanostructures exhibit rugged top surfaces with huge grooves. In **Fig. 3.5d** and **3.5e**, NS-Ag and NS-Al consisted of clustered Ag branches. High magnification SEM images in **Figs. 3.5 g** and **3.5h** demonstrate that these Ag branches were composed of Ag nanoparticles with naked surfaces. By comparison, organics were detected in the NS-Cu in **Fig. 3.5f** and **3.5i** along with Ag particles, and the particle size of NS-Cu in **Fig. 3.5l** was larger than that of NS-Ag and NS-Al in **Fig. 3.5j** and **3.5k** respectively. This means that the Ag nanostructure on the three substrates can be divided into 2 categories: I) Ag nanostructures on Ag and Al substrate and II) Ag nanostructures on Cu substrate.

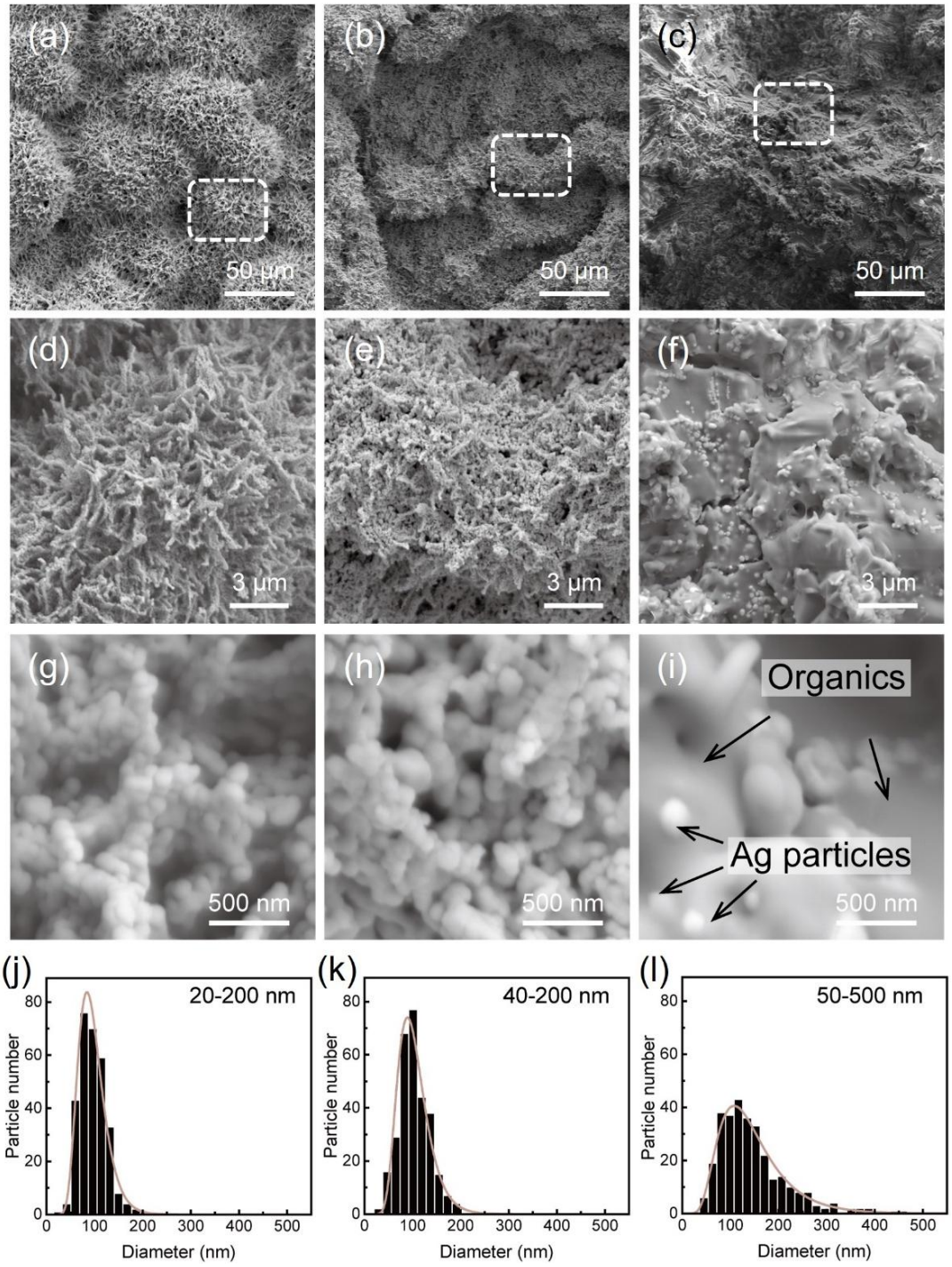

Fig. 3.5 Characterization of the Ag nanostructures from the top view. SEM images of (a) (d) (g) NS-Ag, (b) (e) (h) NS-Al, and (c) (f) (i) NS-Cu. (j), (k), and (l) corresponding particle size distribution of (g), (h), and (i).

The SEM images in **Fig. 3.5** demonstrated that the substrates had significant effects on the top-surface morphology of the Ag nanostructures. The internal morphology changes with substrate were investigated by cross-sectional observation. **Fig. 3.6** shows the cross-section of NS-Ag and NS-Al, and **Fig. 3.7** shows the cross-section of NS-Cu. **Fig. 3.6a, e,** and **Fig. 3.7a** show that the Ag nanostructures could be vertically divided into three distinct regions (I, II, and III). The corresponding particle size distribution of the three distinct regions in each nanostructure are presented in **Fig. 3.8**. Analysis of the cross-sectional SEM images in **Fig. 3.6b–d** and **3.6f-h** and particle size distributions in **Fig. 3.8a, 3.8d, 3.8g,** and **3.8b, 3.8e, 3.8h** revealed that the particle of NS-Ag and NS-Al increased from the top to the bottom regions, which was similar to the tendency on the Au substrates in Chapter 2. The temperature gradient within the Ag-based complex likely originated from the bottom-up heating method employed on the hot plate. Consequently, the higher temperatures experienced by the bottom region accelerated this decomposition process, and the average size of the Ag particles at the bottom region increased by Ostwald ripening [6].

Fig. 3.7b-d show the presence of Ag particles and organics on NS-Cu. Ag particles with a wide size range, such as Ag nanoparticles (NPs), microparticles (MPs), and submicron particles, were detected according to **Fig. 3.8c, f, i**. In addition, NS-Cu exhibited larger particle sizes in the top and middle regions compared to NS-Ag and NS-Al. Prior studies indicated that rapid Ag(I) reduction leads to smaller, spherical Ag particles owing to the limited time for particle growth [7,8]. The organics in NS-Cu might act as capping agents, retarding the Ag(I) reduction and promoting the formation of larger particles [9,10]. By contrast, higher temperatures at the bottom region accelerated the Ag (I) reduction, and the

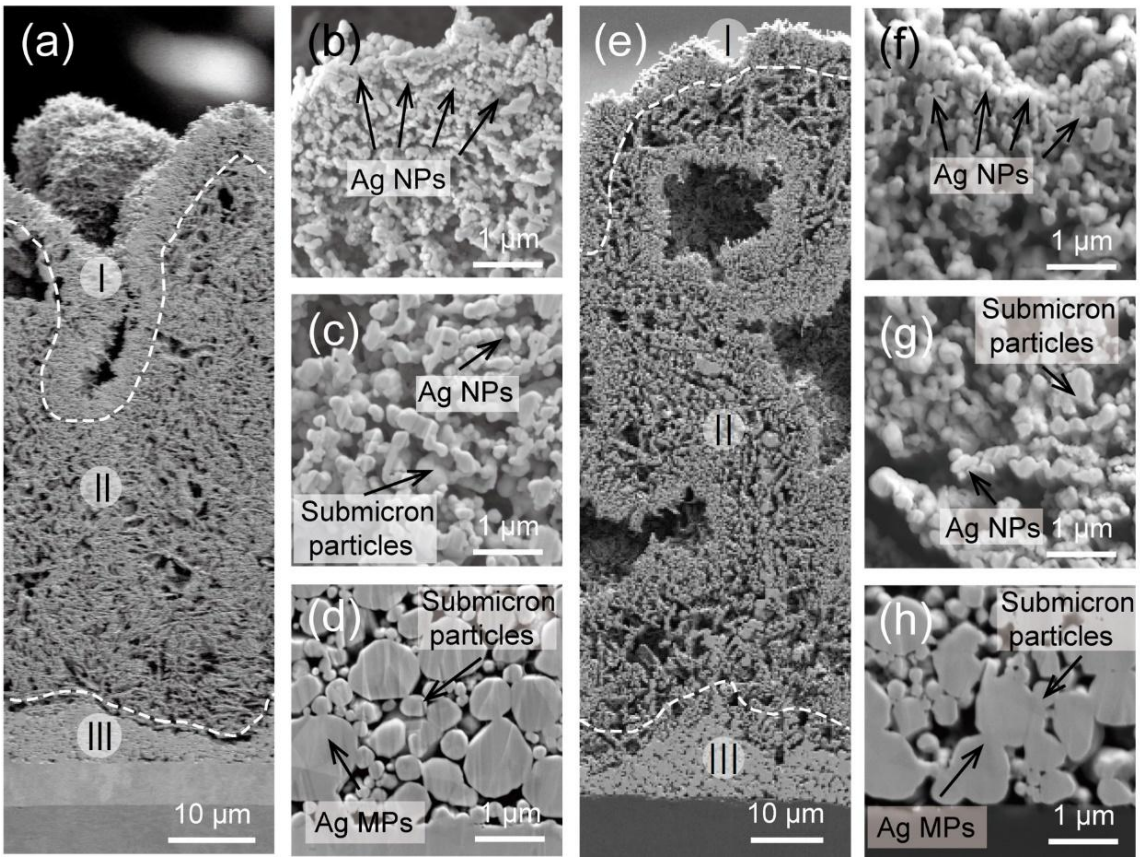

Fig. 3.6 Cross-sections of NS-Ag and NS-Al. (a) Overview of NS-Ag showing regions I, II, and III. High-magnification cross-sectional SEM images of NS-Ag in region (b) I, (c) II (d) III. (e) Overview of NS-Al showing regions I, II, and III. High-magnification cross-sectional SEM images of NS-Al in region (f) I, (g) II (h) III.

Ostwald ripening of newly generated Ag nanoparticles was limited due to the capping effect of organics [11]. Thus, the particle size at the bottom region of NS-Cu was smaller than that of the mid and top regions. Furthermore, the surface of the Cu substrate in **Fig. 3.6d** was etched after thermal decomposition. By comparison, the original substrate in **Fig. 3. 9** demonstrated a smooth surface and straight interface. These results indicated a potential interaction between the Cu substrate and Ag-based complex during thermal decomposition.

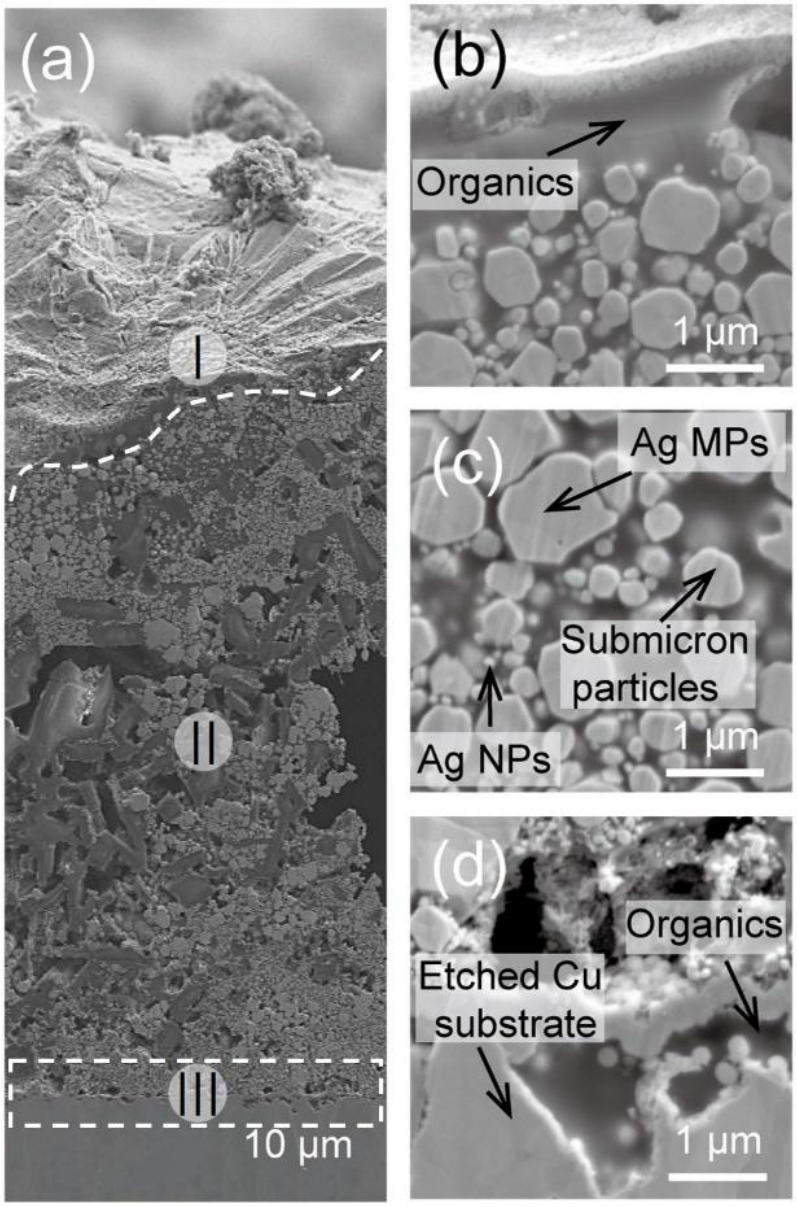

Fig. 3.7 Cross-sections of NS-Cu. (a) Overview (b) region I, (c) region II (d) region III of NS-Cu.

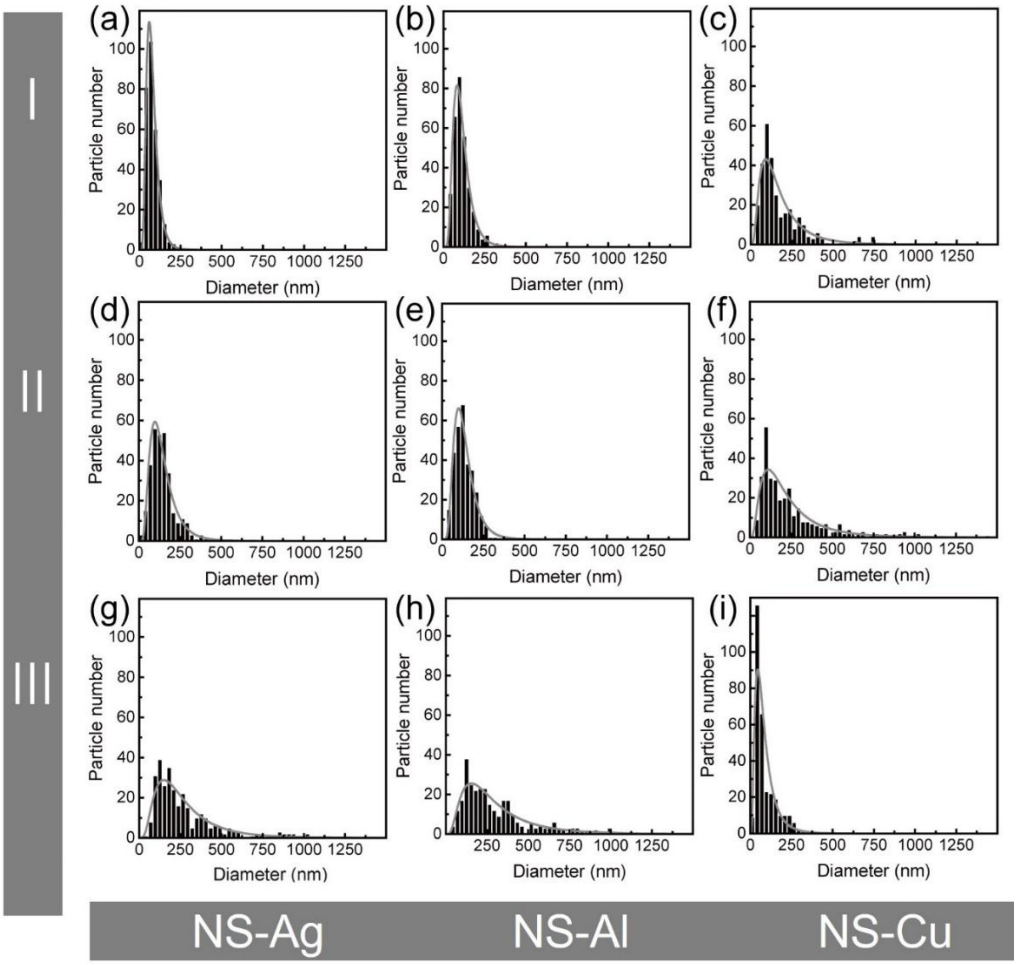

Fig. 3.8 Particle size distribution of Ag nanostructures. Particle size distribution of region I in (a) NS-Ag, (b) NS-Al, and (c) NS-Cu; region II in (d) NS-Ag, (e) NS-Al, and (f) NS-Cu; and region III in (g) NS-Ag, (h) NS-Al, and (i) NS-Cu.

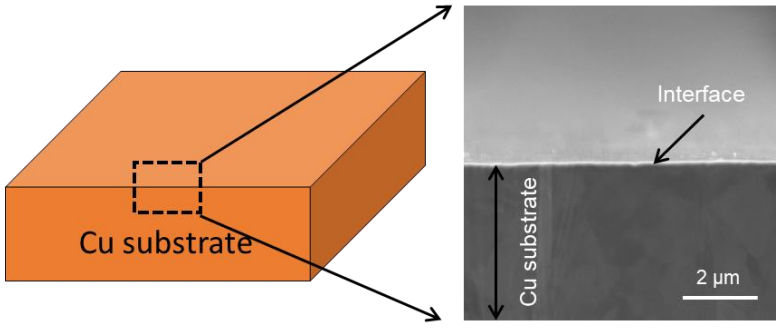

Fig. 3.9 SEM image of the cross-section of the original Cu substrate.

3.3.2 Reactions between Ag-based complex and Cu substrate

EDS was used to investigate the elemental distribution in the Ag nanostructures and identify potential interactions between the Ag-based complex and substrates. **Fig. 3.10** depicts the EDS elemental maps for NS-Ag, NS-Al, and NS-Cu after thermal treatment at 180 °C for 30 min. Notably, the EDS maps of C for NS-Cu in **Fig. 3.10c** and **h** exhibited significantly higher intensity than the faint C maps for NS-Ag and NS-Al in **Fig. 3.10m** and **p**, respectively. This observation was corroborated by the quantitative data presented in **Fig. 3.10q**, which demonstrated that the C content of NS-Cu (12.4%) was substantially higher than that of NS-Ag (0.3%) and NS-Al (0.4%). Furthermore, Cu was detected in the top region

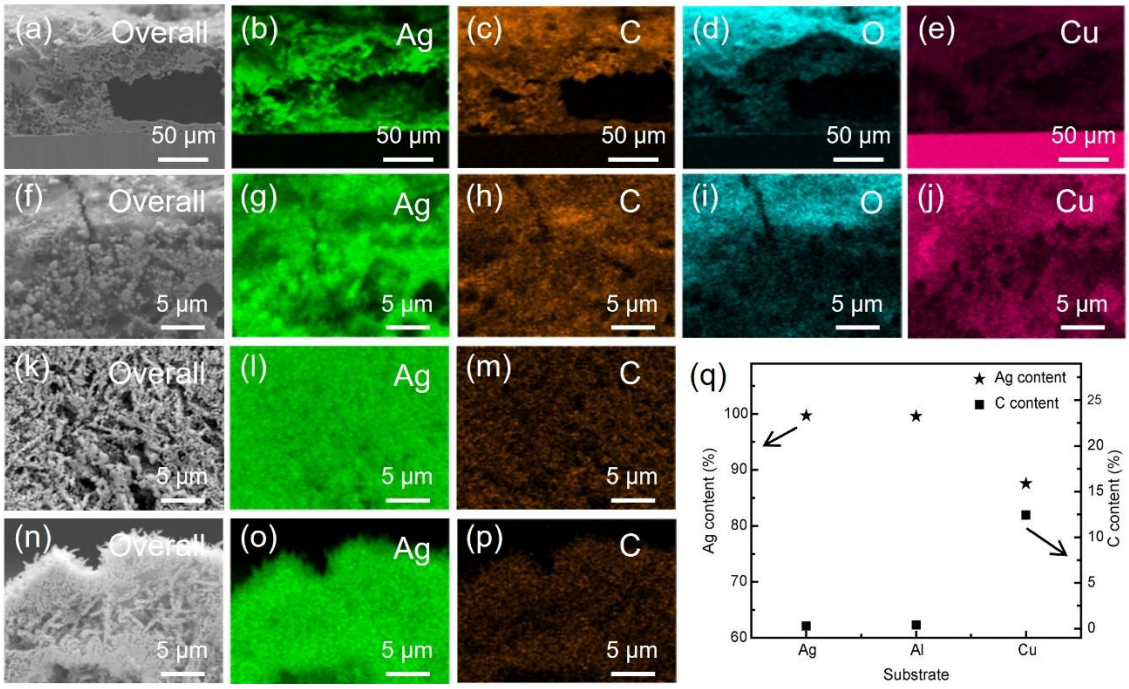

Fig. 3.10 Confirmation of the reaction between the Ag-based complex and Cu substrate. EDS maps of (a)–(e) NS-Cu, (f)–(j) top region of NS-Cu, (k)–(m) NS-Ag, and (m)–(p) NS-Al after thermal treatment at 180 °C for 30 min. (q) Quantitative elemental (Ag and C) compositions of NS-Ag, NS-Al, and NS-Cu.

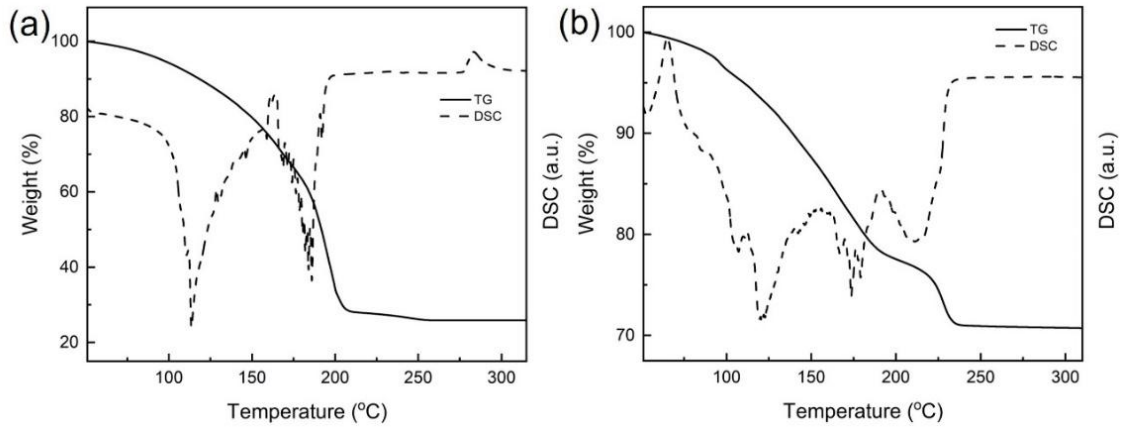

Fig. 3.11 Thermal behaviors of Ag-based complex decomposition. TG and DSC curves for (a) the Ag-based complex and (b) a 1:1 weight ratio mixture of the Ag-based complex and Cu microparticles.

of NS-Cu (**Fig. 3.10e** and **3.10j**). Considering the substantial thickness > 100 μm of NS-Cu in **Fig. 3.10a**, the solid-state diffusion of Cu from the bottom to the top region at a low temperature of 180 °C was highly improbable. This observation indicated a possible interfacial reaction between the liquid Ag-based complex and Cu substrate during thermal decomposition, resulting in the etching of the Cu substrate. The Cu ions released from the etched substrate then diffused from the bottom to the top region via liquid-phase diffusion.

Chemical reactions are typically classified as endothermic or exothermic, with products exhibiting distinct thermal behaviors compared to reactants at elevated temperatures [12]. TG and DSC are widely used to investigate thermal decomposition behavior [5,13]. **Fig. 3.11** depicts the TG and DSC curves for the Ag-based complex and a 1:1 weight ratio mixture of the Ag-based complex and Cu particles. The TG curve of the Ag-based complex in **Fig. 3.11a** demonstrates a significant weight loss in the 80–200 °C range. The two endothermic peaks at 113 and 186 °C correspond to the multistep decomposition of the Ag-based complex [14]. In contrast, the TG curve of the 1:1 mixture containing the Ag-based complex and Cu

microparticles in **Fig. 3.11b** shows a two-step weight loss. The first weight loss in the 80–190 °C range was attributed to the thermal decomposition of the Ag-based complex [15]. The second weight loss occurred in the 190–238 °C range and was attributed to the products formed by the reaction between the Ag-based complex and Cu substrate. The DSC curve in **Fig. 3.11b** corroborated these findings. An exothermic peak at 65 °C and endothermic peak at 211 °C were observed alongside the two endothermic peaks associated with the decomposition of the Ag-based complex. The exothermic peak may indicate the reaction between the Ag-based complex and Cu substrate [16]. The endothermic peak likely corresponds to the thermal decomposition of the products formed during this reaction, coinciding with the observed weight loss in the TG curve.

As depicted in **Fig. 3.3**, a corroborative experiment was conducted to verify the reaction products. The surface conditions of Cu substrates before and after heat treatment with Ag-based complex are depicted in **Fig. 3.12**. As shown in **Fig. 3.12a**, the surface of Cu substrate.

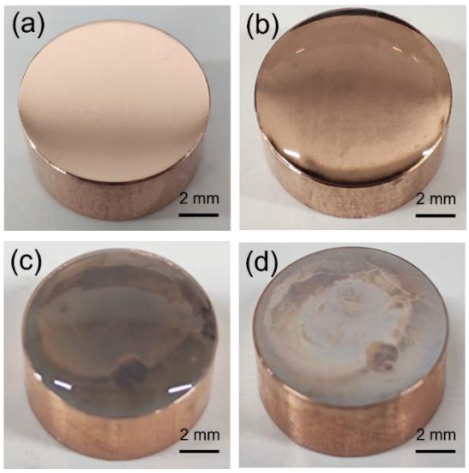

Fig. 3.12 Optical images of (a) original Cu substrate, (b) Cu substrate coated with Ag-based complex, (c) Cu substrate heated with Ag-based complex at 50 °C for 30 min, and (d) the Cu substrate after ultrasonic cleaning.

was polished to remove surface oxides. The colorless transparent Ag-based complex liquid in **Fig. 3.12b** became dark-gray transparent in **Fig. 3.12c** after heating at 50 ºC for 30 min. The dark-gray transparent liquid was removed by ultrasonic cleaning in distilled water, and the obtained Cu substrate was covered by a white-gray layer in **Fig. 3.12d**. The white-gray layer on the Cu substrate was characterized by SEM. **Fig. 3.13** illustrates the SEM images of the top surface of the Cu substrates heated with the Ag-based complex at different temperatures. The SEM images in **Fig. 3.13a-d** indicated that the white-gray layer on the Cu substrates consisted of monodispersed nano- and submicron particles. EDS analysis was conducted to confirm the composition of these particles, and the results were summarized in **Fig. 3.14**. Element Ag with high intensity in **Fig. 3.14d** corresponded to the position of the monodispersed particles in **Fig. 3.14a**, indicating that these particles were Ag. The white-gray layer on the Cu substrate was characterized by XRD. **Fig. 3.15** depicts the XRD patterns of the Cu substrates heated with the Ag-based complex at different temperatures. The characteristic peak of Ag was detected in **Fig. 3.15**, which provides evidence for the generation of Ag after heating. Therefore, it could be hypothesized that these Ag particles resulted from the displacement reaction between the Ag(I) of the Ag-based complex and Cu substrate, rather than from the thermal decomposition of the Ag-based complex. Two pieces of evidence support this hypothesis: i) Cu is less noble than Ag. ii) 50 ºC was much lower than the thermal decomposition temperature of the Ag-based complex. Therefore, this displacement reaction can be expressed by the schematic diagram in **Fig. 3.16** and Equation 3.1 [16]

$$2Ag^{+}\,(l) + Cu\,(s) \longrightarrow Cu^{2+}\,(l) + 2Ag\,(s) \qquad (3.1)$$

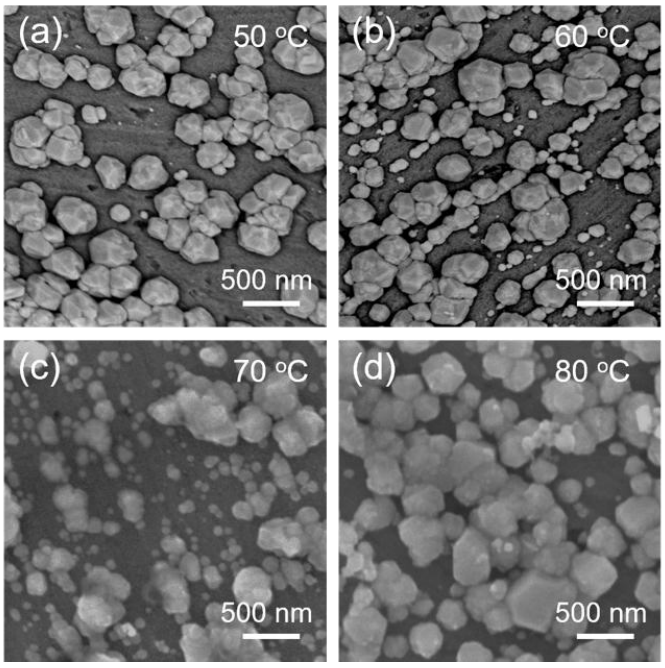

Fig. 3.13 SEM images of Cu substrates heated at (a) 50 °C, (b) 60 °C, (c) 70 °C, and (d) 80 °C after ultrasonic cleaning in Fig. 3.2.

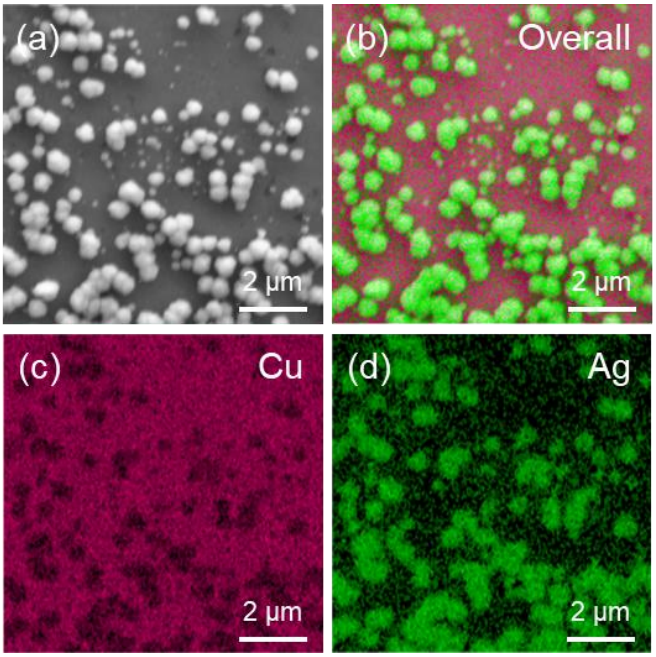

Fig. 3.14 EDS of Cu substrate heat treatment with Ag-based complex at 50 °C after ultrasonic cleaning.

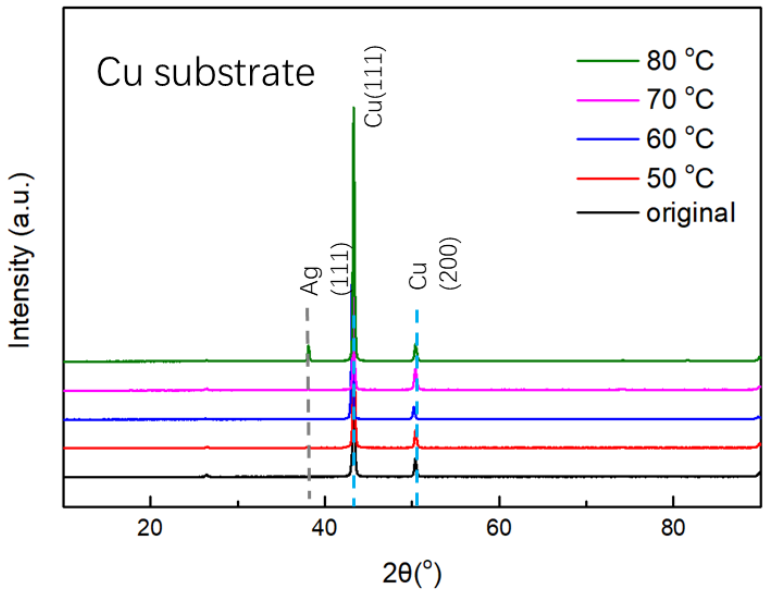

Fig. 3.15 XRD of Cu substrates after ultrasonic cleaning in Fig. 3.3.

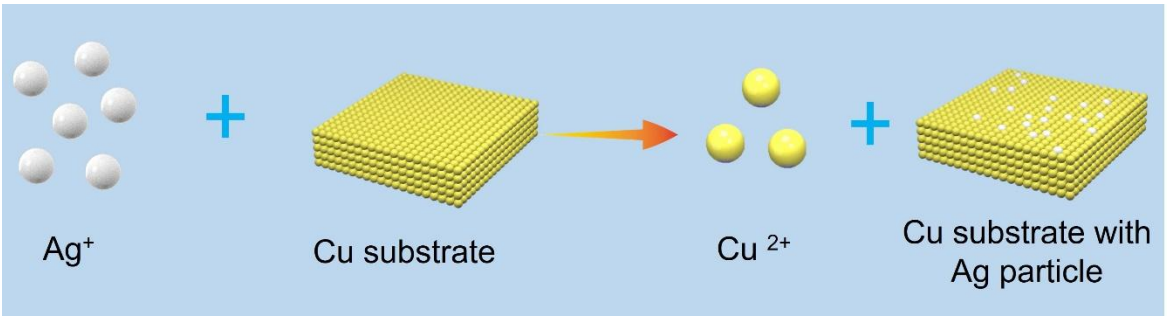

Fig. 3.16 Schematic diagram of displacement reaction between the Ag-based complex and Cu substrate.

A schematic diagram was drawn In **Fig. 3.17** to summarize the thermal decomposition behaviors of the Ag-based complex. Accordingly, the formation of NS-Ag and NS-Al only involved the thermal decomposition of the Ag-based complex. Regarding the formation of NS-Cu, there was a displacement reaction between the Ag-based complex and Cu substrate during the thermal decomposition, which resulted in the formation of Ag particles and Cu

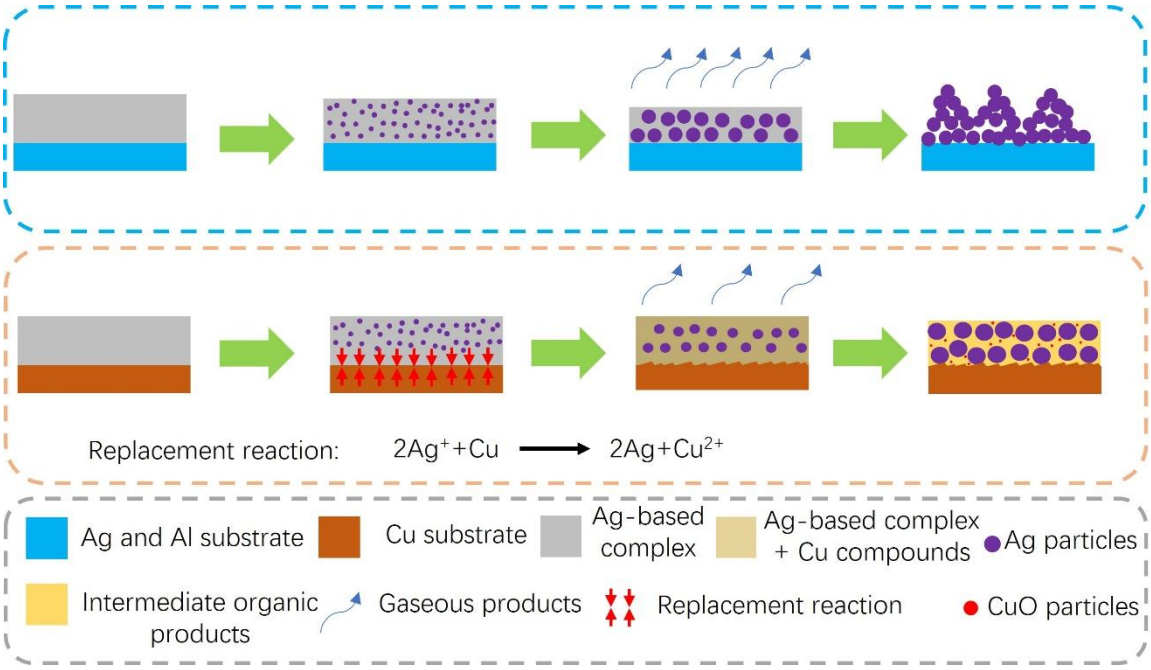

Fig. 3.17 Schematic diagram of the thermal decomposition of the Ag-based complex on Ag, Al, and Cu substrates.

compounds. The Cu compounds with a higher thermal decomposition temperature 211 ºC incompletely decomposed at 180 ºC, resulting in the intermediate organic products and high C content of NS-Cu.

3.4 Conclusion

In this study, the effects of substrate on the decomposition of Ag-based complex were confirmed successfully by analyzing the Ag nanostructure morphology and composition. Accordingly, the thermal decomposition behaviors of Ag-based complexes were divided into two categories, and the determining factor was whether a reaction occurred between the Ag-based complex and the substrate. For the Ag and Al substrates, the thermal decomposition of the Ag-based complex resulted in multilayered NS-Ag and NS-Al consisting of Ag particles

with naked surfaces. Besides thermal decomposition, the formation of NS-Cu involved a displacement reaction between the Ag-based complex and Cu substrate. This reaction led to Cu compounds with a high thermal decomposition temperature of 211 ^{o}C. As the heating temperature of 180 ^{o}C was lower than 211 ^{o}C, incomplete decomposition of the Ag-based complex resulted in organics in the NS-Cu. Overall, the effects of the substrate on the thermal decomposition behavior of Ag-based complexes were revealed, which could guide the selection of suitable substrates for desired Ag nanostructures.

Reference

[1] H. Zhang, W. Wang, H. Bai, G. Zou, L. Liu, P. Peng, W. Guo, Microstructural and mechanical evolution of silver sintering die attach for SiC power devices during high temperature applications, J Alloys Compd 774 (2019) 487–494. https://doi.org/https://doi.org/10.1016/j.jallcom.2018.10.067.

[2] R. Luo, X. Yu, Z. Wu, H. Zhang, Z.-Q. Liu, K. Suganuma, C.-F. Li, Long-time reliable direct bonding of silver flake paste on Al substrate for power electronic die-attachment, Materials Letters: X 13 (2022) 100124. https://doi.org/https://doi.org/10.1016/j.mlblux.2022.100124.

[3] Y. Yuan, H. Wu, J. Li, P. Zhu, R. Sun, Cu-Cu joint formation by low-temperature sintering of self-reducible Cu nanoparticle paste under ambient condition, Appl Surf Sci 570 (2021) 151220. https://doi.org/https://doi.org/10.1016/j.apsusc.2021.151220.

[4] K.S. Bhat, R. Ahmad, Y. Wang, Y.-B. Hahn, Low-temperature sintering of highly conductive silver ink for flexible electronics, J Mater Chem C Mater 4 (2016) 8522–8527. https://doi.org/10.1039/C6TC02751B.

[5] M. Vaseem, S.-K. Lee, J.-G. Kim, Y.-B. Hahn, Silver-ethanolamine-formate complex based transparent and stable ink: Electrical assessment with microwave plasma vs thermal sintering, Chemical Engineering Journal 306 (2016) 796–805. https://doi.org/https://doi.org/10.1016/j.cej.2016.08.003.

[6] Y. Lee, S.-G. Oh, Ostwald ripening and control of Ag ion reduction degree by ammonium hydroxide in alcohol reduction process, Journal of Industrial and Engineering Chemistry 21 (2015) 768–771. https://doi.org/https://doi.org/10.1016/j.jiec.2014.04.010.

[7] S. Chen, J.R. Drehmel, R.L. Penn, Facile Synthesis of Monodispersed Ag NPs in Ethylene Glycol Using Mixed Capping Agents, ACS Omega 5 (2020) 6069–6073. https://doi.org/10.1021/acsomega.9b04492.

[8] K.M. Koczkur, S. Mourdikoudis, L. Polavarapu, S.E. Skrabalak, Polyvinylpyrrolidone (PVP) in nanoparticle synthesis, Dalton Transactions 44 (2015) 17883–17905. https://doi.org/10.1039/C5DT02964C.

[9] B. Ajitha, Y.A. Kumar Reddy, P.S. Reddy, H.-J. Jeon, C.W. Ahn, Role of capping agents in controlling silver nanoparticles size, antibacterial activity and potential application as optical hydrogen peroxide sensor, RSC Adv 6 (2016) 36171–36179. https://doi.org/10.1039/C6RA03766F.

[10] R. Javed, M. Zia, S. Naz, S.O. Aisida, N. ul Ain, Q. Ao, Role of capping agents in the application of nanoparticles in biomedicine and environmental remediation: recent trends

and future prospects, J Nanobiotechnology 18 (2020) 172. https://doi.org/10.1186/s12951-020-00704-4.

[11] Z. Zhang, Z. Wang, S. He, C. Wang, M. Jin, Y. Yin, Redox reaction induced Ostwald ripening for size- and shape-focusing of palladium nanocrystals, Chem Sci 6 (2015) 5197–5203. https://doi.org/10.1039/C5SC01787D.

[12] R.G. Mortimer, 8 - The Thermodynamics of Chemical Equilibrium, in: R.G. Mortimer (Ed.), Physical Chemistry (Second Edition), Academic Press, Burlington, 2000: pp. 255–289. https://doi.org/https://doi.org/10.1016/B978-012508345-4/50011-3.

[13] G.I.N. Waterhouse, G.A. Bowmaker, J.B. Metson, The thermal decomposition of silver (I, III) oxide: A combined XRD, FT-IR and Raman spectroscopic study, Physical Chemistry Chemical Physics 3 (2001) 3838–3845. https://doi.org/10.1039/b103226g.

[14] C. Wang, H. Tatsumi, L. Xu, T. Zhao, P. Zhu, R. Sun, H. Nishikawa, Transparent Liquid Ag-Based Complex for the Facile Preparation of Robust Sintered Ag Joints in Power Devices, ACS Appl Electron Mater (2024). https://doi.org/10.1021/acsaelm.3c01629.

[15] W. Yang, C. Liu, Z. Zhang, Y. Liu, S. Nie, One step synthesis of uniform organic silver ink drawing directly on paper substrates, J Mater Chem 22 (2012) 23012–23016. https://doi.org/10.1039/C2JM34264B.

[16] J.E. House, Chapter 11 - Chemistry of Metallic Elements, in: J.E. House (Ed.), Inorganic Chemistry (Second Edition), Academic Press, 2013: pp. 337–373. https://doi.org/https://doi.org/10.1016/B978-0-12-385110-9.00011-X.

Chapter 4: Low-temperature bonding performance and substrate-dependent bonding mechanism of Ag nanostructures

4.1 Introduction

This dissertation used Ag nanostructures as intermedia for preparing Ag sintered joints. The bonding performance of die-attach materials is important in the formation of robust Ag sintered joints [1]. Chapter 2 and Chapter 3 demonstrated that substrate significantly affects the morphology and gradients of Ag nanostructures. However, the effect of substrate on the bonding performance remains unclear.

This study investigated the effect of the substrate on the bonding behaviors of Ag nanostructures using four common substrates (Au, Ag, Al, and Cu). The Ag nanostructures deposited on each substrate were bonded at a low temperature range (160–220 °C) to form Ag sintered joints. Consequently, the bonding mechanisms of Ag nanostructures on Au, Ag, Al, and Cu substrates were investigated. Additionally, the effect of the substrate on the bonding mechanism was evaluated by measuring the shear strengths of the Ag sintered joints.

4.2 Materials and methods

4.2.1Materials

Silver acetate (99%, FUJIFILM), 2-amino-2-methyl-1-propanol (FUJIFILM), distilled

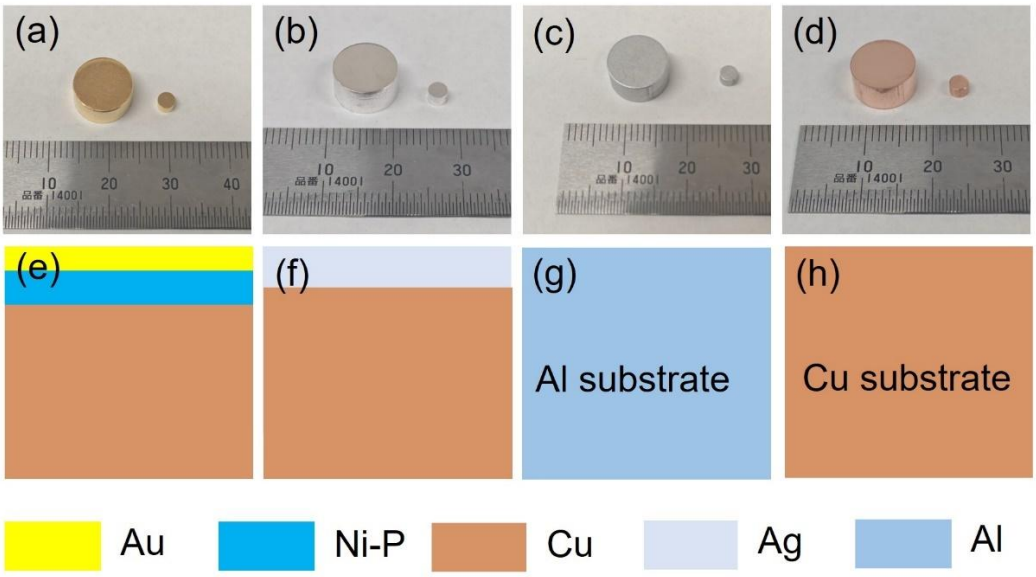

Fig. 4.1 Detailed information of substrates. Optical images of (a) Au, (b) Ag, (c) Al, and (d) Cu substrates. Schematic diagram illustrating the structure of (e) Au, (f) Ag, (g) Al, and (h) Cu substrates.

water and ethanol were directly used without purification. **Fig. 4.1** details the information of the substrate used in this study. As shown in **Fig. 4.1a-d**, electroless nickel immersion gold (ENIG), Ag, Cu (C1020, 99.96%), and Al (A1050, 99.50%) with a diameter of 10 mm and 3 mm were used as dummy substrate and die, respectively. For the ENIG substrate in **Fig. 4.1e**, the top surface of the Cu base was finished in turn with 2 μm Ni-P and 80 nm Au. Therefore, the ENIG substrate in this study was considered the Au substrate. For the Ag substrates in **Fig. 4.1f**, an Ag layer of approximately 4 μm was electroplated on the Cu substrate. **Fig. 4.1g** and **4.1h** demonstrate that the Al and Cu substrates in this study were pure metal. The substrates underwent ultrasound cleaning in ethanol for 9 min before use.

4.2.2 Preparation of Ag nanostructures and Ag sintered joints

Fig. 4.2 depicts the preparation of the Ag nanostructures. As shown in **Fig. 4.2a**, the Ag

nanostructures were prepared following the same conditions as in Chapter 3. First, 60 mg and 10 mg Ag-based complexes were printed on the top surface of the dummy substrate and die, respectively. Subsequently, they were subjected to a two-stage heating profile of 90 ºC 5min and 180 ºC 30 min. The optical images of the Ag-based complex and obtained Ag nanostructure on the four substrates are depicted in **Fig. 4.2b-e** and **4.2f-i**, respectively. The Ag nanostructures on the Au, Ag, Al, and Cu substrates were named NS-Au, NS-Ag, NS-Al, and NS-Cu, respectively. As depicted in **Fig. 4.3a**, the Ag nanostructure on the die was

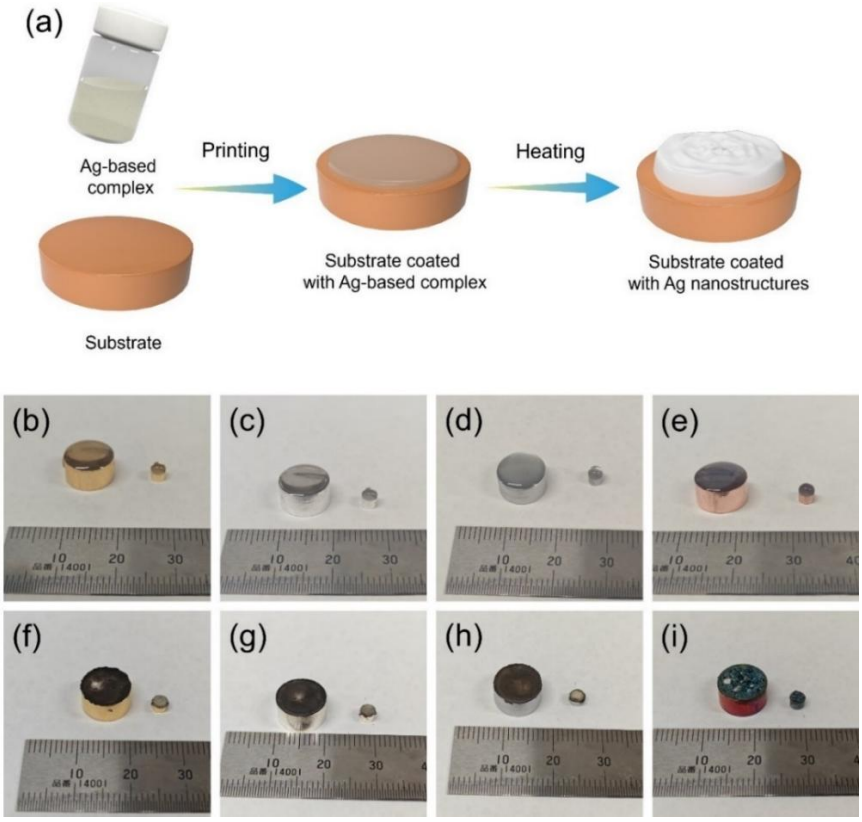

Fig. 4.2 Details of the preparation of Ag nanostructure. (a) Schematic diagrams of the fabrication of Ag nanostructures derived from the Ag-based complex. Optical image of (b) Au, (c) Ag, (d) Al and (e) Cu substrate coated with Ag-based complex. Optical image of Ag nanostructures on the (f) Au, (g)Ag, (h) Al, and (i) Cu substrate.

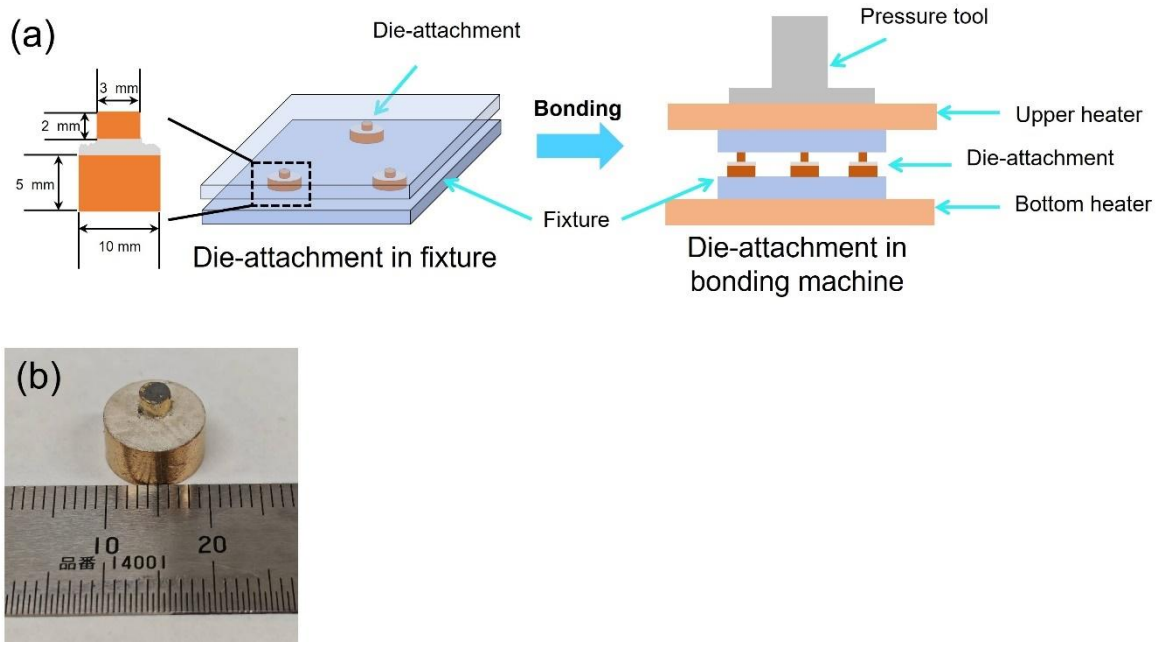

Fig. 4.3 Preparation of Ag sintered joints. (a) Schematic diagrams depicting the preparation of Ag sintered joints. (b) Optical image of representative Ag sintered joints.

flipped over that on the substrate to obtain die-attachment. Three die attachments were placed in a fixture to distribute the pressure uniformly. The die-attachments were bonded at a low-temperature range of 160–220 ºC with 5 MPa for 10–60 min to prepare the Ag sintered joints in the air. **Fig. 4.3b** depicts the optical image of a representative Ag sintered joint.

4.2.3 Characterization

The Ag sintered joints were prepared using a bonding machine (RB-100D, Ayumi Industry Co. Ltd). Shear tests were conducted using a die-shear tester (STR-1000, Rhesca). The cross-section was polished using a cross-section ion polishing machine (IB-19530CP, JEOL). The microstructure and element distribution of the Ag sintered joints were analyzed using a field-emission scanning electron microscope (FE-SEM, FEI Nova Nana SEM 450) equipped with an energy-dispersive spectrometer (EDS). The structure and phase of the fracture surface of

Ag sintered joints were confirmed by X-ray diffraction (XRD, Ultima IV, Rigaku). An in-depth understanding of the bonding behaviors of NS-Au, NS-Al, and NS-Cu were obtained using transmission electron microscopy (TEM, FEI Tecnai G2 F20).

4.2.4 Measurement of porosity ratio

The measurement of the porosity ratio and bonding ratio is depicted in **Fig. 4.4**. **Fig. 4.4a** presents an SEM image of a sintered Ag layer. The porosity of the sintered Ag we quantified by a binary image segmentation process using ImageJ. In this binary image, black areas represent pores. The porosity ratio of the sintered Ag was calculated using Equation 4.1:

$$P = A_b/A_t \times 100\% \quad 4.1$$

where P is the porosity ratio, A_b is the total area of the pores, and A_t is the area of the sintered

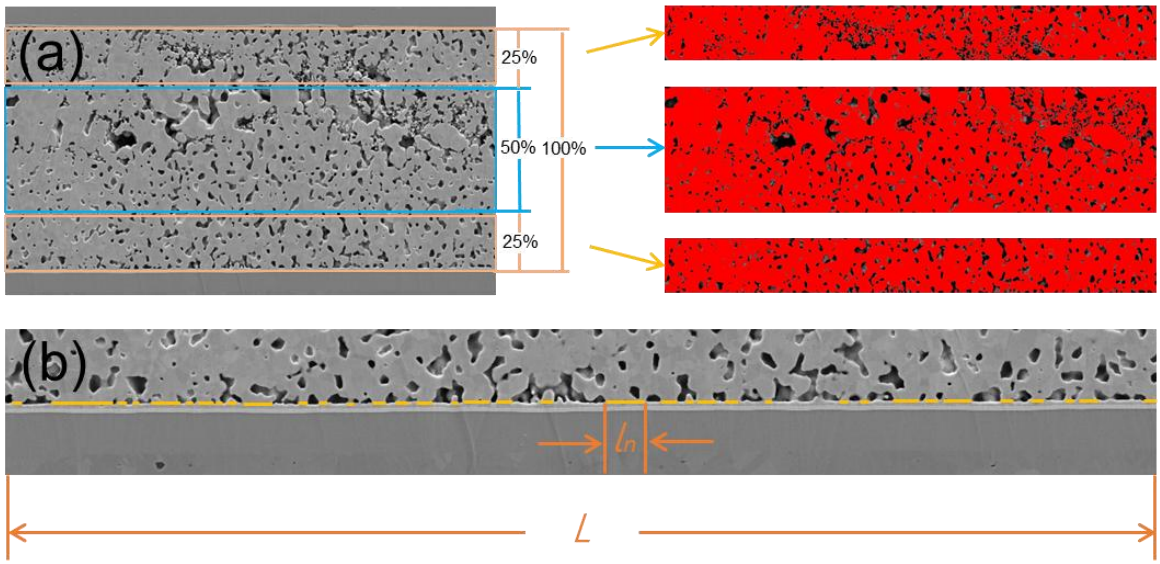

Fig. 4.4 Sample characterizations. SEM images illustrating the measurement of (a) the porosity ratio of Ag sintered joints and (b) the bonding ratio between the sintered Ag layer and substrate.

Ag. The porosity ratio of the Ag sintered joints was determined by calculating three kinds of porosity ratios depending on the position as shown in **Fig 4.4a**: average porosity ratio from 100 % of the sintered Ag, mid porosity ratio from 50 % in the middle of the sintered Ag layer, and edge porosity ratio from 25% + 25% on both sides of the sintered Ag layer.

4.2.5 Measurement of bonding ratio

Fig. 4.4b depicts the formation of necks at the interface between the sintered Ag and substrate. These necks provide mechanical strength at the interface and are therefore valid bonding areas. The bonding ratio was expressed by Equation 4.2:

$$C = \sum l_n / L \times 100\% \qquad 4.2$$

where C is the bonding ratio, l_n is the neck diameter, and L is the total interface length.

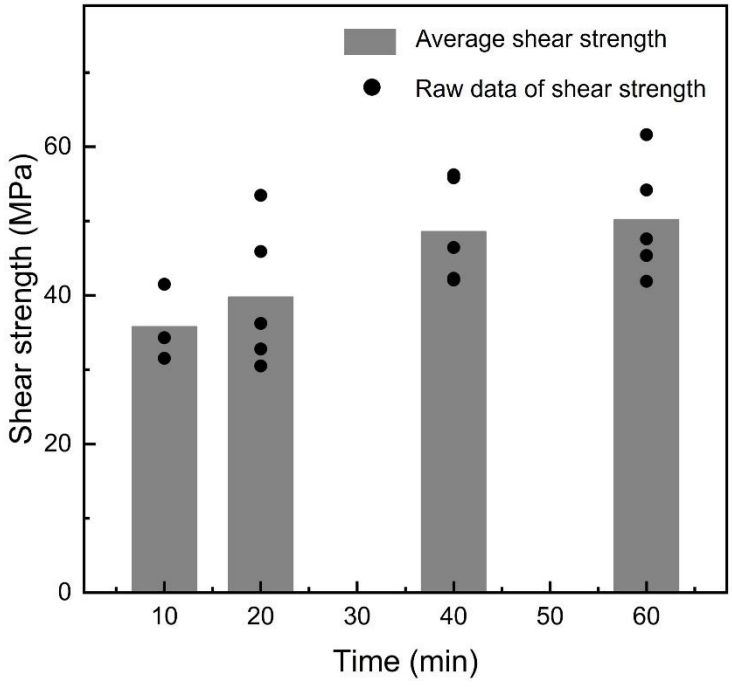

Fig. 4.5 Evolution of shear strength with bonding time.

4.3 Results and discussion

4.3.1 Effect of bonding time

The feasibility of using an Ag-based complex as a die-attach material was successfully confirmed in Chapter 2. However, the effects of bonding time on shear strength remain unclear. Herein, the NS-Au was bonded at a low temperature of 200 ^{o}C with 5 MPa for 10, 20, 40, and 60 min. **Fig. 4.5** shows the evolution of shear strength with bonding time. As depicted in **Fig. 4.5**, an average shear strength of 35.8 MPa was obtained for a short bonding time of 10 min. In addition, the shear strength increased with the increase of bonding time, and a maximum shear strength of 50.2 MPa was obtained at 60 min.

The morphology information of sintered Ag, such as neck and pore, plays an important role in determining the shear strength of Ag joints [2–4]. Therefore, the cross-sections of Ag joints were observed, and the porosity ratio and bonding ratio were calculated based on the cross-section by Image-J. **Fig. 4.6** shows the cross-section of Ag sintered joints derived from different bonding times. **Fig. 4.7** depicts the evolution of the porosity ratio and bonding ratio with bonding time. As depicted in **Fig. 4.6a-c**, the loose region in the sintered Ag layer became smaller with the longer bonding time. Furthermore, the length of necks between Ag particles continuously increased as the bonding time increased from 10 min in **Fig. 4.6a$_1$** to 40 min in **Fig. 4.6b$_1$**. After densification, the Ag nanostructures were sintered into a dense Ag joint with round pores at 60 min in **Fig. 4.6c$_1$** [2]. As the sintering of Ag nanoparticles (NPs) is a process of Ag atom diffusion [1], the prolonged time contributed to the efficient diffusion and allowed more activated Ag atoms to participate in the bonding process [5].

Correspondingly, these morphological changes decreased the porosity ratio from 24.4% to 2.6% in **Fig. 4.7a**. The necks between sintered Ag and Au substrate in **Fig. 4.6i-l** became thicker with a longer bonding time, increasing the bonding ratio in **Fig. 4.7b**. In addition, poly-dispersed Ag particles were observed in **Fig. 4.6a$_1$** and **a$_2$**, and their role in the Ag nanostructure bonding will be discussed in the following section. In summary, the prolonged bonding time promoted Ag nanostructure bonding, facilitated robust joint formation, and increased the shear strength as shown in **Fig. 4.5**.

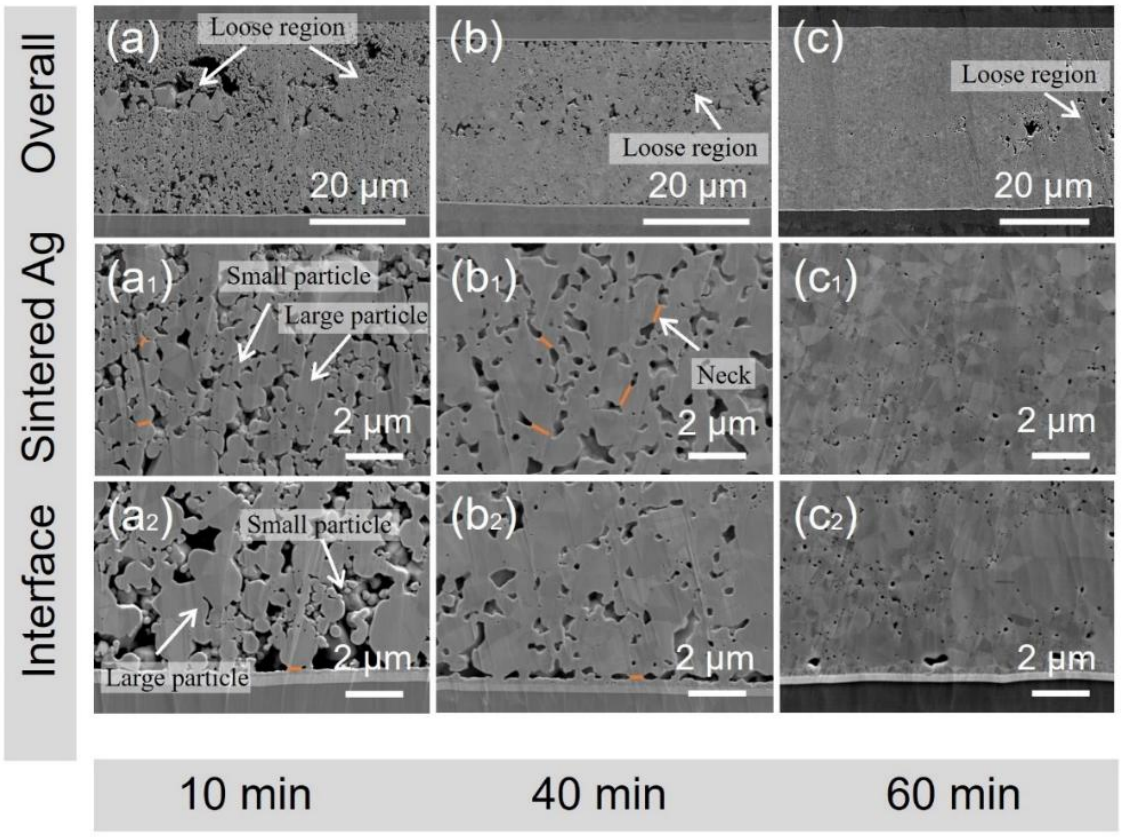

Fig. 4.6 Microstructures of cross-sections of Ag sintered joints derived from NS-Au at 200 ^{o}C with 5 MPa for 10, 40, and 60 min. SEM images of the cross-section of Ag joints derived from different bonding times: (a)-(a$_2$) 10, (b)-(b$_2$) 40, and (c)-(c$_2$) 60 min.

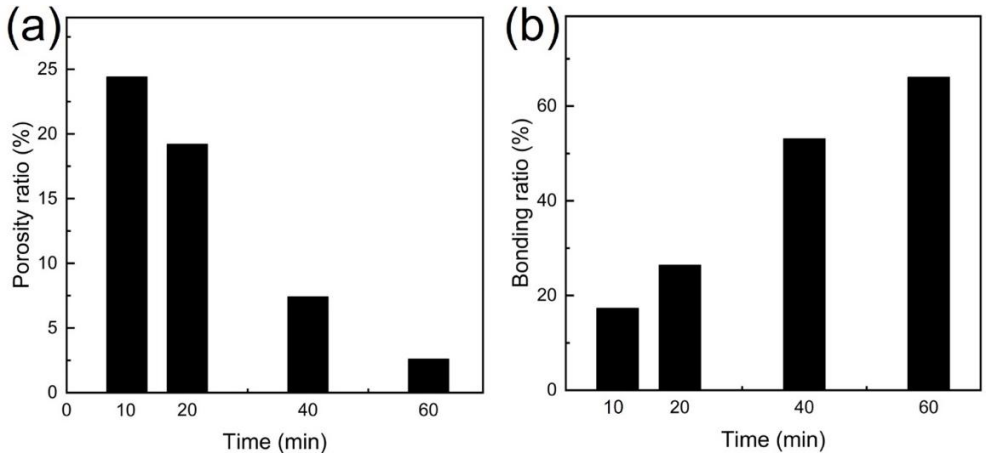

Fig. 4.7 Cross-section information. Evolution of (a) porosity ratio and (b) bonding ratio with the bonding time.

The responsible mechanism for the increase of shear strength in **Fig. 4.5** was revealed by characterizing the surface morphology after the die-shear test using fracture-surface observation. **Fig 4.8** depicts the fracture surfaces of the Ag sintered joints derived from different bonding times, and a schematic diagram in **Fig. 4.9** was drawn to enhance the understanding of the fracture surface. According to the overall views of the substrate side in **Figs. 4.8a-c** and die side in **Figs. 4.8a$_1$-c$_1$**, the fracture occurred at the interface region and inside the sintered Ag layer during the die-shear tests. Therefore, three typical fracture regions in **Fig. 4.9a**, such as the ENIG substrate side (I), inside sintered Ag (II), and sintered Ag side (III), were observed to comprehensively reveal the information of fracture surfaces. When the bonding time is 10 min, monodispersed ductile deformations and spherical Ag particles can be seen in **Figs. 4.8a$_{2\text{-}3}$**, indicating insufficient sintering within the Ag nanostructures. Monodispersed ductile fractures were observed into continuous ductile fractures, when the bonding time was over 40 min, and the amount of spherical Ag particles declined dramatically in **Fig. 4.8b$_{2\text{-}3}$** and **4.8c$_{2\text{-}3}$**. Ductile fractures and spherical Ag particles

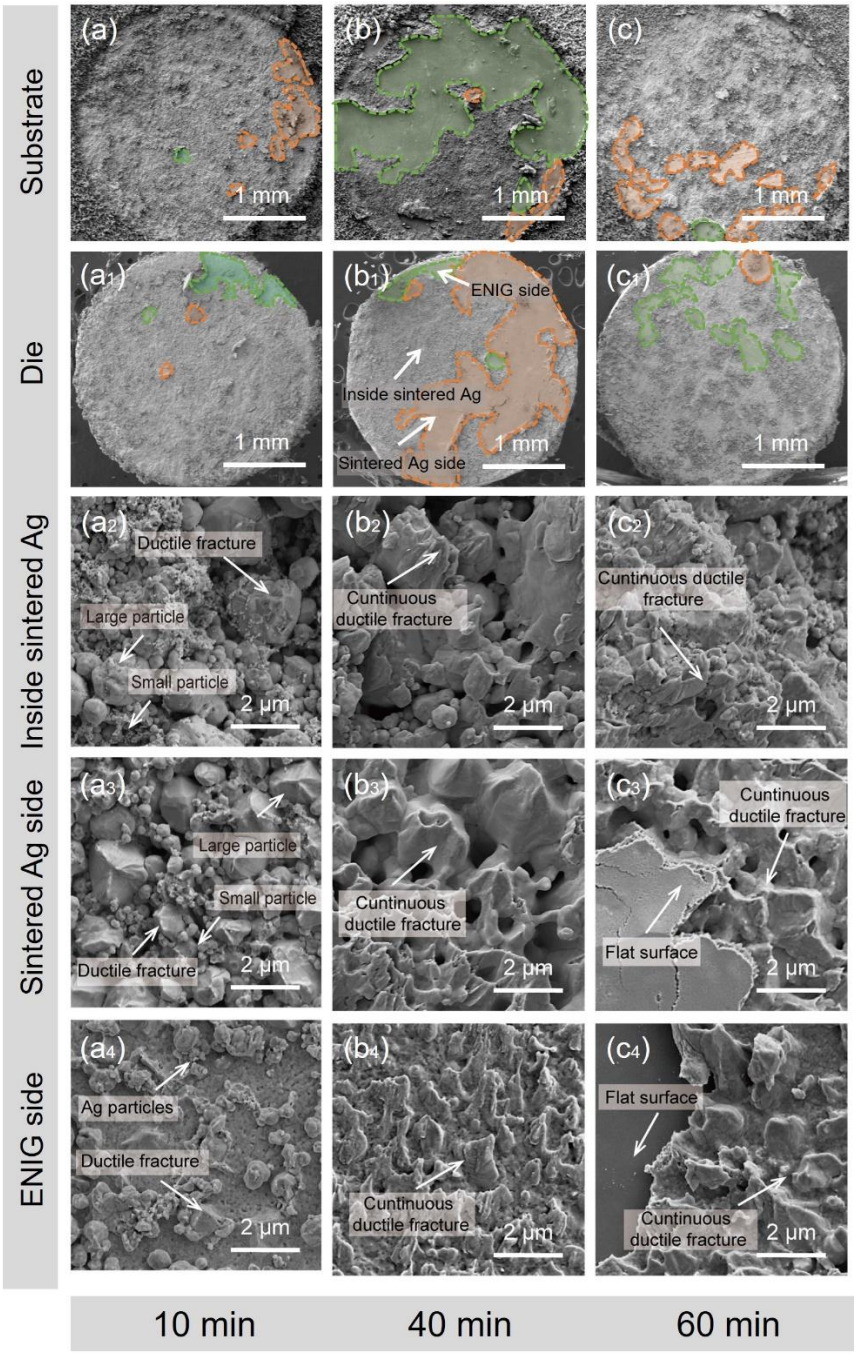

Fig. 4.8 Microstructures of fracture of Ag sintered joint derived from NS-Au at 200 °C with 5 MPa for 10, 40, and 60 min. SEM images depicting overall fracture surfaces (a)-(c) at substrate side and (a_1)-(c_1) die side. (a_2)-(c_2) Fracture surfaces inside the sintered Ag, (a_3)-(c_3) fracture surfaces at the sintered Ag side, and (a_4)-(c_4) fracture surfaces at the ENIG side for different times.

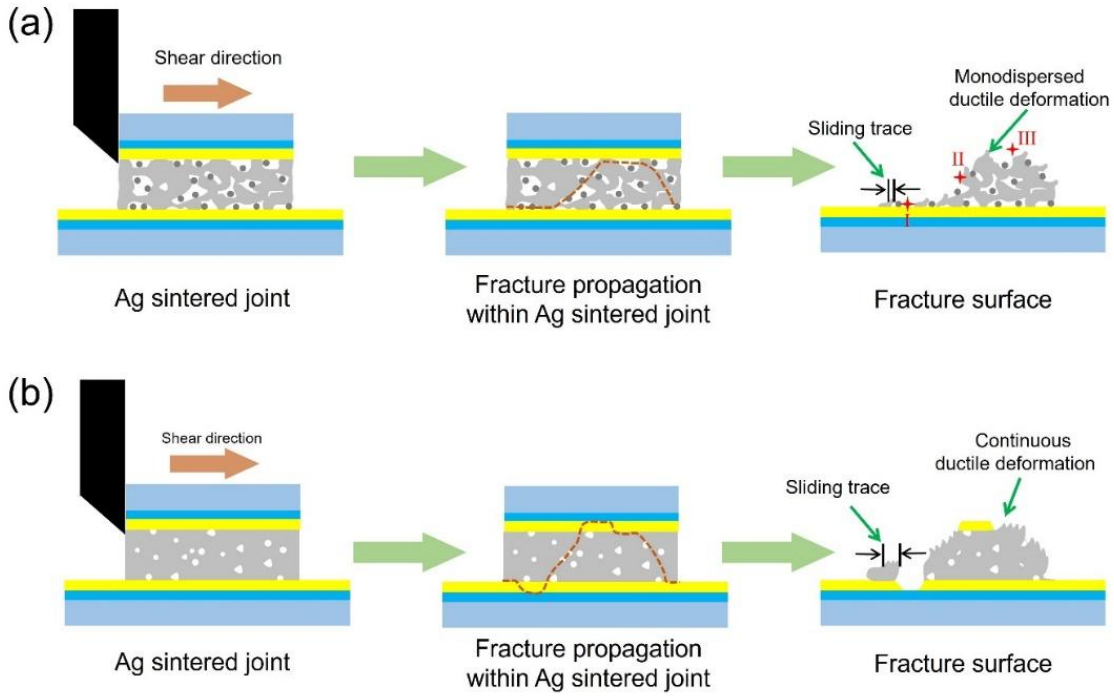

Fig. 4.9 Schematic diagram illustrating the fracture behaviors of (a) insufficiently and (b) sufficiently sintered Ag nanostructures.

left on the substrate side in **Fig. 4.8a$_4$** and **Fig. 4.9a** were converted into continuous ductile fractures in **Fig. 4.8b$_4$**, **c$_4$** and **Fig. 4.9b**. The results indicated that a longer bonding time promoted the sintering of Ag nanostructures, increasing the shear strength in **Fig. 4.5** [6].

In addition to ductile fractures, flat fracture surfaces were observed in **Fig. 4.8c$_{3\text{-}4}$**. EDS was conducted to identify the flat surfaces in **Fig. 4.8c$_3$** and **4.8c$_4$**. **Fig. 4.10** depicts the element distribution of the flat surface of the sintered Ag side and ENIG substrate side. The high intensity of the element Au in **Fig. 4.10b** indicated that the flat surface in **Fig. 4.8c$_3$** was the Au layer of the ENIG substrate. At the position of the flat surface in **Fig. 4.10f**, high-intensity Ni and P were detected in **Fig. 4.10i** and **4.10j**, indicating that the flat surface in **Fig. 4.8c$_4$** was the Ni-P layer of the ENIG substrate. This observed phenomenon indicated the

bonding strength between sintered Ag and the Au layer was sufficient to strip the Au layer from the Ni-P layer during the die-shear test, which confirmed the excellent bonding performance of NS-Au.

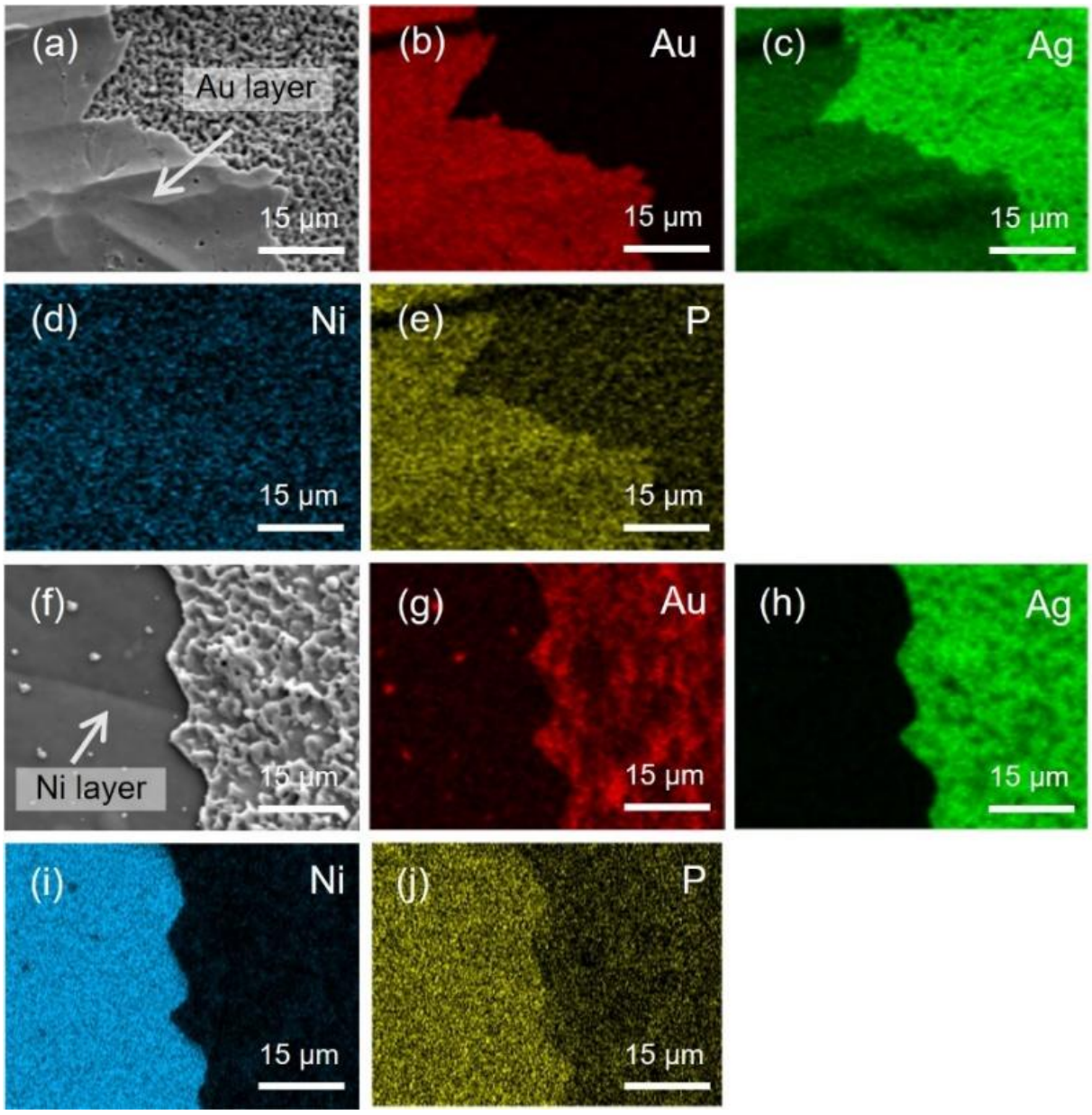

Fig. 4.10 EDS element maps of fracture surface derived from NS-Au at 200 °C with 5 MPa for 60 min at (a)-(e) sintered Ag side and (f)-(j) ENIG substrate side.

4.3.2 Effects of substrates on the bonding performance of Ag nanostructures

According to the results in Chapter 2 and Chapter 3, the substrate substantially influences the morphology and elemental composition of the Ag nanostructures. However, the mechanism by which these factors govern bonding characteristics remains unclear. To address this knowledge gap, the Ag nanostructures were bonded in the 160–220 °C range. Additionally, the shear strength shown in **Fig. 4.5** only increased slightly from 48.6 MPa to 50.2 MPa when the bonding time increased from 40 min to 60 min. Therefore, the bonding time in the following experiments was set to 40 min. Subsequently, the bonding performance of the prepared Ag sintered joints was evaluated using die-shear tests to quantify the joint strength. **Fig. 4.11** shows the evolution results of shear strength with substrate and bonding temperature. **Fig. 4.11a** depicts a significant variation in the shear strength of the Ag sintered joints for each temperature, which could be attributed to the different substrate materials. Furthermore, the shear strength of the Ag sintered joints with the four substrates generally increased with increasing temperatures. Notably, the Ag sintered joints derived from NS-Au exhibited the highest shear strength under the same bonding conditions. The obtained shear strength of 31.1 MPa at 160 °C demonstrated the remarkable low-temperature bonding capability of NS-Au.

The advantage of low-temperature bonding, a comparison of the shear strengths between Ag nanostructure and Ag paste is shown in **Fig. 4.11b** [7–12]. NS-Au demonstrated the best bonding performance, and 48.6 MPa in shear strength of bonded Ag nanostructures at 200 ^{o}C was approximately three times higher than that of bonded Ag paste in previous reports [10]. At a lower temperature at of 160 ^{o}C, the Ag paste hardly formed an Ag sintered

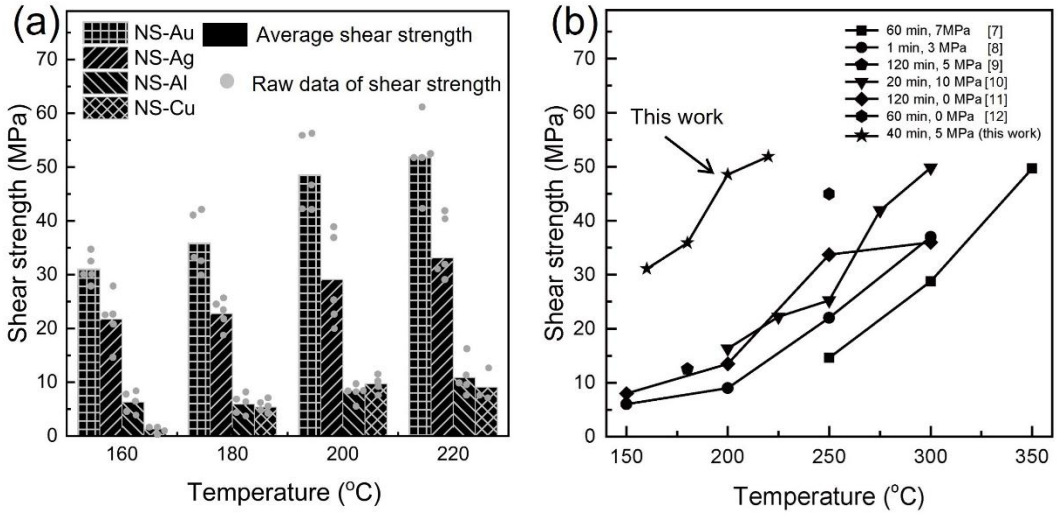

Fig. 4.11 Shear strength of Ag sintered joints at different temperatures. (a) Shear strength of Ag sintered joints derived from NS-Au, NS-Ag, NS-Al, and NS-Cu bonded at 160–220 °C. (b) Comparison of shear strength between bonded NS-Au and previous sintering Ag techniques.

joint with a shear strength over 10 MPa, as 160 °C is even lower than the boiling point of some commonly used organics in Ag paste, such as 288 °C of triethylene glycol [8], 217 °C of terpineol [8], and 340 °C of polyvinyl pyrrolidone (PVP) [10]. By contrast, nanostructures achieved a shear strength of 37.7 MPa at 160 °C. These excellent joint properties indicated the superior low-temperature bonding properties of NS-Au.

4.3.3 Ag sintered joints derived from NS-Au

As shown in **Fig. 4.12**, the evolution of shear strength with bonding temperature was revealed by SEM observation of the cross-sections of Ag sintered joints derived from NS-Au at 160 to 220 °C. **Fig. 4.12a-d** depicted that the Ag sintered joints were composed of two distinct areas: (I) a well-sintered area and (II) a loose area. The well-sintered area was close

to the interface between the Ag sintered layer and the substrate, and the loose area was close to the center of the Ag sintered layer. The loose area was reduced noticeably as the temperature increased from 160 to 220 ^{o}C. As shown in **Fig. 4.12a$_1$-d$_1$** the reduction in the loose area could be attributed to the gradual absorption of Ag NPs in the loose area by the well-sintered area. In addition, the loose area could be considered a defect area in the Ag sintered layer because a larger number of isolated Ag NPs were observed under high magnification view in **Fig.4.12a$_1$-d$_1$**.

Unlike isolated Ag NPs in the loose area, poly-dispersed Ag particles were observed in the well-sintered area of **Fig. 4.12a$_2$** and **b$_2$**, when the bonding temperatures were 160 ^{o}C and 180 ^{o}C. In these poly-dispersed Ag particles, small particles filled the interspaces of large particles, increasing the stacking density for bonding. Necks between large particles were evident, which meant that interconnections inside the Ag sintered layer were initially established. Like the human skeleton, these well-connected large particles provided strength support for the Ag sintered joints, resulting in a shear strength of 31.1 MPa at a low temperature of 160 ^{o}C. This result meant that appropriate temperatures are important in triggering the sintering of Ag NPs [13]. As the bonding temperature increased to 200 ^{o}C, these poly-dispersed particles were converted into a continuous porous structure with thick necks in **Fig. 4.12c$_2$**. As shown in **Fig. 4.12d$_2$**, a dense Ag sintered layer with isolated round pores was obtained at 220 ^{o}C and the corresponding shear strength reached the maximum value of 51.9 MPa. These morphology changes were attributed to the elevated bonding temperature promoting mass transport, such as surface diffusion, responsible for sintering [14,15]. In terms of the interface area shown in **Fig. 4.12a$_3$-d$_3$**, the sintered Ag side

demonstrated similar morphological changing behaviors, and no apparent change was detected on the metallization layer of the substrates. However, the necks between the Ag sintered layer and substrate thickened with increasing temperatures, which could contribute to the increased shear strength with the increased bonding temperature.

As shown in **Fig. 4.12a-d**, the well-sintered area and the loose area were close to the edges and center of the Ag sintered layer, respectively. Therefore, three kinds of porosity ratios were calculated according to their position in the cross-section. **Fig. 4.13** presents the evolution of the porosity ratio and bonding ratio with the bonding temperature. **Fig. 4.13a** shows a noticeable reduction in porosity ratio when the bonding temperature increased from 160 ^{o}C to 220 ^{o}C. This could be attributed to the fact that the increased bonding temperature promoted the sintering of Ag nanostructures, translating the porous Ag sintering joint into a dense one [14,15]. Additionally, the porosity ratio difference between the edge area and mid region also reduced with the increasing bonding temperature. This was because the isolated Ag particles of the loose area were gradually absorbed by the well-sintered area, which converted the loose area into a well-sintered area. **Fig. 4.13b** demonstrated that the bonding ratio of Ag sintered joints increased with the increased bonding temperature. This result was because the necks between the sintered Ag layer and ENIG substrate thickened as the bonding temperature increased from 160 ^{o}C to 200 ^{o}C. The results of **Fig. 4.13** indicated that the connections within the sintered Ag layer and at the interface were promoted by the increasing temperature, which increased the shear strength shown in **Fig. 4.11a**. In summary, the increased temperature results in an increase in shear strength by reducing the loose area,

converting the poly-dispersed Ag particles into dense Ag sintered joints, and promoting the connection between sintered Ag and substrates.

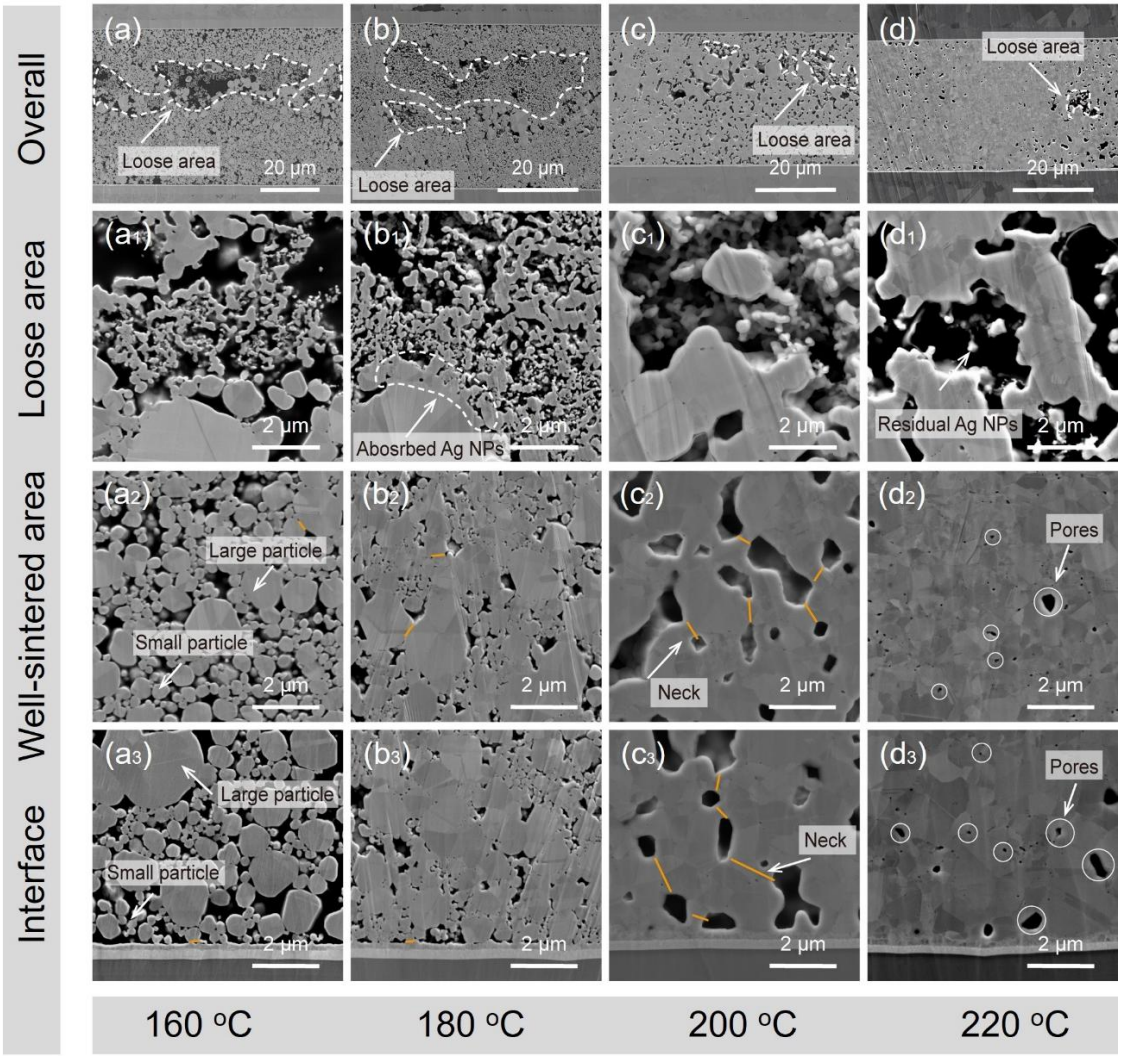

Fig. 4.12 Microstructures of the cross-sections of Ag joints derived from NS-Au with different bonding temperatures. SEM images showing (a)-(d) overall cross-sections, (a_1)-(d_1) loose area of cross-sections, (a_2)-(d_2) well-sintered area of cross-sections, and (a_3)-(d_3) interface of cross-section of Ag sintered joints at different temperatures.

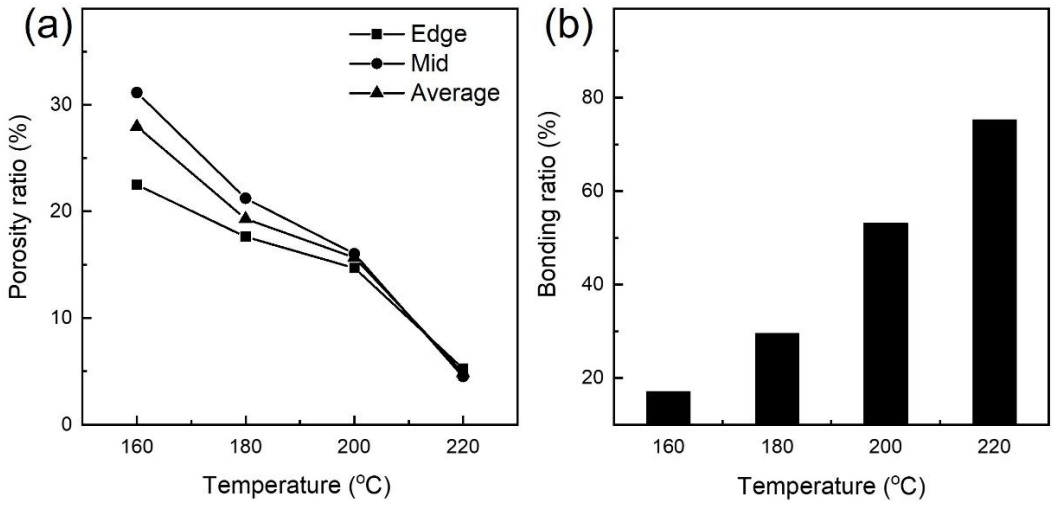

Fig. 4.13 Joint information from cross-sections of Ag sintered joints derived from NS-Au. Evolution of (a) porosity ratio and (b) bonding ratio with the bonding temperature.

The results in **Fig. 4.12** show that the poly-dispersed Ag particles were important in the bonding of NS-Au. Representative SEM images were selected to depict these poly-dispersed Ag particles, and a schematic diagram was drawn to illustrate their sintering behaviors. **Fig. 4.14** depicts the poly-dispersed Ag particles in a cross-section of Ag sintered joints obtained at 180 ^{o}C. **Fig. 4.15** presents a schematic diagram illustrating the sintering of the poly-dispersed Ag particles. As shown in **Fig. 4.14**, stacking larger particles in the red dotted circles resulted in large interspaces, and the small particles filled the interspaces of the large particles, enhancing the packing density of the particles for sintering. Furthermore, small particles are more prone to sintering because of their high surface energy [16]. Consequently, these small particles in **Fig. 4.15a** first underwent sintering and established contact with neighboring particles, resulting in an interlinked network shown in **Fig. 4.15b**. The interlinked network in **Fig. 4.14** indicated that small particles exhibited a position-dependent sintering behavior (I) merging at the center of interspaces, (II) being absorbed next to the

large particles, and (III) forming necks between the large particles. The merged small Ag particles occupied the interspaces, increasing stacking density. Due to Ostwald ripening, small particles close to large particles were absorbed [17], increasing the volume of the large particles and strengthening the interlinked network. The small particles between large particles were transformed into necks between the large particles, which increased the connection within the interlinked network. The results indicated that internal connections were initially established inside the Ag sintered joints, resulting in remarkable low-temperature bonding performance. In addition to acting as necks to strengthen the Ag sintered joints, small Ag particles provide diffusion pathways for Ag atoms during bonding [2,18]. These extensive diffusion pathways enable the transformation of the interlinked network into a dense Ag sintered layer shown in **Fig. 4.15c**.

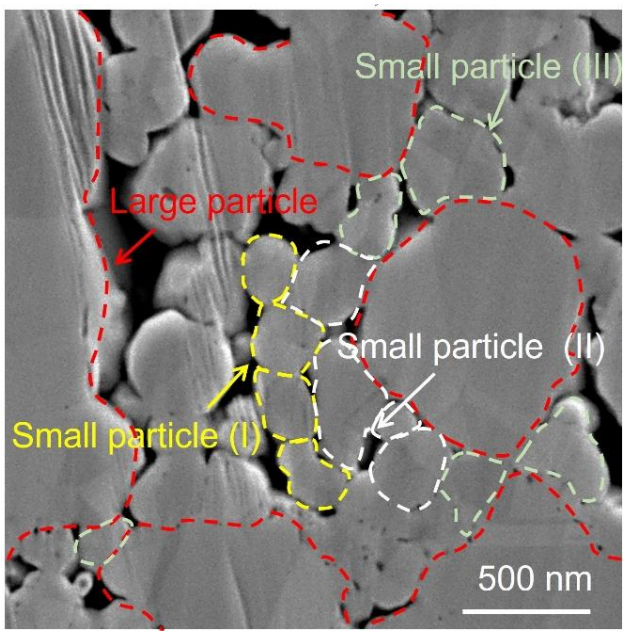

Fig. 4.14 Illustration of position-dependent sintering behavior of filler in the NS-Au (cross-section derived from bonded NS-Au at 180 °C)

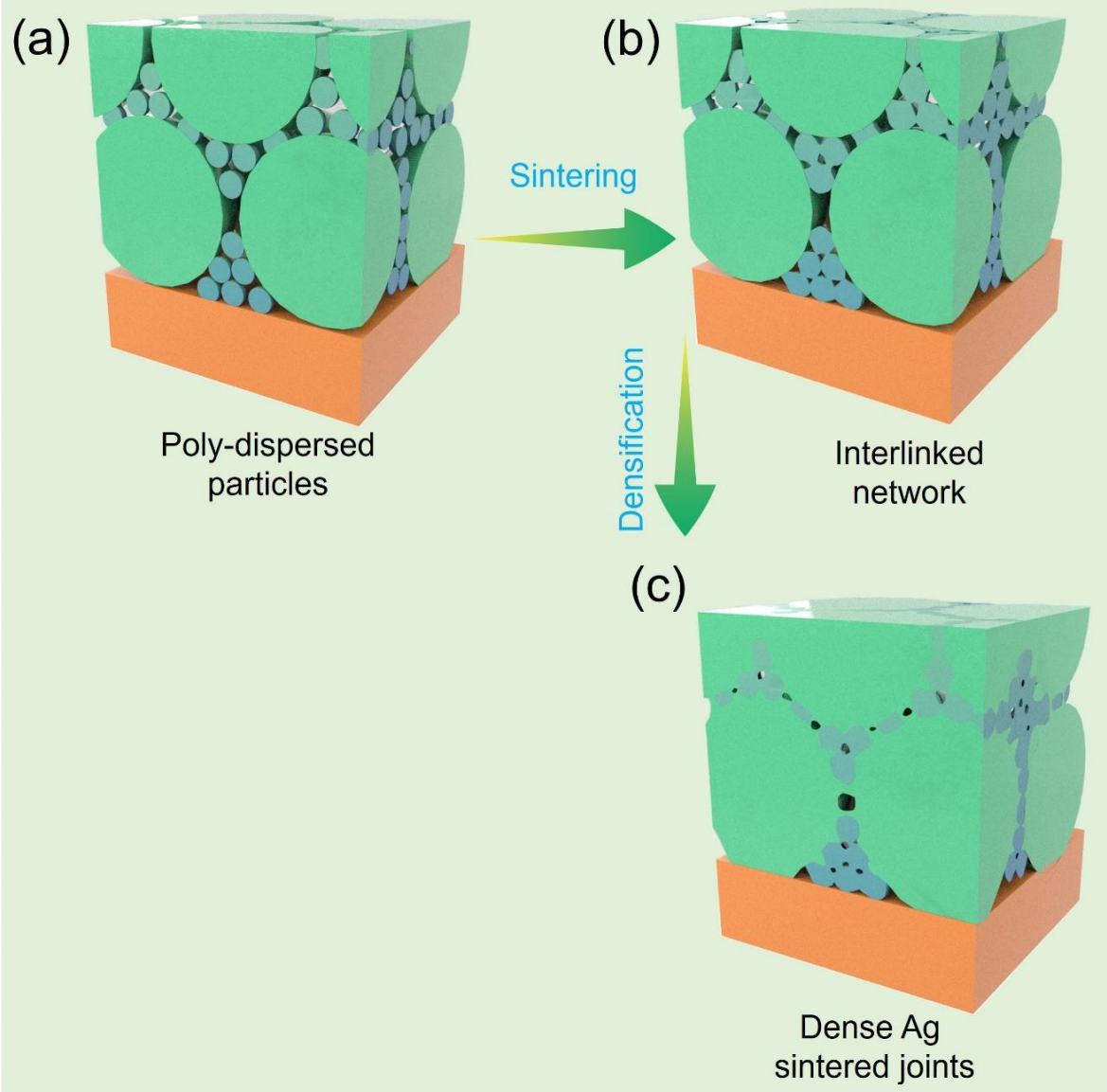

Fig. 4.15 Schematic diagram illustrating the sintering of poly-dispersed particles.

The fracture surfaces were observed to reveal the mechanism of shear strength evolution with temperature. **Fig. 4.16** depicts the fracture surface of Ag sintered joints derived from NS-Au at 160, 180, 200, and 220 ^{o}C. The low magnification fracture surfaces in **Fig. 4.16a-d** and **4.16a$_1$-d$_1$** demonstrated that the Ag sintered joints fractured both within the sintered

Ag layer and at the interface. When the bonding temperature was less than 200 ^{o}C, poly-dispersed particles and monodispersed ductile fractures were detected in **Fig. 4.16a$_2$** and **4.16b$_2$**, and these fractures were located near the large particles. This result meant that the large particles in the interlinked network provided mechanical strength for the Ag sintered joints. As the temperature was over 200 ^{o}C, continuous ductile fractures were observed in **Figs. 4.16c$_2$** and **4.16d$_2$**. These continuous ductile fractures inside the sintered Ag layer indicated significantly enhanced Ag particle sintering within NS-Au [19].

Fractures at the interface resulted in two distinct fracture surfaces: I) Ag sintered layer with a uniform surface and II) ENIG substrate with residual Ag. As shown in **Fig. 4.16a$_3$-d$_3$** and **a$_4$-d$_4$**, monodispersed and small ductile fractures were converted to interconnected ductile fractures, which were similar to the morphology changes in **Fig. 4.16a$_2$-d$_2$**. This result indicated that the interconnection between the Ag sintered layer and substrate was strengthened from 160 to 220 ^{o}C. The results demonstrated that increasing the bonding temperature promoted the sintering of Ag nanostructures and increased shear strength in **Fig. 4.11a**. Furthermore, flat surfaces were observed in **Fig. 4.16d$_{3\text{-}4}$**. EDS analysis was conducted to figure out the two flat surfaces. **Fig.4.17** depicts the element distribution of the flat surface at the sintered Ag side and ENIG substrate side. Similar to **Fig. 4.8d$_{3\text{-}4}$**, the flat fracture surfaces in **Fig. 4.16d$_{3\text{-}4}$** were also attributed to the stripping of the Au layer from the Ni-P layer according to EDS mapping in **Fig. 4.17**.

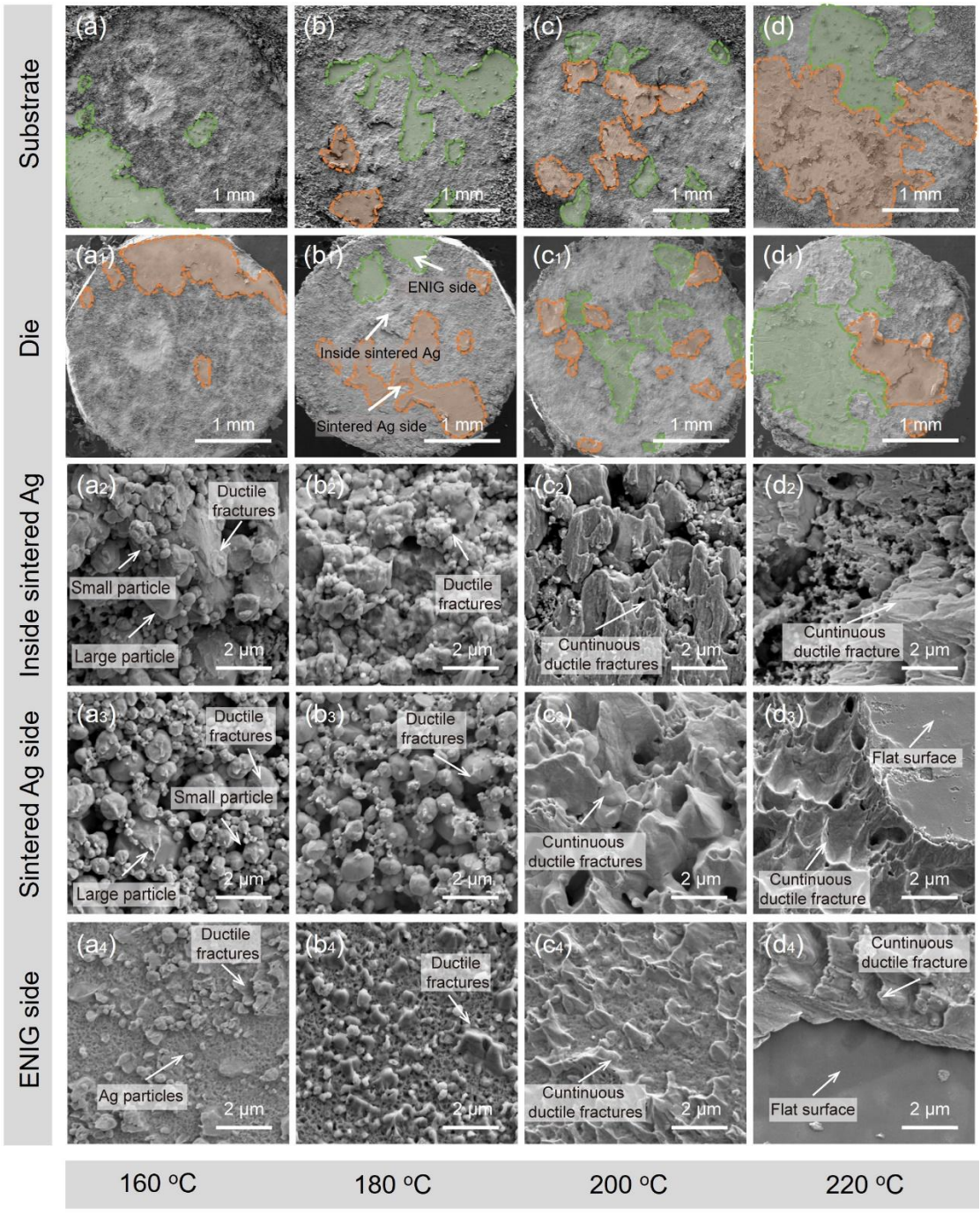

Fig. 4.16 Microstructures of the fracture surfaces of Ag joints derived from NS-Au with different bonding temperatures. SEM images showing overall fracture surfaces at (a)-(d) substrate side (a_1)-(d_1) die side, (a_2)-(d_2) fracture surfaces inside the Ag joints, (a_3)-(d_3) fracture surfaces at the Ag joint side, and (a_4)-(d_4) fracture surfaces at the ENIG side at different temperatures.

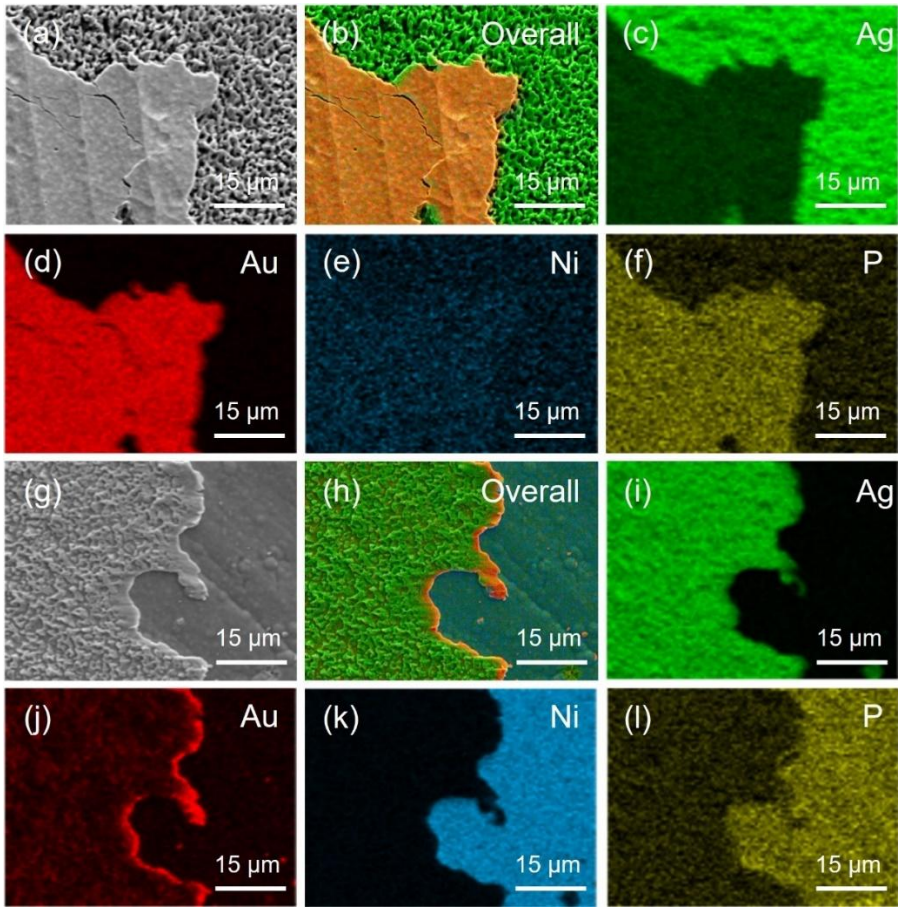

Fig. 4. 17 Element distribution of the fracture surface of Ag sintered joints derived from NS-Au at 220 ºC with 5 MPa for 40 min. EDS mapping at (a)-(f) the Ag joints side and (g)-(l) ENIG substrate side.

As shown in **Fig.4.18**, the reasons for the excellent joint properties were revealed through TEM of the Ag sintered joint derived from NS-Au at 200 ºC. As shown in **Fig. 4.18a**, massive grain boundaries were visible and randomly distributed in the Ag sintered joints. The fracture of bulk metal tends to propagate along the direction of the grain boundary [20]. Therefore, these randomly distributed grain boundaries can block the spread of fractures and complicate the propagation of fractures in one single direction, resulting in excellent joint properties. At the interface region in **Fig. 4.18b**, a distinct dense layer above the Au layer was observed,

and it can also be seen at the bottom NS-Au. This result indicated that the dense layer was generated during the thermal decomposition of the Ag-based complex. On the other hand, no pore was detected at the interface between the Au layer and this dense layer in **Fig. 4.18c**, suggesting an excellent connection between them.

The dense layer was examined using EDS analysis. **Fig. 4.18d** depicts the EDS line scan results at the interface. Ag and Ni were detected at the position of the Au layer, indicating the diffusion of Ag and Ni towards Au. This phenomenon indicated that the Au layer enhanced the bonding ability of the ENIG substrate [21]. In contrast, Au and Ag were not detected in the Ni layer, suggesting that the Ni layer successfully acted as a barrier to retard the contact between the Cu and die-attach material [22]. **Fig. 4.18d** shows that the dense layer could be divided into two layers according to the element content. The intensity of Ni decreased very slightly and reached equilibrium within the layer close to Au layer, indicating that the content of Ni was very low. Therefore, the layer close to the Au layer could be regarded as an Ag-Au mixing layer. The layer close to the sintered Ag shared the same Ag intensity as the sintered Ag, indicating that it could be a dense Ag layer. The results of the EDS maps in **Fig. 4.18e-h** agreed with that of the line scan results. In summary, the dense layer between the Au layer and sintered Ag consisted of an Ag-Au layer and Ag layer. Given the presence of Au and Ag, this dense layer could improve the affinity between the sintered Ag and Au layer. As a result, the connection between the Ag sintered layer and substrate was significantly improved, which was superior to than the connection between the Au layer and Ni-P layer when the bonding temperature was 220 ^{o}C. In summary, the randomly distributed

grain boundaries and automatically generated dense layer contribute to the excellent joint properties.

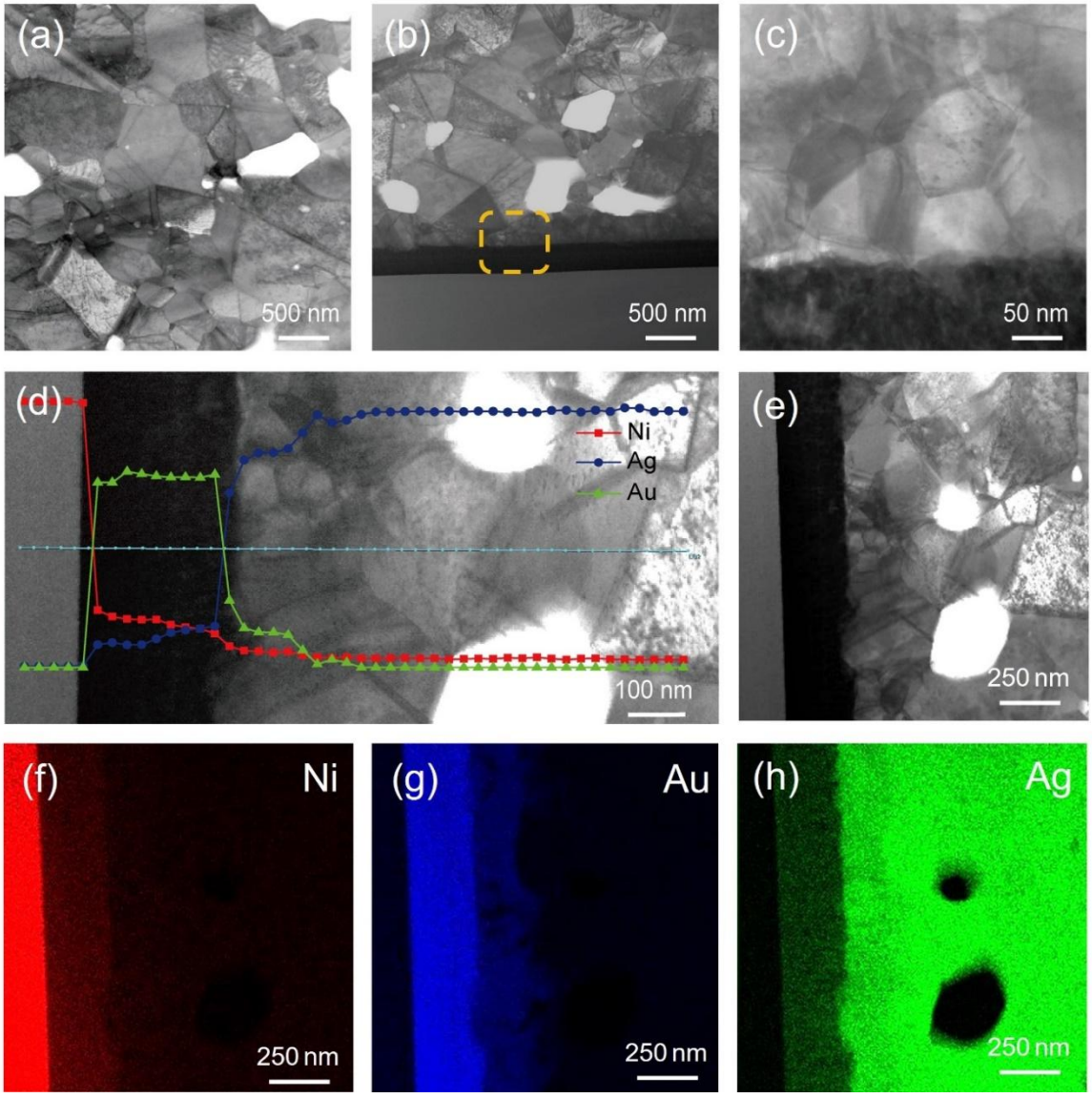

Fig. 4. 18 TEM characterization of the Ag sintered joint derived from NS-Au bonded at 200 °C with 5 MPa for 40 min. TEM images of (a) the sintered Ag and (b) the interface between the sintered Ag layer and substrate. (c) High magnification view of yellow quadrangle in (b). (d) EDS line scanning at the interface region. (e) TEM image of interface and corresponding EDS mapping of (f) Ni, (g) Au, and (h) Ag at the interface region.

4.3.4 Ag sintered joints derived from NS-Ag

Although the shear strength of Ag joints on the Ag substrate was lower than that on the Au substrate as shown in **Fig. 4.11a**, it was comparable to that of previous studies [10]. Therefore, the Ag joints derived from NS-Ag were characterized by cross-section and fracture surface observation. Based on the cross-section, the porosity ratio and bonding ratio of Ag sintered joints on the Ag substrate were calculated by Image-J. **Fig.4.19** presents the cross-section of the Ag sintered joints derived from NS-Ag at different bonding temperatures. **Fig. 4.20** depicts the evolution of the porosity ratio and bonding ratio of the Ag sintered joints with the bonding temperatures. The sintered Ag layers in **Fig. 4.19a-d** consisted of loose areas and well-sintered dense areas, and the loose area reduced apparently with the increasing bonding temperature. This morphology change within the Ag sintered layer in **Fig. 4.19a-d** was similar to that in **Fig. 4.12a-d**. This meant bonding conditions between the sintered Ag layer and substrate could be important in determining the shear difference in **Fig. 4.11a**. Therefore, the magnified cross-sections in **Fig. 4.19** focused on the interfacial morphology between the Ag sintered layer and Ag substrate. At the sintered Ag side, the morphological changes of sintered NS-Ag in **Fig. 19a$_1$-d$_1$** were similar to that of sintered NS-Au in **Fig.4.12a$_3$-d$_3$**, which increased the shear strength from 21.7 MPa to 33.1 MPa in **Fig. 4.11a** and reduced the average porosity ratio from 22.7% to 3.7% in **Fig. 4.20a**. In addition, the necks between the Ag sintered layer and Ag substrates thickened with the increasing bonding temperature, increasing the bonding ratio in **Fig. 4.20b**. However, compared with the well-bonded interface in **Fig. 4.12d$_3$**, visibly blurred boundaries within the necks in **Fig. 4.19d$_2$** indicated that the diffusion between the sintered Ag and Ag substrate was insufficient.

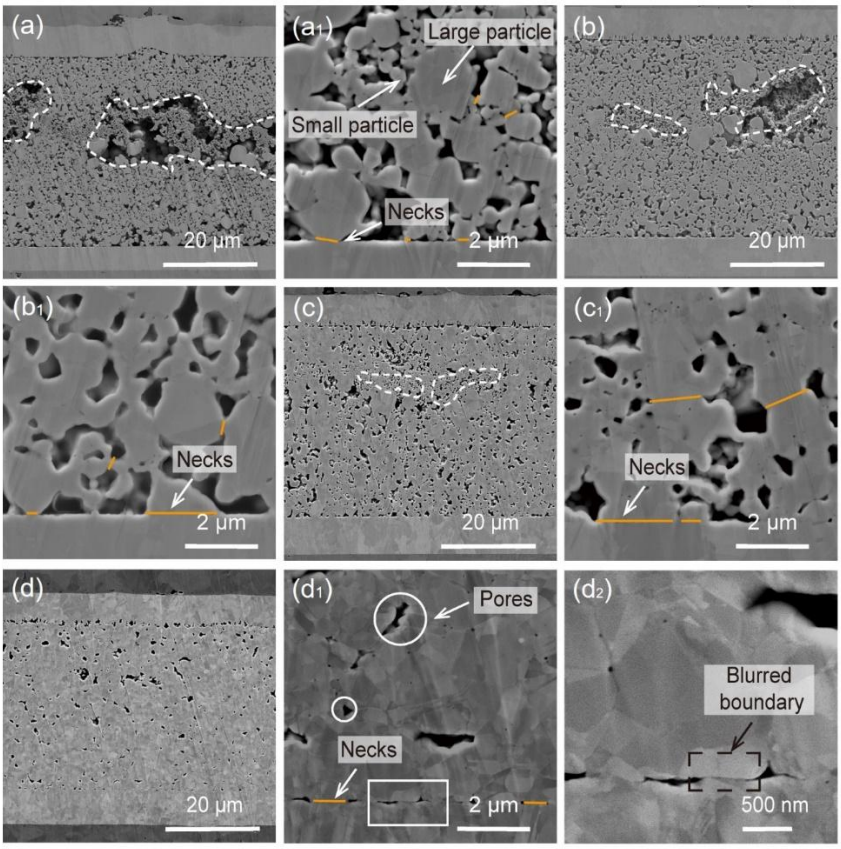

Fig. 4.19 Characterization of the cross-sections of bonded NS-Ag with different bonding temperatures. Cross-sections of (a) 160 °C, (b) 180 °C, (c) 200 °C, and (d) 220 °C. Amplified cross-section of interface of (a_1) 160 °C, (b_1) 180 °C, (c_1) 200 °C, and (d_{1-2}) 220 °C.

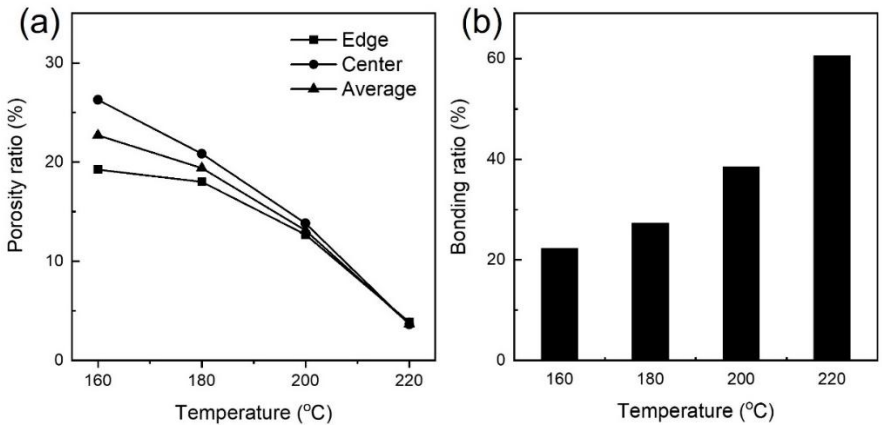

Fig. 4.20 Joint information derived from cross-sections of Ag sintered joints derived from NS-Ag. Evolution of (a) porosity ratio and (b) bonding ratio with the bonding temperature.

This could be due to the presence of a thin oxidation layer on the top surface of the Ag substrate [23]. Previous study had proven that the thermal decomposition of Ag oxide occurred at 727 K (454 ^{o}C) [24]. Bonding at 220 ^{o}C was insufficient to completely break through the oxide layer because reductive flux was not used [25]. These boundaries may act as weak regions during the die-shear process, which contributed to the shear strength of Ag joints derived from NS-Ag being slightly lower than that of Ag joints derived from NS-Au [26].

To confirm the above hypothesis, the Ag sintered joint derived from NS-Ag at 220 ^{o}C was characterized by TEM. **Fig. 4.21** shows the TEM images and EDS results of sintered Ag

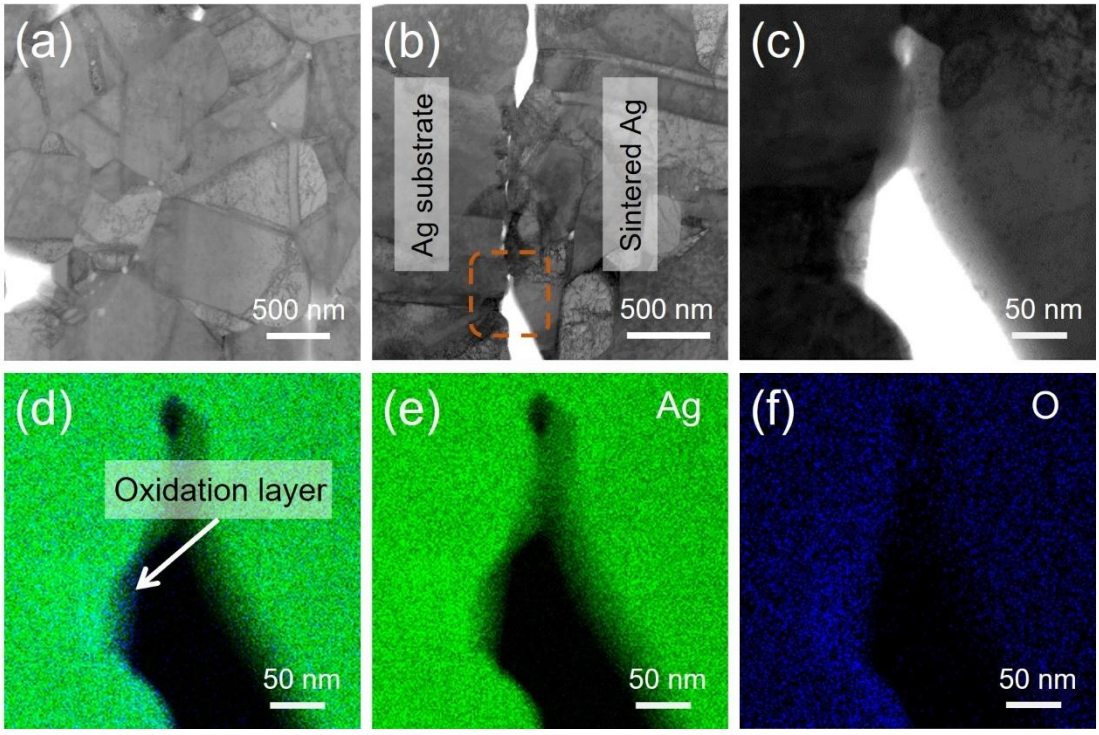

Fig. 4.21 TEM characterization of the Ag sintered joint derived from NS-Ag bonded at 220 ^{o}C with 5 MPa for 40 min. TEM images of (a) the sintered Ag and (b) (c) the interface between the sintered Ag and substrate. (d)-(f) EDS analysis of (c).

joints derived from NS-Ag. Like sintered NS-Au, the sintered Ag derived from NS-Ag exhibited randomly distributed grain boundaries in **Fig. 4.21a**. However, some small voids were observed at the interface in **Fig. 4.21b**, indicating that the sintered Ag did not contact perfectly with the Ag substrate. The EDS results in **Fig. 4.21c-f** showed that a thin Ag oxidation layer existed on the surface of the Ag substrate. This observed phenomenon could contribute to the insufficient connection at the interface between the sintered Ag and Ag substrates.

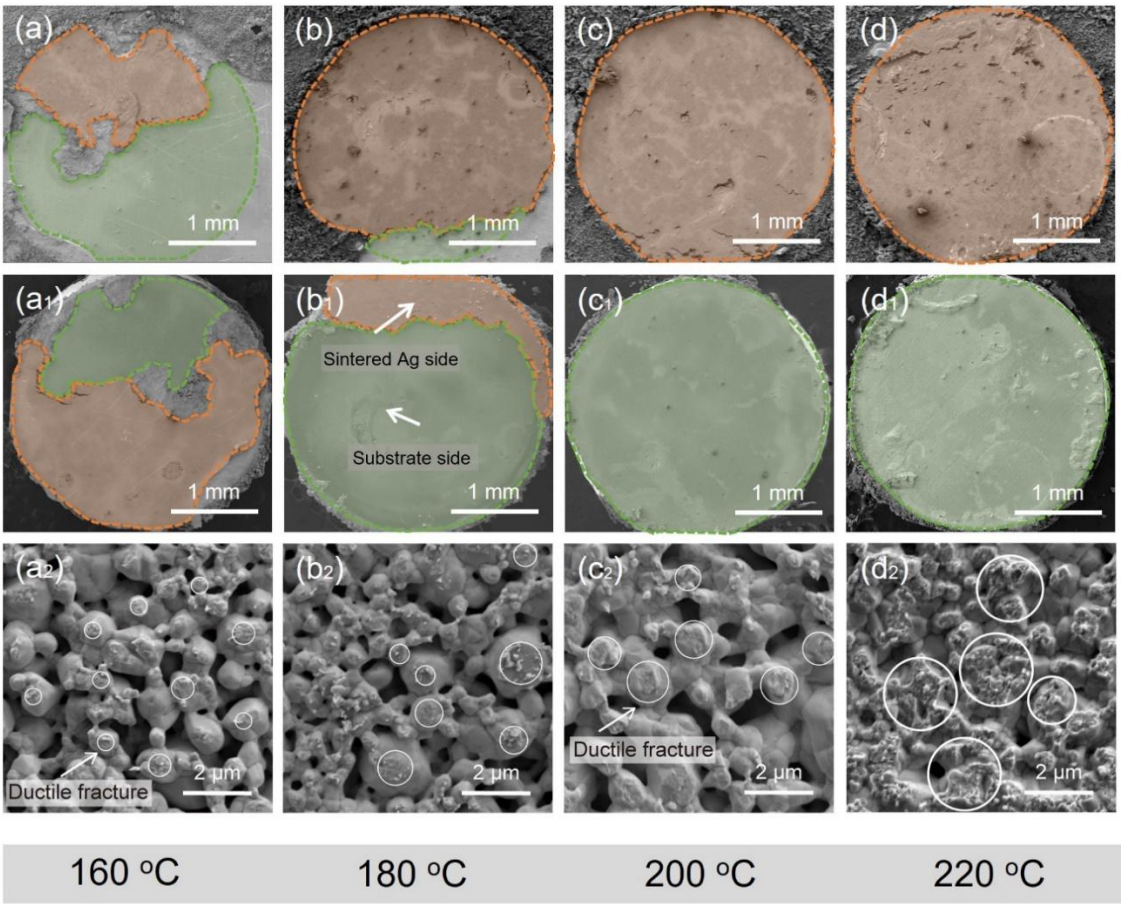

Fig. 4.22 Characterization of the fracture surfaces of bonded NS-Ag with different bonding temperatures. SEM images showing the overall fracture surfaces at the (a)-(d) substrate side and (a_1)-(d_1) die side. (a_2)-(d_2) Magnified SEM images of fracture surfaces at different temperatures.

The fracture surfaces of the Ag sintered joints were observed to reveal the evolution of shear strength with bonding temperature in **Fig. 4.11a**. **Fig. 4.22** depicts the fracture surface of the Ag sintered joints derived from NS-Ag at different bonding temperatures. According to **Fig. 4.22a-d** and **4.22a$_1$-d$_1$**, the Ag joints derived from NS-Ag mainly fractured at the interface between the sintered Ag and Ag substrate. This indicated that the interfacial condition governed the shear strength of the Ag sintered joints with Ag substrate [27]. As shown in **Fig. 4.22a$_2$-d$_2$**, visible fracture points in the white circles were observed on the fracture surface of the Ag sintered joints derived from NS-Ag. Moreover, the diameter of these points increased with increasing bonding temperatures. This may have been due to the fact that the elevated temperature enhanced the mutual diffusion between the Ag nanostructures and substrate [14]. This change contributed to enhancing the connection between the Ag sintered layer and Ag substrate, increasing the bonding ratio and shear strength with increasing bonding temperature in **Fig. 4.20b** and **Fig. 4.11a**, respectively.

4.3.5 Ag sintered joints derived from NS-Al

The shear strength of Ag sintered joints on the Al substrate was much lower than that of the joints on the Au and Ag substrates. The reasons for this low shear strength were determined through SEM observation of the cross-section and fracture surface of Ag sintered joints on Al substrate. The porosity ratio of the Ag sintered joints was measured based on the obtained cross-sections. **Fig. 4.23** shows the cross-section of Ag sintered joints derived from NS-Al at different bonding temperatures. **Fig. 4.24** presents the evolution of the porosity ratio of Ag sintered joints with bonding temperatures. As shown in **Fig. 4.23a-d**, the sintering

behaviors within NS-Al were similar to that of NS-Au in **Fig. 4.12** and NS-Ag in **Fig. 4.19**. This morphology change decreased the porosity ratio in **Fig. 4.24**. The porosity ratio of the Ag joints with Al substrate bonded at 220 °C was 3.1% indicating the remarkable bonding performance of NS-Al. However, the corresponding shear strength was only 7.5 MPa, suggesting that the sintering degree inside NS-Al may not be the primary factor determining the shear strength of the Ag sintered joints. The reason for the poor shear strength was determined by observing the interfaces between the Ag sintered layer and Al substrate. As depicted in **Fig. 4.23a$_1$-d$_1$**, necks were found between the Ag sintered layer and Al substrate. However, delamination of Ag sintered layer was observed at the interface, which indicates the poor connection between the Ag sintered layer and Al substrate.

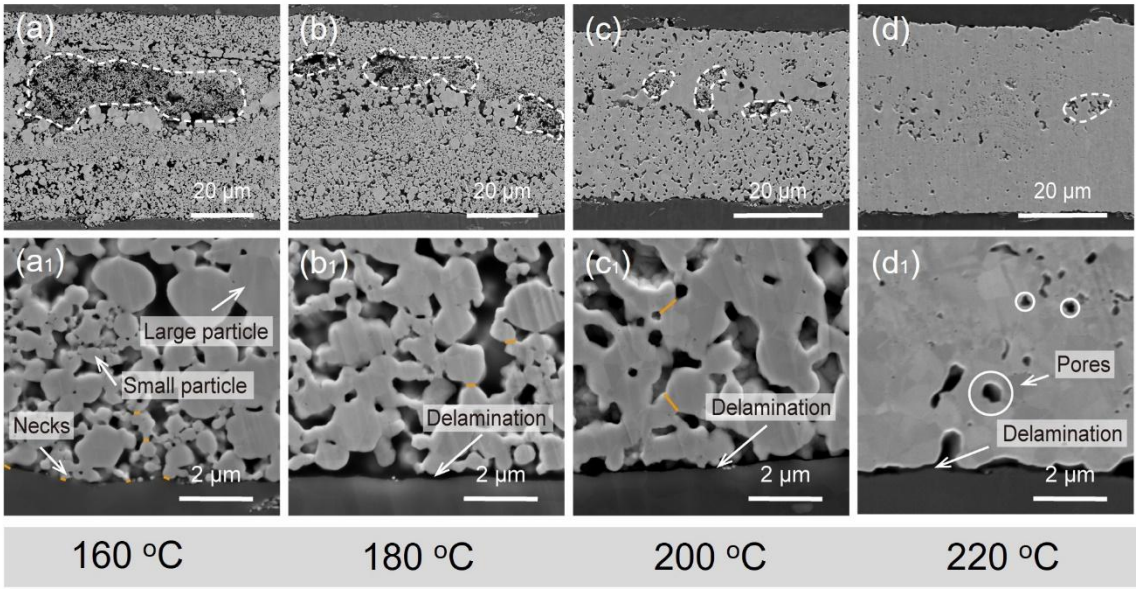

Fig. 4.23 Characterization of the cross-sections of bonded NS-Al with different bonding temperatures. SEM images showing (a)-(d) the overall cross-sections and (a_1)-(d_1) magnified cross-sections of interface at different temperatures.

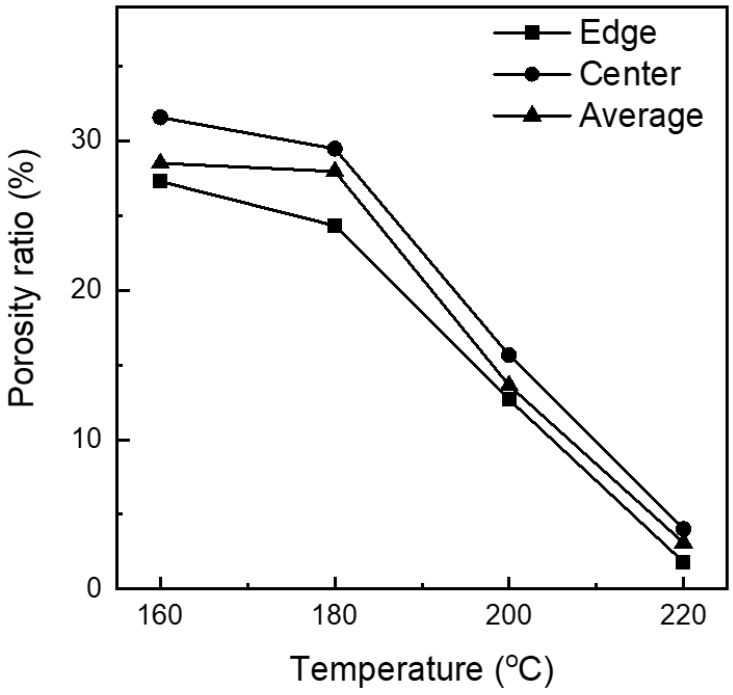

Fig. 4.24 Evolution of the porosity ratio of Ag sintered joints derived from NS-Al with the bonding temperature.

Although the NS-Al demonstrated a similar morphological change with NS-Au and NS-Ag during the bonding process, the shear strength of Ag sintered joints with the Al substrates was much lower than that of the Au and Ag substrates. The reason for the deterioration of shear strength was explained using TEM observation and EDS analysis of the Ag joints derived from NS-Al at 200°C. The results of TEM and EDS analyses are presented in **Fig. 4.25**. The EDS mapping of Al and Ag in **Fig. 4.25c** and **4.25e** revealed no interdiffusion between the bonded Ag and Al substrates. An oxidation layer was observed in **Fig. 4.25d** and **4.25f**. This lack of interdiffusion could be attributed to the blocking effect of the Al oxide layer on the surface of the Al substrate [28]. This means the sintered Ag was attached to the Al substrates by poor physical contact, which contributed to the delamination of sintered Ag in **Fig. 4.23b$_1$-d$_1$**. Although the Al substrate initially exhibited promising bonding, the

presence of a native Al oxide layer ultimately hindered strong bonding between the sintered Ag and Al substrate [28]. This limitation of interfacial reaction likely contributed to the decreased shear strength.

Fig. 4.26 shows the fracture surface of Ag sintered joints derived from NS-Al at different bonding temperatures. **Fig. 4.26a-d** and **4.26a$_1$-d$_1$** depict Ag sintered joints with Al substrate fracture at the interface. In addition, the fracture points in **Fig. 4.26a$_2$-d$_2$** were faint, indicating that the connection between the Ag sintered layer and with Al substrate was poor, resulting in the low shear strength in **Fig. 4.11a**. The results of fracture surface indicated that the interface was the main weak point of the Ag sintered joints with Al substrate, which agreed with the results of cross-section observation.

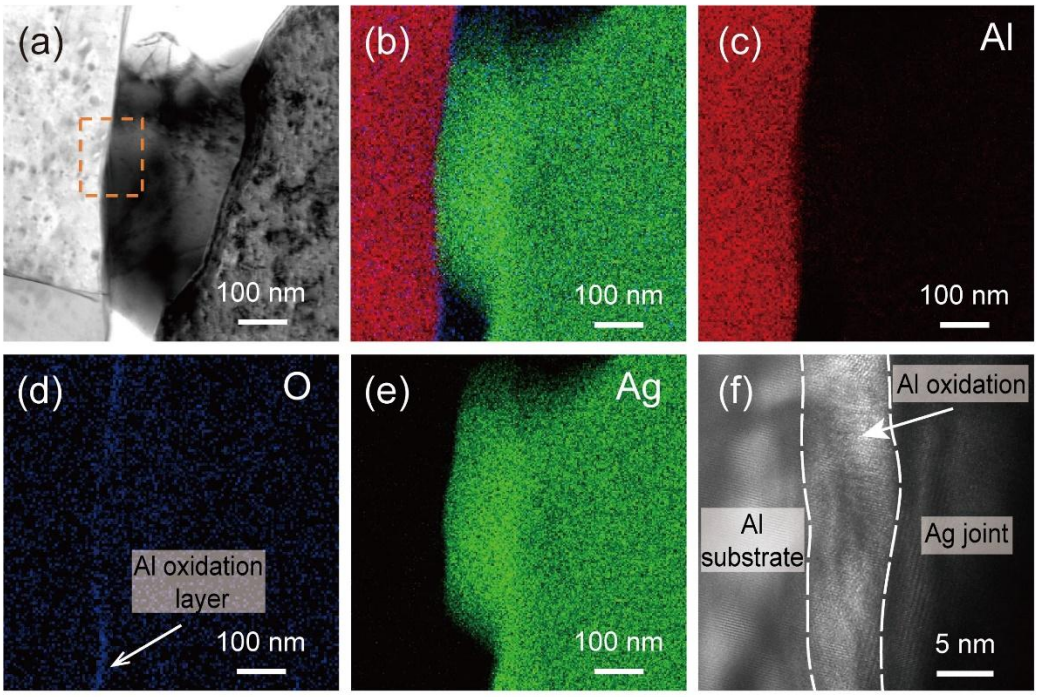

Fig. 4.25 TEM characterization of the Ag sintered joint derived from NS-Al bonded at 200 ºC with 5 MPa for 40 min. (a) TEM, (b)-(e) EDS, and (f) HRTEM analysis of the interface between sintered Ag and Al substrate at the orange rectangle in (a).

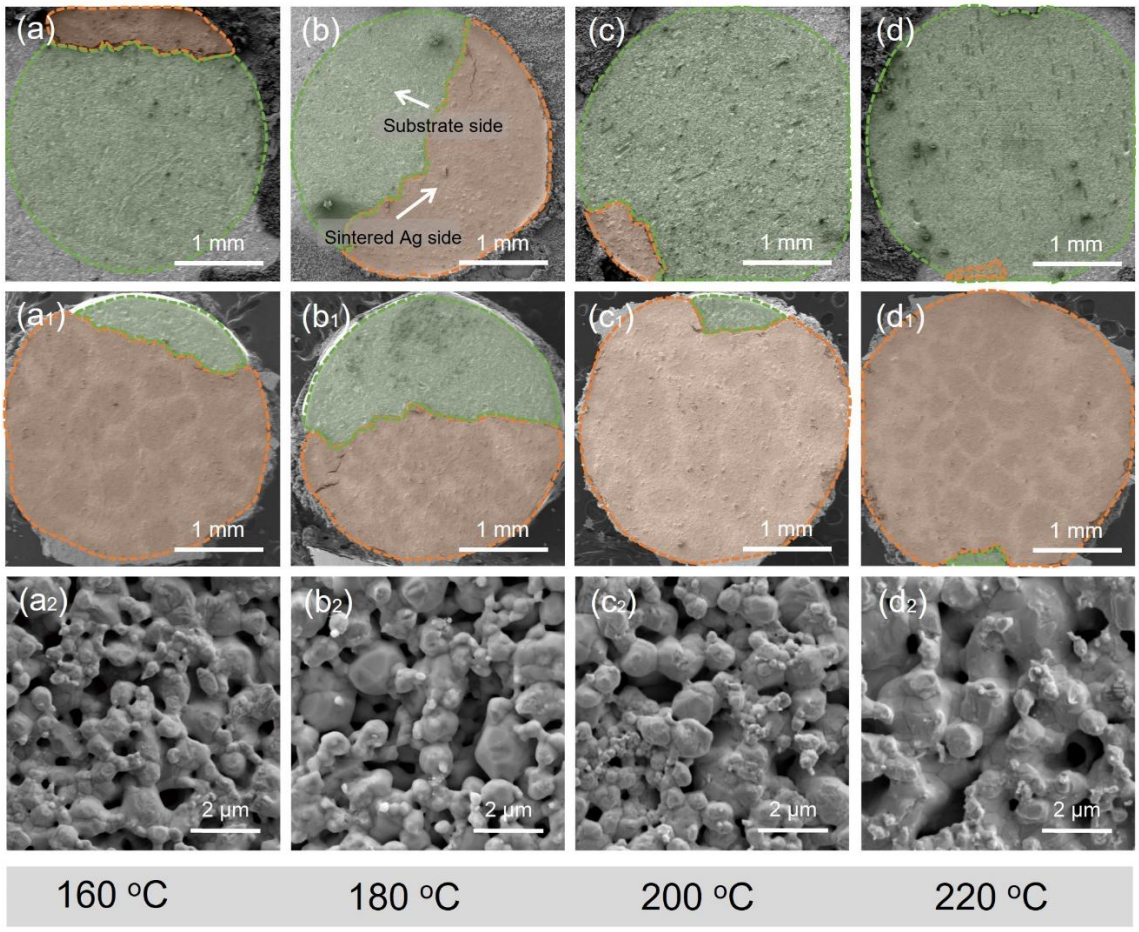

Fig. 4.26 Characterization of the fracture surfaces of bonded NS-Al with different bonding temperatures. SEM images showing the overall fracture surfaces at the (a)-(d) substrate side and (a_1)-(d_1) die side. (a_2)-(d_2) Magnified SEM images of fracture surfaces at different temperatures.

4.3.6 Ag sintered joints derived from NS-Cu

The Ag sintered joints derived from NS-Cu also demonstrated a low shear strength in **Fig. 4.11a**. The cross-sections of the Ag sintered joints with Cu substrates were observed to reveal the bonding behavior of NS-Cu. **Fig. 4.27** depicts the cross-section of the Ag sintered joints derived from the NS-Cu at different bonding temperatures. The cracks induced by the polishing process of cross-section preparation in **Fig. 4.27a-c** indicated poor joint properties.

Monodispersed Ag particles without necks in **Fig. 4.27a$_1$-b$_1$** meant sintering did not occur within NS-Cu at 160 ºC and 180 ºC [29] as the intermediate organic products of incompletely decomposed Cu compounds covered the surface of Ag particles, which blocked the atomic diffusion during the bonding process [30,31]. In this core-shell structure, the organic shell with poor mechanical properties provided limited strength support for the Ag sintered

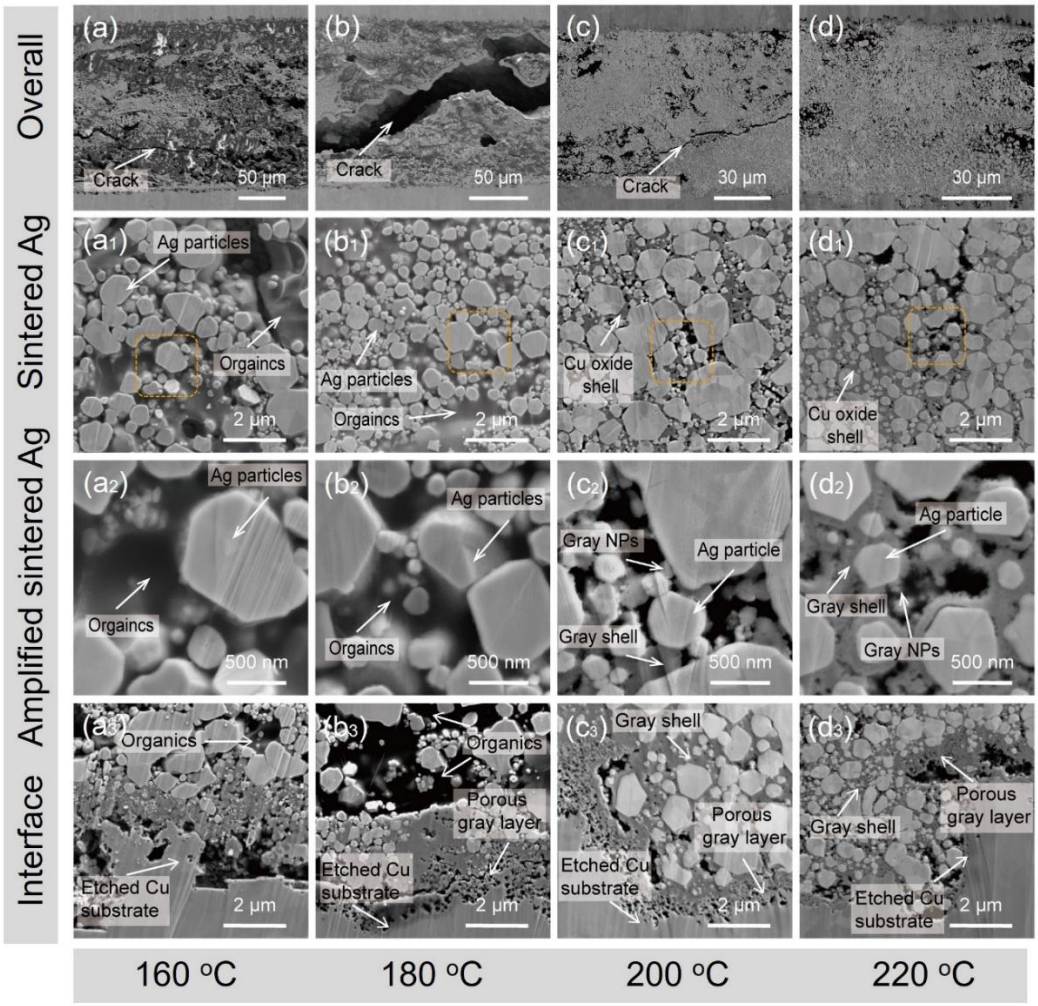

Fig. 4.27 Characterization of the cross-sections of bonded NS-Cu with different bonding temperatures. (a)-(d) SEM images of the overall cross-sections at different temperatures. (a_1)-(d_1) Cross-sections of sintered Ag at different temperatures. (a_2)-(d_2) Amplified SEM images in the orange rectangle of (a_1)-(d_1), respectively. (a_3)-(d_3) SEM images of the cross-sections of the interface at different temperatures.

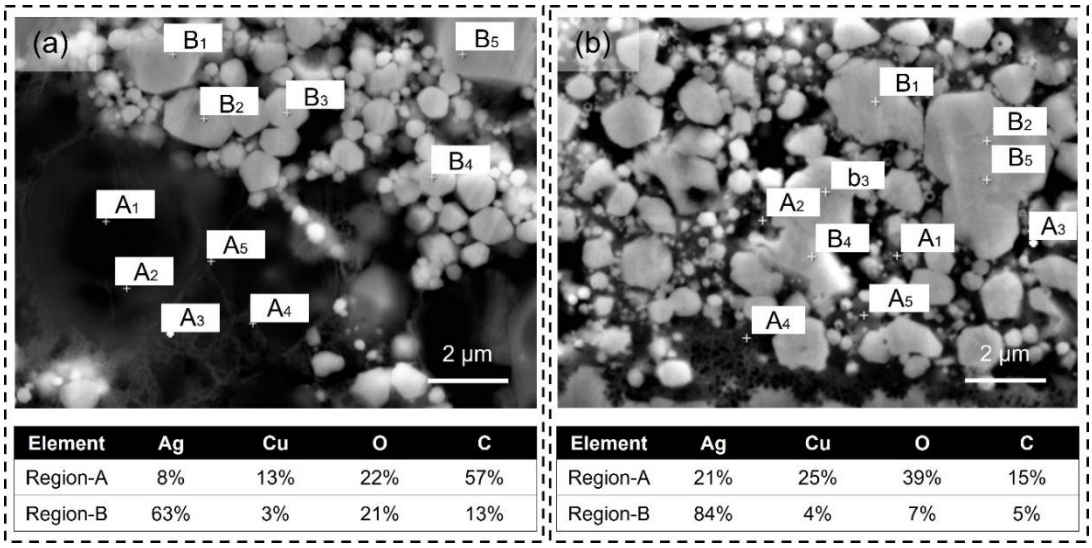

Element	Ag	Cu	O	C
Region-A	8%	13%	22%	57%
Region-B	63%	3%	21%	13%

Element	Ag	Cu	O	C
Region-A	21%	25%	39%	15%
Region-B	84%	4%	7%	5%

Fig. 4.28 Average element content of two distinct regions within sintered Ag derived from NS-Cu at (a) 160 °C and (b) 220 °C.

joints, resulting in poor joint properties. As the bonding temperature increased to 200 °C and 220 °C, the Ag particles in **Fig. 4.27c$_1$** and **4.27d$_1$** were still monodispersed in the Ag sintered joints, and their surfaces were covered by a layer of grayish substance. The high-magnification SEM images in **Fig. 4.27a$_2$-d$_2$** indicated that the intermediate organics were first translated into gray NPs, whose accumulation led to the formation of the gray shell. This gray shell hindered atomic diffusion for sintering by covering the surface of Ag particles [32]. The interface between the Ag sintered layer and Cu substrate was characterized in **Fig. 4.27a$_3$-d$_3$** to investigate the interface condition. Like the phenomenon inside the sintered Ag layer, intermediate organics were converted into porous gray substances at the interface between the Ag sintered layer and Cu substrate.

As the thermal decomposition temperature of generated Cu compounds was 211 °C (DSC curve of **Fig. 3.10b** in Chapter 3), bonding at 220 °C could cause the decomposition of Cu

compounds. The gray substances in **Fig. 4.27c$_2$** and **4.27d$_2$** may be caused by the decomposition of intermediate organics in **Fig. 4.27a$_2$** and **4.27b$_2$**. This hypothesis was confirmed using EDS analysis of the gradients of Ag sintered joints derived from NS-Cu. **Fig. 4.28** shows the EDS point analysis of the cross-section derived from NS-Cu at 160 ^{o}C and 220 ^{o}C. As shown in **Fig. 4.28**, 10 points that are 5 for the organics: Region-A and 5 for the particles: Region-B were detected for each sample. Similar to the thermal decomposition of the Ag-based complex, the decomposition of Cu compounds increased the Cu content and decreased the C and O contents. As the temperature increased from 160 ^{o}C to 220 ^{o}C, the C content dramatically decreased in **Fig. 4.28a** and **4.28b**, indicating the thermal decomposition of Cu compounds. However, the Cu and O content increased simultaneously. The increased O content may be attributed to the fact that the Cu derived from decomposition was oxidized. For this process, Cu (II) was reduced to Cu (0) when the bonding temperature of 220 ^{o}C was higher than the decomposition temperature of 211 ^{o}C for Cu compounds [33]. However, the newly generated Cu nucleus was sensitive to the oxygen in the air, leading to the oxidation of Cu [34,35]. Consequently, more O was trapped in the joint, which increased the O content. In addition, the 15% C content of Region-A in **Fig. 4.28b** indicated that the decomposition of Cu compounds was insufficient. Therefore, Region-A of the 220 ^{o}C group consisted of intermediate organic byproducts and Cu oxides. Previous studies confirmed that both organics and Cu oxides have negative effects on atomic diffusion for bonding [30,36]. Therefore, both the existence and decomposition of Cu compounds have serious negative effects on the sintering of Ag nanostructures in air, leading to low shear strength in **Fig. 4.11a**.

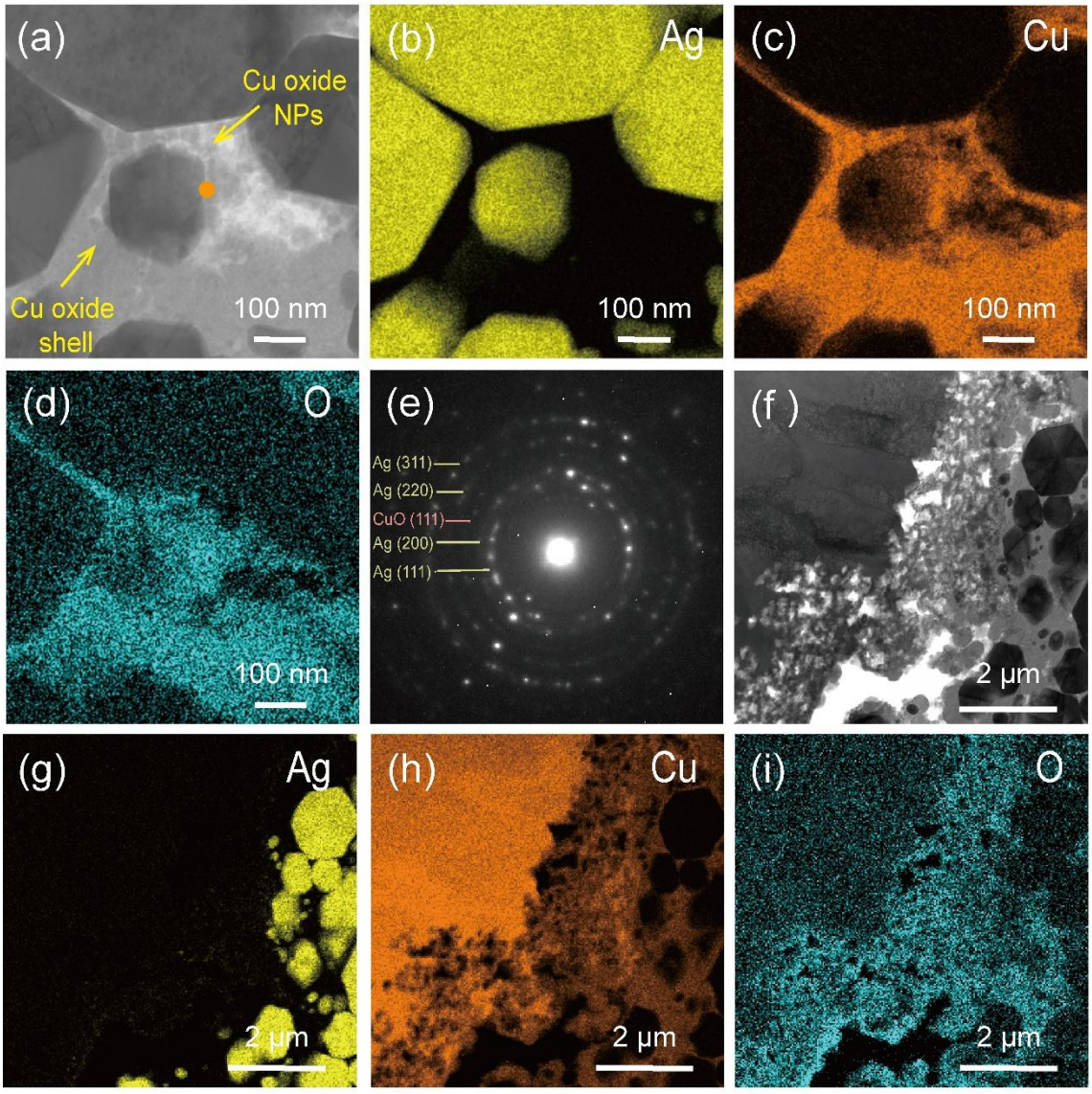

Fig. 4.29 TEM characterization of the Ag sintered joint derived from NS-Cu bonded at 200 °C with 5 MPa for 40 min. (a) TEM images and (b)-(d) EDS mapping of the sintered Ag. (e) SAED of the orange spot in (a). (f) TEM images and (g)-(i) EDS mapping of the interface between sintered Ag and substrate.

The gray substances were identified by TEM characterization of the Ag joints with Cu substrates bonded at 200 °C. **Fig. 4.29** depicts the TEM analysis of Ag joints with Cu substrates bonded at 200 °C. **Fig. 4.29a** depicted that Ag particles were surrounded by gray

NPs and shell. The EDS mappings in **Fig. 4.29c** and **4.29d** detected Cu and O with high intensity at the position of the grayish substance. The orange spot in **Fig. 4.29a** was characterized by selected area electron diffraction (SAED), and the obtained pattern was depicted in **Fig. 4.29e**. The (111) plane of CuO was detected along with Ag, indicating that the grayish substance may contain CuO. Similar to the gray shell, Cu and O with high intensity were detected at the same position of the porous gray layer in **Fig. 4.29g-i**. The phenomenon provided firm evidence to support the CuO generation during the bonding process of NS-Cu. Therefore, the existence of organic intermediates and CuO contributed to the low shear strength of the bonded NS-Cu in **Fig. 4.11a**.

The fracture surfaces of the Ag sintered joints on the Cu substrates were characterized. **Fig. 4.30** shows the fracture surface of the Ag sintered joints derived from NS-Cu at different bonding temperatures. As depicted in **Fig. 4.30a-d** and **4.30a$_1$-d$_1$**, the Ag joints derived from NS-Cu mainly fractured within the sintered Ag. Monodispersed Ag particles were visible in **Fig. 4.30a$_2$-d$_2$**, and no ductile fractures were observed, indicating that the sintering of NS-Cu was insufficient. **Fig. 4.31** illustrates the EDS analysis of the fracture surfaces of Ag sintered joints with Cu substrate at 200 ^{o}C. The C mapping with high intensity in **Fig. 4.31f** indicated that organics were trapped in the sintered Ag layer during the bonding process. **Fig. 4.32** depicts the XRD patterns of the fracture surface from different bonding temperatures. The characteristic peaks of CuO were detected in the XRD patterns in **Fig. 4.32a-d**, suggesting that the organics and CuO hindered the atomic diffusion during the bonding process, which deteriorated the joint property in **Fig. 4.11a**.

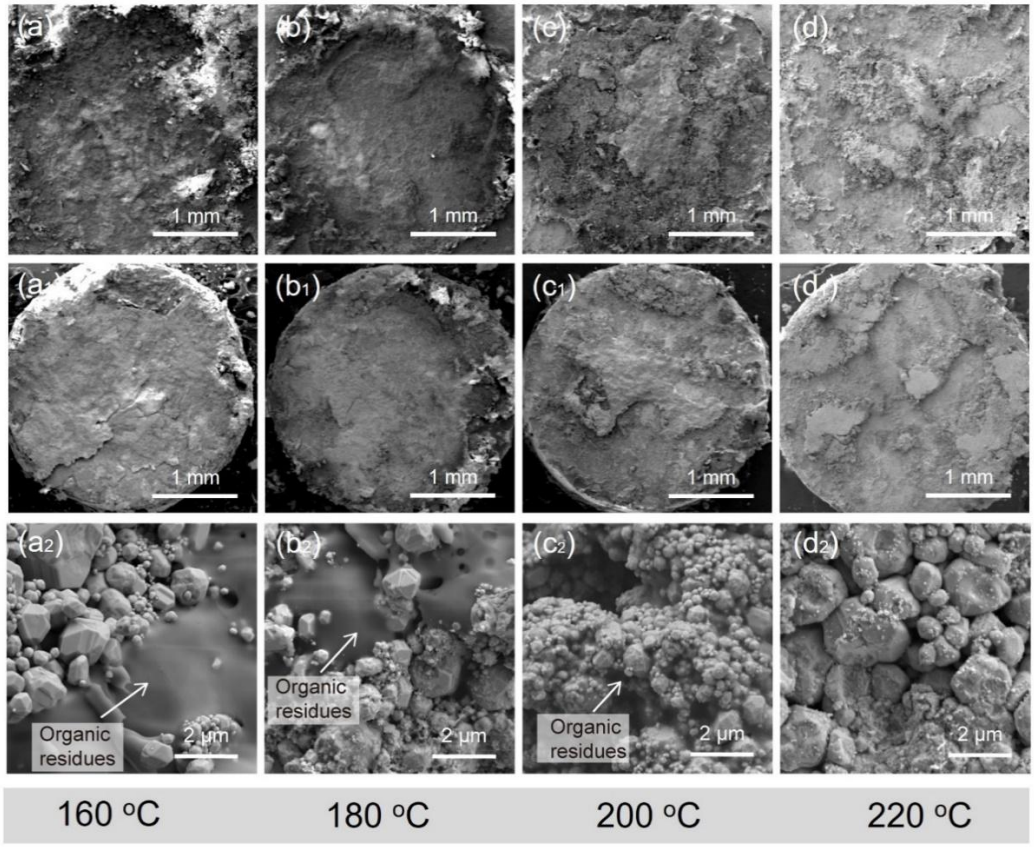

Fig. 4.30 Characterization of the fracture surfaces of bonded NS-Cu with different bonding temperatures. SEM images showing the overall fracture surfaces at (a)-(d) substrate side and (a_1)-(d_1) die side; (a_2)-(d_2) Magnified fracture surfaces at different temperatures.

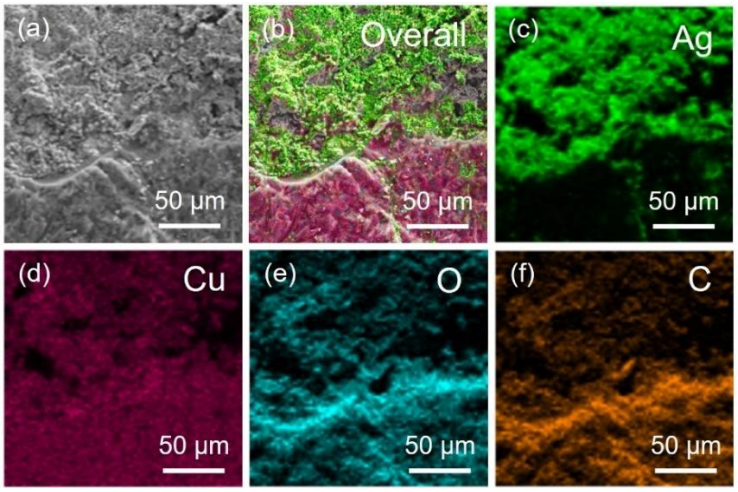

Fig. 4.31 (a)-(f) EDS analysis of fracture surfaces of bonded NS-Cu at 200 °C

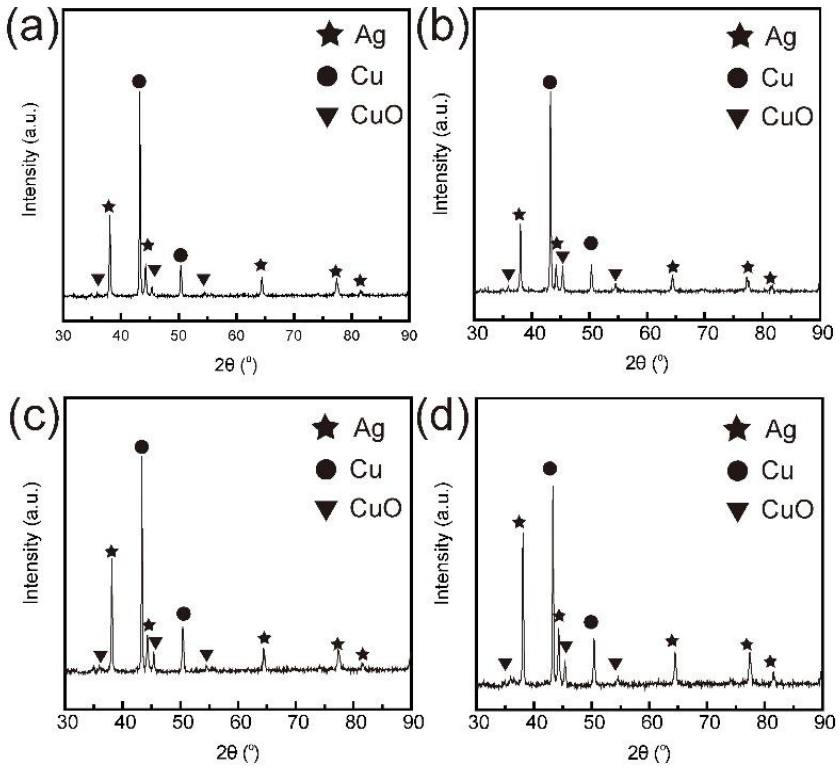

Fig. 4.32 XRD patterns of fracture surfaces of bonded NS-Cu at (a)160 ºC, (b) 180 ºC, (c) 200 ºC, and (d) 220 ºC.

4.4 Conclusion

This study investigated the effects of substrate metal on the bonding mechanism of Ag nanostructures obtained via the thermal decomposition of an Ag-based complex on the substrate. We identified a bonding mechanism that depended on the reaction between the Ag-based complex and substrate. The NS-Au, NS-Ag and NS-Al nanostructures were bonded by the sintering of poly-dispersed particles. Small particles with high surface energy were readily sintered, forming necks that linked large particles even at low temperatures. These necks strengthened the Ag sintered joints and provided diffusion pathways for further densification. Consequently, NS-Au, NS-Ag, and NS-Al exhibited excellent low-temperature

bonding performance, as evidenced by the robust Ag sintered joints formed by NS-Au, which had a shear strength of 31.1 MPa at 160 °C. However, the Al oxide layer on the Al substrate hindered diffusion and weakened the sintered Ag–Al interface, resulting in poor joint properties. In addition, diffusion between Ag particles was not observed for NS-Cu because the organics and CuO hindered the atomic diffusion for sintering. Overall, this work highlighted the importance of substrate selection when Ag-based complexes are used as bonding materials. The results can guide future efforts to optimize joint performance.

Reference

[1] C.-J. Du, X. Li, Y.-H. Mei, G.-Q. Lu, Bonding performance of sintered nanosilver joints on bare copper substrates with different grain structures, Journal of Materials Science: Materials in Electronics 30 (2019) 12860–12868. https://doi.org/10.1007/s10854-019-01601-9.

[2] R.M. German, 1 - Thermodynamics of sintering, in: Z.Z. Fang (Ed.), Sintering of Advanced Materials, Woodhead Publishing, 2010: pp. 3–32. https://doi.org/https://doi.org/10.1533/9781845699949.1.3.

[3] C. Chen, J. Yeom, C. Choe, G. Liu, Y. Gao, Z. Zhang, B. Zhang, D. Kim, K. Suganuma, Necking growth and mechanical properties of sintered Ag particles with different shapes under air and N2 atmosphere, J Mater Sci 54 (2019) 13344–13357. https://doi.org/10.1007/s10853-019-03813-0.

[4] Y.J. Kim, B.H. Park, S.K. Hyun, H. Nishikawa, The influence of porosity and pore shape on the thermal conductivity of silver sintered joint for die attach, Mater Today Commun 29 (2021). https://doi.org/10.1016/j.mtcomm.2021.102772.

[5] A. Hu, J.Y. Guo, H. Alarifi, G. Patane, Y. Zhou, G. Compagnini, C.X. Xu, Low temperature sintering of Ag nanoparticles for flexible electronics packaging, Appl Phys Lett 97 (2010) 153117. https://doi.org/10.1063/1.3502604.

[6] T. Wang, X. Chen, G.-Q. Lu, G.-Y. Lei, Low-Temperature Sintering with Nano-Silver Paste in Die-Attached Interconnection, J Electron Mater 36 (2007) 1333–1340. https://doi.org/10.1007/s11664-007-0230-5.

[7] H. Yang, W. Zhu, Study on the main influencing factors of shear strength of nano-silver joints, Journal of Materials Research and Technology 9 (2020) 4133–4138. https://doi.org/https://doi.org/10.1016/j.jmrt.2020.02.040.

[8] X. Lu, Z. Lv, Y. Sun, M. Murugesan, C. Zhou, X. Zhang, J. Liu, Enhanced Mechanical and Thermal Properties of Ag Joints Sintered by Spark Plasma Sintering, J Electron Mater 51 (2022) 6310–6319. https://doi.org/10.1007/s11664-022-09849-4.

[9] S. Chen, Y.-H. Mei, M. Wang, X. Li, G.-Q. Lu, Large-Area Bonding by Sintering of a Resin-Free Nanosilver Paste at Ultralow Temperature of 180 °C, IEEE Trans Compon Packaging Manuf Technol 12 (2022) 707–710. https://doi.org/10.1109/TCPMT.2022.3159033.

[10] C. Wang, G. Li, L. Xu, J. Li, D. Zhang, T. Zhao, R. Sun, P. Zhu, Low Temperature Sintered Silver Nanoflake Paste for Power Device Packaging and Its Anisotropic Sintering Mechanism, ACS Appl Electron Mater 3 (2021) 5365–5373. https://doi.org/10.1021/acsaelm.1c00857.

[11] D. Yang, Y. Huang, Y. Tian, Microstructure of Ag Nano Paste Joint and Its Influence on Reliability, Crystals (Basel) 11 (2021) 1537. https://doi.org/10.3390/cryst11121537.

[12] Z. Zhang, C. Chen, A. Suetake, M.-C. Hsieh, K. Suganuma, Reliability of Ag Sinter-Joining Die Attach Under Harsh Thermal Cycling and Power Cycling Tests, J Electron Mater 50 (2021) 6597–6606. https://doi.org/10.1007/s11664-021-09221-y.

[13] Z.Z. Fang, H. Wang, 13 - Sintering of ultrafine and nanosized ceramic and metallic particles, in: R. Banerjee, I. Manna (Eds.), Ceramic Nanocomposites, Woodhead Publishing, 2013: pp. 431–473. https://doi.org/https://doi.org/10.1533/9780857093493.3.431.

[14] A. Molinari, Fundamentals of Sintering: Solid State Sintering, in: F.G. Caballero (Ed.), Encyclopedia of Materials: Metals and Alloys, Elsevier, Oxford, 2022: pp. 471–480. https://doi.org/https://doi.org/10.1016/B978-0-12-819726-4.00096-X.

[15] J. Yan, A review of sintering-bonding technology using ag nanoparticles for electronic packaging, Nanomaterials 11 (2021). https://doi.org/10.3390/nano11040927.

[16] Z. Deng, G. Zou, R. Du, Q. Jia, H. Zhang, L. Liu, Particle Size Effects of Nano-Ag Films on the Interface Sintered Bonding for Die Attachment, J Electron Mater 53 (2024) 473–488. https://doi.org/10.1007/s11664-023-10786-z.

[17] Y. Lee, S.-G. Oh, Ostwald ripening and control of Ag ion reduction degree by ammonium hydroxide in alcohol reduction process, Journal of Industrial and Engineering Chemistry 21 (2015) 768–771. https://doi.org/https://doi.org/10.1016/j.jiec.2014.04.010.

[18] S. Chen, H. Zhang, Silver Sintering and Soldering: Bonding Process and Comparison, in: K.S. Siow (Ed.), Die-Attach Materials for High Temperature Applications in Microelectronics Packaging: Materials, Processes, Equipment, and Reliability, Springer International Publishing, Cham, 2019: pp. 1–33. https://doi.org/10.1007/978-3-319-99256-3_1.

[19] Z. Wu, W. Liu, J. Feng, Z. Wen, X. Zhang, X. Wang, C. Wang, Y. Tian, Novel Cu@Ag Micro/Nanoparticle Hybrid Paste and Its Rapid Sintering Technique via Electromagnetic Induction for High-Power Electronics, ACS Omega 8 (2023) 31021–31029. https://doi.org/10.1021/acsomega.3c02854.

[20] Y. Zuo, C. Zhao, A. Robador, M. Wickham, S.H. Mannan, Quasi-in-situ observation of the grain growth and grain boundary movement in sintered Cu nanoparticle interconnects, Acta Mater 236 (2022) 118135. https://doi.org/https://doi.org/10.1016/j.actamat.2022.118135.

[21] Q. Xu, Y. Mei, X. Li, G.Q. Lu, Correlation between interfacial microstructure and bonding strength of sintered nanosilver on ENIG and electroplated Ni/Au direct-bond-copper (DBC) substrates, J Alloys Compd 675 (2016) 317–324. https://doi.org/10.1016/j.jallcom.2016.03.133.

[22] J.M. Park, D.Y. Hyeon, H.S. Ma, S. Kim, S.T. Kim, Y.N. Nguyen, I. Son, S. Yi, K.T. Kim, K. Il Park, Enhanced output power of thermoelectric modules with reduced contact resistance by adopting the optimized Ni diffusion barrier layer, J Alloys Compd 884 (2021). https://doi.org/10.1016/j.jallcom.2021.161119.

[23] J. Schnadt, A. Michaelides, J. Knudsen, R.T. Vang, K. Reuter, E. Lægsgaard, M. Scheffler, F. Besenbacher, Revisiting the structure of the p(4×4) surface oxide on Ag(111), Phys Rev Lett 96 (2006). https://doi.org/10.1103/PhysRevLett.96.146101.

[24] G.I.N. Waterhouse, G.A. Bowmaker, J.B. Metson, The thermal decomposition of silver (I, III) oxide: A combined XRD, FT-IR and Raman spectroscopic study, Physical Chemistry Chemical Physics 3 (2001) 3838–3845. https://doi.org/10.1039/b103226g.

[25] T. Matsuda, K. Inami, K. Motoyama, T. Sano, A. Hirose, Silver oxide decomposition mediated direct bonding of silicon-based materials, Sci Rep 8 (2018). https://doi.org/10.1038/s41598-018-28788-x.

[26] M.I. Kim, J.-H. Lee, Die sinter bonding in air using Cu@Ag particulate preform and rapid formation of near-full density bondline, Journal of Materials Research and Technology 14 (2021) 1724–1738. https://doi.org/https://doi.org/10.1016/j.jmrt.2021.07.059.

[27] Y. Liu, C. Chen, Z. Zhang, M. Ueshima, T. Sakamoto, T. Naoe, H. Nishikawa, Y. Oda, K. Suganuma, Development of crack-less and deformation-resistant electroplated Ni/electroless Ni/Pt/Ag metallization layers for Ag-sintered joint during a harsh thermal shock, Mater Des 224 (2022) 111389. https://doi.org/https://doi.org/10.1016/j.matdes.2022.111389.

[28] L.M. Chew, T. Stegmann, E. Schwenk, M. Dubis, W. Schmitt, A New Development of Direct Bonding to Aluminum and Nickel Surfaces by Silver Sintering in air Atmosphere, in: 2019 IEEE 69th Electronic Components and Technology Conference (ECTC), 2019: pp. 87–93. https://doi.org/10.1109/ECTC.2019.00021.

[29] L. Ma, Y. Wang, Q. Jia, H. Zhang, Y. Wang, D. Li, G. Zou, F. Guo, Low-Temperature-Sintered Nano-Ag Film for Power Electronics Packaging, J Electron Mater 53 (2024) 228–237. https://doi.org/10.1007/s11664-023-10763-6.

[30] M.A. Asoro, D. Kovar, P.J. Ferreira, Effect of surface carbon coating on sintering of silver nanoparticles: in situ TEM observations, Chemical Communications 50 (2014) 4835–4838. https://doi.org/10.1039/C4CC01547A.

[31] Y. Tao, Y. Tao, B. Wang, L. Wang, Y. Tai, A facile approach to a silver conductive ink with high performance for macroelectronics, Nanoscale Res Lett 8 (2013) 296. https://doi.org/10.1186/1556-276X-8-296.

[32] S.R. Esa, G. Omar, S.H. Sheikh, M. Fadzullah, K.S. Siow, B.A. Rahim, B. Çoşut, Diffusion Mechanism of Silver Particles in Polymer Binder for Die Attach Interconnect Technology, 2020.

[33] Y. Yong, M.T. Nguyen, T. Yonezawa, T. Asano, M. Matsubara, H. Tsukamoto, Y.C. Liao, T. Zhang, S. Isobe, Y. Nakagawa, Use of decomposable polymer-coated submicron Cu particles with effective additive for production of highly conductive Cu films at low sintering temperature, J Mater Chem C Mater 5 (2017) 1033–1041. https://doi.org/10.1039/c6tc04360g.

[34] J. Xin, Y. Gao, C. Zhang, L. Yang, S. Liu, K. Li, M. Zhou, Y. Liu, J. Zhang, W. Cai, High performance Cu sintering joint for power devices enabled by in-situ generation of Cu particles with multi-level hierarchical structures, J Mater Process Technol 329 (2024) 118435. https://doi.org/https://doi.org/10.1016/j.jmatprotec.2024.118435.

[35] W. Li, C.-F. Li, F. Lang, J. Jiu, M. Ueshima, H. Wang, Z.-Q. Liu, K. Suganuma, Self-catalyzed copper–silver complex inks for low-cost fabrication of highly oxidation-resistant and conductive copper–silver hybrid tracks at a low temperature below 100 °C, Nanoscale 10 (2018) 5254–5263. https://doi.org/10.1039/C7NR09225C.

[36] J. Liu, H. Chen, H. Ji, M. Li, Highly Conductive Cu–Cu Joint Formation by Low-Temperature Sintering of Formic Acid-Treated Cu Nanoparticles, ACS Appl Mater Interfaces 8 (2016) 33289–33298. https://doi.org/10.1021/acsami.6b10280.

Chapter 5：Formation of Ag-Cu composite joint on Cu substrate and its electromigration property

5.1 Introduction

Chapters 3 and 4 confirmed a reaction between the Ag-based complex and Cu substrate, resulting in the formation of Cu compounds in the Ag nanostructure. During the bonding process, the Cu compounds resulted in organics and Cu oxides within the Ag joints, which hindered atom diffusion and resulted in poor shear strength. This makes the Cu substrate, which is the most widely used in power device packaging, unsuitable for Ag-based complexes.

Residual organics and Cu oxides are the most serious issues caused by the Cu compounds. We predict the removal of organic compounds and the prevention of Cu oxide formation if the Ag-based complex on Cu substrate is heated in an oxygen-free atmosphere. Hence, the obtained nanostructure could consist of Ag and Cu. This suggests that these obtained nanostructures could create Ag-Cu composite joints. In previous studies, it was expected that the electromigration (EM) resistance of Ag was improved by preparing Ag-Cu composite joints [1–3]. However, the EM properties of Ag or Ag-Cu composite joints are rarely studied.

In this study, Ag-Cu composite nanostructures were created on the Cu substrate by the Ag-based complex decomposition. The microstructures and sintering behaviors of the Ag-Cu composite nanostructure were investigated. Furthermore, we proposed a new approach to

fabricate EM samples, and comparison experiments of EM behaviors of Ag joints and Ag-Cu composite joints were executed to confirm the effects of Cu on the EM properties of Ag joints.

5.2 Materials and methods

5.2.1 Materials

The following materials were utilized without additional purification: silver acetate (99%, FUJIFILM), 2-amino-2-methyl-1-propanol (AMP, FUJIFILM), ethylene glycol (EG, FUJIFILM), distilled water, and ethanol. The Cu and Ag substrates were treated according to the same method as in Chapter 3 before use.

5.2.2 Ag-Cu composite nanostructure preparation

In a typical process of Ag-Cu composite nanostructure preparation, 60 and 10 mg Ag-based complexes were printed on substrates and dies, respectively. The results in Chapters 3 and 4 indicated that the Cu atoms derived from the decomposition of Cu compounds were oxidized in the air. Therefore, Ag nanostructures in this study were prepared and bonded in oxygen-free atmospheres. Heating in a formic acid atmosphere is an ideal approach for preparing Ag-Cu composite nanostructures. A vacuum is also required before a formic acid atmosphere can be formed, which causes the liquid Ag-based complex to boil violently. Therefore, the Ag-Cu composite nanostructures were prepared by a two-step decomposition process. **Fig. 5.1** depicts the two-step decomposition process and temperature profiles. **Fig. 5.1a** presents the flow of the two-step decomposition process. Following the temperature

profile in **Fig. 5.1b**, the Ag-based complex was first heated in a N_2 atmosphere with O_2 <1000 ppm. As shown in **Fig. 5.1c**, the decomposed Ag-based complexes were then heated at 230 ^oC for 15 min in a reductive formic acid atmosphere to decompose the generated Cu compounds. The nanostructures derived from the first step and second step is named NS-N_2-180 and NS-FA-230, respectively. The Ag nanostructure on the Ag substrate was prepared by the same dwelling conditions (90 ^oC for 5 min, 180 ^oC for 15 min, 230 ^oC for 15 min) but in air.

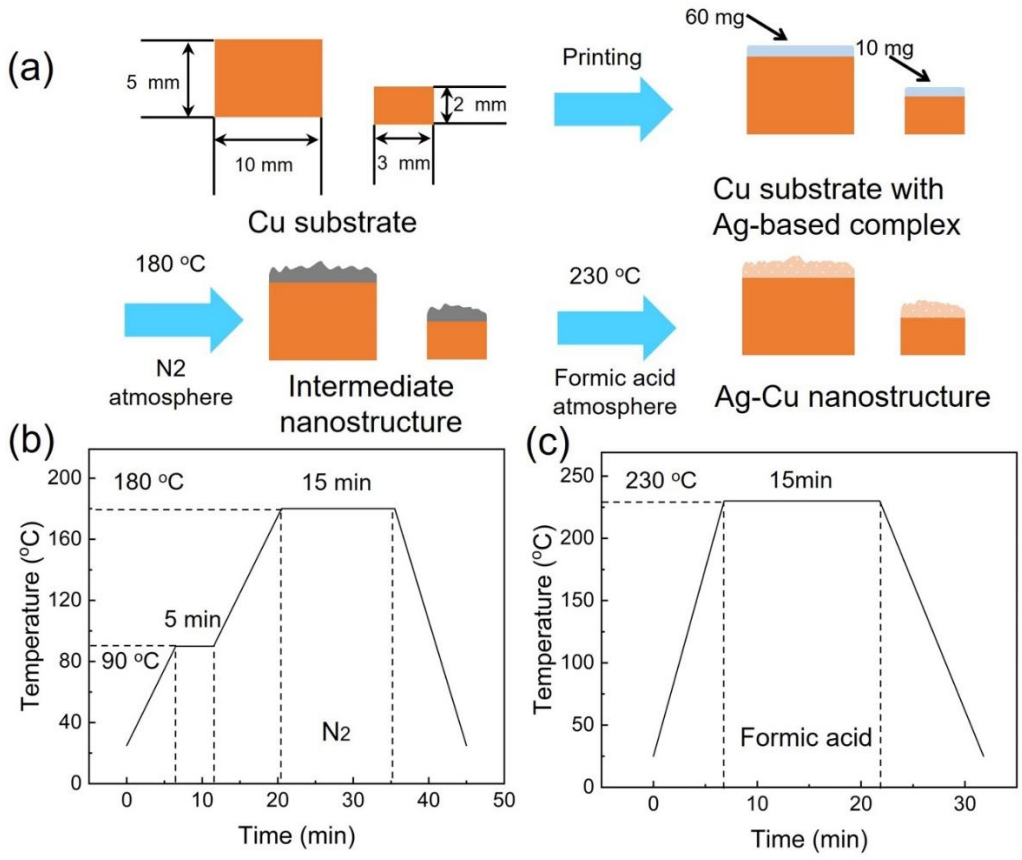

Fig. 5.1 Preparation of Ag-Cu composite nanostructures. (a) Schematic diagram illustrating the two-step decomposition process. Heating profile of the (b) first and (c) second step of the two-step decomposition process.

5.2.3 Ag-Cu composite joint preparation

Fig.5.2 shows the preparation of the joints. **Fig. 5.2a** and **5.2b** illustrate the preparation process of the Ag-Cu composite joints and EM test using joints, respectively. The corresponding heating profile is presented in **Fig. 5.2c**. As depicted in **Fig. 5.2a**, the Ag-Cu composite nanostructure on the die was flipped over that on the substrate to obtain die-attachment. Following the heating profile in **Fig. 5.2c**, the die-attachments were bonded at 220, 250, and 280 ºC for 40 min with 5 MPa in a formic acid atmosphere. The joints for the EM sample preparation in **Fig. 5.2b** were derived by bonding two nanostructures on substrates with the same diameter of 10 mm. The Ag-Cu composite joints and Ag joints for EM samples were obtained at 280 ºC for 40 min with 5 MPa in a formic acid atmosphere and air, respectively.

5.2.4 Preparation of EM samples

Research on the EM properties of Ag joints is rare because it is difficult to fulfill the strict dimensional requirement of the EM test. Schematic diagrams in **Fig. 5.3** and optical images in **Fig. 5.4** depict the detailed process of reducing the size of the EM sample. The joints embedded in resin were cut into several Ag-joint blocks with a thickness and width of about 1.5 mm in **Fig. 5.3a b** and **Fig. 5.4a b**. As depicted in **Fig. 5.3c** and **Fig. 5.4c**, the Ag-joint blocks were further cut into Ag-joint bars. If the size of the Ag-joint bars is directly reduced by polishing, the joint area could act as a weak point and break. Therefore, the resin was used again to fix the Ag-joint bars and provide strength support in **Fig. 5.3d** and **Fig. 5.4d**. As depicted in **Fig. 5.3e** and **Fig. 5.4e**, the specimen was polished from the bottom and lateral

sides to expose the Ag joint bars at the corner of the resin. With the support of resin, the size of Ag-joint bar can be reduced safely, resulting in the Ag-joint line in **Fig.5.3f** and **Fig.5.4f**. After the resin was removed, the size of Ag-joint line in **Fig. 5.3g** and **Fig. 5.4g** was continuously reduced by a cross-sectional polishing machine. Finally, the EM sample was prepared by fixing the treated Ag-joint line on the glass substrate via soldering in **Fig. 5.3h** and **Fig. 5.4h**. The EM samples of the Ag-Cu composite joints and Ag joints were named EM-Ag-Cu and EM-Ag, respectively.

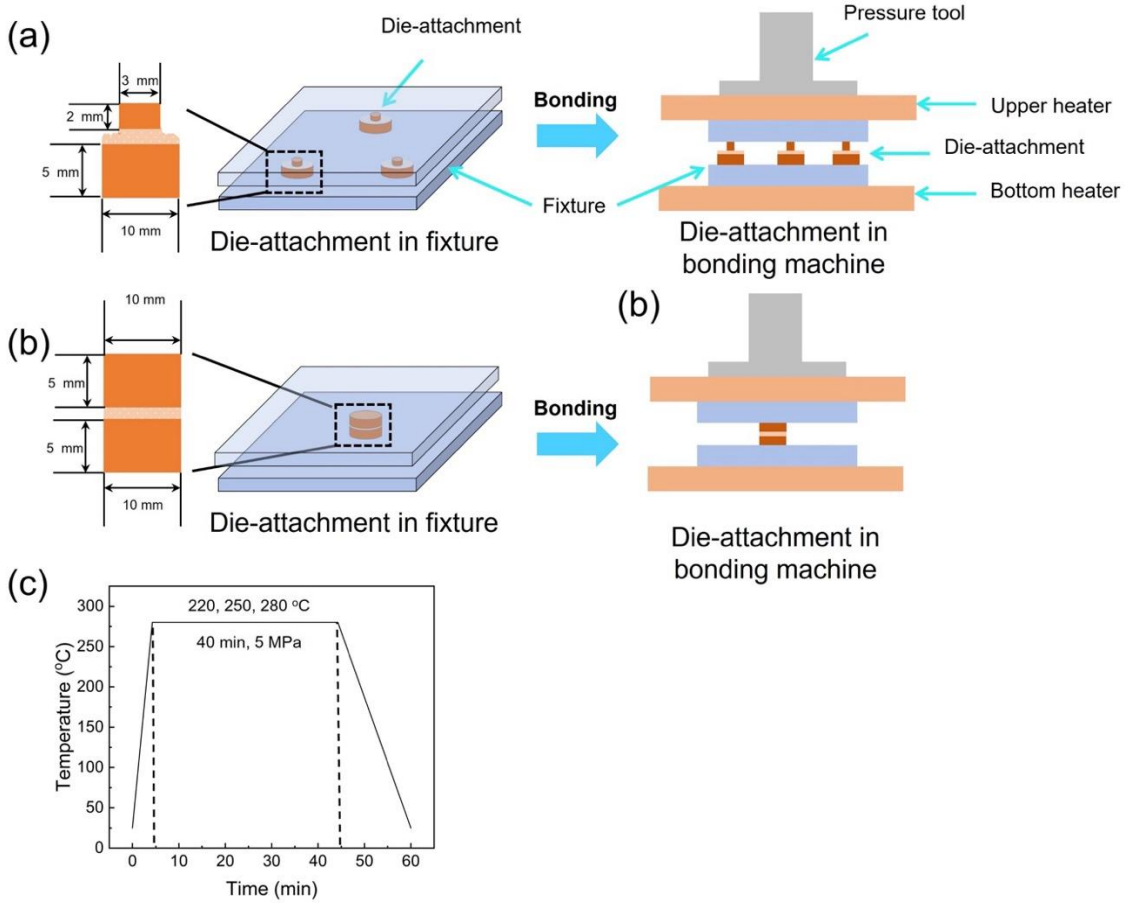

Fig. 5.2 Preparation of Ag-Cu composite joints. Schematic diagrams showing the preparation of the (a) Ag-Cu composite joints and (b) sintered joints for the EM test. (c) Heating profile of bonding process.

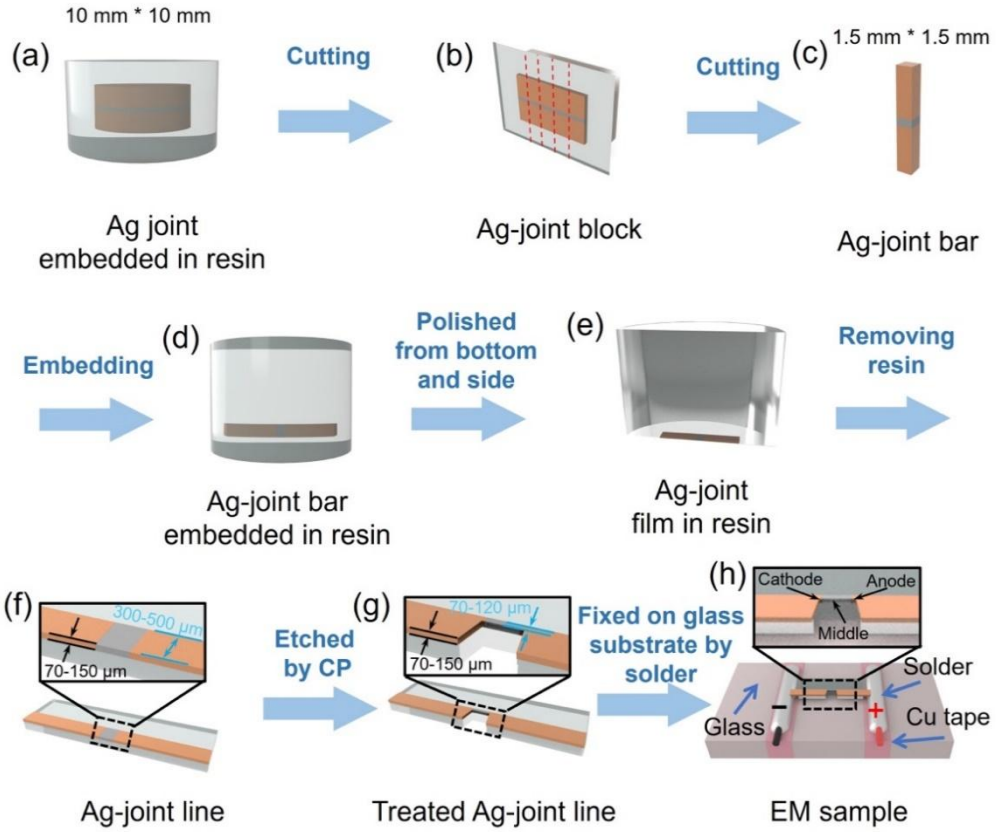

Fig. 5.3 (a)-(h) Schematic diagram illustrating the flow of EM sample preparation.

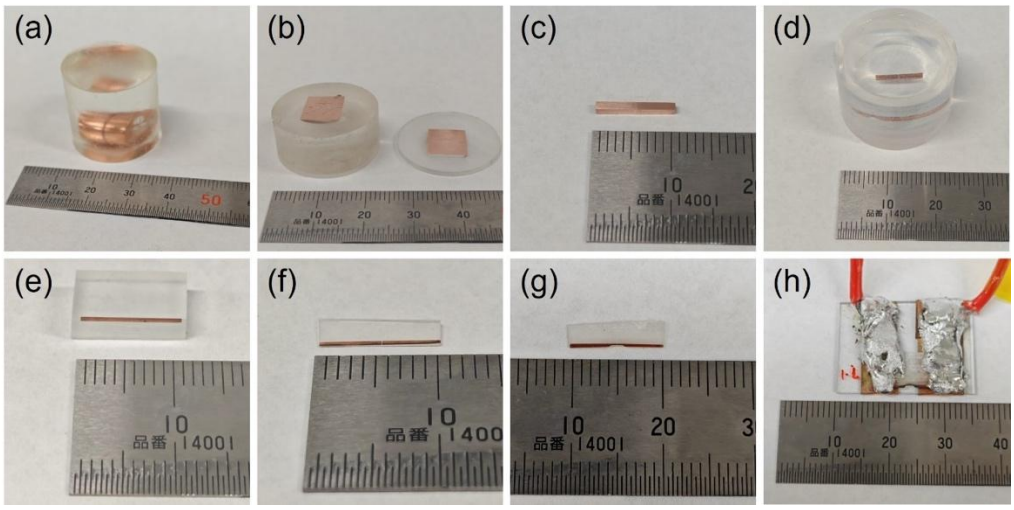

Fig. 5.4 Optical images of EM sample preparation. Optical image of step (a) a, (b) b, (c) c, (d) d, (e) e, (f) f, (g) g, and (h) h in previous schematic diagram.

5.2.5 EM test of Ag-Cu composite joint and Ag joint

Oxidation of Cu is a serious issue during the EM process of Cu stripe [4,5]. In previous studies, the surface Cu stripes were covered by a passive layer to prevent contact between Cu and air [4]. However, the passive layer hindered the observation of morphological changes during EM tests. Herein, we designed an experimental equipment that can automatically provide a reductive atmosphere during the EM process. **Fig. 5.5** presents the optical images and schematic diagram of this equipment. **Fig. 5.5a** illustrates the optical image of the EM equipment. As shown in **Fig. 5.5b**, a beaker that contained 3 mg EG was placed in a plastic box, and the conductive wires of the EM sample passed through the cover and were fixed by glass cement. The box was closed gently and tightly, and the EM sample was hung inside the box by the wires. The plastic box was then tightly sealed with polyamide tape and metal tape. The EM equipment was placed in an oven and connected to a power supply. The EM tests were conducted with a current density of 6×10^4 A/cm^2 at 100 °C for 50, 100, and 200 h. Three positions located at the cathode, middle, and anode in **Fig. 5.3h** were observed by SEM to reveal the morphological changes during the EM process.

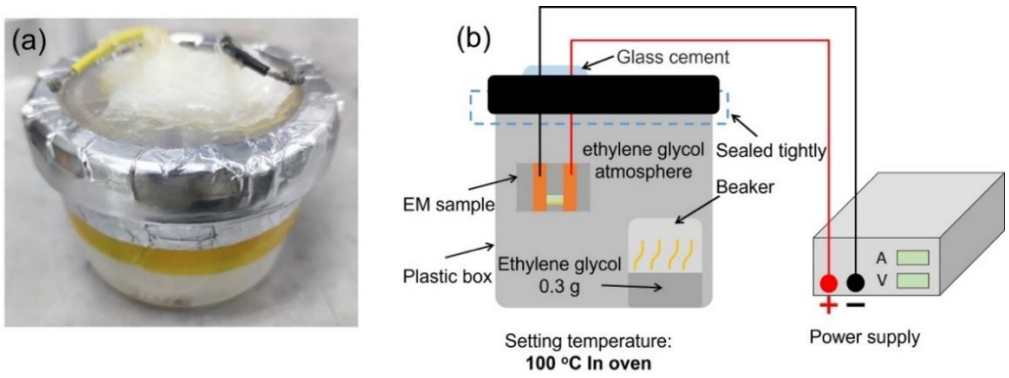

Fig. 5.5 Configuration of EM test. (a) Optical image of EM equipment; (b) Schematic diagram of EM test.

5.2.6 Characterization

The two-step decomposition process as shown in **Fig. 5.1b** and **5.1c** was first conducted in a reflow machine at 180 ºC for 15 min in an N_2 atmosphere with O_2 < 1000 ppm (SMT Scope SK-5000). The second step was conducted in a bonding machine at 230 ºC for 15 min in a formic acid atmosphere (RB-100D, Ayumi Industry Co., Ltd.). The compositions of the thermally decomposed Ag-based complexes were investigated using X-ray diffraction (XRD, Ultima IV, Rigaku). The bonding process was performed using a hot-press machine (RB-100D, Ayumi Industry Co., Ltd.). The cross-section of the sintered Ag joint was fabricated by sandpaper polishing and ion polishing (IB-19530CP, JEOL). The current was provided by a power supply (MS3010D, Xianfeng, China), and the EM tests were conducted in an oven (SH-242 ESPEC). Scanning electron microscope (SEM, FEI Nova Nana SEM 450) and energy dispersive spectrometer (EDS) were used to analyze the microstructure and elemental distribution.

5.3 Results and discussion

5.3.1 Characterization of Ag-Cu composite nanostructures

Chapter 4 confirmed that there is a reaction between the Ag-based complex and Cu substrate during Ag nanostructure preparation, resulting in the formation of Cu compounds. The generated Cu compounds exhibited a higher decomposition temperature of 211 ºC than the Ag-based complex. During bonding in the air, the incomplete decomposition of generated Cu compounds led to organic residuals and Cu oxides inside the Ag joints, which

significantly deteriorated the shear strength. The negative effects of the Cu compounds were eliminated by heating the Ag-based complex on the Cu substrate by a two-step decomposition process in **Fig. 5.1**. The purpose of the first step, 180 ^{o}C in N_2, is to decompose the Ag-based complex whose thermal decomposition temperature is approximately 180 ^{o}C. The purpose of the second step, 230 ^{o}C in formic acid, is to decompose Cu compounds and prevent Cu oxidation. To verify the results of the two-step decomposition process, the obtained nanostructures were characterized by XRD. **Fig. 5.6** shows the XRD patterns of the Ag nanostructures derived from the two-step decomposition process. As shown in **Fig. 5.6**, the XRD pattern of Ag nanostructures derived from the first step exhibited five characteristic peaks of Ag *fcc* crystal, indicating the decomposition of the Ag-based complex. After 15-min heating at 230 ^{o}C in a formic acid atmosphere, Cu characteristic peaks and Ag characteristic peaks were detected in **Fig. 5.6**. **Fig. 5.7**presents the color change of the nanostructure during the two-step decomposition process. The black color of NS-N_2-180 in **Fig. 5.7a** could be attributed to Cu compounds. Comparing **Fig. 5.7a** and **5.7b**, the color changed from black to purple. In summary, the results in **Fig. 5.6** and **Fig. 5.7** confirmed the generation of Cu, indicating that the target of each step was successfully achieved.

The XRD patterns and optical images in **Fig. 5.6** and **Fig. 5.7** demonstrated that the Ag-based complex and Cu compounds decomposed at 180 ^{o}C and 230 ^{o}C, respectively. The morphological changes during the two-step decomposition process were characterized by SEM observation. The top surfaces of the two nanostructures are shown in **Fig. 5.8.** Rugged surfaces with huge grooves were observed in **Fig. 5.8a** and **b**. The amplified SEM image in **Fig. 5.8a$_1$** demonstrated that abundant nanoparticles were uniformly distributed on a solid

gray film. This film may be attributed to incompletely decomposed Cu compounds. As the heating temperature increased to 230 °C, the solid gray substance was converted into massive particles in **Fig. 5.8b1**. This morphological change could be due to the decomposition of Cu compounds. NS-FA-230 was characterized by EDS to confirm the decomposition of Cu compounds. **Fig. 5.9** depicts the EDS results of NS-FA-230. Element Cu with high intensity was detected in **Fig. 5.9c**, which corresponds to the position of the microparticles in **Fig. 5.9a** and **5.9b**. This indicated that the generated Cu compounds successfully decomposed to Cu particles, resulting in Ag-Cu composite nanostructures.

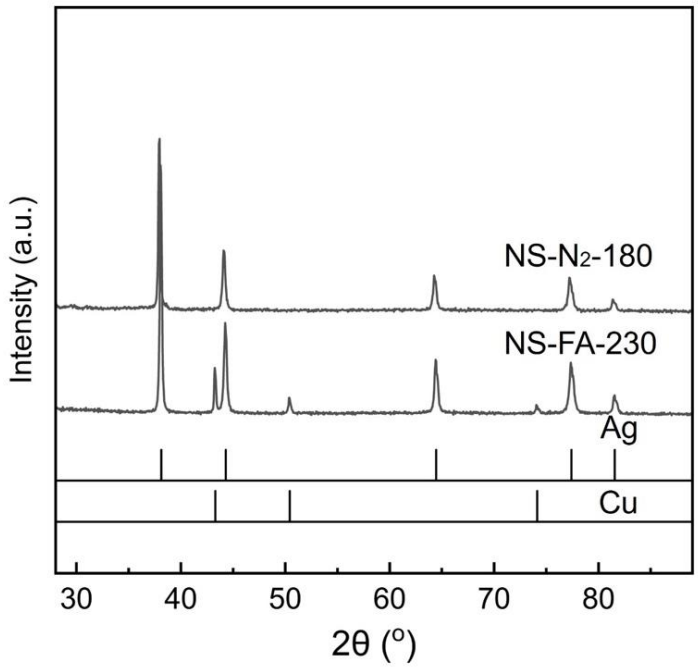

Fig. 5.6 XRD of NS-N_2-180 and NS-FA-230.

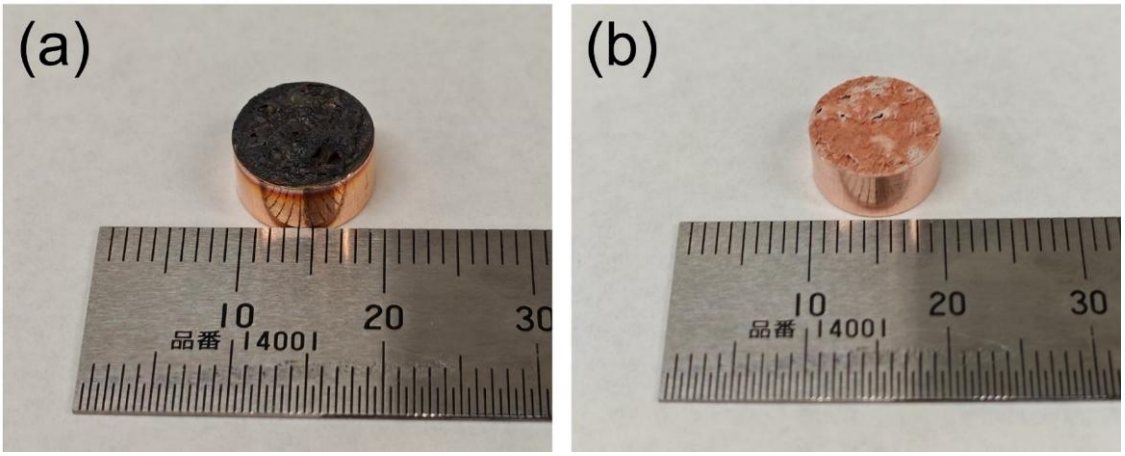

Fig. 5.7 Optical image of (a) NS-N2-180 and (b) NS-FA-230.

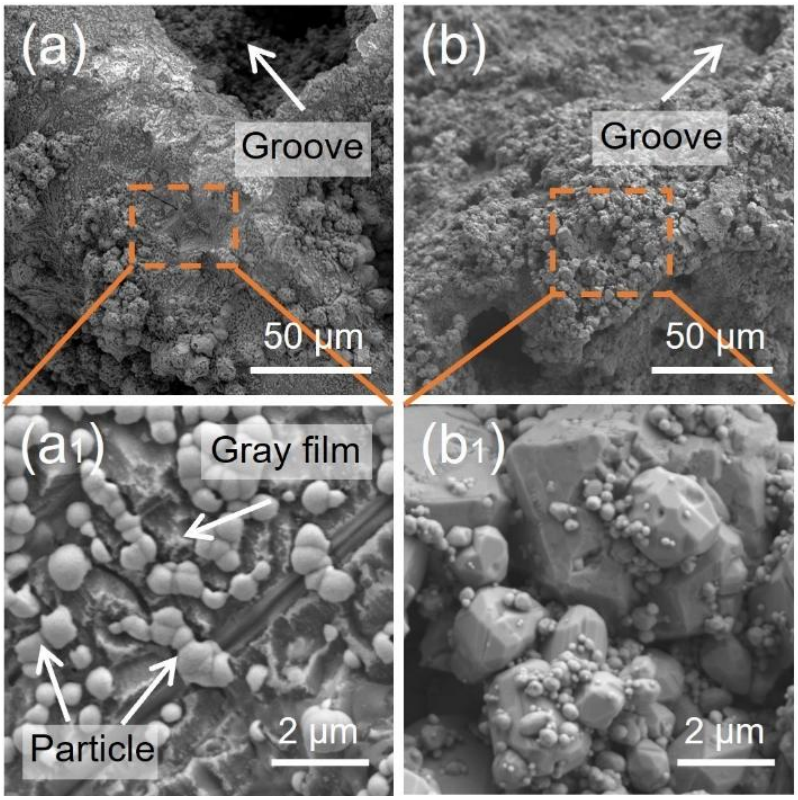

Fig. 5.8 Morphological changes of top surface during the two-step decomposition process. SEM images of (a) (a_1) NS-N_2-180 and (b) (b_1) NS-FA-230.

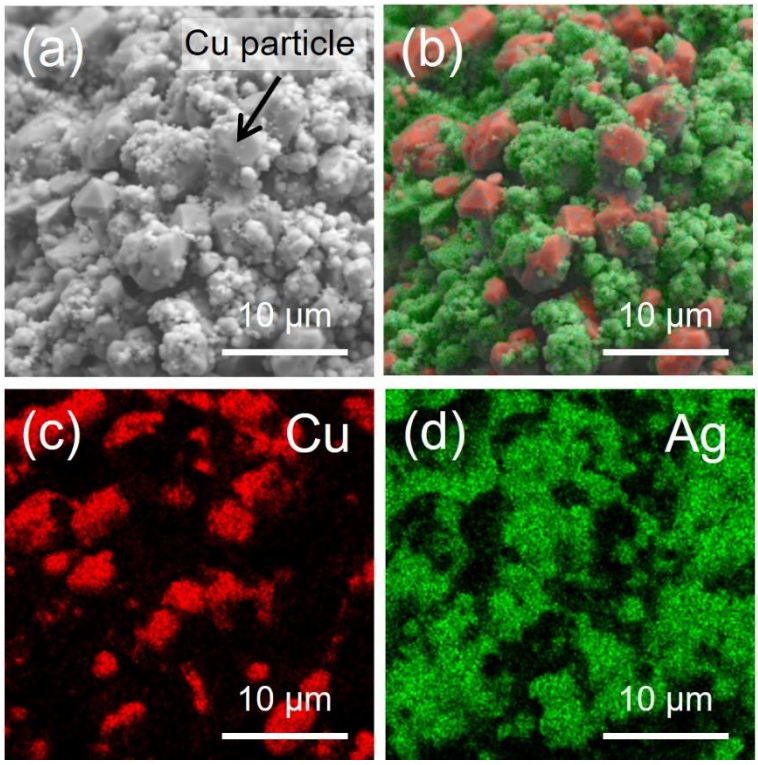

Fig. 5.9 Element distribution of Ag-Cu composite nanostructure. (a) SEM image of NS-FA-230 and corresponding EDS map of (b) overall, (c) Cu and (d) Ag.

Internal changes during the Ag-Cu composite nanostructure preparation were investigated by cross-sectional observations. **Fig. 5.10** presents the cross-sections of NS-N_2-180 and NS-FA-230. The SEM images in **Fig. 5.10a** and **5.10b** demonstrated that the cross-sections of NS-N_2-180 and NS-FA-230 exhibited a wave structure with huge pores. Three typical regions, top, middle, and bottom, of the cross-section were amplified to reveal the internal morphology of NS-N_2-180 and NS-FA-230. **Fig. 5.10a$_{1\text{-}3}$** and **5.10b$_{1\text{-}3}$** show the amplified SEM images. As depicted in **Fig. 5.10a$_{1\text{-}3}$**, abundant particles were observed along with organics. The particles and organics could be attributed to the decomposition of the Ag-based complex and the generation of Cu compounds, respectively. In terms of NS-FA-230, only particles were observed in **Fig. 5.10b$_1$-b$_3$**, indicating the decomposition of Cu compounds.

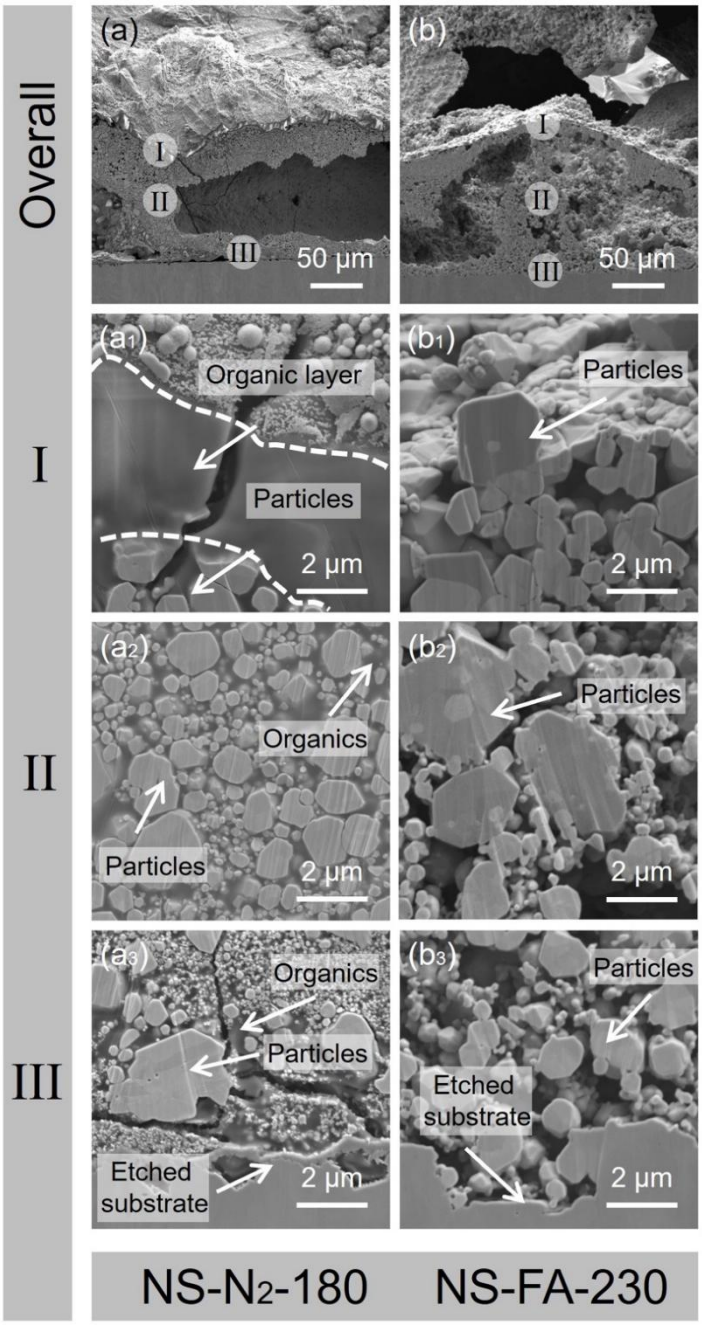

Fig. 5.10 Cross-section of nanostructures. (a) Cross-section of NS-N2-180. (a_1) (a_2) (a_3) Corresponding magnified SEM image of I, II and III in (a), respectively. (b) Cross-section of NS-FA-230. (b_1) (b_2) (b_3) Corresponding magnified SEM image of I, II and III in (b), respectively.

Fig. 5.10 demonstrates that the nanostructures underwent a noticeable morphological change during the two-step decomposition process. The observed morphological change was investigated using EDS. **Fig. 5.11** shows the EDS results of NS-N_2-180. Element Ag with high intensity was detected at the left bottom of **Fig. 5.11c**, corresponding to the particles in **Fig. 5.11a** and **5.11b** and indicating that the particles in **Fig. 5.10a$_1$-a$_3$** are Ag particles. As shown in **Fig. 5.11d-f**, Cu, C, and O were detected at the position of organics in **Fig. 5.11a** and **5.11b**, indicating that the organics in **Fig.5.10a$_{1-3}$** were Cu compounds. In Chapter 3, we have confirmed that the reaction between the Ag-based complex and Cu substrate resulted in Cu compounds with a high decomposition temperature of 211 ^{o}C. Heating at 180 ^{o}C was enough to decompose the Ag-based complex but not to Cu compounds, which was why NS-N_2-180 consisted of particles and organics. In addition, there was a larger amount of organics in **Fig. 5.10a$_1$** than in **Fig. 5.10a$_2$** and **5.10a$_3$.** This was because the Ag-based complex decomposed to Ag and reacted with Cu substrates simultaneously. Due to the density difference, Ag particles with higher density moved downwards and Cu compounds with lower density moved in the opposite direction. As a result, the accumulated Cu compounds led to an organic layer on the top of NS-N_2-180 in **Fig. 5.10a** and **5.10a$_1$**.

Fig. 5.12 shows the detailed EDS results of NS-FA-230. Randomly distributed dotted Cu and continuous Ag were detected in **Fig. 5.12c** and **d**, respectively, indicating the decomposition of Cu compounds during the second step of the two-step decomposition process. Cu with high intensity was detected in **Fig. 12g**, which demonstrated that the products of Cu compound decomposition in the nanostructures were Cu particles. Additionally, the decomposition of the Cu compound layer resulted in a Cu rich layer on the

top surface of NS-FA-230 in **Fig. 5.12c** and **g**. In the middle and bottom regions of NS-FA-230, the decomposition of Cu compounds resulted in randomly distributed Cu particles in **Fig. 5.12k** and **5.12o**. Notably, some Ag nanoparticles were embedded inside Cu particles as shown in **Fig. 5.10b$_1$** and **5.10b$_2$**, which could be attributed to the fact that some Ag nanoparticles acted as seeds to facilitate the nucleation of Cu during the decomposition of Cu compounds [6]. In summary, the two-step decomposition process resolved the issues of organics and Cu oxidation derived from Cu compounds. The obtained Ag-Cu composite nanostructures are expected to be used to fabricate Ag-Cu composite joints.

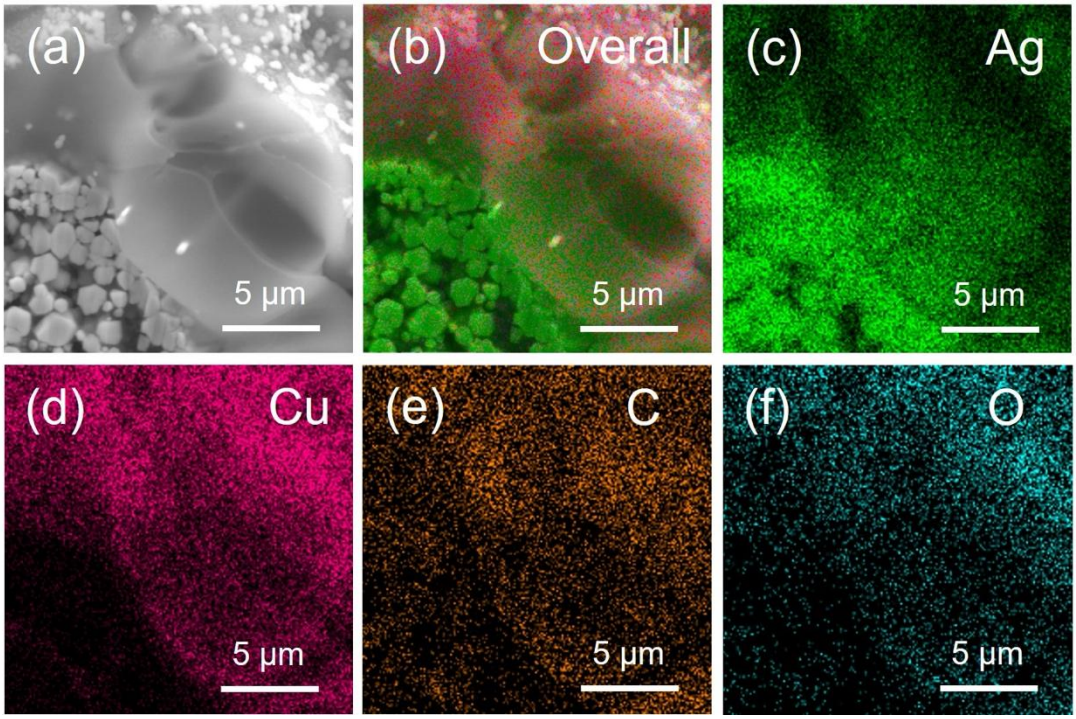

Fig. 5.11 Element distribution of the top region of NS-N_2-180. (a) SEM image and corresponding EDS map of (b) overall, (c) Ag, (d) Cu, (e) C, and (f) O of the top region of NS-N_2-180.

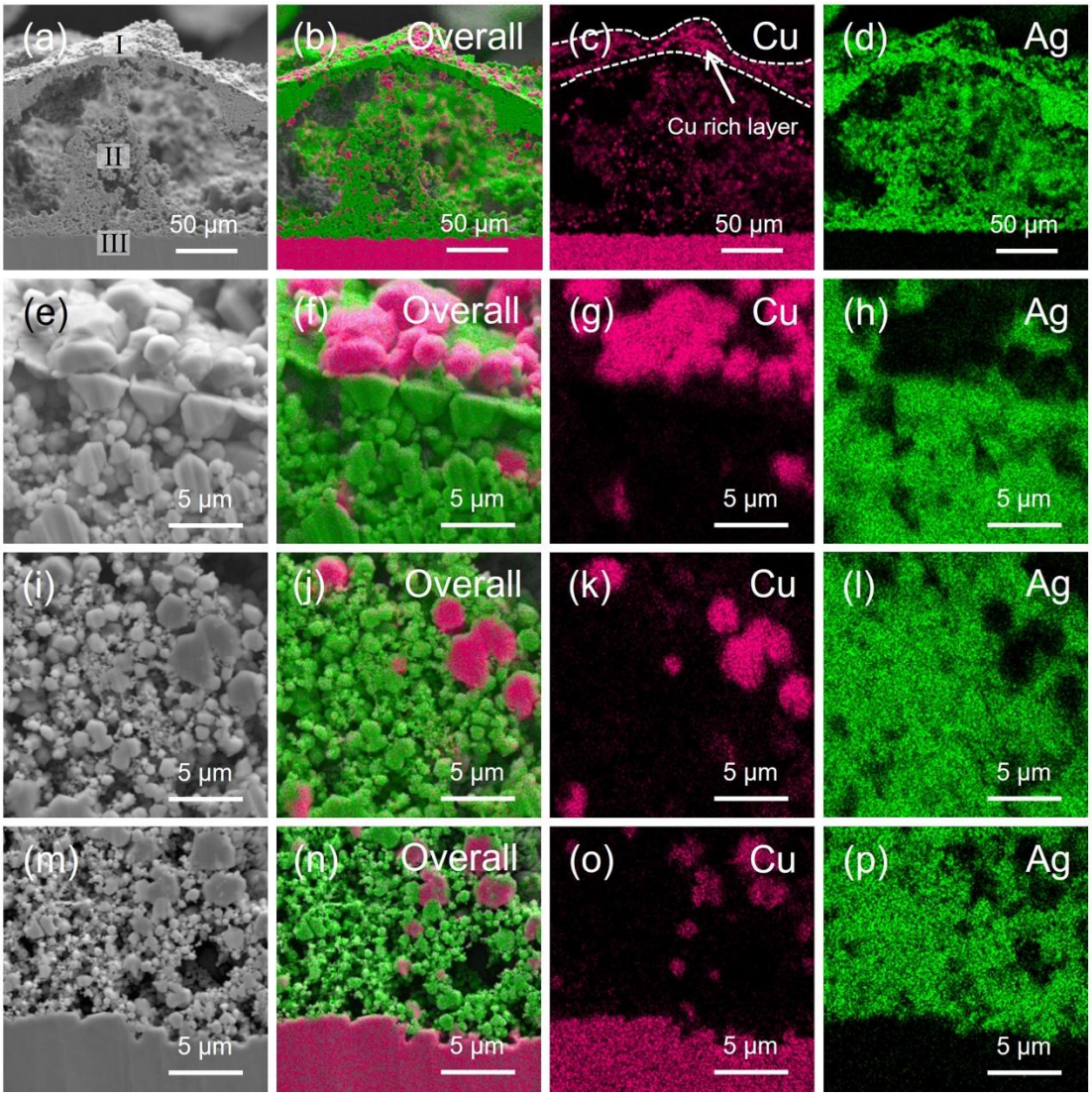

Fig. 5.12 Element distribution of Ag-Cu composite nanostructure. (a) SEM image and corresponding EDS map of (b) overall, (c) Cu, and (d) Ag of NS-FA-230. (e) SEM image and corresponding EDS map of (f) overall, (g) Cu, and (h) of region I in NS-FA-230. (i) SEM image and corresponding EDS map of (j) overall, (k) Cu, and (l) of region II in NS-FA-230. (m) SEM image and corresponding EDS map of (n) overall, (o) Cu, and (p) of region III in NS-FA-230.

Fig. 5.13 presents a schematic diagram illustrating the formation process of Ag-Cu composite nanostructures during the two-step decomposition process. In the first step, the Ag-based complex started to decompose with the elevated temperature. At the same time, the

Ag-based complex (Ag^{+}) reacted with the Cu (0) substrate, resulting in Cu compounds (Cu^{2+}) with a higher decomposition temperature of 211 ºC. A heating temperature of 180 ºC is enough to decompose the Ag-based complex but not for Cu compounds. Ag particles derived from the decomposition of the Ag-based complex exhibit a higher density than the Cu compounds. Thus, the Ag particles and Cu compounds tended to move downwards and upwards in the remaining liquid insufficiently decomposed Ag-based complex, respectively. The upward movement of the Cu compounds led to an organic layer at the top surface. In the second step, a heating temperature of 230 ºC decomposed Cu compounds. Consequently, the organics layer at the top region and tapped organics at the middle and bottom regions decomposed to a Cu rich layer and randomly distributed Cu particles, respectively. Finally, the two-step decomposition process yielded Ag- Cu composite nanostructures.

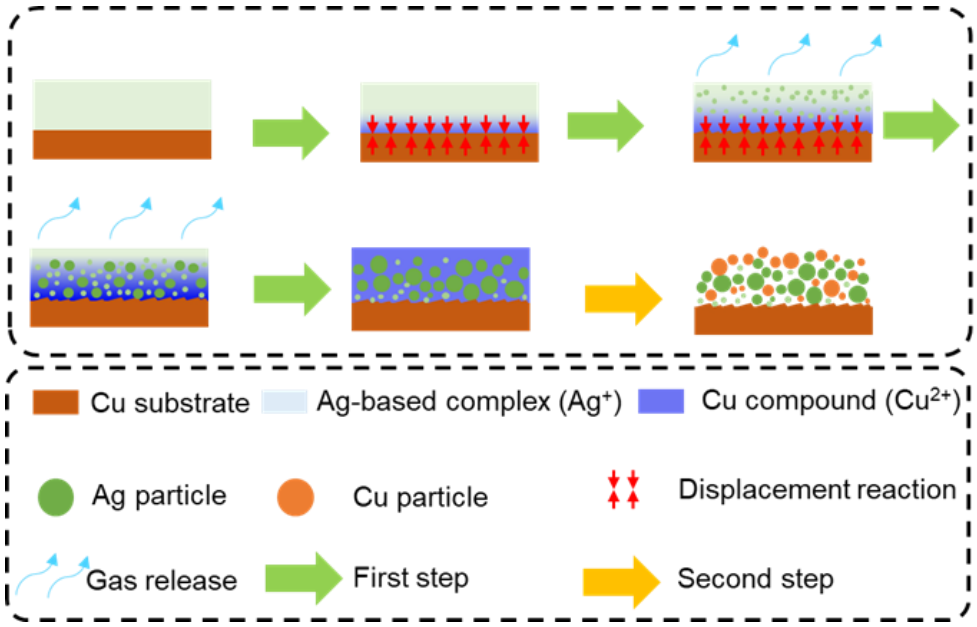

Fig. 5.13. Schematic diagram illustrating the decomposition of Ag-based complex during the two-step decomposition process.

5.3.2 Characterization of Ag-Cu composite joints

The above results demonstrated that the designed two-step decomposition process fabricated Ag-Cu composite nanostructures. However, the feasibility of using the Ag-Cu composite nanostructure remains unknown. As Cu oxidation affected the die-bonding negatively, the bonding of Ag-Cu composite nanostructures was conducted in a formic acid atmosphere [7,8]. The shear strength of the sintered Ag-Cu composite joints was measured by shear tests. **Fig. 5.14** depicts the shear strength of the Ag-Cu composite joints. The shear strength increased with the increasing temperature, and an average shear strength of 30.8 MPa at 220 ºC indicated that the bonding of the Ag-Cu composite nanostructures resulted in robust joints. This indicated that the serious issues of Cu compounds were overcome, rendering the Cu substrate acceptable for Ag-based complexes in die-bonding.

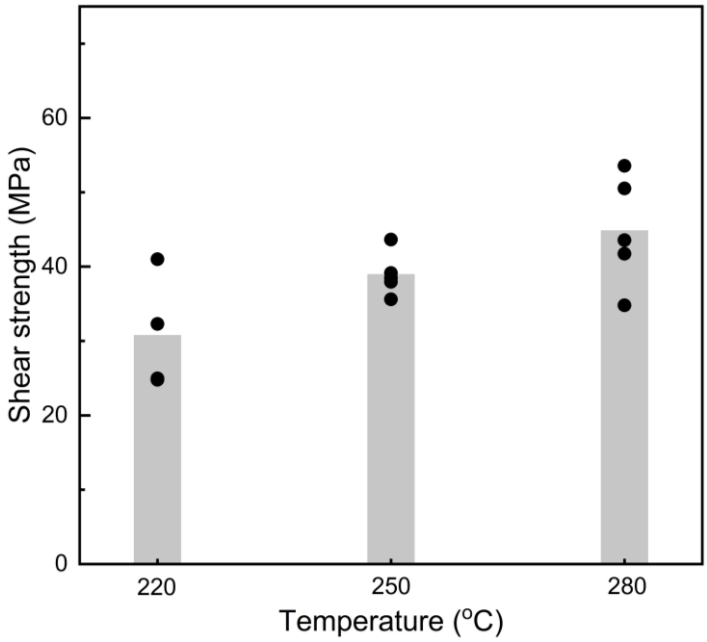

Fig. 5.14 Evolution of shear strength with bonding temperature.

Joint properties such as shear strength and thermal conductivity are related to joint morphology such as neck number and thickness and pore diameter and shape [9–11]. To reveal the evolution of shear strength with temperature, the cross-section of Ag-Cu composite joints was characterized by SEM observation. **Fig. 5.15** shows the cross-sections of the Ag-Cu composite joints. Cu rich lines were observed in the overviews of cross-sections in **Fig. 5.15a-c**, which could be attributed to the Cu rich layer on the top surface of the Ag-Cu composite nanostructures in **Fig. 5.12c** and **5.12g**. The amplified SEM image in **Fig. 5.15a$_1$** demonstrated that thick necks and close contact were formed within the Ag-Cu composite joints at 220 ºC. The pore size reduced significantly as the bonding temperature increased to 250 ºC in **Fig. 5.15b$_1$**. In addition, the approximate round Cu particles in **Fig. 5.15a$_1$** became irregular Cu in **Fig. 5.15b$_1$**. The pore shrinkage and Cu particle deformation could be due to atom diffusion during the bonding process [9,12]. In addition, interdiffusion between the Ag phase and Cu phase could occur during this process [13]. The diffusion coefficient of Cu atoms into Ag lattices is 1.5×10^{-12} cm^2/s at 300 ºC [14]. Even at a higher temperature of 455 ºC, the diffusion coefficient of Ag atoms into Cu lattices is 8.4×10^{-15} cm^2/s, which is lower than that of Cu into Ag [15]. The difference in the diffusion coefficient meant that more Cu atoms diffused into the Ag phase, resulting in irregular Cu. When the bonding temperature increased from 250 ºC to 280 ºC, the irregular pores in **Fig. 5.15b$_1$** were converted into approximate spherical pores in **Fig. 5.15c$_1$**, indicating a high sintering degree [9]. These morphology changes demonstrate that the elevated temperature promoted the sintering of Ag-Cu composite joints, increasing the shear strength in **Fig. 5.14**.

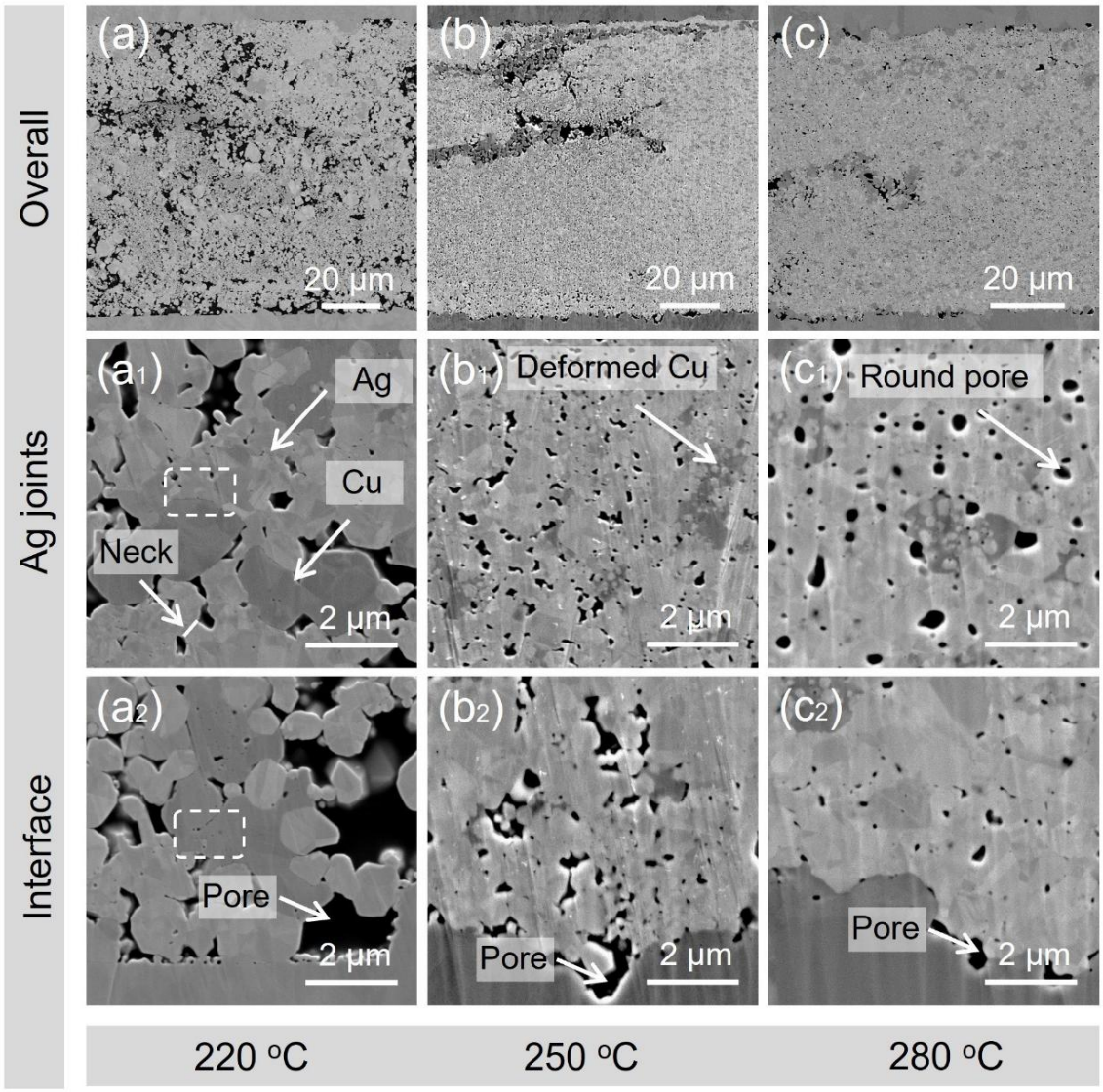

Fig. 5.15 Cross-section of Ag-Cu composite joints. SEM images of cross-section of Ag-Cu composite joints obtained at (a)-(a_2) 220 °C, (b)-(b_2) 250 °C, and (c)-(c_2) 280 °C.

The reaction between the Ag-based complex and Cu substrate resulted in the depletion of Cu substrate and the rugged top surface of the Cu substrate. This rugged top surface led to large pores between the sintered Ag-Cu and Cu substrate in **Fig. 5.15a2**. When the bonding temperature increased to 250 °C and 280 °C, the volume of the pores between sintered Ag-Cu reduced significantly because elevated temperature promotes the mass transport for

sintering [16]. Considering pores are vacancies, the Ag and Cu atoms were driven toward the pores with accelerated mass transport, reducing the volume of pores in **Fig. 5.15b2** and **c2** [17,18]. Simultaneously, the connection between the sintered Ag-Cu and Cu substrate was enhanced, increasing the shear strength in **Fig. 5.14**.

A schematic diagram was drawn to illustrate the bonding process of Ag-Cu composite nanostructures. **Fig. 5.16** shows the bonding process of Ag-Cu composite nanostructures and the distribution of Cu phase within the Ag-Cu composite joints. At the initial stage, neck formation with elevated bonding temperatures resulted in close connections among the particles of the Ag-Cu composite nanostructures. The neck formation provided diffusion paths for densification, which reduced the pore size within the sintered Ag-Cu layer and at the interface region. This increased the density of the Ag-Cu composite joints and the shear strength in **Fig. 4.14**. In addition, the Cu rich layer on the top surface of the nanostructures led to a Cu rich line within the Ag-Cu composite joints, and the approximate spherical Cu particles were transformed into irregular Cu phases during the bonding process. This indicated that Cu particles also participated in the bonding of the Ag-Cu composite nanostructures.

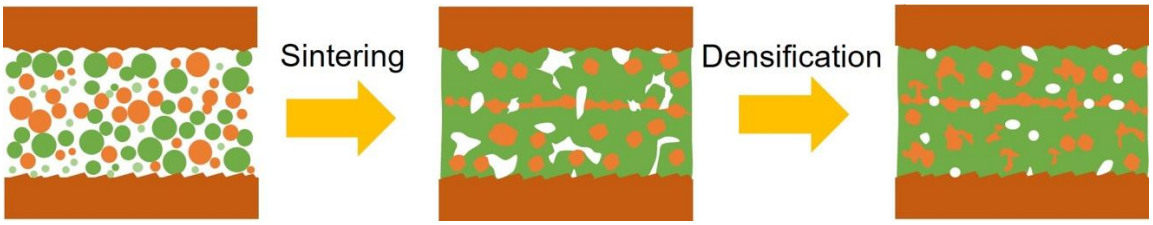

Fig. 5.16 Schematic diagram depicting the bonding process of Ag-Cu composite nanostructures.

Besides thermal and electrical conductivity, Ag and Cu also exhibit excellent ductility. During the die shear test, elevated external force tends to cause the deformation of Ag or Cu sintered joints [19]. The deformation on the fracture surface is usually regarded as an index that reveals the evolution of the shear strength of the joints [20]. **Fig. 5.17** shows the fracture surfaces of the Ag-Cu composite joints. **Fig. 5.17a-c** present the overall fracture surface of Ag-Cu composited joints. Ductile deformations were observed in the fracture surfaces of **Fig. 5.17a$_1$-c$_1$**, indicating a strong connection within the Ag-Cu composite joints [20]. To reveal the relationship between the fracture surface and shear strength evolution, the white rectangle areas in **Fig. 5.17a$_1$-c$_1$** were displayed by amplified SEM images. Even though ductile deformations were observed in **Fig. 5.17a$_2$**, the large pores and isolated spherical particles indicated insufficient sintering within the nanostructures. When the bonding temperature increased to 250 ºC, large pores disappeared, and spherical particles were integrated into the sintered Ag-Cu in **Fig. 5.17b$_2$**. Furthermore, continuous ductile deformations were observed indicating that the sintering of the Ag-Cu composite nanostructure was enhanced. As the bonding temperature increased to 280 ºC, the fracture surface in **Fig. 5.17c$_2$** was full of ductile deformations, indicating a high sintering degree. In summary, the inhomogeneous fracture surface was converted into a homogeneous fracture when the bonding temperature increased from 220 ºC to 280 ºC because the elevated bonding temperature enhanced the mass transport responsible for particle sintering, which increased the interconnection within the sintered Ag-Cu and the shear strength in **Fig. 5. 14**.

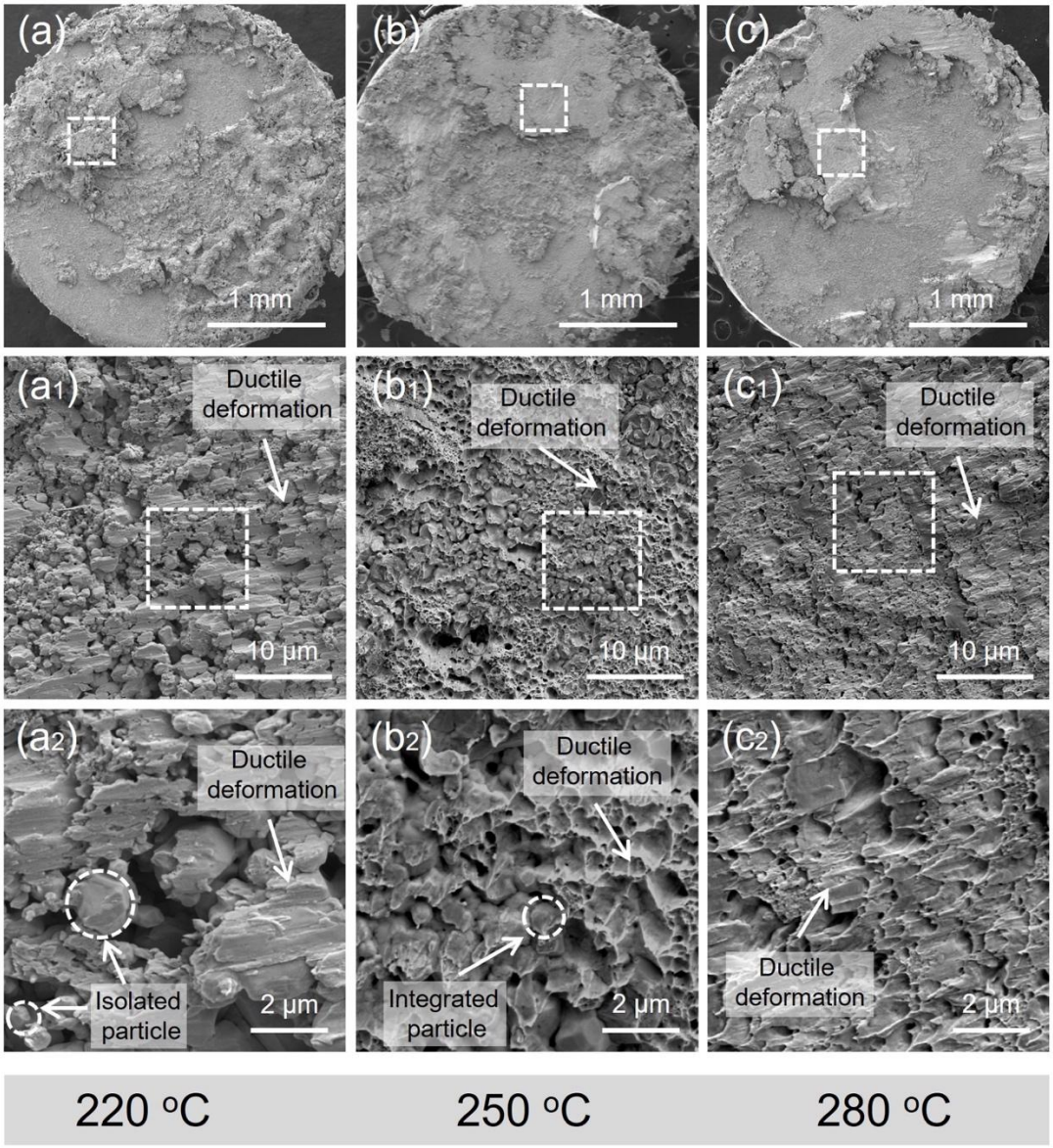

Fig. 5.17 Cross-section of Ag-Cu composite joints. SEM images of the cross-section of Ag-Cu composite joints obtained at (a)-(a_2) 220 °C, (b)-(b_2) 250 °C, and (c)-(c_2) 280 °C.

After die-shear tests, visible Cu in the cross-sections of **Fig. 5.15** became invisible in the fracture surface of **Fig. 5.17**. To figure out the role of Cu during die-shear tests, the fracture surface of Ag-Cu composite joints derived from 280 °C was characterized by EDS. **Fig. 5.18** shows the EDS results of the fracture surface. Element Cu and Ag with high intensity in **Fig.**

5.18c and **5.18d** indicated that the fully deformed fracture surface in **Fig. 5.18a** consisted of Ag and Cu. The deformed Cu in **Fig. 5.18a** and **5.18b** indicated that the Cu component participated in the bonding of Ag-Cu composite nanostructures and was important in providing mechanical strength for the Ag-Cu composite joints [21]. Previous studies reported that diffusion between doped particles and Ag particles was difficult during the preparation of Ag-AlN, Ag-SiC, and Ag-diamond composite joints, which deteriorated the bonding performance [22–24]. In addition, the doped particles only filled the pores of porous sintered Ag instead of providing strength. Therefore, Ag-Cu composite nanostructures derived from the thermal decomposition of Ag-based complex could be a better choice when preparing Ag composite joints.

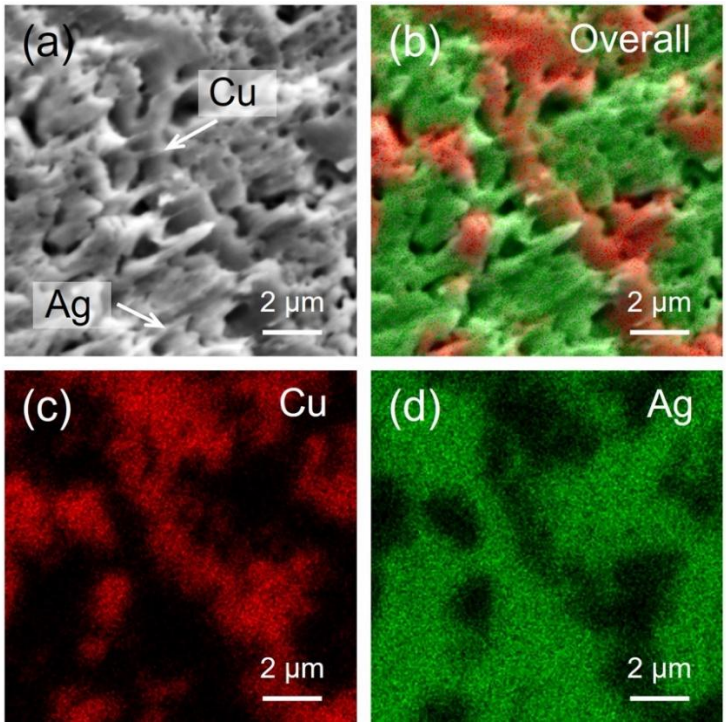

Fig. 5.18 Element distribution of fracture surface of Ag-Cu composite joint obtained at 280 °C. (a) SEM image of fracture surface and corresponding EDS map of (b) overall, (c) Ag and (d) Cu.

5.3.3 EM behavior of Ag-Cu composite joints and Ag joints

Besides the high-temperature reliability, sintered Ag provides mechanical support, facilitates electrical connections, and promotes heat dissipation from the dies [25–29]. However, a serious issue of sintered Ag is poor EM resistance, which is one of the common causes of interconnection failures [30]. Previous studies have demonstrated that Cu exhibited comparable thermal and electrical conductivity to Ag and had significantly better EM resistance than Ag [31]. Many previous studies expected that Ag-Cu composite joints would improve the EM resistance [1–3]. However, the EM properties of Ag or Ag-Cu composite joints are rarely studied because it is difficult to reduce the size of joints to a micron scale. In this study, the EM sample of pure Ag joints and Ag-Cu composite joints were prepared according to the flow in **Fig. 5.3**. The current density and temperature of the EM test were set to 6×10^4 A/cm^2 and 100 ^{o}C, respectively. **Fig. 5.19** and **Fig. A-2.1** show the morphological changes of EM-Ag-Cu with EM time. **Fig. 5.19a-c** and **Fig. A-2.1a-c** demonstrate that the morphology of the EM-Ag-Cu underwent a subtle change as the EM time increased from 0 h to 100 h. This subtle change was investigated by the amplified SEM images in **Fig. 5.19a$_1$-a$_3$**, **5.19b$_1$-b$_3$**, and **5.19c$_1$-c$_3$**. Cross-sections with neat surfaces were observed in **Fig. 5.19a$_1$-a$_3$**. As the EM time increased to 50h, abundant nanoparticles appeared on the surface of the Ag phase in **Fig. 5.19b$_{1-3}$**, but the Cu phase maintained a neat surface in **Fig. 5.19b$_3$**. As shown in **Fig. 5.19c$_{1-3}$**, the generated nanoparticles on the Ag phase experienced apparent growth when the EM time increased from 50 h to 100 h. However, the Cu phase continued to maintain a neat surface. As the EM time increased to 200 h, the surface of EM-Ag-Cu became brush-like in **Fig. 5.19d**, which resulted from the generation of Ag

whiskers and nodule-like Ag hillocks on the Ag phase according to the magnified SEM images in **Fig. 5.19d$_{1\text{-}3}$**. In addition, the Cu phase with neat surfaces in **Fig. 5.19d$_3$** confirmed that the EM resistance of Cu was much better than Ag.

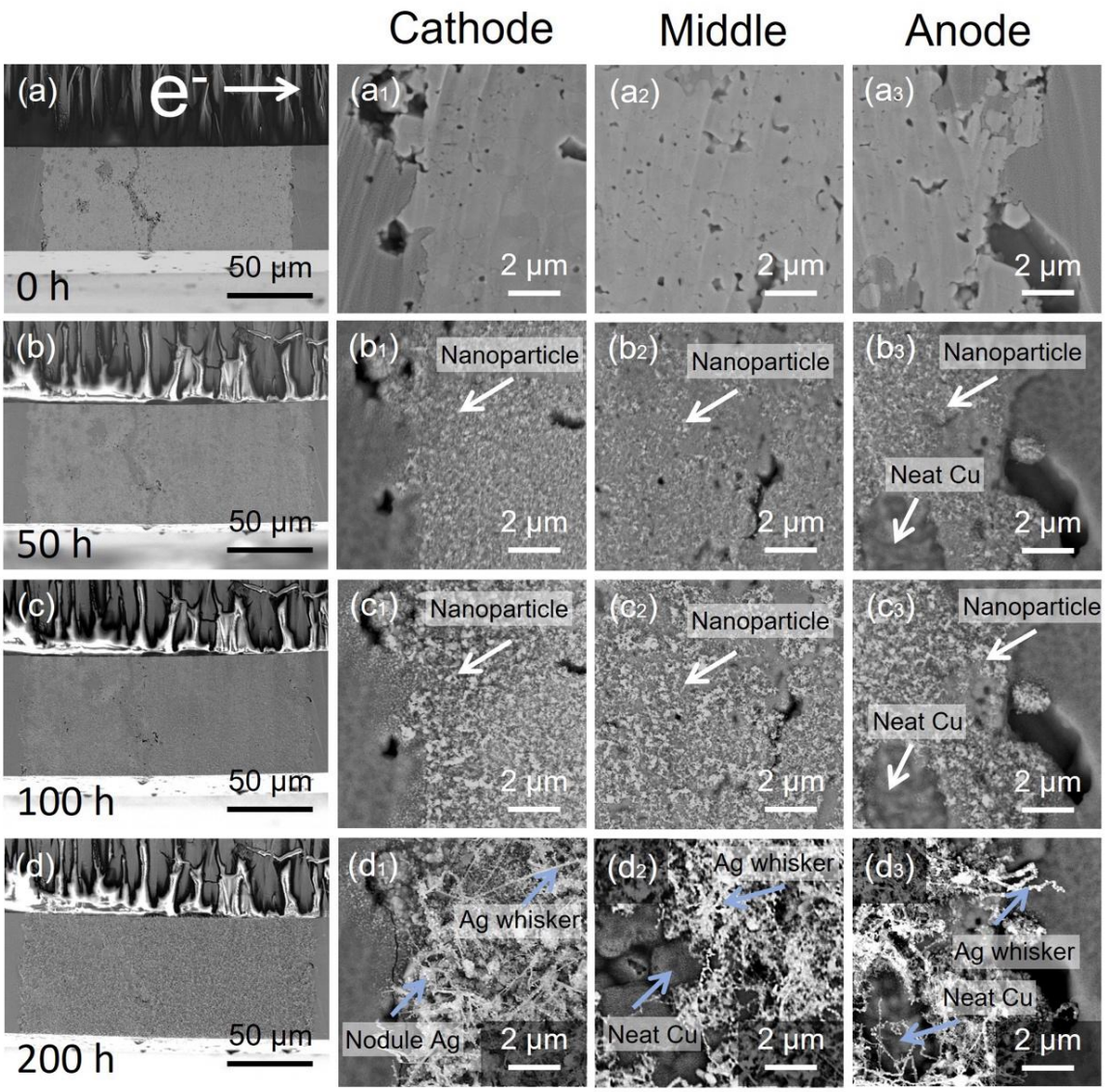

Fig. 5.19 Morphological changes of EM-Ag-Cu with EM time. SEM images of EM-Ag-Cu with EM time for (a)-(a$_3$) 0 h, (b)-(b$_3$) 50 h, (c)-(c$_3$) 100 h and (d)-(d$_3$) 200 h.

The EM behaviors of EM-Ag-Cu were investigated in **Fig. 5.19**. However, the EM behaviors of Ag joints remain unclear. The EM behaviors of the Ag joints and Ag-Cu composite joints were compared by the EM test of the Ag joints under the same conditions as the Ag-Cu composite joints. **Fig. 5.20** and **Fig. A-2.2** show the morphology changes of EM-Ag during the EM process. **Fig. 5.20a-c** shows that Ag particles appeared on the surface of EM-Ag when the EM time increased to 50 h and 100h. Comparing **Fig. 5.20a$_{1-3}$** and **b$_{1-3}$** revealed some emerging nanoparticles and pits as the EM time increased to 50 h. In addition, all emerging pits were distributed at the boundaries of the Ag grains, indicating depletion of Ag at the boundaries. Unlike EM-Ag-Cu, the EM of EM-Ag demonstrated non-uniform morphology changes at the cathode side and anode side. Comparing **Fig. 5.19b$_3$** and **5.19c$_3$** determined that the size of emerging particles demonstrated a negligible change as the EM time extended from 50 h to 100 h. By contrast, the particles in the white circles of **Fig. 5.20b$_3$** and **5.20c$_3$** grew apparently, which indicated that the Ag atoms migrated from the cathode side to the anode side during the EM process [30]. The grain in the orange quadrangle of **Fig. 5.20a$_3$** and **b$_3$** disappeared in **Fig. 5.20c$_3$**. This is because the dislocation induced by current stress destroyed the lattice structures of Ag [32]. Furthermore, the size of pits in **Fig. 5.20b$_{1-3}$** and **Fig. 5.20c$_{1-3}$** increased with the extended EM time, indicating that more Ag atoms had migrated. As the EM time increased to 200 h, two brushy belts were observed at the two interfaces in **Fig. 5.20d**. Magnified SEM images in **Fig. 5.20d$_1$** and **5.20d$_3$** demonstrated that the two brush-like belts consisted of Ag whiskers and nodule-like Ag hillocks.

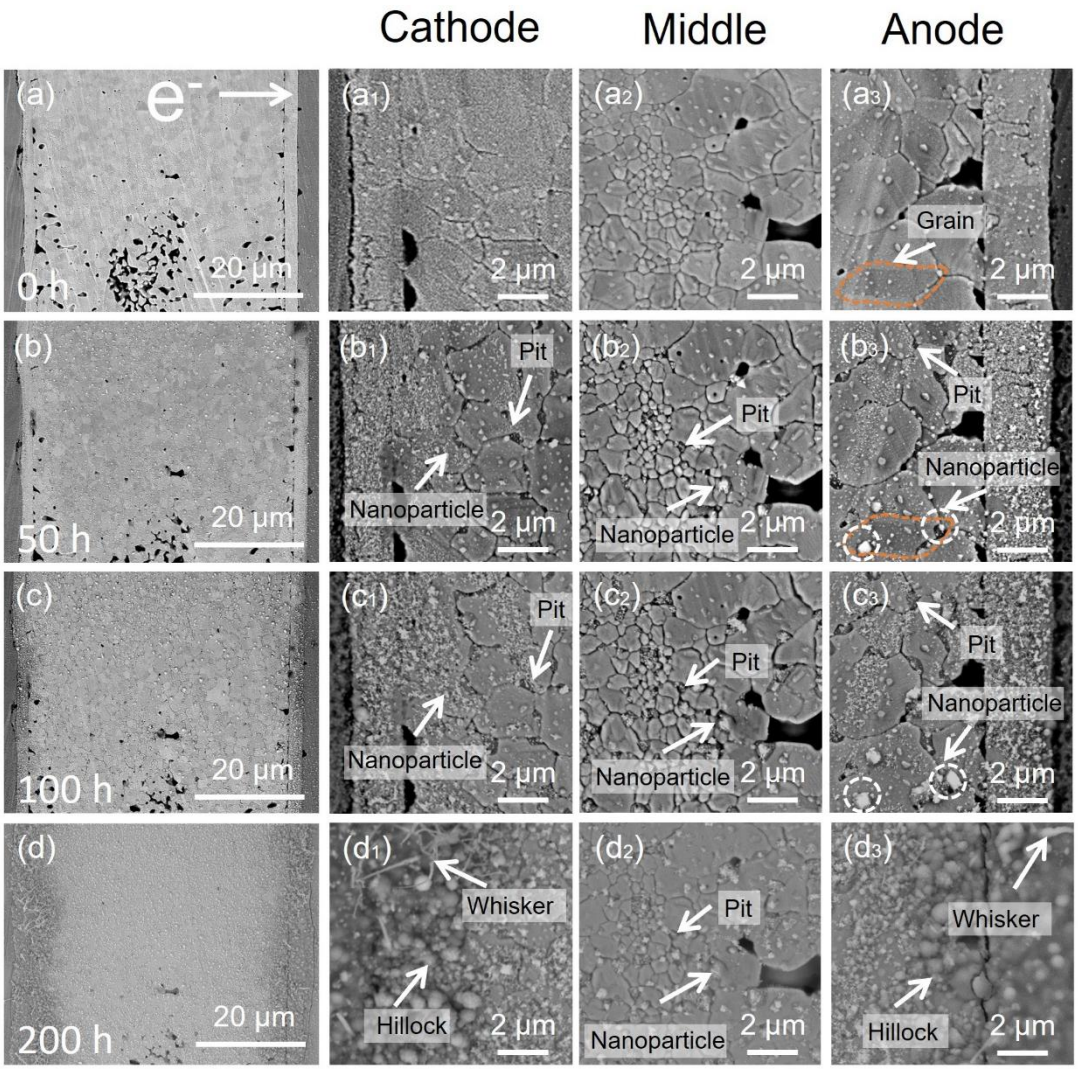

Fig. 5.20 Morphological changes of EM-Ag with EM time. SEM images of EM-Ag with EM time for (a)-(a_3) 0 h, (b)-(b_3) 50 h, (c)-(c_3) 100 h, and (d)-(d_3) 200 h.

In previous studies, the EM of metal stripes usually resulted in pores at the cathode side and hillocks or particles at the anode side [30]. However, the generated Ag nanoparticles and whiskers are uniformly distributed on the surface of EM-Ag-Cu. We have created schematic diagrams to compare the EM behaviors of EM-Ag-Cu and EM-Ag. **Fig. 5.21** shows schematic diagrams illustrating the morphology change during the EM process. When a

current is applied to a metal interconnect, the momentum of the electrons is transferred to the atoms, and atoms will be displaced from their lattice position if the current density reaches a threshold value [32,33]. The movement of atoms along the direction of electron flow results in atomic flux, which can be considered a kind of self-diffusion in response to the applied current and is described by Equation 5.1 [34]:

$$J = -\frac{DC}{kT}\left(Z^{*}eE - \Omega\frac{\delta\sigma}{\delta x}\right) \quad 5.1$$

Here, D represents the diffusivity, C denotes the atom concentration, T is the absolute temperature, k is Boltzmann's constant, Z^{*} is the effective charge number, e is the fundamental electronic charge, E is the electric field, Ω is the atomic volume, and $\frac{\delta\sigma}{\delta x}$ represents the stress gradient along the line.

Many paths are associated with the diffusion of atoms, such as bulk, grain boundary, and free surface. The activation energy of the different diffusion paths in Ag and Cu is listed in **Table 5.1** [35–38]. **Table 5.1** shows that surface diffusion of the two metals exhibits the lowest activation energy, indicating the lowest energy barrier. Consequently, surface

Table 5.1 Activation energies associated with different diffusion paths in Ag and Cu [35–38].

Diffusion path	Ag	Ref.	Cu	Ref
Bulk diffusion	1.95 eV	[35]	2.2 eV	[38]
Grain boundary diffusion	0.78-0.93eV	[35,36]	0.88-0.95 eV	[38]
Surface diffusion	0.3-0.6 eV	[37]	0.8-0.9 eV	[38]

could play a dominant role in the EM process. As a result, atoms are driven by the electron wind and move along the surface during the EM process, resulting in nanoparticles on the surfaces [38,39]. Nanoparticles only appeared on the surface of the Ag phase, and the Cu phase retained a naked surface in **Fig. 5.19b$_3$, 5.19c$_3$**, and **Fig. 5.21a$_1$, 5.21b$_1$**. This is because the activation energy of the surface diffusion of Ag is lower than that of Cu in **Table 5.1**. This contributes to the fact that Ag atoms migrate more easily than Cu during the EM process, agreeing with the results in a previous study [31].

Fig. 5.21a$_2$ and **5.21b$_2$** demonstrate that whiskers formed on the surface of Ag phases as the EM time increased to 200 h. The growth of whiskers was driven by compressive stress release [30,40,41]. There are two possible routes for the formation of compressive stress in EM-Ag-Cu: I) electron flow-induced lattice strain [42] and II) coefficient of thermal expansion (CTE) mismatch between the Ag phase and Cu phase [43]. The impingement of wind force could cause breakage, discontinuity, and slippage of planes during the EM process [32,44,45]. These changes in atomic scale result in high dislocation density and lattice strain, and higher current density leads to higher strain. The generation of lattice strain contributes to the build-up of compressive stress [42]. Joule heating and applied temperature of 100 ^{o}C increased the temperature of the EM sample, which was approximately 109.3 ^{o}C [46]. The difference in volume change between the Ag phase and Cu phase resulted in stress as the sample temperature increased from room temperature to 109.3 ^{o}C. Therefore, the release of these generated stresses during the EM process led to Ag whiskers and nodule-like Ag hillocks.

The reason for emerging Ag nanoparticles and whiskers spreading over the entire surface

of EM-Ag-Cu might have been due to stress distribution. Lin et al. demonstrated that the lattice strain induced by electron flow in a single-phase Ag-2.26 at.% Cu strip was significantly smaller than that in a two-phase Ag-27.98 at.% Cu strip [41]. With so many randomly distributed Cu phases on the surface of EM-Ag-Cu in **Fig. A-2.1**, the stress induced by lattice strain and CTE mismatch could be uniformly distributed in the EM-Ag-Cu. Consequently, the uniformly distributed stress led to the generation of Ag whiskers and hillocks all over the surface of EM-Ag-Cu. It was reported that the size of generated Ag hillocks increased with longer EM duration, while the Ag whiskers grew in length and became curly as the EM time was extended [47]. It could be expected that the Ag hillocks and whiskers will continue to grow with extended EM time.

Fig. 5.21 c-c$_2$ and **5.21d-d$_2$** show that the EM behavior of EM-Ag agreed with the typical EM behavior of Ag, which involves the formation of Ag particles at the anode side [30]. In addition, abundant pits formed at the grain boundaries, and their size increased with the increasing EM time. The formation of pits at grain boundaries may be attributed to the fact that the atoms at grain boundaries have a higher energy state [48]. During the EM process, the energy of Ag atoms at the grain boundary could easily increase to the activation energy of surface diffusion, and the depletion of Ag atoms results in pits at the grain boundary. Ag whiskers and hillocks formed at the interface between the sintered Ag and substrate in **Fig. 5.20d$_1$, 5.20d$_3$** and **Fig. 5.21c$_2$, 5.21d$_2$**. This is because the CTE mismatch between the sintered Ag and substrate induced stress at the interface. The stress release resulted in Ag whiskers and hillocks at the interface, which proved that CTE mismatch could be a source of stress generation. By contrast, the emerging nanoparticles and pits at the middle region only

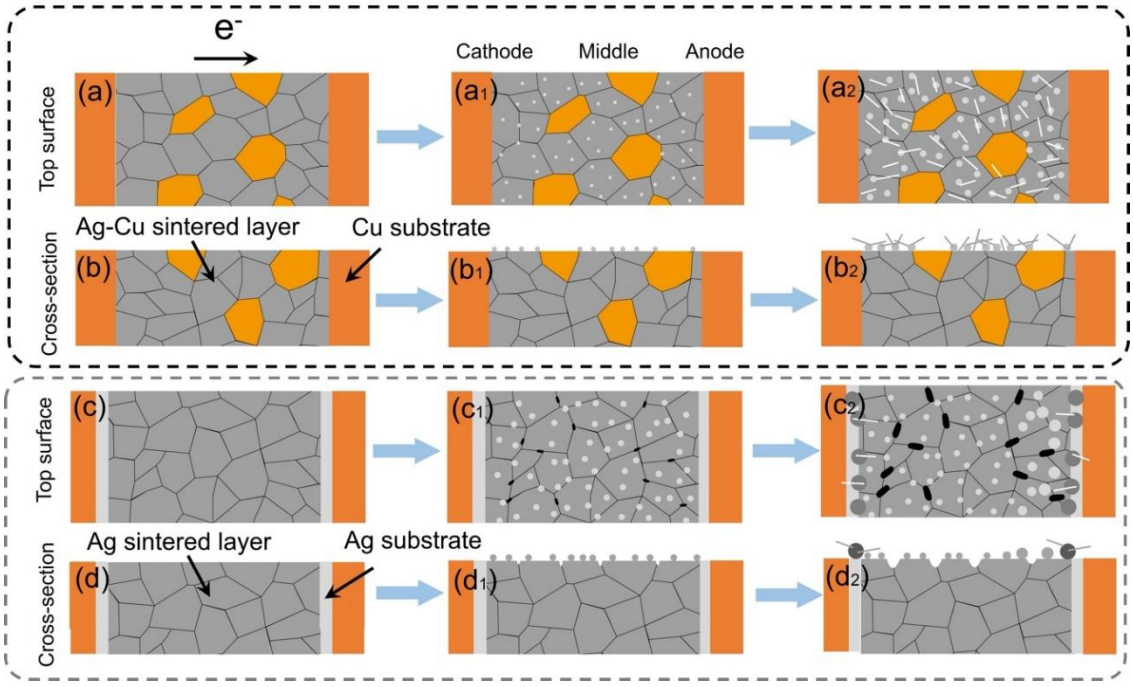

Fig. 5.21 Schematic diagram illustrating the EM test of EM-Ag-Cu and EM-Ag.

changed slightly during the EM process, which could be due to the long distance between the middle area and the source of stress.

We hypothesized that stress was responsible for the generation of Ag whiskers during the EM process. In **Fig. 5.19** and **Fig. 5.20** Ag-Cu joints and Ag joints with high density were utilized to prepare EM-Ag-Cu and EM-Ag. Compared with a porous structure, stress accumulates more easily in a dense structure. We identified some porous regions in the Ag joints. This is because the die-attachment used for EM-Ag has a large diameter of 10 mm. Unevenly distributed pressure during the bonding process led to insufficient sintering in some areas. The role of stress during the EM process was confirmed by preparing a porous EM-Ag under the same condition as EM-Ag. **Fig. 5.22** and **Fig. A-2.3** show the SEM images of the EM results of porous EM-Ag. The overall SEM images in **Fig. 5.22a-d** revealed no

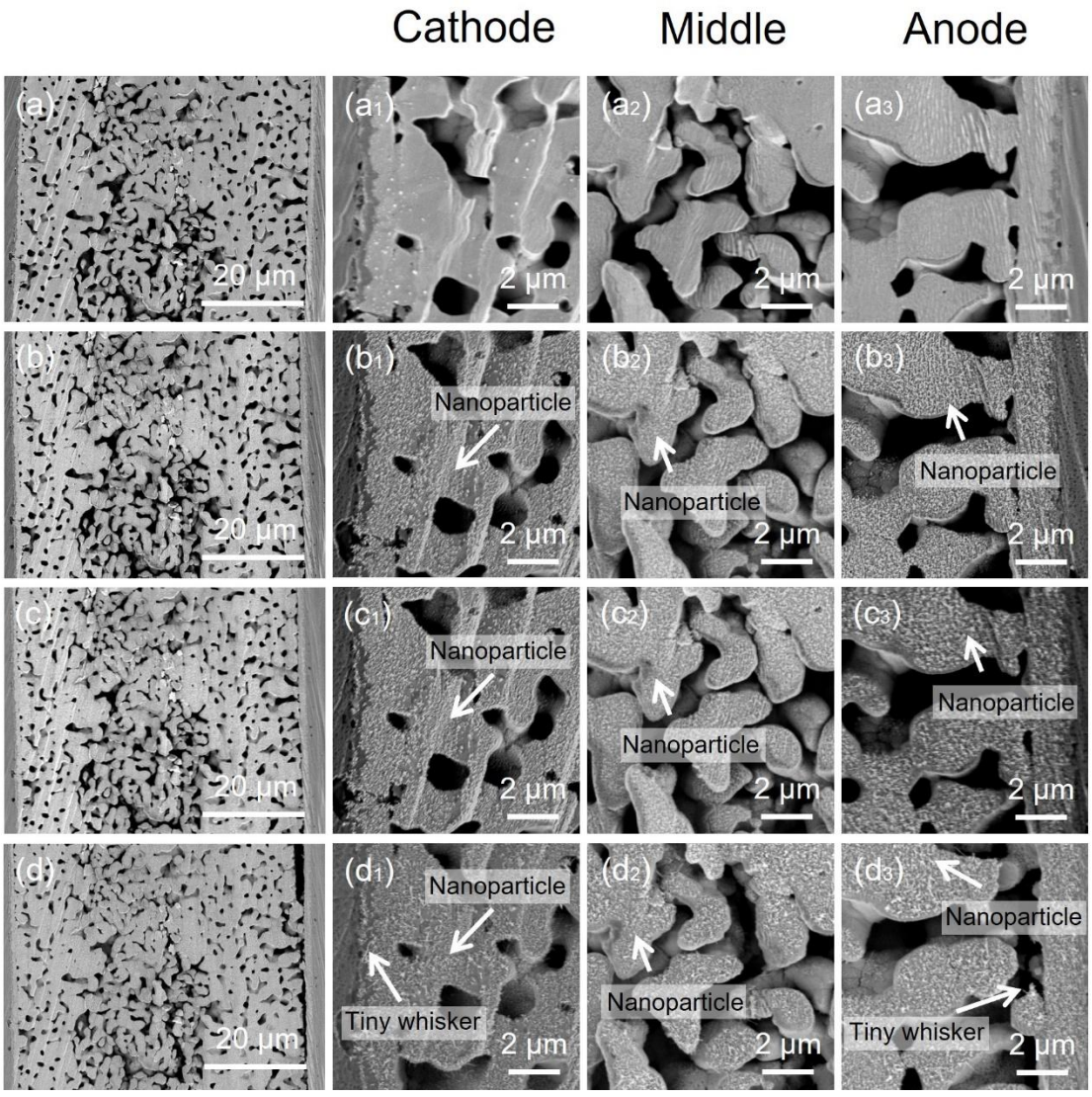

Fig. 5.22 Morphological changes of porous EM-Ag with EM time. SEM images of porous EM-Ag with EM time for (a)-(a_3) 0 h, (b)-(b_3) 50 h, (c)-(c_3) 100 h, and (d)-(d_3) 200 h.

apparent changes when the EM time increased from 0 h to 200 h. The crack in **Fig. 5.22d** might have been caused by an external force during the preparation of the SEM sample. **Fig. 5.22a**$_{1\text{-}3}$, **5.22b**$_{1\text{-}3}$, and **5.22c**$_{1\text{-}3}$ demonstrated that extending the EM time to 50 h resulted in Ag particles forming on the porous EM-Ag. However, these particles did not grow

significantly when the time was extended to 100 h. When the EM time increased to 200 h, only a few tiny Ag whiskers were observed at the regions close to the interface in **Fig. 5.22d$_1$** and **5.22d$_3$**. However, the size of the emerging particles did not change significantly. These subtle changes in porous EM-Ag may be due to the porous structure rendering stress accumulation difficult, which confirmed the assumption about the role of stress during the EM test.

5.4 Conclusion

In this study, the issues derived from Cu compounds were successfully solved by a two-step decomposition process. The obtained Ag-Cu nanostructures were bonded into robust Ag-Cu composite joints with a high shear strength of 30.8 MPa at 220 ºC for 40 min with 5 MPa. This high shear strength confirmed the feasibility of using an Ag-based complex as die-attach material on a Cu substrate. In addition, the EM behaviors of Ag-Cu composite joints and A joints were investigated with a current density of 6×10^4 A/cm^2 at 100 ºC. Abundant Ag nanoparticles and whiskers formed all over the surface of EM-Ag-Cu during the EM process, which could be attributed to the stress induced by lattice strain and CTE mismatch between the Ag phase and Cu phase. The EM-Ag exhibited typical EM behaviors, which involved the growth of Ag particles at the anode side. However, the EM behaviors of EM-Ag were less obvious than EM-Ag-Cu because of the smaller lattice strain in single-phase Ag and lower CTE-inducing stress. We believe that the results can guide researchers in determining if adding Cu will enhance the EM resistance of Ag joints.

Reference

[1] W. Lv, J. Liu, Y. Mou, Y. Ding, M. Chen, F. Zhu, Fabrication and Sintering Behavior of Nano Cu-Ag Composite Paste for High-Power Device, IEEE Trans Electron Devices 70 (2023) 3202–3207. https://doi.org/10.1109/TED.2023.3268252.

[2] C. Chen, D. Kim, Y. Liu, T. Sekiguchi, Y. Su, X. Long, C. Liu, C. Liu, K. Suganuma, Development of micron-sized Cu–Ag composite paste for oxidation-free bare Cu bonding in air condition and its deterioration mechanism during aging and power cycling tests, Journal of Materials Research and Technology 24 (2023) 8967–8983. https://doi.org/10.1016/j.jmrt.2023.05.104.

[3] Q. Jia, G. Zou, W. Wang, H. Ren, H. Zhang, Z. Deng, B. Feng, L. Liu, Sintering Mechanism of a Supersaturated Ag-Cu Nanoalloy Film for Power Electronic Packaging, ACS Appl Mater Interfaces 12 (2020) 16743–16752. https://doi.org/10.1021/acsami.9b20731.

[4] C..-K. Hu, L. Gignac, G. Lian, C. Cabral, K. Motoyama, H. Shobha, J. Demarest, Y. Ostrovski, C.M. Breslin, M. Ali, J. Benedict, P.S. McLaughlin, J. Ni, X.H. Liu, Mechanisms of Electromigration Damage in Cu Interconnects, in: 2018 IEEE International Electron Devices Meeting (IEDM), 2018: pp. 5.2.1-5.2.4. https://doi.org/10.1109/IEDM.2018.8614678.

[5] I.H. Tseng, P.N. Hsu, W.Y. Hsu, D.P. Tran, B.T.H. Lin, C.C. Chang, K.N. Tu, C. Chen, Effect of oxidation on electromigration in 2-μm Cu redistribution lines capped with polyimide, Results Phys 31 (2021). https://doi.org/10.1016/j.rinp.2021.105048.

[6] A.I. Titkov, O.A. Logutenko, A.M. Vorobyov, E. Yu. Gerasimov, I.K. Shundrina, N. V. Bulina, N.Z. Lyakhov, Synthesis of ˜10 nm size Cu/Ag core-shell nanoparticles stabilized by an ethoxylated carboxylic acid for conductive ink, Colloids Surf A Physicochem Eng Asp 577 (2019) 500–508. https://doi.org/10.1016/j.colsurfa.2019.06.008.

[7] J. Xin, Y. Gao, C. Zhang, L. Yang, S. Liu, K. Li, M. Zhou, Y. Liu, J. Zhang, W. Cai, High performance Cu sintering joint for power devices enabled by in-situ generation of Cu particles with multi-level hierarchical structures, J Mater Process Technol 329 (2024). https://doi.org/10.1016/j.jmatprotec.2024.118435.

[8] R. Gao, S. He, J. Li, Y.-A. Shen, H. Nishikawa, Interfacial transformation of preoxidized Cu microparticles in a formic-acid atmosphere for pressureless Cu–Cu bonding, Journal of Materials Science: Materials in Electronics 31 (2020) 14635–14644. https://doi.org/10.1007/s10854-020-04026-x.

[9] R.M. German, 1 - Thermodynamics of sintering, in: Z.Z. Fang (Ed.), Sintering of Advanced Materials, Woodhead Publishing, 2010: pp. 3–32. https://doi.org/https://doi.org/10.1533/9781845699949.1.3.

[10] C. Chen, J. Yeom, C. Choe, G. Liu, Y. Gao, Z. Zhang, B. Zhang, D. Kim, K. Suganuma, Necking growth and mechanical properties of sintered Ag particles with different shapes under air and N2 atmosphere, J Mater Sci 54 (2019) 13344–13357. https://doi.org/10.1007/s10853-019-03813-0.

[11] Y.J. Kim, B.H. Park, S.K. Hyun, H. Nishikawa, The influence of porosity and pore shape on the thermal conductivity of silver sintered joint for die attach, Mater Today Commun 29 (2021). https://doi.org/10.1016/j.mtcomm.2021.102772.

[12] Z.Z. Fang, H. Wang, Densification and grain growth during sintering of nanosized particles, International Materials Reviews 53 (2008) 326–352. https://doi.org/10.1179/174328008X353538.

[13] S.T. Chua, K.S. Siow, Microstructural studies and bonding strength of pressureless sintered nano-silver joints on silver, direct bond copper (DBC) and copper substrates aged at 300 °C, J Alloys Compd 687 (2016) 486–498. https://doi.org/10.1016/j.jallcom.2016.06.132.

[14] G. DiGiacomo, P. Peressini, R. Rutledge, Diffusion coefficient and electromigration velocity of copper in thin silver films, J Appl Phys 45 (1974) 1626–1629. https://doi.org/10.1063/1.1663466.

[15] D.B. Butrymowicz, J.R. Manning, M.E. Read, Diffusion in Copper and Copper Alloys, Part II. Copper-Silver and Copper-Gold Systems, J Phys Chem Ref Data 3 (1974) 527–602. https://doi.org/10.1063/1.3253145.

[16] Z.Z. Fang, H. Wang, 13 - Sintering of ultrafine and nanosized ceramic and metallic particles, in: R. Banerjee, I. Manna (Eds.), Ceramic Nanocomposites, Woodhead Publishing, 2013: pp. 431–473. https://doi.org/https://doi.org/10.1533/9780857093493.3.431.

[17] A. Molinari, Fundamentals of Sintering: Solid State Sintering, in: F.G. Caballero (Ed.), Encyclopedia of Materials: Metals and Alloys, Elsevier, Oxford, 2022: pp. 471–480. https://doi.org/https://doi.org/10.1016/B978-0-12-819726-4.00096-X.

[18] J. Yan, A review of sintering-bonding technology using ag nanoparticles for electronic packaging, Nanomaterials 11 (2021). https://doi.org/10.3390/nano11040927.

[19] X. Shen, J. Li, S. Xi, High Strength Die-Attach Joint Formation by Pressureless Sintering of Organic Amine Modified Ag Nanoparticle Paste, Nanomaterials 12 (2022). https://doi.org/10.3390/nano12193351.

[20] Z. Wu, W. Liu, J. Feng, Z. Wen, X. Zhang, X. Wang, C. Wang, Y. Tian, Novel Cu@Ag Micro/Nanoparticle Hybrid Paste and Its Rapid Sintering Technique via Electromagnetic Induction for High-Power Electronics, ACS Omega 8 (2023) 31021–31029. https://doi.org/10.1021/acsomega.3c02854.

[21] E.B. Choi, Y.-J. Lee, J.-H. Lee, Rapid sintering by thermo-compression in air using a paste containing bimodal-sized silver-coated copper particles and effects of particle size and

surface finish type, J Alloys Compd 897 (2022) 163223. https://doi.org/https://doi.org/10.1016/j.jallcom.2021.163223.

[22] J. Wang, S. Yodo, H. Tatsumi, H. Nishikawa, Reliability-enhanced microscale Ag sintered joint doped with AlN nanoparticles, Mater Lett 349 (2023) 134845. https://doi.org/https://doi.org/10.1016/j.matlet.2023.134845.

[23] B. Hu, F. Yang, Y. Peng, C. Hang, H. Chen, C. Lee, S. Yang, M. Li, Effect of SiC reinforcement on the reliability of Ag nanoparticle paste for high-temperature applications, Journal of Materials Science: Materials in Electronics 30 (2019) 2413–2418. https://doi.org/10.1007/s10854-018-0514-y.

[24] Y. Xu, X. Qiu, W. Li, S. Wang, N. Ma, M. Ueshima, C. Chen, K. Suganuma, Development of high thermal conductivity of Ag/diamond composite sintering paste and its thermal shock reliability evaluation in SiC power modules, Journal of Materials Research and Technology 26 (2023) 1079–1093. https://doi.org/https://doi.org/10.1016/j.jmrt.2023.07.254.

[25] X. Lu, W. Ke, C. Zhou, Y. Wu, Q. Zhang, S. Huang, W. Xia, L. Ye, A. Zehri, J. Liu, The influence of sintering process on thermal properties of nano-silver paste, in: 2018 19th International Conference on Electronic Packaging Technology (ICEPT), 2018: pp. 1157–1160. https://doi.org/10.1109/ICEPT.2018.8480545.

[26] T.F. Chen, K.S. Siow, Comparing the mechanical and thermal-electrical properties of sintered copper (Cu) and sintered silver (Ag) joints, J Alloys Compd 866 (2021) 158783. https://doi.org/https://doi.org/10.1016/j.jallcom.2021.158783.

[27] H. Zhang, H. Zhang, Q. Jia, C. Yin, Z. Deng, W. Guo, Z. Wan, Novel SiC-Based Power Device Bonding Materials of Nano Foam Sheet and Its Characteristic and Properties, IEEE Trans Compon Packaging Manuf Technol 13 (2023) 897–905. https://doi.org/10.1109/TCPMT.2023.3288389.

[28] M.-H. Roh, H. Nishikawa, S. Tsutsumi, N. Nishiwaki, K. Ito, K. Ishikawa, A. Katsuya, N. Kamada, M. Saito, Effect of temperature and substrate on shear strength of the joints formed by sintering of micro-sized Ag particle paste without pressure, Journal of Materials Science: Materials in Electronics 28 (2017) 7292–7301. https://doi.org/10.1007/s10854-017-6414-8.

[29] Z. Hu, Y. Tang, Y. Zhang, R. Gao, X. Li, Y. Bai, X. Tian, J. Hao, C. Yang, X. Wang, X. Liu, Degradation in Electrothermal Characteristics and Failure Mechanism of SiC JBS With Different Die Attach Materials Under 300 ◦C Power Cycle Stress, IEEE J Emerg Sel Top Power Electron 12 (2024) 3619–3628. https://doi.org/10.1109/JESTPE.2024.3380026.

[30] Z. Jin, Y.A. Shen, F. Huo, Y.C. Chan, H. Nishikawa, Electromigration behavior of silver thin film fabricated by electron-beam physical vapor deposition, J Mater Sci 56 (2021) 9769–9779. https://doi.org/10.1007/s10853-021-05862-w.

[31] Z. Jin, F. Huo, X. Liu, H. Nishikawa, Electromigration Comparison Study of Sn, Ag, and Cu Stripes Fabricated by Electron-Beam Physical Vapor Deposition, in: 2022 International Conference on Electronics Packaging (ICEP), 2022: pp. 203–204. https://doi.org/10.23919/ICEP55381.2022.9795382.

[32] H.C. Huang, K.L. Lin, A.T. Wu, Disruption of crystalline structure of Sn3.5Ag induced by electric current, J Appl Phys 119 (2016). https://doi.org/10.1063/1.4944033.

[33] F.C. Shen, C.Y. Huang, H.Y. Lo, W.Y. Hsu, C.H. Wang, C. Chen, W.W. Wu, Atomic-Scale Investigation of Electromigration with Different Directions of Electron Flow into High-Density Nanotwinned Copper through In Situ HRTEM, Acta Mater 219 (2021). https://doi.org/10.1016/j.actamat.2021.117250.

[34] I.A. Blech, C. Herring, Stress generation by electromigration, Appl Phys Lett 29 (1976) 131–133. https://doi.org/10.1063/1.89024.

[35] H.C. Kim, T.L. Alford, D.R. Allee, Thickness dependence on the thermal stability of silver thin films, Appl Phys Lett 81 (2002) 4287–4289. https://doi.org/10.1063/1.1525070.

[36] E. Misra, N.D. Theodore, J.W. Mayer, T.L. Alford, Failure mechanisms of pure silver, pure aluminum and silver-aluminum alloy under high current stress, Microelectronics Reliability 46 (2006) 2096–2103. https://doi.org/10.1016/j.microrel.2006.01.011.

[37] P. Jepiti, S. Yoon, J. Kim, Electromigration Reliability in Ag Lines Printed with Nanoparticle Inks: Implications for Printed Electronics, ACS Appl Nano Mater 5 (2022) 2569–2577. https://doi.org/10.1021/acsanm.1c04144.

[38] C.S. Hau-Riege, An introduction to Cu electromigration, Microelectronics Reliability 44 (2004) 195–205. https://doi.org/10.1016/j.microrel.2003.10.020.

[39] K. Sasagawa, M. Hasegawa, M. Saka, H. Abé, Governing parameter for electromigration damage in the polycrystalline line covered with a passivation layer, J Appl Phys 91 (2002) 1882–1890. https://doi.org/10.1063/1.1432120.

[40] S.K. Lin, Y. Yorikado, J. Jiang, K.S. Kim, K. Suganuma, S.W. Chen, M. Tsujimoto, I. Yanada, Microstructure development of mechanical-deformation-induced Sn whiskers, J Electron Mater 36 (2007) 1732–1734. https://doi.org/10.1007/s11664-007-0284-4.

[41] Y. chen Liu, Y. si Yu, S. kang Lin, S.J. Chiu, Electromigration effect upon single- and two-phase Ag-Cu alloy strips: An in situ study, Scr Mater 173 (2019) 134–138. https://doi.org/10.1016/j.scriptamat.2019.08.008.

[42] S.K. Lin, Y.C. Liu, S.J. Chiu, Y.T. Liu, H.Y. Lee, The electromigration effect revisited: Non-uniform local tensile stress-driven diffusion, Sci Rep 7 (2017). https://doi.org/10.1038/s41598-017-03324-5.

[43] T. Ishizaki, D. Miura, A. Kuno, R. Nagao, S. Aoki, Y. Ohshima, T. Kino, M. Usui, Y. Yamada, Power cycle reliability of Cu nanoparticle joints with mismatched coefficients of thermal expansion, Microelectronics Reliability 64 (2016) 287–293. https://doi.org/10.1016/j.microrel.2016.07.031.

[44] P.C. Liang, K.L. Lin, Non-deformation recrystallization of metal with electric current stressing, J Alloys Compd 722 (2017) 690–697. https://doi.org/10.1016/j.jallcom.2017.06.032.

[45] M.F. Wu, K.L. Lin, The twin formation under electric current stressing and its effect on the properties of copper, Journal of Materials Research and Technology 31 (2024) 2414–2423. https://doi.org/10.1016/j.jmrt.2024.06.235.

[46] T.L. Alford, E. Misra, S.K. Bhagat, J.W. Mayer, Influence of Joule heating during electromigration evaluation of silver lines, Thin Solid Films 517 (2009) 1833–1836. https://doi.org/10.1016/j.tsf.2008.08.196.

[47] A. Mansourian, S.A. Paknejad, Q. Wen, G. Vizcay-Barrena, R.A. Fleck, A. V. Zayats, S.H. Mannan, Tunable Ultra-high Aspect Ratio Nanorod Architectures grown on Porous Substrate via Electromigration, Sci Rep 6 (2016). https://doi.org/10.1038/srep22272.

[48] T. Brink, L. Langenohl, H. Bishara, G. Dehm, Universality of grain boundary phases in fcc metals: Case study on high-angle [111] symmetric tilt grain boundaries, Phys Rev B 107 (2023). https://doi.org/10.1103/PhysRevB.107.054103.

Chapter 6: Conclusion and future work

6.1 Summary

This dissertation presents the investigation of using an Ag-based complex as die-attach material. In this process, organic-free Ag nanostructures derived from the thermal decomposition of Ag-based complex were used as intermedia to fabricate Ag sintered joints. The factors that affect the bonding performance of Ag nanostructures were investigated from two perspectives. From the perspective of the Ag-based complex, the effect of thermal decomposition conditions, such as thermal decomposition time and temperature, of Ag-based complex on the bonding performance of Ag nanostructures was studied. For the other perspective, the effect of substrates was investigated based on four commonly used substrates, Au, Ag, Al, and Cu. The results of each investigation in this dissertation are shown below.

In **Chapter 2**, the feasibility of using an Ag-based complex as die-attach material was successfully confirmed on Au substrate. Subsequently, the effect of thermal conditions of the Ag-based complex was investigated to optimize the fabrication of Ag nanostructures. The results showed that extending the thermal decomposition time at 180 ^{o}C increased the bonding performance of Ag nanostructures. For a short time, insufficient decomposition of the Ag-based complex resulted in trapped organics in the Ag nanostructures. During the bonding process, gasification of trapped organics induced defects within the Ag sintered joints, deteriorating the shear strength. Extending time at 180 ^{o}C reduced the organic content but did not significantly increase the particle size. Therefore, the naked Ag particles rendered the Ag nanostructures high bonding performance as the thermal decomposition increased to

60 min, resulting in a high average shear strength of 50.3 MPa. In terms of the thermal decomposition temperature, a low temperature of 160 ^{o}C resulted in insufficient decomposition and tapped organics in the Ag nanostructures. Excessive decomposition occurred at 200 ^{o}C, which resulted in the sintering of Ag particles within the Ag nanostructures and reduced the surface energy before bonding. Heating at 180 ^{o}C for 40 min dramatically reduced the trapped organics without causing sintering. The obtained Ag nanostructures consisted of tiny nanoparticles with naked surfaces, resulting in a high shear strength of 48.6 MPa at 200 ^{o}C. In summary, thermal conditions could determine the bonding performance of Ag nanostructures through two factors: I) the content of trapped organics and II) the sintering of Ag particles. These results indicated that optimizing the thermal decomposition conditions of Ag-based complexes is an effective way to improve the bonding performance of Ag nanostructures.

In **Chapter 3**, three commercially available substrates, Ag, Al, and Cu, were used to investigate the effects of substrate on the formation and composition of Ag nanostructures. The Ag nanostructures on the Ag and Al substrates exhibited a multilayered structure, and the Ag particles of nanostructures exhibited a naked surface. By contrast, the particles of Ag nanostructures on the Cu substrate were surrounded by organics. This significant difference could be attributed to the reaction between the Ag-based complex and Cu substrate, which resulted in Cu compounds with a high thermal temperature of 211 ^{o}C. Heating at 180 ^{o}C is enough for the Ag-based complex to decompose but not for the Cu compounds, resulting in incomplete decomposition of Cu compounds and organics in the Ag nanostructures. In summary, the reaction between the Ag-based complex and substrate played an important role

in determining the morphology and composition of Ag nanostructures. These results could provide guidelines in selecting suitable substrates for Ag nanostructure preparation.

In **Chapter 4**, the effect of substrate on the bonding performance of Ag nanostructures was investigated based on four substrates Au, Ag, Al, and Cu. The Ag nanostructures on the Au, Ag, and Al substrates shared the same bonding behaviors because a reaction did not occur between the Ag-based complex and substrates. The bonding of the three Ag nanostructures involved the sintering of poly-dispersed Ag particles. In these ploy-dispersed Ag particles, small particles filled the interspaces of large particles, increasing the stacking density for bonding. During the bonding process, these small particles first underwent sintering, resulting in necks between large particles. The formation of necks built up massive diffusion paths within the sintered Ag. As a result, the three Ag nanostructures demonstrated an excellent low-temperature bonding property. The interface conditions between the Ag nanostructures and substrate determined the shear strength of the Ag sintered joints. The formation of the Ag-Au mixing layer at the interface improved the affinity between the sintered Ag layer and Au substrate, resulting in a shear strength of 31.1 MPa at 160 ^{o}C. By contrast, the oxide layer on the top surface of the Al substrate hindered the diffusion between the sintered Ag layer and substrate, resulting in a low shear strength. The generation of Cu compounds resulted in organics and CuO within the Ag nanostructures on the Cu substrate, which hindered the diffusion during the bonding process, resulting in low shear strength.

In **Chapter 5**, a two-step decomposition process was designed to overcome the issues of Cu compounds. During this process, the decomposition of the Ag-based complex and Cu

compounds resulted in Ag-Cu nanostructures. The Ag-Cu composite joints with a shear strength of 30.8 MPa obtained at 220 ºC for 40 min with 5 MPa confirmed the feasibility of using Ag-based complex as die-attach material on Cu substrate. The Cu phase in the obtained Ag-Cu composite joints was expected to enhance the electromigration (EM) resistance. Consequently, the EM behaviors of the Ag-Cu composite joints and Ag joints were investigated with a current density of 6×10^4 A/cm^2 at 100 ºC. The results demonstrated that Ag whiskers and hillocks were generated all over the surface of the EM sample from the Ag-Cu composite joint. This result could be because the current-inducing lattice strain and coefficient of thermal expansion (CTE) mismatch resulted in compressive stress all over the EM sample from the Ag-Cu composite joint. The release of stress during the EM process resulted in the Ag whiskers and hillocks. By contrast, the EM of Ag joints resulted in the growth of Ag particles at the anode side, which agreed with the typical EM behaviors of Ag. The results may enhance the understanding of the effect of Cu on the EM behaviors of Ag joints.

6.2 Future work

6.2.1 Optimization of the formular of Ag-based complex

In this dissertation, the Ag-based complex was synthesized using silver acetate and 2-Amino-2-methyl-1-propanol (AMP). The Ag-based complex showed an Ag content of 26.7%, which was lower than that of Ag paste [1]. The bondline thickness was increased by printing the Ag-based complex on both substrate and die. However, directly fabricating Ag-nanostructures on the backside of the die could result in thermal damage and contamination.

An effective means of ensuring the thickness of bondline and protecting the die is to increase the Ag content of the Ag-based complex. Since the Ag-based complex consists of Ag precursor and complex agent [2], there are two routes to increase the Ag content: I) using an Ag precursor with high Ag content and II) reducing the molar mass of the complex agent. The theoretical Ag content of silver acetate is 64.6%. Therefore, silver oxalate and silver carbonate with a theoretical Ag content of 71.0% and 78.3%, respectively, could be promising candidates for the Ag precursor [3,4]. Ethylenediamine could be a promising candidate for the complex agent because its molar mass of 60.1 $g \cdot mol^{-1}$ is lower than the 89.1 $g \cdot mol^{-1}$ of AMP [5]. Therefore, using an Ag precursor with high Ag content and a complex agent with low molar mass is expected to increase the Ag content of the Ag-based complex, enabling Ag nanostructure fabrication only on the substrate.

6.2.2 Optimization of heating method for preparing Ag nanostructures

Poly-dispersed particles in the Ag nanostructures are important in determining the bonding performance. Although the dense layer of Ag nanostructure consisted of poly-dispersed particles, the existence of temperature gradient increased the particle size to micro-scale, which decreased the surface energy. This could also reduce interfacial bonding ability as the dense layer was close to the substrate. **Fig. 5.10** shows that a uniform heating atmosphere resulted in Ag-Cu nanostructures with poly-dispersed particles. However, a high heating temperature of 230 ^{o}C increased the particle size. As shown in **Fig. 6.1**, it is expected that decomposing the Ag-based complex in a uniform heating atmosphere at an appropriate temperature could result in Ag nanostructures full of poly-dispersed particles with desirable

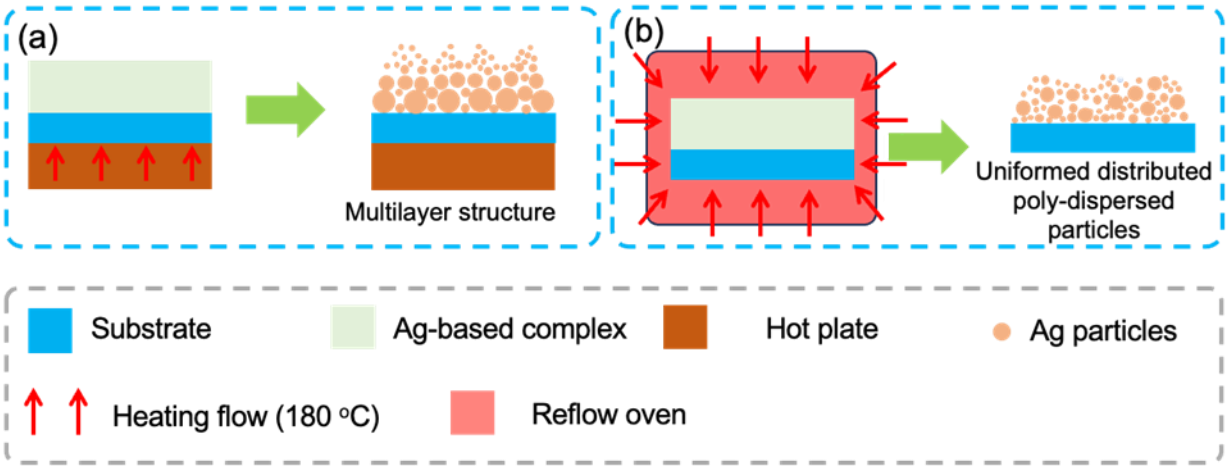

Fig. 6.1 Schematic diagram illustrating the effect of heating method (a) hot plate and (b) reflow oven on the formation of Ag nanostructure.

sizes, which exhibit high bonding performance. Therefore, we would like to improve the bonding performance by investigating the effects of temperature distribution on Ag nanostructure formation.

6.2.3 Reliability assessment and improvement under thermal aging

Ag joints experience a serious decline in shear strength because of the coarsening of the sintered Ag layer [6]. This coarsening increased the pore size and decreased the bonding ratio between the sintered Ag and substrate[7]. Coarsening of Ag sintered joints during the thermal aging process is related to the diffusion of atoms [8]. Consequently, some Ag pastes doped with high-temperature particles such as AlN, SiC, and diamond were used to prepare Ag sintered joints [9–11]. During the aging process, these added particles increase the thermal aging resistance by acting as barriers to block the diffusion of Ag atoms for coarsening.

However, the diffusion for sintering was also blocked during the bonding process, increasing the bonding temperature and pressure.

In electronics, Ni can be used as a barrier layer to prevent diffusion between the Cu substrate and bondline. Li et al. used a composite conductive ink that contained Cu-based complex and Ni-based complex to prepare a Cu-Ni conductive film [12]. The Cu-based complex and Ni-based complex exhibited thermal decomposition temperatures of ~150 ºC and ~210 ºC, respectively. During the heating process, the Cu-based complex first decomposed to produce Cu particles. Subsequently, Ni atoms derived from the Ni-based complex were deposited on the surface of Cu particles, resulting in Cu@Ni core-shell particles. The Ni shell prevented the Cu particle from being oxidized and had no seriously negative effects on the sintering, resulting in a low resistivity of 29 μΩ·cm after photonic sintering. Ag@Ni core-shell particles are expected to be prepared by an Ag-Ni composite complex. During the bonding process, the Ni shell could participate in the sintering of Ag@Ni core-shell particles. On the other hand, the Ni shell on the surface of Ag particles blocks the diffusion of Ag atoms during the thermal aging process. Thus, the thermal aging resistance of Ag sintered joints will be improved without increasing the bonding temperature and pressure.

6.2.4 EM resistance enhancement of Ag sintered joint

In Chapter 5, the EM behaviors of Ag joints and Ag-Cu composite joints were investigated. The EM of Ag joints agreed with the typical EM behaviors of Ag, and the formation of Ag particles at the anode side and pits at the grain boundaries indicated the depletion of Ag in

the Ag joints [13]. In the Ag-Cu composite joints, EM resulted in Ag whiskers and hillocks on the Ag phase, but the Cu phase kept a neat surface. This meant EM occurred at the Ag phase. However, the lifetime of connections that was a key indicator for evaluating the EM resistance was not investigated in this study [14,15]. Therefore, the lifetime of Ag-Cu composite joints and Ag joints should be investigated.

On the other hand, EM did not occur at the Cu phase in the Ag-Cu composite joint. The Cu phase existed in the Ag-Cu composite joint in the form of particles, which did not prevent the occurrence of EM of Ag. In Chapter 4, Cu compounds decomposed during the bonding process in air, resulting in a CuO shell on the surface of Ag particles. In Chapter 5, Cu compounds decomposed during the two-step decomposition process, resulting in Cu particles in the nanostructures. If the nanostructures derived from the first step were used as die-attach material, the decomposition of Cu compounds during the bonding process in a formic acid atmosphere could result in a Cu shell on the surface of Ag particles. Because surface diffusion plays a dominant role in the EM process [14,16] , covering the surface of Ag particles by Cu may improve the EM resistance of Ag-Cu composite joints by restricting the movement of Ag atoms during EM.

Another possible reason why the addition of Cu did not prevent Ag from electromigration is that the amount of Cu was small. If more Cu, which has better EM resistance, were added to the Ag sintered joints, the Cu phase might act as a barrier to prevent the Ag from electromigration. The Cu content in the Ag sintered joints could be controlled by optimizing the Ag-based complex decomposition on the Cu substrate. The reaction begins when the Ag-

based complex is printed on the Cu substrates. As shown in **Fig. 6.2a**, if the Ag-based complex is left on the substrate for a longer time, more Cu from the substrate will participate in the reaction, resulting in a higher amount of Cu in the Ag sintered joints. However, this method cannot precisely control the Cu content. The amount of Cu involved in the reaction depends on the thickness of the copper layer. If the thickness of the Cu layer in **Fig. 6.2b** is controlled, the content of Cu dissolved in the Ag-based complex can also be controlled. The Cu content in the nanostructure can be precisely controlled because the thickness of the Cu layer can be accurately determined by electroplating.

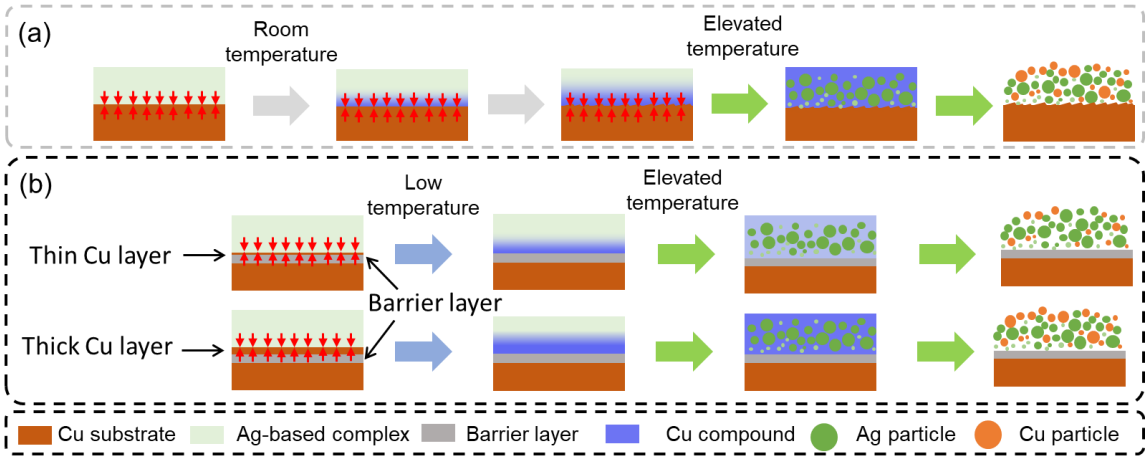

Fig. 6.2 Schematic diagram illustrating two ways for controlling the Cu content in the Ag-nanostructures. Controlling the Cu content in the Ag nanostructure by (a) adjusting the holding time on the Cu substrate and (b) adjusting the thickness of the Cu plating layer.

Reference

[1] H. Fang, C. Wang, S. Zhou, Q. Kang, T. Wang, D. Yang, Y. Tian, T. Suga, Rapid pressureless and low-temperature bonding of large-area power chips by sintering two-step activated Ag paste, Journal of Materials Science: Materials in Electronics 31 (2020) 6497–6505. https://doi.org/10.1007/s10854-020-03207-y.

[2] M. Vaseem, G. McKerricher, A. Shamim, Robust Design of a Particle-Free Silver-Organo-Complex Ink with High Conductivity and Inkjet Stability for Flexible Electronics, ACS Appl Mater Interfaces 8 (2016) 177–186. https://doi.org/10.1021/acsami.5b08125.

[3] Y. Dong, X. Li, S. Liu, Q. Zhu, J.-G. Li, X. Sun, Facile synthesis of high silver content MOD ink by using silver oxalate precursor for inkjet printing applications, Thin Solid Films 589 (2015) 381–387. https://doi.org/https://doi.org/10.1016/j.tsf.2015.06.001.

[4] Y. Chang, D.Y. Wang, Y.L. Tai, Z.G. Yang, Preparation, characterization and reaction mechanism of a novel silver-organic conductive ink, J Mater Chem 22 (2012) 25296–25301. https://doi.org/10.1039/c2jm34569b.

[5] Y. Dong, Z. Lin, X. Li, Q. Zhu, J.-G. Li, X. Sun, A low temperature and air-sinterable copper–diamine complex-based metal organic decomposition ink for printed electronics, J Mater Chem C Mater 6 (2018) 6406–6415. https://doi.org/10.1039/C8TC01849A.

[6] H. Zhang, W. Wang, H. Bai, G. Zou, L. Liu, P. Peng, W. Guo, Microstructural and mechanical evolution of silver sintering die attach for SiC power devices during high temperature applications, J Alloys Compd 774 (2019) 487–494. https://doi.org/https://doi.org/10.1016/j.jallcom.2018.10.067.

[7] S.A. Paknejad, G. Dumas, G. West, G. Lewis, S.H. Mannan, Microstructure evolution during 300 °c storage of sintered Ag nanoparticles on Ag and Au substrates, J Alloys Compd 617 (2014) 994–1001. https://doi.org/10.1016/j.jallcom.2014.08.062.

[8] S.T. Chua, K.S. Siow, Microstructural studies and bonding strength of pressureless sintered nano-silver joints on silver, direct bond copper (DBC) and copper substrates aged at 300 °C, J Alloys Compd 687 (2016) 486–498. https://doi.org/10.1016/j.jallcom.2016.06.132.

[9] J. Wang, S. Yodo, H. Tatsumi, H. Nishikawa, Reliability-enhanced microscale Ag sintered joint doped with AlN nanoparticles, Mater Lett 349 (2023) 134845. https://doi.org/https://doi.org/10.1016/j.matlet.2023.134845.

[10] B. Hu, F. Yang, Y. Peng, C. Hang, H. Chen, C. Lee, S. Yang, M. Li, Effect of SiC reinforcement on the reliability of Ag nanoparticle paste for high-temperature applications, Journal of Materials Science: Materials in Electronics 30 (2019) 2413–2418. https://doi.org/10.1007/s10854-018-0514-y.

[11] Y. Xu, X. Qiu, W. Li, S. Wang, N. Ma, M. Ueshima, C. Chen, K. Suganuma, Development of high thermal conductivity of Ag/diamond composite sintering paste and its thermal shock reliability evaluation in SiC power modules, Journal of Materials Research and Technology 26 (2023) 1079–1093. https://doi.org/https://doi.org/10.1016/j.jmrt.2023.07.254.

[12] W. Li, L. Li, F. Li, K. Kawakami, Q. Sun, T. Nakayama, X. Liu, M. Kanehara, J. Zhang, T. Minari, Self-Organizing, Environmentally Stable, and Low-Cost Copper–Nickel Complex Inks for Printed Flexible Electronics, ACS Appl Mater Interfaces 14 (2022) 8146–8156. https://doi.org/10.1021/acsami.1c21633.

[13] Z. Jin, Y.A. Shen, F. Huo, Y.C. Chan, H. Nishikawa, Electromigration behavior of silver thin film fabricated by electron-beam physical vapor deposition, J Mater Sci 56 (2021) 9769–9779. https://doi.org/10.1007/s10853-021-05862-w.

[14] C.S. Hau-Riege, An introduction to Cu electromigration, Microelectronics Reliability 44 (2004) 195–205. https://doi.org/10.1016/j.microrel.2003.10.020.

[15] P. Jepiti, S. Yoon, J. Kim, Electromigration Reliability in Ag Lines Printed with Nanoparticle Inks: Implications for Printed Electronics, ACS Appl Nano Mater 5 (2022) 2569–2577. https://doi.org/10.1021/acsanm.1c04144.

[16] K. Sasagawa, M. Hasegawa, M. Saka, H. Abé, Governing parameter for electromigration damage in the polycrystalline line covered with a passivation layer, J Appl Phys 91 (2002) 1882–1890. https://doi.org/10.1063/1.1432120.

Appendix-1

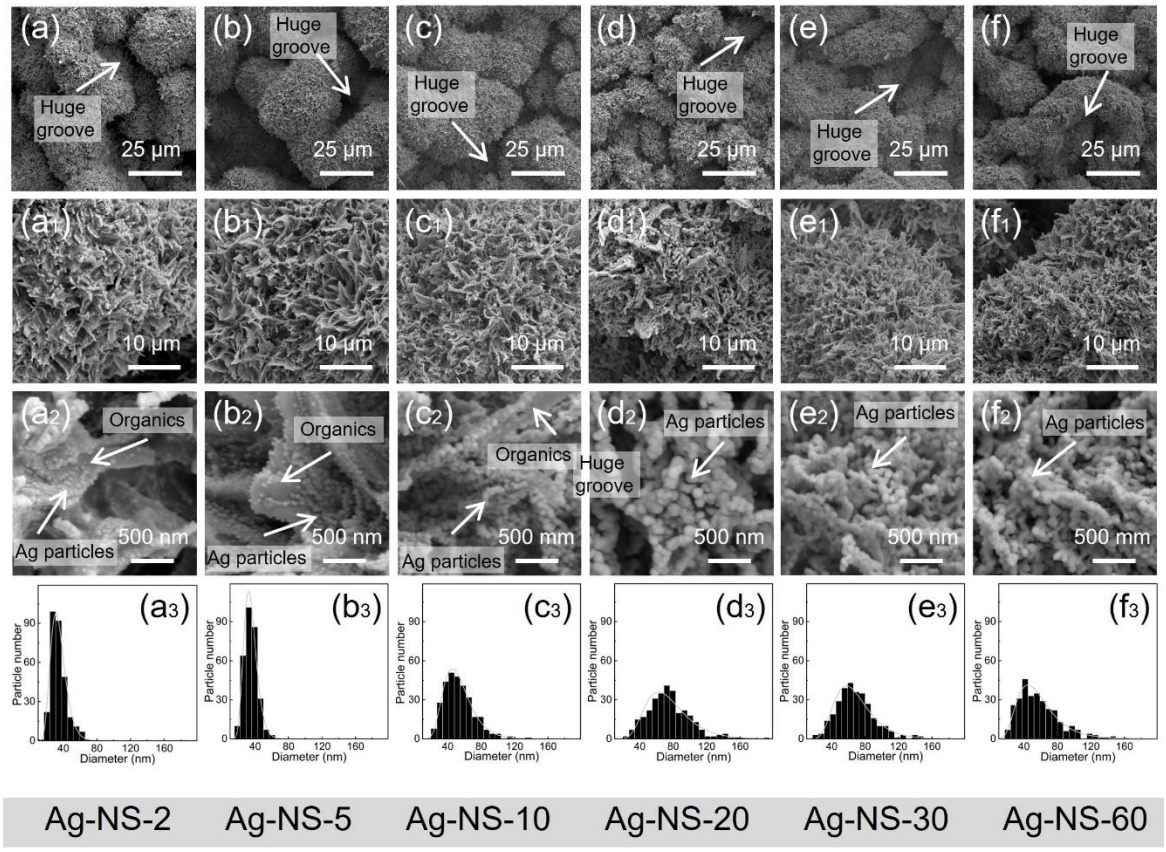

Fig. A1.1 Top surface of Ag nanostructure. SEM image of (a) Ag-NS-2, (b) Ag-NS-5, (c) Ag-NS-10, (d) Ag-NS-20, (e) Ag-NS-30, and (f) Ag-NS-60. (a1)-(f1), (a2)-(f2) magnified SEM images of (a)-(f) respectively. (a3)-(f3) particle size distribution of (a2)-(f2) respectively.

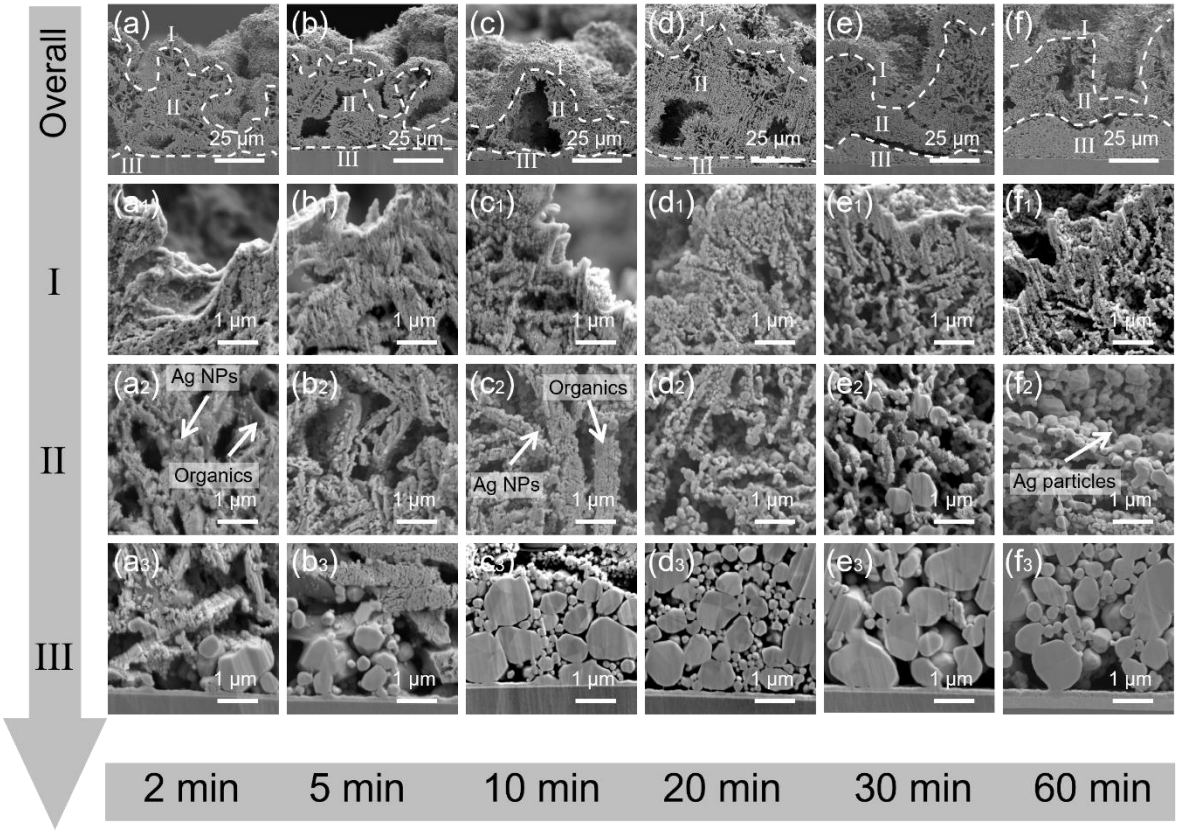

Fig. A1.2 Cross-section of Ag nanostructure. Cross-section of (a) Ag-NS-2, (b) Ag-NS-5, (c) Ag-NS-10, (d) Ag-NS-20, (e) Ag-NS-30, and (f) Ag-NS-60. Amplified SEM images in (a_1)-(f_1) top, (a_2)-(f_2) mid, and (a_3)-(f_3) interface of (a)-(f) respectively.

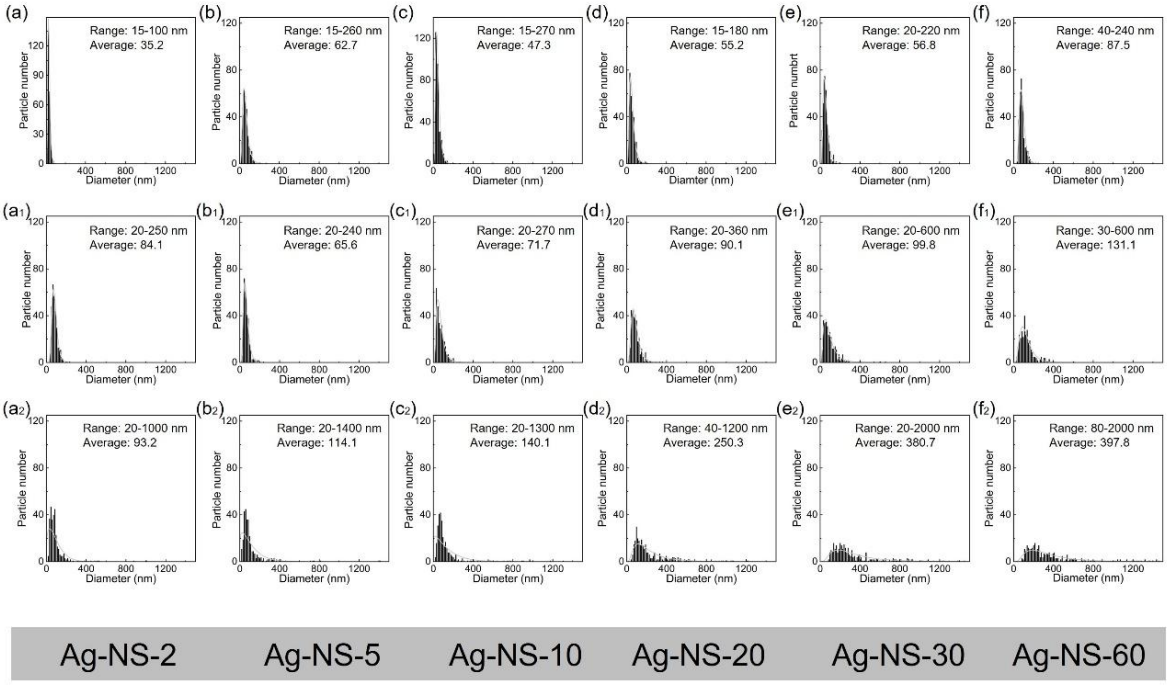

Fig. A1.3 Particle size distribution of Ag nanostructures. Particle size distribution of (a)-(f) I, (a_1)-(f_1) II, and (a_2)-(f_2) III of the Ag-NS-2, Ag-NS-5, Ag-NS-10, Ag-NS-20, Ag-NS-30, and Ag-NS-60, respectively.

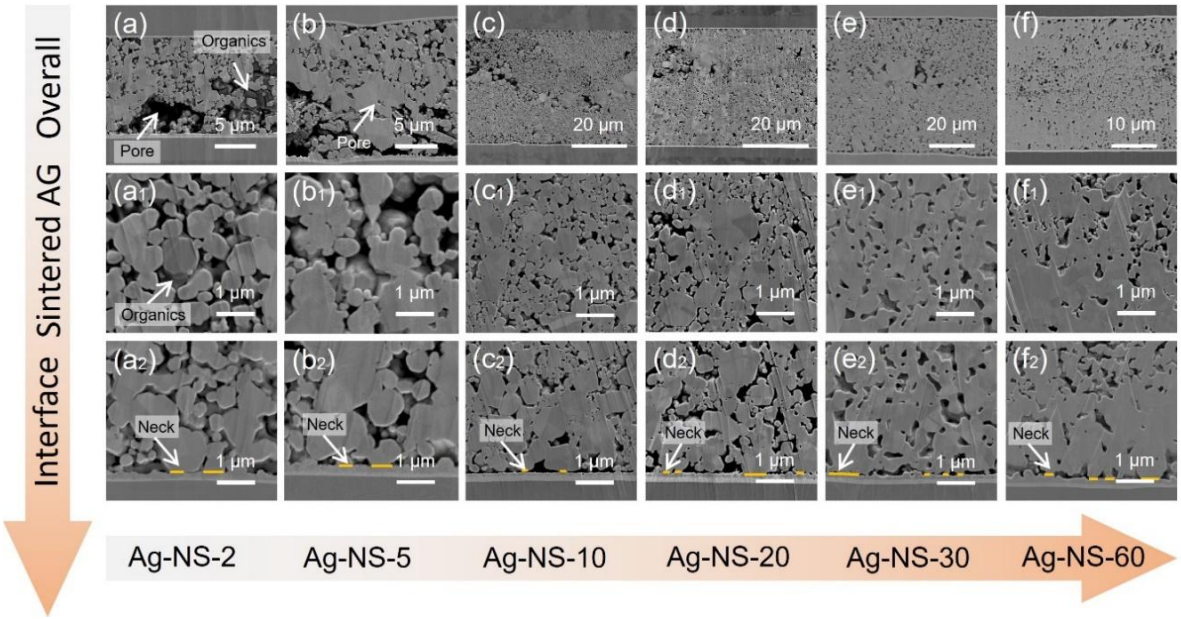

Fig. A1.4 SEM images of the cross-sections of the sintered Ag joint derived from (a)-(a_2) Ag-NS-2, (b)-(b_2) Ag-NS-5, (c)-(c_2) Ag-NS-10, (d)-(d_2) Ag-NS-20, (e)-(e_2) Ag-NS-30, and (f)-(f_2) Ag-NS-60.

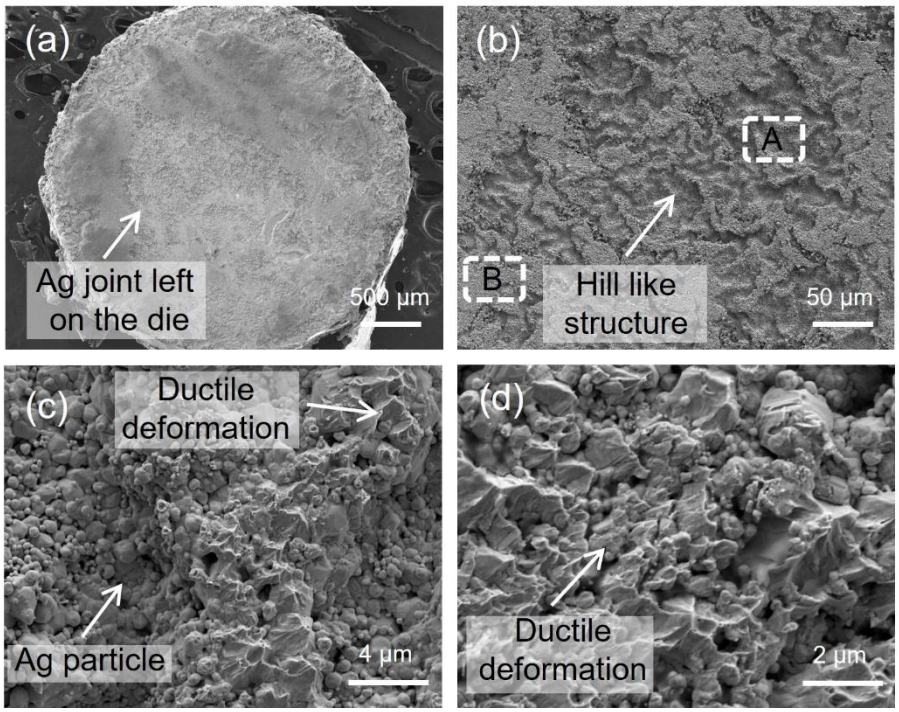

Fig. A1.5 (a) Fracture surfaces of Ag joints derived from Ag-NS-5. (b) Amplified SEM image of the fracture surface. (c), (d) Amplified SEM images of white rectangles A and B respectively.

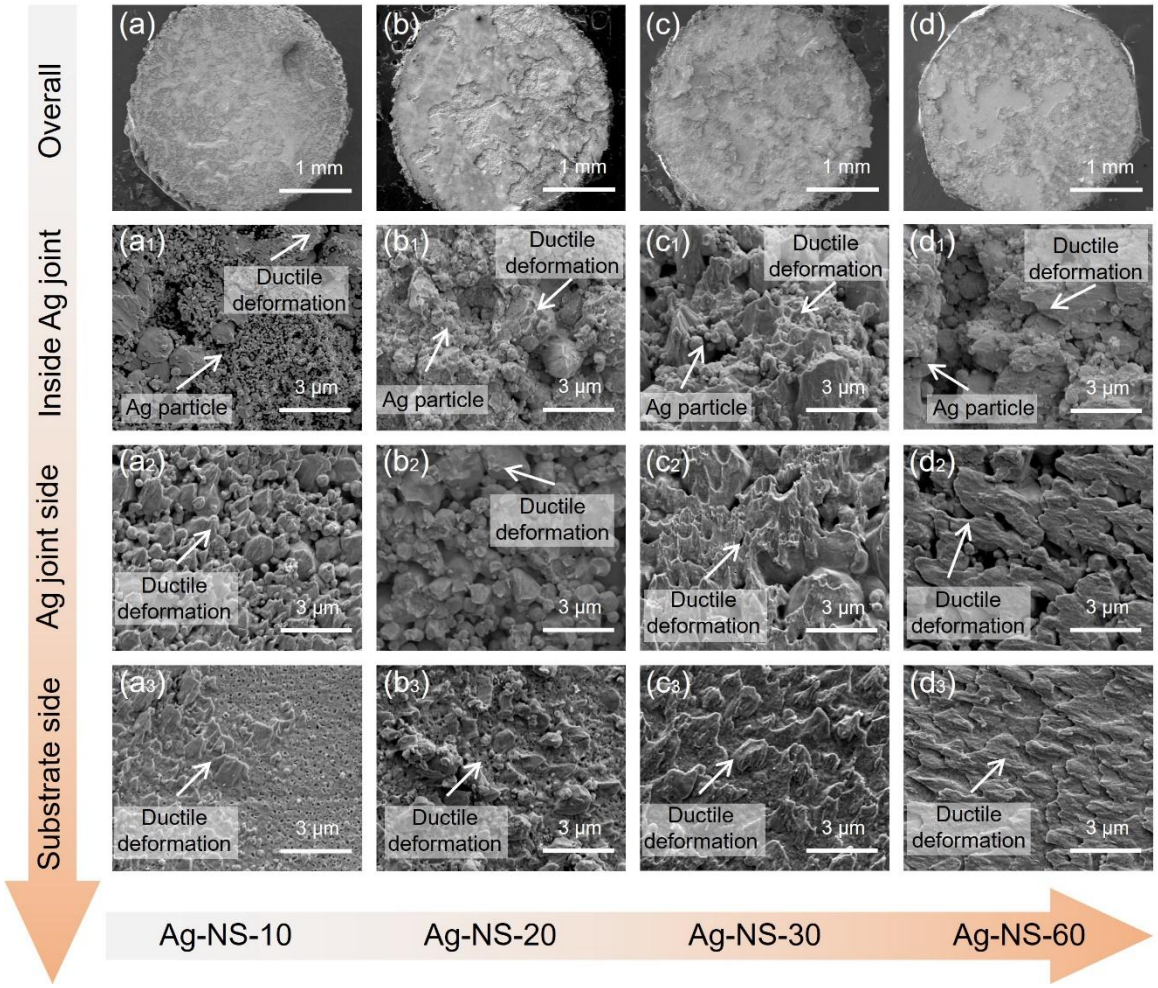

Fig. A1.6 Microstructure of the fracture surfaces of Ag joints boned at 200 °C, 40 min, and 5 MPa derived from (a)-(a_3) Ag-NS-10, (b)-(b_3) Ag-NS-20, and (c)-(c_3) Ag-NS-30, and (c)-(c_3) Ag-NS-60.

Appendix-2

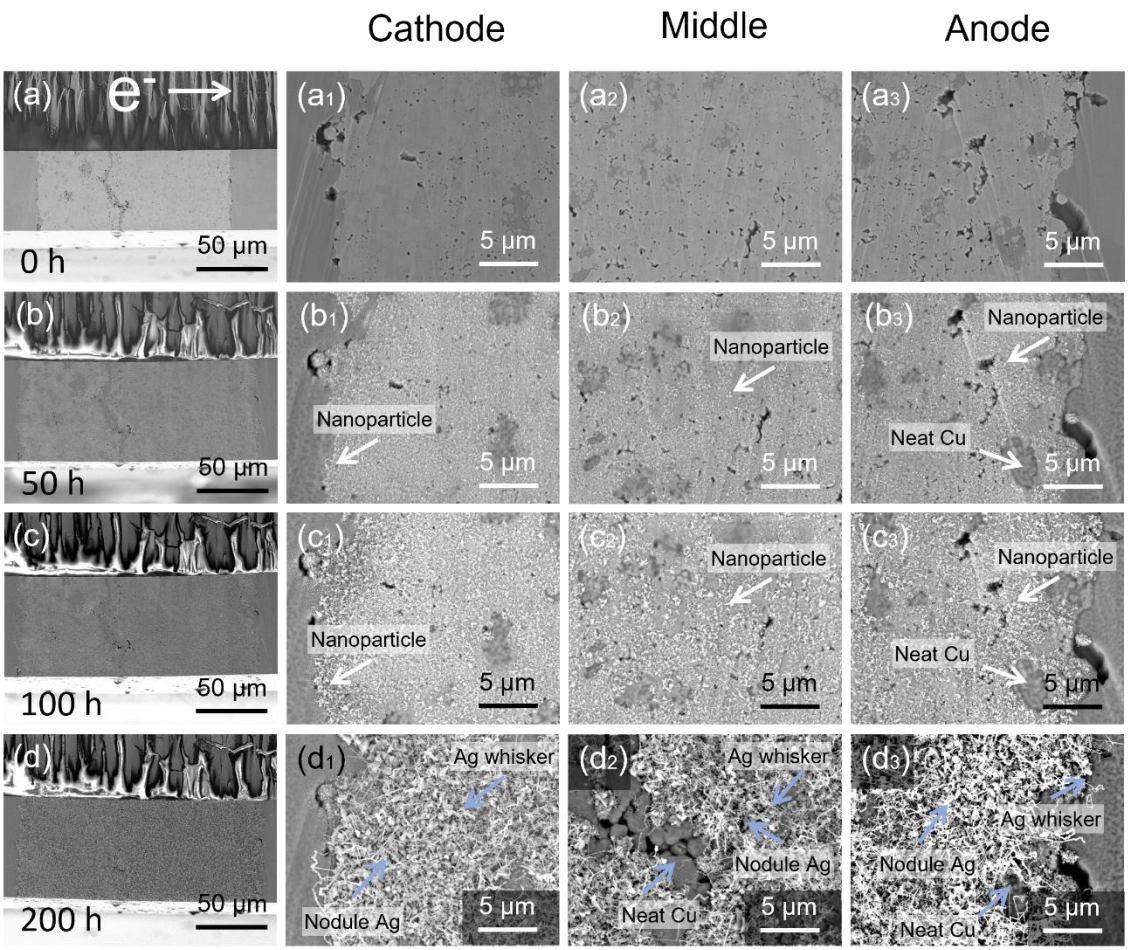

Fig. A-2.1 Morphological changes of EM-Ag-Cu with EM time. SEM images of EM-Ag-Cu with EM time for (a)-(a_3) 0 h, (b)-(b_3) 50 h, (c)-(c_3) 100 h and (d)-(d_3) 200 h.

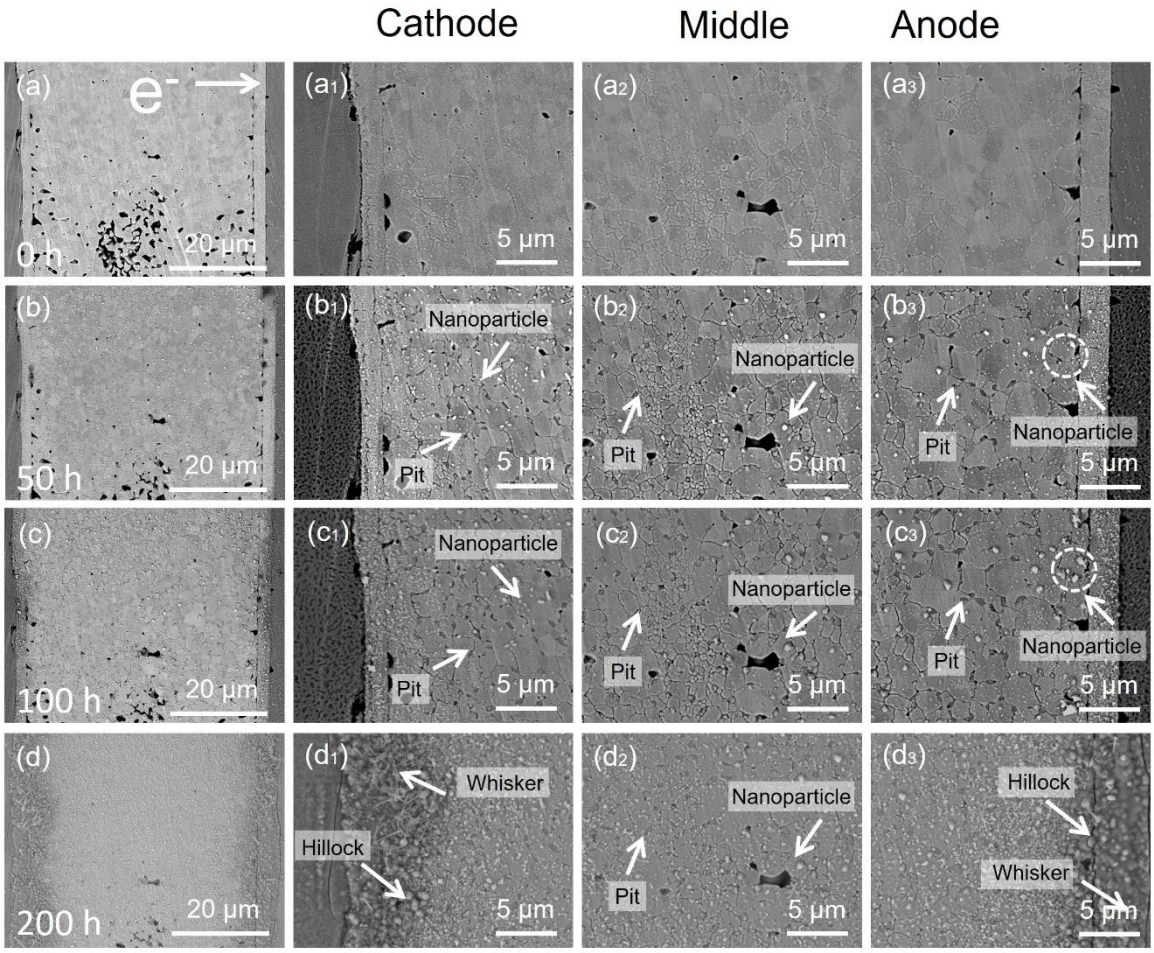

Fig. A-2.2 Morphological changes of EM-Ag with EM time. SEM images of EM-Ag with EM time for (a)-(a_3) 0 h, (b)-(b_3) 50 h, (c)-(c_3) 100 h, and (d)-(d_3) 200 h.

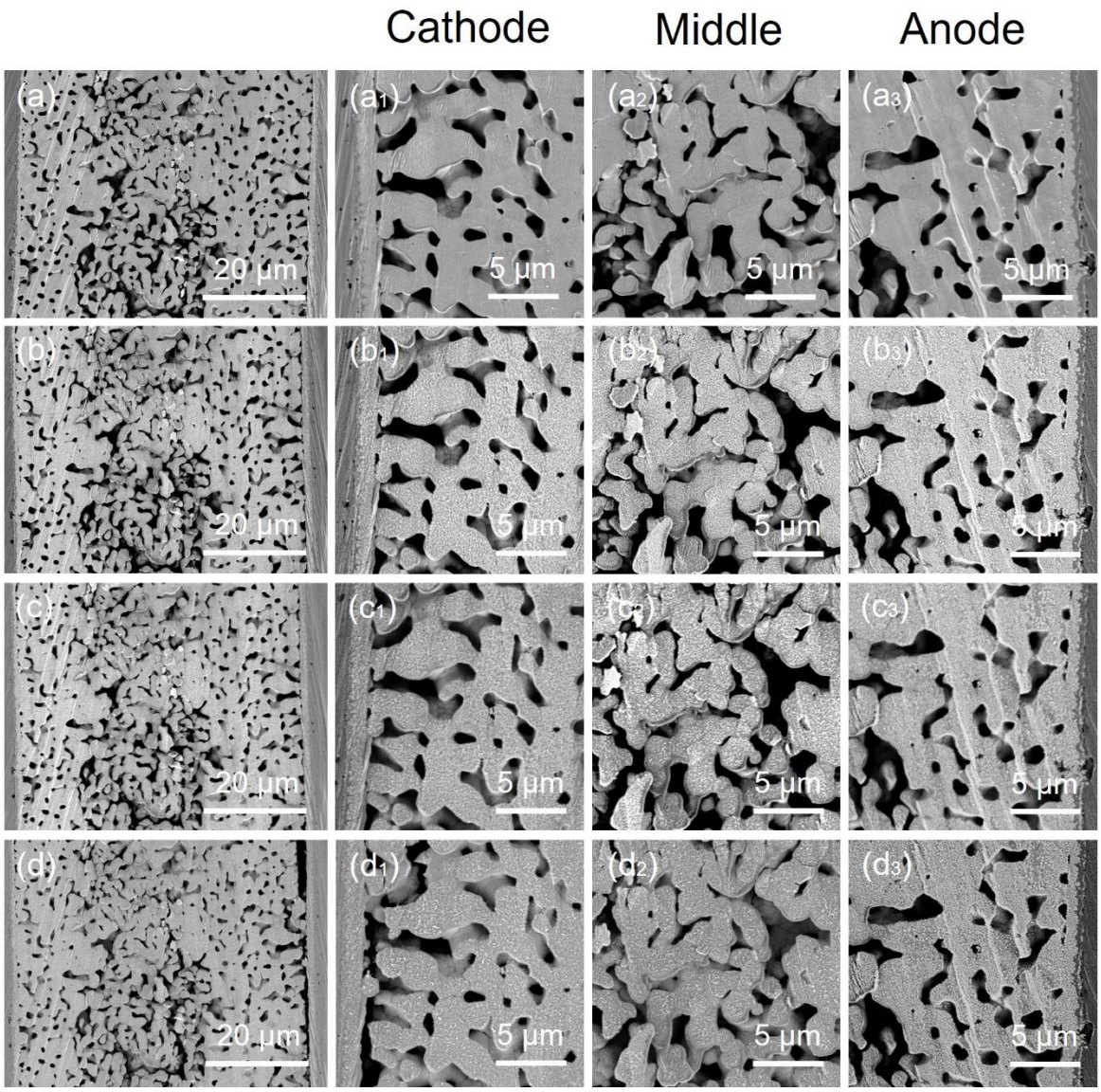

Fig. A-2.3 Morphological changes of porous EM-Ag with EM time. SEM images of porous EM-Ag with EM time for (a)-(a_3) 0 h, (b)-(b_3) 50 h, (c)-(c_3) 100 h and (d)-(d_3) 200 h.

Acknowledgment

I would like to express my sincerest gratitude to the people who have helped me during my doctoral course.

First of all, I would like to express my deepest appreciation to my supervisor *Prof. Hiroshi Nishikawa*, for providing me with the opportunity to conduct research in his laboratory and for guiding me in the writing of my thesis. In addition, the advanced equipment available in his lab helped me a lot in completing my doctoral research. His rigorous research attitude has had a great impact not only on my studies but also on my life.

In addition, I would like to express my gratitude to *Assoc. Prof. Hiroaki Tatsumi* for his guidance in my academic paper writing and experiments. Besides being a teacher, he is more like a friend. His optimistic attitude towards work and study has also encouraged me to overcome the difficulties in my life. I would also like to thank the professors in Shenzhen, *Prof. Pengli Zhu, Assoc. Prof. Liang Xu, and Prof. Tao Zhao*. They were so generous to provide an experimental opportunity for me when I was unable to enter Japan due to the epidemic. During this time, I was able to complete the initial feasibility study of my doctoral course, which saved me a lot of time.

I would also like to express my sincere gratitude to the members and alumni of Nishikawa Laboratory, *Dr. Runhua Gao, Dr. Zhi Jin, Dr. Jianhao Wang, Dr. Fupeng Huo, Dr. Xunda Liu, Dr. Peng Zhang, Ms. Sachiko Sakata, Mr. Ichizo Sakamoto, Mr. Takuya Naoe, Mr. Jiahui Li, Mr. Pak Seongwoo, Mr. Chi-hsuan Lin, Mr. Xinjie Wang, Mr. Yu-Yen Chen, Mr. Shunya Nitta, Ms. Ji-hyun Kim, Ms. Kasumi Koike*.

I would like to express my gratitude to the *China Scholarship Council* (*CSC*) for financial support. I also would like to express my sincere gratitude to my family and girlfriend, who helped me to release my stress during the doctoral course. Your companionship and waiting are the motivation for me to complete my doctoral program.

Research achievements

I list of publications

1. **C. Wang**, H. Tatsumi, L. Xu, T. Zhao, P. Zhu, R. Sun, H. Nishikawa, Transparent Liquid Ag-Based Complex for the Facile Preparation of Robust Sintered Ag Joints in Power Devices, ACS Appl Electron Mater 6 (2024) 1718–1728.

2. **C. Wang**, H. Tatsumi, H. Nishikawa, Thermal decomposition temperature-dependent bonding performance of Ag nanostructures derived from metal–organic decomposition, J Mater Sci 59 (2024) 19038–19056.

3. **C. Wang**, H. Tatsumi, H. Kotadia, H. Nishikawa, Substrate-Dependent Sintering Mechanism of Ag Nanostructures Derived from Ag-Based Complex, ACS Appl Electron Mater 6 (2024) 7360–7371.

II Conference

1. C. Wang, X. Zhang, Y. Zhang, T. Zhao, P. Zhu, R. Sun, H. Nishikawa, L. Xu, Pressureless and low temperature sintering by Ag paste for the high temperature die-attachment in power device packaging, in: 2022 IEEE 72nd Electronic Components and Technology Conference (ECTC), 2022: pp. 2256–2262.

2. C. Wang, H. Tatsumi, H. Nishikawa, Ag Sintered Joints on ENIG Cu Substrates by an Ag-Based Complex, in: 2024 International Conference on Electronics Packaging (ICEP), 2024: pp. 95–96.